Free surface disturbances and nonlinear runup around offshore structures

by

Clifford Owen Groome Ohl

The Queen's College

Oxford

Trinity Term 1999

A thesis submitted in partial fulfillment of the requirements for the degree of
Doctor of Philosophy at the University of Oxford

University of Oxford

Department of Engineering Science

Parks Road

Oxford OX1 3PJ

Free surface disturbances and nonlinear runup around offshore structures

Clifford Owen Groome Ohl

British Marshall Scholar

The Queen's College

A thesis submitted in partial fulfillment of the requirements for the degree of
Doctor of Philosophy at the University of Oxford

Trinity Term 1999

ABSTRACT

Diffraction of regular waves, focused wave groups, and random seas by arrays of vertical bottom mounted circular cylinders is investigated using theoretical, computational, and experimental methods. Free surface elevation η is the defining variable used to test the potential theory developed. In addition, the nonlinearity of focused wave groups is investigated through the Creamer nonlinear transform and analysis of numerical wave tank data.

Linear focused wave group theory is reviewed as a method for predicting the probable shape of extreme events from random wave spectra. The Creamer nonlinear transform, a realistic model for steep waves on deep water, is applied in integral form to simulate nonlinear focused wave groups. In addition, the transform is used to facilitate analysis of nonlinear wave-wave interactions within focused wave groups from a uni-directional numerical wave tank developed at Imperial College London.

Experiments in an offshore wave basin at HR Wallingford are designed to measure free surface elevation at multiple locations in the vicinity of a multicolumn structure subjected to regular and irregular waves for a range of frequencies and steepness. Results from regular wave data analysis for first order amplitudes are compared to analytical linear diffraction theory, which is shown to be accurate for predicting incident waves of low steepness. However, second and third order responses are also computed, and the effects in the vicinity of a second order near trapping frequency are compared to semi-analytical second order diffraction theory.

Analytical linear diffraction theory is extended for application to focused wave groups and random seas. Experimental irregular wave data are analysed for comparison with this theory. Linear diffraction theory for random seas is shown to give an excellent prediction of incident wave spectral diffraction, while linear diffraction theory for focused wave groups works well for linearised extreme events.

ACKNOWLEDGMENTS

I would like to acknowledge the generous support of the Marshall Aid Commemoration Commission, who funded the first two years of this work, as well as the new Oxford Marshall Scholarship programme, who provided the third year's funding. Furthermore, I wish to thank Catherine Reive and Beverly Potts, the most proficient administrators of these schemes, whose efforts are so well received yet rarely acknowledged.

To my supervisors, Prof Rodney Eatock Taylor and Dr Alistair Borthwick, I am grateful for their patience, support, encouragement, and faith when it was most needed. In addition, I wish to recognise the contributions of Dr Paul Taylor, whose work with me on the Creamer nonlinear transform has led to several publications. His further advice and aid in editing this thesis are greatly appreciated.

Subsequently, I thank Dr Roger Wilkinson, Director of the Offshore Group at HR Wallingford, for supporting the experiments conducted at his facility. Moreover, I thank the many technical staff whose efforts and ideas enabled the tests to proceed from concepts to reality. Specifically, I wish to mention John, Martin, and Wally at the offshore wave basin at HR, as well as Les Smith in the electronics workshop at HR for his expertise in wave probe design specifications and testing. I also thank John Hastings, head of the metal workshop at Oxford University's Department of Engineering Science, and Andy Soffe for their input in designing the wave probes and deck support structure and the expert construction of the same.

For showing me the road to Oxford and dragging me the first few meters, I thank Professors Thom Brennan and Dave Peeler of the US Naval Academy. I further thank Professors Rameswar Bhattacharyya and Dave Kriebel of the Naval Architecture, Ocean, and Marine Engineering Department at USNA, who assured me that they do, indeed, study the ocean at Oxford. Prof Kriebel taught me everything I used to know about waves and still more about writing technical reports; I can only hope that the figures contained herein are labelled sufficiently to suit his tastes.

I also thank my family for coping whilst I studied overseas and for understanding that I won't be returning in the near future. I especially thank my brother Raymond for his tireless support and encouragement, and I wish him luck in his parallel quest for a doctorate in Astronomy at the University of Virginia, NASA Goddard Space Flight Center, Johns Hopkins University, Cape Canaveral, and everywhere else he's been studying, researching, and working.

Finally, I thank the friends who have made my stay at Oxford (punting, rowing, theatre, diving, pubs, flying, concerts, dinners, drinks. . .) an unforgettable experience. Foremost, I should single out John "Bull" Tate, a true Old Taberdar; Mark "Jake-the-Snake" Ferrigan, philosopher, mechanic, aviator extraordinare; and Rashid Amin Khatib-Shahidi, an outstanding gentleman and future diplomat. Also, Alex "the Hun Scum" Menden, Joe "Smallwood" Smallwood, Simon "The Poet" East, Toby "Champagne Charlie" Stone, Matthew "Kids-need-love-too" Liao, Ara "Scrabblemaster" Barsam, Derek "Kevin Bacon Game" Kilmer, Ron "Indiana" Chen, Mark "Mr Congressman" Schneider, Jen "Marxist" Saunders, Sarah "Philosopher" Soong, Jeanne "Operastar" Fischer, Abhi "Stochastic" Sarkar, and, last but not shortest, Frank "Straightman" Pasquale. I trust we will maintain contact in succeeding years. I also thank Mary for her companionship in this most crucial final year.

Cliff Ohl, Oxford, Trinity 1999

Contents

List of Figures

Chapter 1
Introduction

Wave-induced free surface motions around offshore structures are modelled herein using analytical linear diffraction theory. In addition, experiments in an offshore wave basin at HR Wallingford have been designed and measurements undertaken. The results of subsequent data analysis have been compared to linear theory and, in certain cases, to semi-analytical second order diffraction theory. Particular emphases are given to large diameter multicolumn arrays, random seas, and focused wave groups (extreme or freak waves). The nonlinear nature of these events are examined through the Creamer nonlinear transform (CNT).

Diffraction theory assumes that viscous effects are negligible and fluid motions are small. This is valid for certain large bodies, including ships and floating platforms such as barges, and the columns of gravity based structures (GBSs), semi-submersibles, and tension leg platforms (TLPs).

1.1 Background

Offshore structures supported by large diameter columns vary from GBSs in relatively shallow waters to semi-submersibles and TLPs at greater depths. In such cases, the columns cause a significant disturbance to the ambient wave field and experience large runup effects (see below). Damage to the lowest decks of semi-submersible platforms (Eatock Taylor & Wu 1997) and gravity platforms (Swan, Taylor & Van Langen 1997) has been reported within the offshore industry. In addition, experiments on various multicolumn structures (Owen & Padilla Perez 1987 and Swan *et al.* 1997) have demonstrated higher than expected local wave elevations, which suggests the presence of certain nonlinearities.

Two closely related problems considered in the design of ocean platforms are 'upwelling' and 'runup.' Upwelling is the local modification (and possible amplification) of the incident surface wave in the vicinity of the hull form. In contrast, runup is the local modification immediately adjacent to a given surface-piercing element, leading to fluid flow on the surface of the body. These phenomena can cause local wave elevation to be significantly greater than that of the undisturbed incident wave and are of particular interest due to the growing numbers of large diameter, multicolumn offshore structures. From Swan *et al.* (1997) the Brent Bravo GBS model tests indicated the presence of significant runup around the columns and upwelling beneath the centre of the platform deck; this was most predominant in high waves (large steepness) of high frequency (short wavelength).

The reason for predicting upwelling and runup is the necessity for designers to maintain a sufficient air gap, which is the vertical distance from the underside of the platform deck to the wave crest in extreme design storm conditions. While the deck clearance must be sufficient such that the wave does not strike the lower deck, it must also be minimized in order to avoid raising the centre of gravity and exposed vertical surface area of the platform, which may affect the wind loading and will increase the wind overturning moments. Aside from elevation effects, upwelling alters the local wave kinematics near the platform. If such an alteration results in increased horizontal velocity, drag forces may be amplified on low-level appendages such as conductors and risers.

As demonstrated in the experiments of Swan *et al.* (1997) on a structure of three bottom mounted, tapering columns, both upwelling and runup as well as the associated structural forces may be amplified significantly at specific incident wave frequencies. These critical frequencies may be associated with a phenomenon known as near-trapping, which is dependent upon the geometry of the structure (cylinder diameter and spacing) relative to the wavelength. The terminology is based upon the similarity to trapping of waves near a body in a long narrow channel, in which energy at specific frequencies is bound near the surface of the body and does not radiate to infinity. However, due to the presence of far field radiation from cylinder arrays in the open ocean, the events are known as near-trapping.

1.2 Literature Review: Diffraction Theory and near-trapping

The following sections discuss the development of potential-based diffraction theory and the analysis of near-trapping events. Diffraction theory is discussed from both linear (first order) and nonlinear (higher order) theories for a single cylinder through to arrays of circular cylinders. In addition, some results of numerical wave tank simulations and experimental comparisons are presented. The trapping of waves in a channel and over various bottom topographies is discussed, along with the analysis of near-trapping for cylinder arrays.

1.2.1 Linear diffraction

Wave body interaction analysis is a three-dimensional, fully nonlinear problem, which, even in regular seas, remains unsolved. However, given certain assumptions and simplification, low order analytical models have been derived. If the typical dimension (i.e. column diameter) is large compared with the surface wave amplitude and wavelength, then viscous effects can be neglected and diffraction effects are dominant. In addition, the flow is assumed to be incompressible and irrotational; and surface tension effects are assumed to be negligible. These last three assumptions imply that the flow field can be represented by a scalar velocity potential, satisfying the Laplace equation within the fluid domain. While there is an implicit time dependence in the velocity potential, the problem is studied in the frequency domain, which reduces computation time. Through a perturbation expansion, this potential may then be expressed as the sum product of linear and higher order components and some small expansion parameter. The potential may then be solved at each order successively by using the lower order solutions to generate the boundary conditions necessary to solve for the higher order components.

Solutions of the first order (linear) diffraction problem have been successfully applied and are generally accepted in the offshore industry. Work in this area was begun by Havelock (1940), who developed a closed form analytical solution for the diffraction of incident regular waves from a single cylinder in water of infinite depth. This result was extended to finite water depth by McCamy & Fuchs (1954). Comprehensive reviews of analytical and numerical analyses were undertaken by Yeung (1982) and Mei (1983).

Based on linear potential theory, Hung, Sincock & Eatock Taylor (1987) produced numerical studies of upwelling, free surface elevation, and the related local kinematic effects around various surface-piercing structures; Owen & Padilla Perez (1987) ran parallel experimental investigations. Generally, the model test results agreed well with the theoretical predictions and confirmed the suitability of linear analyses for preliminary platform design. However, some significant discrepancies between the physical and numerical models could be attributed not only to viscous effects, but also to nonlinearity of the potential flow.

1.2.2 Higher order diffraction

The primary obstacle in developing higher order diffraction theory is the inhomogeneous free surface boundary condition, which must be addressed at second order. This problem requires an integration, containing quadratic products of the first order velocity potential and its derivatives, over the entire free surface. In 1989 Chau completed a summary of several of the major developments to that date and some new techniques for the integral evaluation.

In treating the forces only, Lighthill (1979) noted that the second order problem in regular waves can be considered in the same way as for the first order but with the addition of an apparent fluctuating pressure distribution on the free surface, at a frequency double that of the first order wave. Proportional to the nonlinear free surface boundary condition and a result of the first order wave analysis, this double frequency pressure distribution is derived from the first order solution and may be used in the solution of second order forces.

Moving away from consideration of forces only and extending the analysis to the explicit second order velocity potential, Molin (1979) likened this second order problem to a forced mechanical oscillation and separated it into the following two components:

(1) a forced, 'locked-wave' component which satisfies the inhomogeneous free surface condition.

(2) a 'free-wave' component which satisfies the homogeneous free surface condition.

Based on the above velocity potential decomposition, Kriebel (1990) developed a second order solution for the diffraction of a monochromatic wave (a regular wave of single frequency component) with a bottom mounted, circular cylinder. Using the velocity potential solution to determine the theoretical free surface elevation around the cylinder to second order, he predicted that the maximum second order runup on the cylinder exceeded that from the linear theory by more than 50% in cases of steep waves ($kA \geq 0.25$, where k and A are the wavenumber and wave amplitude, respectively). Subsequently, Kriebel (1992) conducted laboratory experiments measuring wave runup around a large diameter, vertical circular cylinder in monochromatic nonlinear waves. These confirmed that the second order theory explains a significant portion of the nonlinear runup. For very steep waves in deep water ($kA \geq 0.25$ and $kd \geq 1.5$, where d is the water depth), measured maximum runup was found to exceed that of the linear theory prediction by 60 to 80%, while, in the same cases, the second order theory prediction was exceeded by only 20 to 40%.

Using the same locked- and free-wave component contributions, Eatock Taylor & Huang (1997a) presented a solution for the second order potential generalized for an axisymmetric body in monochromatic waves. In addition, Huang & Eatock Taylor (1996a) developed a semi-analytical solution of the second order problem for monochromatic waves passing a truncated vertical circular cylinder (i.e. a surface piercing cylinder not extending to the sea floor) at finite water depth. To satisfy the boundary condition beneath the cylinder, the fluid domain is divided into two regions, where first and second order velocity potentials are described separately and matched on the interface using the pressure and normal-velocity continuity conditions. Numerical results obtained from this solution indicated that both the first and second order free surface elevation in the vicinity of a truncated cylinder are, in many cases, very close to those obtained for bottom-seated cylinders. Again, for large amplitude waves, it was often found (Eatock Taylor & Huang 1996a and 1997a) that the maximum free surface elevation predicted by second order theory significantly exceeded that given by linear theory.

Following on from previous results for second order diffraction from a bottom mounted circular cylinder in regular waves (Kim & Yue 1989), Kim & Yue (1990) generalized the second order theory to include bichromatic waves (i.e. those containing two frequency components). This was further extended to solve the case of truncated cylinders in bichromatic waves by Eatock Taylor & Huang (1997b) for the second order velocity potential. Considering incident, diffracted, and radiated potentials, the bichromatic problem requires the solution of wave-body interactions at the sum and difference frequencies for all possible pairs of the frequency components of the incident waves. With increased complexity, this extension allows the application of the second order theory to Gaussian irregular incident waves conforming to some given spectrum.

Studying a vertical bottom mounted circular cylinder in regular waves, Malenica & Molin (1995) used eigenfunction expansions and an integral equation technique to develop expressions for the third order velocity potential. However, they only considered velocity potential components relevant to the calculation of third order forces and did not develop any expressions for the third order diffracted free surface elevation. While first and second order results were verified through comparison with the free surface elevation calculations of Kim & Yue (1989), third order force calculations were compared with experimental data (Moe 1993). The structure tested was a 1:40 scale model of a single truncated cylinder from the Snorre TLP, with full scale radius 12.5m and draught 37.5m. These experiments tested incident wave frequencies within the range $0.2 < ka < 2.1$, where k is the wavenumber of the first order incident wave and a is the cylinder radius. For comparison with their theory for bottom mounted cylinders, Malenica & Molin chose these tests of a truncated cylinder as "for $ka > 1$ the first order wave field hardly reaches the bottom of the column and both structures can be regarded as equivalent (for the first- and third-order loads; not for the second-order ones!)." In addition, second order loads measured during these experiments showed very close agreement with calculated values. However, the third order force measurements showed significant scatter, causing comparison with the theoretical values to be inconclusive. With regard to the validation of their theory, Malenica & Molin expressed regret over the lack of reliable experimental data and the possibility that physical experiments were insufficiently reliable for the measurement of third order forces.

1.2.3 Diffraction from cylinder arrays

In the case of a wave incident on an array of bodies, computation of the velocity potential must account for both the diffraction of the incident field by each body and the multiple scattering due to the other bodies. This multiple scattering is such that a portion of the scattered wave from each individual body is directed towards the other bodies in the array. Responding in turn to this secondary excitation, these bodies send corresponding radiation waves, which may be received and returned in a like manner, and so on. All of this radiated wave energy contributes to the total excitation and scattering of the original bodies in the array. First identified in studies of pile arrays and twin-hull vessels, early work on this problem was limited to the evaluation of forces, to include the amplitude and phase of the first order force and the mean second order drift force, which may be calculated from the first order potential (Kagemoto & Yue 1986).

One solution to the full hydrodynamic interaction problem is the calculation of diffraction by the entire array of bodies acting as a single unit; several numerical methods (utilizing hybrid element method) for this calculation are available as discussed by Mei (1978). However, as the number of members increase, such computations become difficult. Alternatively, a diffraction solution may be found for individual bodies in the array and multiple scattering for the array configuration may be modelled through an interaction theory based upon the individual body properties.

Studying the two-dimensional scattering of acoustic radiation by an array of circular cylinders, Twersky (1952) developed an iterative method which included successive reflections among the cylinders. An addition theorem for the cylindrical wave functions was used to express the waves around one cylinder in terms of the waves at the other cylinders. This iterative method for multiple-scattering computation was later extended to surface waves. However, as the number of interacting wave components grows rapidly as the number of bodies in the array increases, the calculation becomes unmanageable and convergence could not initially be proven (Linton & Evans

1990).

A third possibility, the direct matrix method can be used to solve for the amplitudes of the wave components around each body simultaneously based on the boundary conditions of the respective bodies. Approximating the circular scattered waves emanating from a given body as a plane wave at the other body, Simon (1982) produced a substantially simplified direct matrix solution of a uniformly spaced linear array of axisymmetric bodies in heaving motion only. Replacing diverging waves at one body caused by the scattering of another body with a single plane wave, the approximation is valid only for large-spacing and has been shown to introduce significant errors in some cases (see Kagemoto & Yue 1986). This simplification is known as both the plane-wave and wide-spacing approximation. McIver & Evans (1984) extended the last approach to study wave forces on arrays of fixed vertical circular cylinders. They included a correction term in this plane-wave approximation and obtained improved results over Simon at smaller cylinder spacing (in relation to wavelength).

The above wide-spacing approximation assumes that the amplitudes of the local waves due to one body is negligible at neighbouring bodies and the evanescent wavefield in the interaction may be ignored. However, for typical body dimension $2a$ (cylinder diameter, with cylinder radius a), interbody spacing $2h$, and wavelength λ (with wavenumber $k = \frac{2\pi}{\lambda}$), this wide-spacing assumption can take several forms. Srokosz & Evans (1979) based the assumption on large spacing in comparison to wavelength ($kh \gg \frac{1}{2}$). The other relevant parameter is the ratio of interbody spacing to body dimension, $\frac{h}{a}$. Even for small kh but fixed, large values of $\frac{h}{a}$, Srokosz & Evans obtained good results for two widely spaced rolling plates in two dimensions (i.e. vertical hinged wave absorbing plates). Comparisons between the results of exact calculations and those assuming wide-spacing for two-dimensional vertical cylinders showed that, for fixed $\frac{h}{a}$, the results did not always improve with increasing kh while, for fixed kh, the error clearly reduced as $\frac{h}{a}$ increased (Kagemoto & Yue 1986). Practically, for small $\frac{h}{a}$, local waves must be present regardless of wavelength; while, for $\frac{h}{a} \gg 1$, overall interaction effects and the relative importance of evanescent waves diminish.

Finally, for the validity of this wide-spacing approximation, initial conclusions were that both parameters are critical (i.e. $kh \gg \frac{1}{2}$ and $\frac{h}{a} \gg 1$). However, upon introduction of a finite water depth d, the analyses and numerical results of Kagemoto & Yue (1986) showed $\frac{h-a}{d} \gg \frac{1}{2}$ to be a more critical condition for validity. In addition, for fixed $\frac{h}{a}$ and $\frac{d}{a}$, they demonstrated the increased importance of evanescent wave interactions for shorter waves.

Combining the multiple-scattering technique and the direct matrix method discussed above, Kagemoto & Yue (1986) developed an exact algebraic method for calculating the wave hydrodynamics of an array of bodies, based on the diffraction properties of an isolated body. The wavefield around each body is represented as a series of waves of undetermined amplitude. A transformation is then applied to express the influence of the wave system at one body in terms of those at the other bodies. Through this, a set of linear algebraic equations is derived to satisfy the diffraction characteristics of the array of bodies. The system is then solved simultaneously for the unknown amplitude coefficients, the number of unknowns being NM for N bodies and M average wave components per body. Assuming linearised diffraction theory, an adequate number of terms, and no member overlap, this method is applicable to any number of bodies of arbitrary geometry and configuration. However, as would be expected, the calculations are greatly simplified for axisymmetric bodies.

In comparison to numerical results from a model of the entire assembly using a three-dimensional hybrid-element diffraction method, the above theory of Kagemoto & Yue (1986) was found to give reasonable agreement for several configurations of two and four truncated or bottom-seated vertical cylinders for all first order quantities. In addition, application of the theory to an array of 33 composite cylindrical legs produced results similar to experimental data from model tests for a proposed floating airport.

Eatock Taylor & Sincock (1989) applied a hybrid boundary element technique to provide a linear diffraction analysis for complex geometries. Through the computer program DYHANA, this hybrid technique coupled a finite element discretisation of the inner flow field near the structure with either a boundary element (boundary integral element; BIE) or an eigenseries representation (boundary series element; BSE) of the outer far field behaviour. The velocity potential was then solved for at the nodes of the inner finite element domain and along fictitious boundaries throughout the fluid. To verify the accuracy of the method in comparisons with the closed form solution of McCamy & Fuchs (1954), single cylinder results were produced which showed a 5% maximum error in the modulus of the scattered velocity potential. This hybrid method was then used to compute the upwelling of regular waves in the vicinity of a TLP structure with 4 truncated columns arranged at the corners of a square and connected by horizontal pontoons. Although maintaining a square configuration, cylinder spacing was varied from $h = 2a$ to $6a$ (where $2h$ is the separation between the cylinder centres and a is the cylinder radius). Finally, some results for random seas were calculated based on modification of the mean square surface amplitude for an incident spectrum. While the resultant profiles resembled the regular wave calculations, the overall magnification effects were substantially reduced (i.e. from an 80% increase in runup on the cylinder to a 25% increase relative to the incident wave). However, these calculations were limited to frequencies below 1.14 $\frac{\mathrm{rad}}{\mathrm{s}}$, the maximum frequency for which the diffraction analysis was computed.

Concentrating on bottom mounted circular cylinders and simplifying the velocity potential expression in the vicinity of a particular cylinder, Linton & Evans (1990) improved significantly the above direct matrix method. Their method provided simple formulae for the first and mean second order forces on the cylinder in the array and also an efficient method for the calculation of the first order velocity potential (from which follows the free surface amplitude). Subsequently, free surface elevation calculations for the diffraction of two circular cylinders were compared with free surface elevations calculated using the wide-spacing assumption and plane-wave approximation of McIver & Evans (1984), as discussed above. For the two cases presented, $h = 8a$ and $h = 2.4a$, the maximum error was found to be less than 6% and approximately 15%, respectively. In addition, the two methods were seen to produce progressively similar results as the wavelength increased (i.e. lower kh) and the magnitude of the scattered wave decreased relative to the incident. This is then in contrast with the previous assumption (see above) of $kh \gg \frac{1}{2}$ for plane-wave approximation validity.

Subsequently, Kim (1993) extended the above theory to the complementary radiation problem. Obtaining analytical radiation potentials for motions with six degrees of freedom as well as expressions for added mass and wave damping, he expressed the local, evanescent waves in the radiation problem (i.e. the standing wave system around the body). Kim (1993) generalized this theory for application to arrays of deep-draft truncated vertical circular cylinders and the study of multiple cylinder configurations such as tension-leg platforms and semi-submersibles.

A semi-analytical solution to the second order diffraction from an array of vertical bottom mounted circular cylinders was presented by Malenica, Eatock Taylor & Huang (1999). A continuation of similar approaches that were initiated independently by Huang & Eatock Taylor (1996b) and Malenica (1997), the method obtains the second order potential by combining eigenfunction expansions with an integral representation. Solution of this potential allows computation of local flow characteristics, such as free surface elevation, pressure, and velocities, as well as the evaluation of third order forces. To validate the method, two primary comparisons were made. Second order surge forces on a four column structure were compared to those computed by Chen, Molin & Petitjean (1995), using an indirect method from the first order velocity potential. In addition, the vertical distributions of the second order potential on two cylinders were compared with those obtained by Chau (1989) through a boundary integral equation technique. Both of these comparisons were found to be favourable, and further results were published to serve as a benchmark for subsequent work.

One alternative to the analytical and semi-analytical approaches above has been presented by Ferrant (1999), using a boundary element method (BEM) and time domain simulation to calculate the fully nonlinear diffraction from arrays of bottom mounted circular cylinders. Based on potential flow theory, the solution has the advantage of substituting an absorbing zone on the outer free surface mesh for the corresponding radiation condition of analytical methods. In addition, with a reduction in computing time requirements, the method may eventually allow for interaction of a complex wave system with a body. Nonlinear incident regular waves were represented analytically through a stream function model and expressed as a truncated Fourier series.

Validation of the above model for a single vertical circular cylinder was presented through comparisons with both analytical methods and experimental measurements. For waves of very low steepness ($kA = 0.06$, $\frac{A}{\lambda} = \frac{1}{105}$), the third order force calculations of Ferrant (1999) were found to compare very well with the previous analytical results of Malenica & Molin (1995). However, investigations of the influence of wave amplitude for this single cylinder case revealed significant differences between the two methods. For example, at $kA = 0.12$ ($\frac{A}{\lambda} = \frac{1}{52}$), the third order force predicted by the analytical theory exceeded the fully nonlinear result by 18%. Comparisons with the experimental third order force measurements of Huseby & Grue (1998), testing a single cylinder in long waves at the University of Oslo, were made for $ka = 0.245$ and steepness varying from $kA = 0.05$ to 0.15. Although again some oscillations were found in the experimental data (see Malenica & Molin 1995 above), very close agreement was achieved. Finally, profiles of fully nonlinear runup were compared with the results of first and second order analytical methods for $ka = 1$ and $kA = 0.005$, 0.025, and 0.15. According to Ferrant, "the runup at the waterline is a very sensible local quantity which is very demanding in terms of accuracy." For $kA = 0.005$ the fully nonlinear runup was found to be identical to the second order results, and only a small difference (less than 5%) was found at the rear part of the cylinder for $kA = 0.025$. However, for the steepest wave ($kA = 0.15$), considerable differences existed between the fully nonlinear and second order runup, with fully nonlinear runup exceeding the second order analytical runup by approximately 10% at the front of the cylinder.

Finally, results were also presented for an array of four bottom mounted vertical cylinders centred at the corners of a square with side length $2h = 8a$ in water of depth $d = 10a$. Moderate steepness ($kA = 0.094, ka = \frac{\pi}{5}$) incident waves were simulated at a heading of $\beta = 0°$ (two upwave and two downwave cylinders) for a duration of 10 wave periods. Force calculations revealed significant differences between the forces on the cylinders, with second order forces on the upwave cylinders 5 times that on the downwave cylinders. Third order forces were found to be twice as large on the upwave cylinders relative to the downwave cylinders, whereas drift forces were primarily concentrated on the downwave cylinders. In addition, the maximum free surface observed in the steady state nonlinear simulation was compared with a corresponding linear result. Significant differences were noted in the free surface elevation between the upwave cylinders, where the nonlinear analysis yielded short resonant waves, possibly correlated with the large second and third order forces on these cylinders. Validation of this multiple cylinder method through comparison with analytical theories or experimental data was identified as a future objective.

1.2.4 Numerical wave tank simulations

Aside from the analytical methods employing velocity potential theory as discussed above, other methods of computing the free surface around a three dimensional body include numerical wave tank (NWT) simulations, which may include many nonlinear effects. These NWT methods differ from the above approach of Ferrant (1999) in that they simulate the process of incident wave generation and propagation. Through a finite difference scheme, Park, Kim & Miyata (1999) developed an NWT based on a modified marker and cell (MAC) method and solution of the Navier-Stokes (NS) equation for two fluid layers. Viscous stresses and surface tension were neglected in the dynamic free surface condition, while the fully nonlinear kinematic free surface condition was applied. Incident waves were simulated from the velocity profile of a flexible flap wavemaker at the inflow boundary, while waves passing out of the NWT were numerically dissipated in a damping zone at the tank end.

Utilising particles specified with fluid velocity according to their location, the MAC method identifies marker particles throughout all the fluid occupied regions and requires significant computer storage for large computations. However, the modified MAC method of Park *et al.* (1999) reduces the storage required by identifying marker particles only on the free surface and making use of a marker density function M_ρ, which takes the average value of the density in the free surface cells and provides an indication of the amount of water and air in a given cell. Similar to the fractional volume of fluid (VOF) method (Hirt & Nichols 1981), this modified MAC method identifies the free surface as a point where M_ρ takes the mean value of the density of the two fluids. By not specifying the exact location of the free surface elevation η, this method allows the consideration of overturning and breaking waves, including the spray and foam associated with these highly nonlinear processes.

Simulating a truncated vertical circular cylinder in a rectangular wave tank, Park *et al.* (1999) compared their NS-MAC NWT results with the experimental results of Mercier & Niedzwecki (1994). Comparison was also made with the fully nonlinear potential-based desingularized boundary integral equation method (DBIEM) NWT of Celebi, Kim & Beck (1998) and the analytical second order diffraction computations of Kim & Yue (1989), as discussed above. Conducting experiments at the OTRC wave basin (50 m × 33 m × 6 m deep) at Texas A&M University, Mercier & Niedzwecki (1994) measured upwelling and runup at five locations near the vertical truncated cylinder (radius 23 cm, draft 1.34 m), as well as horizontal forces and pitch moments and hydrodynamic pressure at the bottom centre of the cylinder. The model was tested in regular waves of periods ranging from $T = 0.7$ to 2.5 s, and equivalent NWT results were computed by Park *et al.* (1999) for $T = 0.87$, 1.00, 1.40, and 2.00 s for constant wave steepness of $\frac{H}{\lambda} = \frac{1}{21}$, where H is the incident wave height.

Through FFT analysis, results were separated into first, second, and third order components. In the free surface elevation measurements, Park *et al.* (1999) found very close agreement between their NS-MAC NWT method, the previous DBIEM NWT, and the experimental results at first order, while the analytical first order diffraction computation was found to be slightly less accurate. In particular, at wave probe locations upwave of the cylinder, on the upwave cylinder face, and to the side of the cylinder, runup and upwelling were significantly underpredicted (by as much as 20% at $T = 0.87$ s for runup at the upwave cylinder face). At second order, results from the NS-MAC and DBIEM NWTs continued to compare well with those of the experiments. In contrast, the analytical second order diffraction computation was found to greatly overpredict the amplification of higher frequency waves, particularly on the cylinder surface, where second order runup on the upwave and downwave surfaces was overestimated by factors of 6 and 3, respectively. Finally, at third order, the NS-MAC and DBIEM NWTs provided reasonable agreement with experimental results apart from runup on the cylinder surface for the shorter period waves, which was either overpredicted by as much as a factor of 2 or underpredicted by 80% for $T = 0.87$ s. However, Mercier & Niedzwecki (1994) found that the wave amplitude at this period was insufficient and may have resulted in unreliable data.

The above results of Park *et al.* (1999) provide strong evidence for the use of NWT simulations in the computation of diffracted wave fields around three dimensional bodies in steep waves and for the preference of these methods over analytical diffraction theory, particularly for high frequency waves (short period).

1.2.5 Trapping and near-trapping of waves

Ursell (1951) first identified trapped modes in first order wave theory in his study of a submerged horizontal cylinder in an open channel, corresponding to a long narrow wave tank. With the restrictions of small radius and infinite depth, he proved that, while some energy radiated to infinity, energy at discrete frequencies below a certain cutoff was trapped near the cylinder and did not radiate. Utilizing the theory of elliptic partial differential equations in unbounded domains, Jones (1953) extended this to include submerged cylinders of arbitrary cross-section, but symmetrical about a vertical plane. Subsequently, Ursell (1987) then reproduced this result using the theory of bounded symmetric linear operators and Kelvin's minimum energy theorem of classical hydrodynamics.

Prompted by the observation of regular large amplitude oscillations in the vicinity of an island, Longuet-Higgins (1966) demonstrated the trapping of wave energy around islands. Using first order inviscid shallow water theory to study a submerged circular sill and various bottom contours, he proved the existence of certain eigenfrequencies at which the rate of decay was extremely slow. Essentially due to internal reflections at the sill's edge and dependent upon the sill's dimensions, Longuet-Higgins made the analogy with a resonating bell, whose energy radiates slowly to infinity. Renardy (1983) refined the analysis of Longuet-Higgins through a full linear theory for both inviscid and weakly viscous fluid and obtained results comparing favourably with experimental studies as cited therein.

Evans & Linton (1991) made numerical calculations for a vertical cylinder of rectangular cross-section placed at the centre of a long narrow wave channel and, subsequently, for symmetric rectangular indentations in the tank walls. With the origin at the cylinder centre and for a tank of width $2h$ and depth d, a Neumann boundary condition of no flow ($\frac{\partial \Phi}{\partial y} = 0$ on $y = h$) was imposed at the tank wall. The lowest cutoff frequency for this Neumann mode was then calculated as $w_c = \sqrt{gk_c \tanh k_c d}$, $k_c h = \frac{\pi}{2}$. Dependent upon the dimensions of the rectangular cylinder relative to the channel and for discrete values of $k < k_c$, trapped modes were found antisymmetric about the vertical centreplane of the wave tank and either symmetric or antisymmetric about a transverse vertical plane through the cylinder centre (i.e. normal to the tank sides). Finally, Evans & Linton extended the work on trapped waves from the surface wave problem to more general cases governed by the Helmholtz equation, to include acoustic waves.

Proceeding with the similar case of acoustic waves, Callan, Linton & Evans (1991) studied trapped modes within a two-dimensional waveguide of two parallel lines, separated a distance $2h$ and enclosing a circle of radius $a < h$ positioned along the centreline. This case can be equally applied to surface waves in a narrow wave tank, as above, enclosing a vertical bottom mounted circular cylinder. Subsequently, Evans *et al.* (1994) extended this analysis to prove the existence of at least one trapped mode for an obstruction of fairly general shape, but symmetric about the centreline of a two-dimensional acoustic waveguide. Evans *et al.* applied a Dirichlet condition ($\Phi = 0$ on $y = h$), causing the dynamic pressure to vanish on the waveguide wall. Having no physical interpretation in the context of water waves, this Dirichlet mode has a somewhat higher wavenumber cutoff at $k_c h = \pi$.

Maniar & Newman (1997) utilized Linton & Evans' (1990) method to study the forces on bottom mounted circular cylinders. With waves incident at angle β relative to the x-axis and in water of depth d, Maniar & Newman considered a long array of N cylinders (primarily $N = 100$) with radius a, spacing $2h$, aligned along the x-axis at $y = 0$. For $\beta = 90°$ and $N = \infty$, this configuration is identical to a single cylinder of radius a at the centre of a narrow channel of width $2h$ as described above.

Identifying the spacing to wavelength ratio kh as the most significant in terms of scattering, Maniar & Newman (1997) examined the force on a single cylinder in an array relative to the force on a single isolated cylinder, identified here as $\frac{|X^j|}{|F|}$. For longer wavelengths, $\frac{kh}{\pi} < 0.3$, $\frac{|X^j|}{|F|}$ was found to be very near unity. However, for kh slightly less than $\frac{n\pi}{2}$, where n is an integer, a sequence of narrow peaks were found in the plot of $\frac{|X^j|}{|F|}$ versus kh. For $N = 9$, $\beta = 0°$, and two configurations of $\frac{a}{h} = \frac{1}{2}$ and $\frac{1}{4}$, this highest peak was approximately three times the force on a single isolated cylinder. Corresponding to the cutoffs for Newman and Dirichlet modes as identified above, these peaks were located at kh slightly below $\frac{\pi}{2}$ and π for $\frac{a}{h} = \frac{1}{2}$ and $\frac{1}{4}$, respectively.

In subsequent examples (Maniar & Newman), with $N = 100$, $\beta = 0°$, and $\frac{a}{h} = \frac{1}{2}$, the maximum load on any cylinder was found to be $\frac{|X^j|}{|F|} = 35$ at $kd = 1.39071$. This amplification was shown to increase without limit as N increases; but, for a large, finite array, pure trapping proved to be impossible due to energy radiation in the far field. Also, for a range of headings β, near-trapping was observed at kh similar to those identified as trapping modes in the above studies of cylinders in the centre plane of a channel. However, the Dirichlet mode was found to exist only for $\frac{a}{h} < 0.677$, while other, smaller peaks were observed at higher wavenumbers, corresponding to weakly damped modes where radiation is small but non-zero. Finally, Maniar & Newman (1997) made the practical observation that, with the consideration of viscous damping and other nonlinear effects, the excessive free surface amplitudes and peak loads predicted would be substantially reduced.

Returning to the problem of cylinders within a channel, Evans & Porter (1997a) applied multipole expansion methods and addition theorems for Bessel functions to generalise the above results of Callan *et al.* (1991). Evans & Porter extended Callan *et al.'s* analysis to N bottom mounted circular cylinders of arbitrary size, with arbitrary spacing along the centreline of a long narrow wave tank. Again studying the trapped modes antisymmetric with respect to the channel centreplane, Evans & Porter identified both Neumann and Dirichlet modes, corresponding to zero normal velocity and zero dynamic pressure on the channel wall, respectively. Evans & Porter (1997a) demonstrated that $\leq N$ trapped modes existed, with the exact number dependent upon the geometry. In addition, they refined the above estimate of Maniar & Newman (1997) and established the physical limit for the existence of Dirichlet modes as $\frac{a}{h} \leq 0.6789$ for a single cylinder. This limit was found to increase with the addition of a second, identical cylinder and increasing distance between cylinders.

Motivated by the work of Maniar & Newman (1997), Evans & Porter (1997b) studied near-trapping effects on arrays of N bottom mounted cylinders of radius a. These cylinders were equally spaced along the circumference of a circle, with centre to centre spacing $2h$, gap between cylinder surfaces g, and heading $\beta = 0°$. For discussion and standardisation, a gap-to-diameter ratio was defined as $\frac{g}{2a} = \frac{h}{a} - 1$. Again using the first order theory of Linton & Evans (1990), Evans & Porter concentrated on the cases of $N = 4$, 5, and 6, due to their direct relevance within the offshore industry. In one example, plotting $\frac{|X^j|}{|F|}$ versus ka for $N = 4$ and varying the spacing from $\frac{a}{h} = 0.5$ to 0.8 ($\frac{g}{2a} = 1$ to 0.25), near-trapping peaks were observed from $ka \approx 1.66$ to 4.08 with $\frac{|X^j|}{|F|} \approx 2.3$ to 54.2, respectively. In addition, the free surface was found to be 3.5 and 150 times the incident wave amplitude, respectively, for the two cases. Analysing the effect of the gap-to-diameter ratio, it was found that both peak $\frac{|X^j|}{|F|}$ and $(ka)_{\text{peak}}$ increase with decreasing $\frac{g}{2a}$. Finally, through the complex roots of the system's determinant and introducing an integer p relating phase change between cylinders, Evans & Porter (1997b) developed expressions associated with the force peaks at near-trapping frequencies.

Using first order theory and the multipole expansion method, Utsunomiya & Eatock Taylor (1999) studied trapped modes around N bottom mounted vertical cylinders. The cylinders were equally spaced a distance $2s$ along a plane perpendicular to the walls of a long narrow channel, with distance s between the end cylinders and the channel walls. By cancelling standing wave components at large $|x|$, cutoff wavenumbers k_c were found at much higher values than the initial problem. Subsequently, for both Neumann and Dirichlet trapped modes, the existence of N trapped modes was then demonstrated, provided that $\frac{a}{s} \leq 0.6789$ (Evans & Porter 1997a). After this limit the highest trapped Dirichlet mode is lost and $N - 1$ trapped modes exist.

Utsonomiya & Eatock Taylor (1999) also made a comparison with the near-resonant phenomenon in a long array of cylinders, as discussed by Maniar & Newman (1997). Comparing Dirichlet trapped mode wavenumbers of the second highest modes in the channel with the wavenumber of the peak $\frac{|X^j|}{|F|}$ within the array, very close similarity was found as N increased for a range of $\frac{a}{s}$. A further analogy was made with the classic periodic structure of a mass-spring system, with fixed and free boundary conditions corresponding to Neumann and Dirichlet trapped modes, respectively.

Lastly, employing a semi-analytical diffraction theory for arrays of bottom mounted circular cylinders, Malenica *et al.* (1999) extended the studies of near-trapping in an array to second order. The authors divided the total second order free surface elevation $\eta^{(2)}$ into the following two parts: $\eta^{(21)}$, due to quadratic products of first order quantities, and $\eta^{(22)}$, directly from the second order potential. For $N = 4$ cylinders and water of depth $d = 3a$, the free surface elevation was then studied along the centreline of an array for two configurations, $\frac{a}{h} = 0.5$ and 0.6, for which Evans & Porter (1997b) had identified first order near-trapping at $ka = 1.66$ and 2.771. While both $\eta^{(21)}$ and $\eta^{(22)}$ were large at these first order frequencies, their relative phases were such that $\eta^{(2)}$ showed no significant response. However, analysing response at half the first order near-trapping frequencies, corresponding to $ka = 0.468$ and 0.600, the first order free surface and corresponding quadratic products, $\eta^{(1)}$ and $\eta^{(21)}$, were found to be low. In contrast, the contribution from the second order potential and the total second order free surface, $\eta^{(22)}$ and $\eta^{(2)}$, exhibited amplification as high as $\frac{|\eta^{(2)}|}{kA^2} = 40$ for $\frac{a}{h} = 0.6$. Coupled with studies of first and second order runup in the array as a function of ka for $\frac{a}{h} = 0.6$, these results suggest that second order near-trapping occurs when the frequency of the second order components is equal to the frequency of first order near-trapping.

1.3 Literature Review: Focused Wave Groups

The following sections discuss the development of the theory of focused wave groups and the derivation of the Creamer nonlinear transform (CNT). Also known as NewWaves, extreme waves, or freak waves, focused wave groups arise from the interaction of many spectral components within a random sea. The CNT, used for simulating wave-wave interactions in the spatial domain, may be used to analyse some aspects of the nonlinear interactions of these components.

1.3.1 Focused wave groups

As discussed by Tromans, Anaturk & Hagemeijer (1991), in regions such as the North Sea and the Gulf of Mexico, design criteria for offshore structures are largely driven by the estimated environmental loads induced by extreme storms in the region. In this structural design and assessment, the random condition is conventionally modelled using a deterministic, monochromatic, periodic wave theory that assumes the wave height and period to correspond to some extreme environmental condition (such as the highest wave arising on average in a three hour interval in the sea state of the most extreme storm expected in a one hundred year interval). Alternatively, a computationally demanding time domain simulation, including the random, spectral, and directional properties of the extreme storm, can be run to determine structural response within a given time interval (such as three hours in the above case).

Several accurate computational programs exist within industry for such time domain simulations of the above random wave problem (Tromans *et al.* 1991). In comparison with these solutions, deterministic calculations using the monochromatic wave method outlined above yield poor results. From Tromans *et al.* (1991), "the periodic wave used in deterministic practice tends to overestimate wave kinematics and hence the fluid load; by contrast the drag force coefficients in the Morison equation are too small and tend to underpredict the fluid load."

The dominant effect is dependent upon the structure's size and configuration and its environment. To avoid time domain computations while retaining the related accuracy, the deterministic method was reformulated using a probabilistic, focused wave group analysis. Accounting for the irregular shape and random background of large ocean waves, this method models the sea as a set of independent wavelets of random amplitude. Focused wave groups then occur at a point where the crests of many of the wavelets coincide. Calculating the most probable ocean surface elevation around a crest, this analysis includes all spectral properties of the sea-state.

Van de Graaf & Tromans (1991) used this method to produce a first order model that successfully predicted the damage to an early structure in the Gulf of Mexico caused by an extreme hurricane load. In 1991, Tromans *et al.* outlined the derivation of this theory, and demonstrated its use in the prediction of extreme loads on single columns and arrays. Results were subsequently compared with those of deterministic solutions (using Stokes fifth-order wave kinematics) and time domain simulations. Results from the focused wave group analysis were found to resemble closely those of the time domain, while the periodic wave method was seen to render poor results, most particularly as the depth decreases.

Noting that the kinematic uncertainties of irregular water waves are most severe at the free surface of an extreme crest (where the kinematics are largest), Taylor (1992) extended the above first order model to incorporate the effects of the lowest order nonlinearities in the fluid mechanics. Most significantly, his model addressed the straining and advection of short wave components by longer waves in the spectrum and allowed for more accurate prediction of the free surface elevation, horizontal fluid velocities, and related forces.

Total force estimates from Taylor's theory beneath the extreme crest compared well with those of an empirical delta-stretching model, which modifies linear wave theory for the estimation of wave kinematics above the still water level. While this empirical model applies only for broadbanded wave spectra, the fully-nonlinear model is valid irrespective of spectral shape and "reflects the relative importance of both nonlinearity and spectral bandwidth on both surface shape and flow kinematics," according to Taylor (1992). A summary of this theory's derivation and a discussion of its further application are provided by Eatock Taylor & Wu (1997), who also provided results for the diffraction of extreme, focused waves upon a single cylinder.

Jonathan & Taylor (1995) provided detailed comparisons between the predictions of focused wave group theory and measurements made offshore in the North Sea. Measurements were taken from two free surface elevation sensors (one radar and one laser sensor separated approximately 40 m) and a water particle velocity meter all mounted on Shell's Tern platform. The 9 hours of analysed data were from a storm with significant wave height and peak period relatively constant at $H_s = 12$ m and $T_p = 14$ s and a spectral tail decaying with ω^{-4}. The large nonlinear crests from the record were linearised by subtracting the averaged large crest and large trough profiles. This effectively removes second order nonlinearity, producing a near linear free surface profile. Subsequent comparisons of the linearised free surface elevation time profiles to the predictions of focused wave group theory showed excellent agreement. As per Jonathan & Taylor, "for large crests, NewWave gives excellent agreement with offshore measurements."

1.3.2 Creamer nonlinear transform (CNT)

Combining a transformation of variables with a perturbation expansion, Creamer *et al.* (1989) presented an approximation that exactly captures the second order nonlinear behaviour of surface waves on deep water ($kd \geq 1.5$). For irrotational motion and neglecting surface tension, this approximation does well at higher orders and captures the important features of short waves interacting with longer waves, to include varying local gravity fields and velocity fields. Applied to a linear representation of a water wave in space, this Creamer nonlinear transform (CNT) leads to a nonlinear representation of the free surface and velocity potential in terms of the equivalent wavenumber components. Through the equations of motion, associated horizontal and vertical velocities may then be calculated on the free surface. For a regular wave of slope $kA = 0.2$, where A is the wave amplitude, the CNT free surface and horizontal and vertical surface velocities were found to be very close to that calculated by Stokes nonlinear theory. However, due to the form of the nonlinearities, wave breaking occurs at $kA = 1$ as opposed to 0.41 for a Stokes wave.

Taking into account only the second order nonlinear effects, Taylor (1992) applied the CNT to linear focused wave groups, as presented above. Developing equations for the horizontal wave kinematics at the moment of focus of an extreme wave crest, he observed that, following transformation, the extreme wave crest become higher, narrower, and steeper while the troughs become less deep, broader, and more rounded.

In a subsequent publication, Taylor (1998) compared an expansion of the CNT to Stokes 5th order theory for regular waves. The CNT was found to generate the correct leading order terms for each harmonic and "the surface profiles only differ at 5th order for the fundamental and at two orders higher than the leading order term for all of the harmonics (i.e. at 4th order in wave height for the 2nd harmonic, etc.)". As above, the CNT reproduced accurately both the shape of the free surface and the associated velocity fields for regular Stokes waves. Finally, Taylor (1998) identified a critical limitation of the CNT, its inability to predict amplitude dispersion and associated phase speed modifications at 3rd order. Due to resonant-wave interactions, these phase speed modifications are not reproduced by the CNT, making it incapable of simulating long scale time evolution. However, for short time scales, the CNT was identified as a tool for estimating the local bound wave components of steep waves.

1.4 Objectives

The "validation" of higher order diffraction theories has typically consisted of comparison with previously derived theoretical results. Comparisons with experimental results have been primarily based upon the forces and/or moments experienced by structures, which are integrated quantities, as opposed to the more rigorous test of free surface elevation, which is directly comparable to the velocity potential. Where comparisons of theoretical free surface elevation to experimental measurements have been conducted, these have been for experiments involving single cylinders. Obviously, these single cylinder cases do not constitute a test of the complex scattering problem for the interactions of multiple bodies and are of little interest for the practical design of large offshore structures. While more complex geometries such as a TLP or GBS with truncated or tapering columns have been tested, these have been of sufficient complexity to render direct comparison with the most basic theories impossible.

While much research into the computation of wave diffraction has been undertaken, the majority of this has concentrated on the development of higher order potential flow theories or fully nonlinear NWT methods for regular waves. However, it is generally accepted that regular waves are unrealistic for the simulation of extreme storm design conditions, for which focused wave group events or random wave spectra are more characteristic. For focused wave groups, first order diffraction calculations have been made for only single cylinder cases, while, for random seas, calculations of diffracted statistics have involved relatively few frequency components.

In light of the above, this thesis investigates the diffraction of regular waves, focused wave groups, and random seas by arrays of vertical bottom mounted circular cylinders using theoretical, computational, and experimental methods. Free surface elevation is the defining aspect used to test the potential theory developed. The principal project objectives are as follows:

- To carry out theoretical and computational investigations, based initially upon diffraction due to arrays of bottom mounted cylinders in regular waves at first order.
- To expand the above analysis to focused wave groups and random seas at first order.
- To apply the Creamer nonlinear transform (CNT) in integral form (at second order and beyond) to focused wave groups.
- To use the CNT as a tool for the analysis of nonlinear wave-wave interactions within the focused wave group.
- To test an array of four bottom mounted circular cylinders in regular and irregular waves at the offshore wave basin, HR Wallingford.
- To analyse free surface elevation measurements made during the regular wave experiments, and to compare the results with those predicted by first and second order diffraction theory.
- To study the effects of alterations of frequency and steepness of incident waves on the diffracted field and to include the near-trapping of second order components as observed in experiments.
- To analyse free surface elevation time histories collected from the irregular wave experiments, and to compare these results with those predicted by the first order theory for incident focused wave groups as well as the diffraction theories for focused wave groups and random seas developed herein.

1.5 Synopsis

The above objectives are met through the following chapters and sections:

- The preceding introduction, Chapter 1, discusses the background of the problem, reviews the relevant scientific literature, and presents the current research objectives.
- Chapter 2 describes the derivation of linear velocity potential theory for regular waves and focused wave groups. Linear diffraction theory is reviewed for arrays of vertical bottom mounted circular cylinders, and the theory is then developed to extend its application from incident regular waves to focused wave groups and random seas.
- Nonlinear theory for the formation and evolution of focused wave groups is then given in Chapter 3, which

reviews the necessary computations associated with Creamer nonlinear transform (CNT). The accuracy of the CNT at reproducing a very steep, nonlinear surface and computing associated kinematics is demonstrated by comparisons with independently developed fully nonlinear numerical wave tank (NWT) calculations. In addition, the global nonlinearity of focused wave groups, including both resonant and non-resonant wave-wave interactions, is analysed through the aid of the CNT.

- Chapter 4 describes the design of diffraction experiments in both regular and irregular incident waves at the offshore wave basin, HR Wallingford. The experimental objectives and timetable are defined; both the model and the basin dimensions and properties are detailed; and the experimental procedures, to include model installation, wave probe calibration, and data acquisition, are described.
- The results for regular wave tests are presented in Chapter 5, which begins with comparison of the videos made during the tests to free surface elevation contour plots as computed by linear diffraction theory from Chapter 2. Data handling procedures are then considered, including data truncation, frequency analysis, amplitude computation, and set up and set down computation. Finally, the results are presented and discussed with extensive comparison to linear diffraction theory and, in the case of near-trapping effects, to the second order results of Malenica *et al.* (1999).
- The irregular wave tests are analysed and discussed in Chapter 6, which begins with discussion of the data handling procedures, including truncation of the original time series and the definition of the relevant incident wave spectra. The computation of theoretical and experimental comparisons for both the random seas and the focused wave groups is then discussed. The results are then presented for these comparisons, with some discussion of observed nonlinear behaviour.
- The conclusions in Chapter 7 contain further discussion of comparisons between theory and experiment. This includes possible explanations for discrepancies between various results, particularly in the case of steep waves and near-trapping phenomena. In addition, opportunities for further research are identified.
- The appendices A and B provide a glossary of technical terms and standardised mathematical nomenclature used throughout the thesis.

Chapter 2
Linear Diffraction Theory for Regular Waves, Focused Wave Groups, and Random Seas

2.1 Introduction

A three-dimensional coordinate system is used here. The sea floor is idealised as a plane parallel to the undisturbed free surface at a uniform depth of d. In Cartesian coordinates, the positive z-axis points vertically upwards and is perpendicular to the undisturbed free surface, where the origin is located. A subscript I indicates the incident wave, while S indicates the scattered wave as produced by the diffraction process. All symbols used are listed in Appendix B or defined where they appear.

2.2 Linear Incident Waves

The two principal wave conditions studied using linear (first order) theory are regular and focused. The regular wave is an Airy (small amplitude sinusoidal) wave of a single frequency (monochromatic). In contrast, the focused wave group, also known as an extreme or freak wave, is composed of a full wave spectrum in which all components come into phase at a given point in the field. The following subsections detail the formulation of the equations necessary to define the incident wave prior to the diffraction computation.

2.2.1 Regular waves

Assuming irrotational flow, a scalar velocity potential $\Phi(x, y, z, t)$ exists, where $\mathbf{u} = \nabla\Phi$, $\mathbf{u}$ is the velocity vector, and ∇ is the gradient vector. Conservation of mass requires this potential to satisfy the Laplace equation,

$$\nabla^2\Phi = 0. \tag{1}$$

In addition, Φ must satisfy the rigid impermeable and free surface boundary conditions as follows:

- The rigid impermeable boundary condition requires that no fluid flows through any rigid surfaces. At the sea floor, this is represented by:

$$\frac{\partial\Phi}{\partial z} = 0 \qquad \text{at} \qquad z = -d. \tag{2}$$

- The free surface boundary condition stipulates that fluid particles on the free surface remain on the free surface, where the pressure is atmospheric. The vertical elevation of the free surface, $z = \eta(x,t)$, must then satisfy the following two conditions:

(a) Dynamic condition. This requires that the pressure at the free surface is atmospheric. The pressure is given by the Bernoulli equation,

$$p = -\rho_w[g\eta + \frac{\partial \Phi}{\partial t} + \frac{1}{2}\left|\nabla\Phi\right|^2], \tag{3}$$

in which p is pressure, ρ_w is the density of water, η is free surface elevation above still water level, and g is the acceleration due to gravity. With atmospheric pressure defined as zero at the free surface, this leads to

$$\frac{\partial \Phi}{\partial t} + g\eta + \frac{1}{2}\left|\nabla\Phi\right|^2 = 0 \qquad \text{on} \qquad z = \eta. \tag{4}$$

(b) Kinematic condition. This requires that the normal velocity of free surface is equal to that of the fluid, leading to

$$\frac{\partial \eta}{\partial t} + \frac{\partial \Phi}{\partial x}\frac{\partial \eta}{\partial x} + \frac{\partial \Phi}{\partial y}\frac{\partial \eta}{\partial y} - \frac{\partial \Phi}{\partial z} = 0 \qquad \text{on} \qquad z = \eta. \tag{5}$$

Both of these conditions are satisfied by setting the substantial derivative of the pressure from (3) on the free surface to zero as follows:

$$\frac{Dp}{Dt} = \left[\frac{\partial}{\partial t} + \nabla\Phi \cdot \nabla\right] p = 0. \tag{6}$$

Substituting (3) into (6) produces a free surface boundary condition of the form

$$\frac{\partial^2 \Phi}{\partial t^2} + g\frac{\partial \Phi}{\partial z} + 2\nabla\Phi \cdot \nabla\frac{\partial \Phi}{\partial t} + \frac{1}{2}\nabla\Phi \cdot \nabla\left(\nabla\Phi \cdot \nabla\Phi\right) = 0 \qquad \text{on} \qquad z = \eta. \tag{7}$$

The wave elevation, η, associated with this equation is given by

$$\eta\left(x,t\right) = -\frac{1}{g}\left[\frac{\partial \Phi}{\partial t} + \frac{1}{2}\nabla\Phi \cdot \nabla\Phi\right]. \tag{8}$$

For the first order theory, terms of second order and above in (7) and (8) are neglected and the boundary condition is applied on the mean free surface, $z = 0$. This last approximation is shown to be consistent when (7) and (8) are expanded as a Taylor series about $z = 0$. The resulting first order, combined free surface boundary condition is then

$$\frac{\partial^2 \Phi}{\partial t^2} + g\frac{\partial \Phi}{\partial z} = 0 \qquad \text{on} \qquad z = 0, \tag{9}$$

and the first order wave elevation is

$$\eta(x,t) = -\frac{1}{g}\frac{\partial \Phi}{\partial t}. \tag{10}$$

From the boundary conditions (9) and (2), and through separation of variables, the solution of (1) for an incident wave of frequency ω (in radians per second) is found of the form

$$\Phi_I = \mathrm{Re}\left\{f_0(z)\,\mathrm{e}^{\mathrm{i}(kx-\omega t)}\right\}, \tag{11}$$

where Re is the real part of the bracketed expression. The radian wave frequency, ω, and the wavenumber, k, satisfy the first order dispersion relation,

$$k \tanh kd = \frac{\omega^2}{g}, \tag{12}$$

and $f_0(z)$ is the depth attenuation function as given by

$$f_0(z) = -\frac{\mathrm{i}gA}{\omega}\frac{\cosh k(z+d)}{\cosh kd}, \tag{13}$$

where A is the amplitude of the incident wave. Finally, through (10) and (11) and with $z = 0$, the free surface elevation is found to be

$$\eta(x,t) = \mathrm{Re}\left\{A\mathrm{e}^{\mathrm{i}(kx-\omega t)}\right\}. \tag{14}$$

2.2.2 Focused wave groups

As discussed in the literature review, regular sinusoidal waves are a common assumption in engineering design; however, a more realistic extreme condition is given by the focused wave group in a random seaway. Tromans *et al.* (1991) outlined the theory of this focused wave group beginning from a representation of the ocean surface by a sum of numerous wavelets,

$$\eta(x,y,t) = \sum_n A_n \cos\left(k_n x \cos\beta_n + k_n y \sin\beta_n - \omega_n t + \varsigma_n\right), \tag{15}$$

where ς_n is a random phase angle, n is a large integer, and β_n is the angle of incidence of component n with the x-axis. From the one-sided directional surface power spectrum $f(\omega_n, \beta_n)\, S(\omega_n)$, the expected value of the amplitude A_n is given by

$$E(A_n) = \sqrt{2S(\omega_n)\, f(\omega_n, \beta_n) \bigtriangleup \omega \bigtriangleup \beta}, \tag{16}$$

where f is the complex directional component associated with the frequency and angle of incidence, S is the magnitude of the surface power spectrum of component n, and A_n itself is a Rayleigh distributed random variable. Mainly uni-directional seas are of more common, practical interest in the case of focused wave groups and storm conditions. As per Tromans *et al.* (1991), who assumed that the directional component of the power spectrum is independent of frequency and considered only small values of β_n (i.e. unidirectional seas with $\beta = 0$), (16) becomes

$$E(A_n) = \sqrt{2S(\omega_n) \triangle \omega}. \tag{17}$$

A focused wave group is produced when many wavelets come into phase. A crest is defined as passing at time t_0 when $\eta_1 = \alpha > 0$ and $\frac{\mathrm{d}\eta_1}{\mathrm{d}t} = \dot{\eta}_1 = 0$. For the elevation η at some arbitrary point x, y at time $t = t_0 + \tau$, the probability density functions (pdfs), $f(\eta)$, $f(\eta_1)$, and $f(\dot{\eta}_1)$, are all known. In addition, the joint and conditional pdfs are also known. From this, the conditional pdf

$$f(\eta \mid \eta_1 = \alpha, \dot{\eta}_1 = 0),$$

then represents a description of the elevation η for a large crest as dependent on the crest of elevation α at time t_0.

As η_1 and $\dot{\eta}_1$ are statistically independent and uncorrelated, from the definitions of conditional probability (Newland 1993),

$$\begin{aligned} f(\eta \mid \eta_1, \dot{\eta}_1) &= \frac{f(\eta, \eta_1, \dot{\eta}_1)}{f(\eta_1 \mid \dot{\eta}_1) f(\dot{\eta}_1)} \\ &= \frac{f(\eta, \eta_1, \dot{\eta}_1)}{f(\eta_1) f(\dot{\eta}_1)}, \end{aligned} \tag{18}$$

where $f(\eta, \eta_1, \dot{\eta}_1)$ is the pdf from a Gaussian, or normal, distribution in three variables.

The pdf for a m-dimensional multivariate normal distribution of the random vector $\mathbf{x} = [x_1, x_2, \ldots, x_m]'$ is given (see Johnson and Wichern 1998 for example) by

$$f(\mathbf{x}) = \frac{1}{(2\pi)^{\frac{m}{2}} |\Sigma|^{\frac{1}{2}}} \mathrm{e}^{-(\mathbf{x}-E(\mathbf{x}))' \Sigma^{-1} (\mathbf{x}-E(\mathbf{x}))/2}, \tag{19}$$

where $E(\mathbf{x})$ is a vector of the expected, or mean, values of $\mathbf{x}$ and Σ is the covariance matrix defined as

$$\Sigma = \begin{bmatrix} \sigma_{11} & \sigma_{12} & \cdots & \sigma_{1m} \\ \sigma_{21} & \sigma_{22} & \cdots & \sigma_{2m} \\ \vdots & \vdots & & \vdots \\ \sigma_{m1} & \sigma_{m2} & \cdots & \sigma_{mm} \end{bmatrix}. \tag{20}$$

The variance of variable x_i is defined here as $\sigma_{ii} = \sigma_i^2$, while the covariance of variables x_i and x_j is defined as σ_{ij}.

Following the above model, the variances and covariances associated with (18) are defined as

$$\begin{array}{ll} E\left(\eta_1^2\right) = E\left(\eta^2\right) = \sigma^2, & E\left(\dot{\eta}_1^2\right) = \dot{\sigma}^2, \\ E\left(\eta\dot{\eta}_1\right) = \dot{\rho}\sigma\dot{\sigma}, & E\left(\eta_1\eta\right) = \ddot{\rho}\sigma^2, \end{array} \tag{21}$$

where $\dot{\rho}$ and $\ddot{\rho}$ are the respective correlation coefficients. Assuming that mean values for free surface elevation are zero, the numerator of (18) becomes

$$\begin{aligned} f\left(\eta, \eta_1, \dot{\eta}_1\right) \quad = \quad & -\frac{1}{(2\pi)^{\frac{3}{2}}\,\sigma^2\dot{\sigma}\sqrt{1-\ddot{\rho}^2-\dot{\rho}^2}} \cdot \\ & \exp\left\{-\frac{1}{2\left(1-\ddot{\rho}^2-\dot{\rho}^2\right)^2}\left(\frac{\left(1-\dot{\rho}^2\right)\eta_1^2+\eta^2-2\ddot{\rho}\eta\eta_1}{\sigma^2}+\frac{\left(1-\ddot{\rho}^2\right)\dot{\eta}_1^2}{\dot{\sigma}^2}+\frac{2\dot{\rho}\eta\dot{\eta}_1-2\dot{\rho}\eta\dot{\eta}_1}{\sigma\dot{\sigma}}\right)\right\}, \end{aligned} \tag{22}$$

while the denominator is

$$f\left(\eta_1\right) f\left(\dot{\eta}_1\right) = \frac{1}{2\pi\sigma\dot{\sigma}} \exp\left\{-\frac{\eta_1^2}{2\sigma^2} + \frac{\dot{\eta}_1^2}{2\dot{\sigma}^2}\right\}. \tag{23}$$

Taking the values of $\eta_1 = \alpha$ and $\dot{\eta}_1 = 0$ at the crest, some manipulation produces the normal distribution

$$f\left(\eta \mid \eta_1 = \alpha, \dot{\eta}_1 = 0\right) = \frac{1}{\sqrt{2\pi}\sigma_2} \mathrm{e}^{-\frac{\left(\eta-\eta_d^\star\right)^2}{2\sigma_2^2}}, \tag{24}$$

with standard deviation

$$\sigma_2^2 = \sigma^2\left(1-\ddot{\rho}^2-\dot{\rho}^2\right), \tag{25}$$

and expected and most probable value

$$\eta_d^\star = \alpha\rho\left(\tau\right), \tag{26}$$

where $\rho\left(\tau\right)$ is the autocorrelation function of the surface power spectrum $S\left(\omega_n\right)$.

From examination of (24), (25) and (26), as maximum crest elevation α increases the expected value of the elevation $\eta_d^\star$ also increases. The standard deviation, however, remains constant. This indicates that, with increasing crest elevation α, the free surface elevation η becomes more deterministic and is normally distributed about the expected and most probable value $\eta_d^\star$. From the work of Lindgren (1980) in the analysis of the maxima of normal processes, the elevation around this crest may then be described using the Slepian model process as

$$\eta^\star\left(\tau\right) = \alpha\rho\left(\tau\right) + g\left(\tau\right), \tag{27}$$

where $\alpha\rho\left(\tau\right)$ is deterministic and $g\left(\tau\right)$ is a non-stationary, Gaussian process (independent of α) with zero mean and standard deviation σ_2 from (25). This standard deviation σ_2 of $g\left(\tau\right)$ increases from zero at the crest ($\tau = 0$) to become asymptotic with the standard deviation of the underlying wave process σ at a very long time interval

τ from the crest. In addition, with increase in the time interval τ, the deterministic component $\alpha\rho(\tau)$ decays to zero. The imposed conditioning from the crest then weakens to leave the underlying random wave process.

To calculate $\eta^\star$, the autocorrelation function $\rho(\tau)$ may be found from a Fourier transform of the surface power spectrum,

$$\rho(\tau) = \frac{1}{\sigma^2}\int_0^\infty S(\omega)\cos\omega t \,\mathrm{d}\omega \approx \frac{1}{\sigma^2}\sum_n (S_n \triangle \omega_n)\cos\omega_n\tau, \tag{28}$$

while the deterministic component from (27)) that dominates when α is large is

$$\eta_d^\star(\tau) = \frac{\alpha}{\sigma^2}\sum_n C_n \cos\omega_n\tau, \tag{29}$$

where $C_n = (S_n \triangle \omega_n)$. Extending (29) to include spatial dependencies, but limiting this to uni-directional seas, the wavenumber k_n is included to obtain

$$\eta_d^\star(X,\tau) = \frac{\alpha}{\sigma^2}\sum_n C_n \cos(k_n X - \omega_n\tau), \tag{30}$$

where $X = x - x_0$ and x_0 is the position of occurrence of a large crest. A model for extreme waves that is commonly referred to as NewWave, this is the average shape of a large crest of maximum elevation α.

From equation (29), a large crest is then generated when all of the wavelets composing the spectrum come into phase, producing a free surface elevation which is identical in shape on average to the autocorrelation function $\rho(\tau)$ for the wave spectrum. Although the wavelet amplitudes of equation (15) have changed such that $C_n \propto A_n^2$, this is because large crests are generated more often by the higher energy spectral components coming into phase as opposed to the low energy components. This relationship agrees with a statistical theorem for the components contributing to the extremes in normal processes (Lindgren 1980).

Figure 2.1 demonstrates the evolution of a focused wave group, a NewWave compatible with a standard JONSWAP (JOint North Sea WAve Program) spectrum. The group begins with longer wavelength (lower frequency) components concentrated towards the negative end of the x-axis. Moving with faster celerity, these components overtake those at smaller wavelength to come into focus and form an extreme crest at $t = 0$ and $x = 0$. The spectral components comprising the group then defocus, with longer wavelength components overtaking smaller wavelength components.

2.3 Linear Diffraction from a Cylinder Array

As per Linton & Evans (1990), the first order interaction of regular waves with arrays of N bottom-mounted vertical circular cylinders is considered. This first order regular wave case is then extended to the first order diffraction of focused wave groups and random seas.

Figure 2.2 details the coordinate system used for the multiple cylinder cases. Both Cartesian (x, y, z) and polar (r, θ, z) coordinate systems are used with the z-axis positive upward and the origin at the mean free surface, $z = 0$. In addition, N local polar coordinate systems are applied, where N is the number of cylinders in the array. These local coordinate systems are in the form (r_j, θ_j, z), for $j = 1, ..., N$, and have origins at the centre of the jth cylinder, $(x_j, y_j, z = 0)$. The incident wave heading is β, expressed in radians counterclockwise from the positive x axis to the wave ray.

2.3.1 Regular waves

With the aforementioned assumptions of linear theory, the velocity potential may be assumed to be of the form

$$\Phi(x, y, z, t) = \mathrm{Re}\left\{\phi(x, y)\ f_0(z)\ \mathrm{e}^{-\mathrm{i}\omega t}\right\}, \tag{31}$$

where the depth attenuation function, $f_0(z)$, is defined in (13) above. Similarly, ω and k are time and spatial characteristics of the incident wave as defined above.

In light of the above simplification and applying the generating function for Bessel functions, the incident velocity potential may be written in terms of the local coordinate system of the jth cylinder as

$$\begin{aligned} \phi_I &= \mathrm{e}^{\mathrm{i}k(x\cos\beta\ +\ y\sin\beta)} = \mathrm{e}^{\mathrm{i}kr\cos(\theta-\beta)} \\ &= I_j \mathrm{e}^{\mathrm{i}kr_j\cos(\theta_j-\beta)} \\ &= I_j \sum_{n=-\infty}^{\infty} J_n(kr_j)\, \mathrm{e}^{\mathrm{i}n\left(\frac{\pi}{2}-\theta_j+\beta\right)}, \end{aligned} \tag{32}$$

where I_j is a phase factor associated with the jth cylinder. This phase factor is

$$I_j = \mathrm{e}^{\mathrm{i}k(x_j\cos\beta\ +\ y_j\sin\beta)}. \tag{33}$$

In the case of multiple cylinders, as discussed by Linton & Evans (1990), the presence of a cylinder in the wave field produces a scattered wave which is in turn scattered by the adjacent cylinders and so on. All possible interactions of these scattered waves are described by associating a general wave potential with each cylinder to describe all waves radiating away from that cylinder. With the incident wave potential, this completely defines the total wave field.

This scattered wave may be said to be of the form

$$\phi_S^j = \sum_{n=-\infty}^{\infty} A_n^j Z_n^j H_n\left(kr_j\right) \mathrm{e}^{in\theta_j}, \tag{34}$$

for some set of complex coefficients A_n^j and with $Z_n^j = J_n'\left(ka_j\right)$. This definition of Z differs from that used in Linton & Evans (1990) and produces a better conditioned matrix for the solution of coefficients.

Following from the above discussion, the total potential is then

$$\begin{aligned} \phi &= \phi_I + \sum_{j=1}^{N} \phi_S^j \\ &= I_j \sum_{n=-\infty}^{\infty} J_n\left(kr_j\right) \mathrm{e}^{in\left(\frac{\pi}{2}-\theta_j+\beta\right)} + \sum_{j=1}^{N} \sum_{n=-\infty}^{\infty} A_n^j Z_n^j H_n\left(kr_j\right) \mathrm{e}^{in\theta_j}. \end{aligned} \tag{35}$$

Graf's addition theorem for Bessel functions is then applied in the form

$$\mathrm{e}^{in\theta_j} H_n\left(kr_j\right) = \sum_{m=-\infty}^{\infty} J_m\left(kr_k\right) H_{n+m}\left(kR_{jk}\right) \mathrm{e}^{im(\pi-\theta_k)} \mathrm{e}^{i(n+m)\alpha_{jk}} \tag{36}$$

to produce

$$\begin{aligned} \phi\left(r_k, \theta_k\right) =& \sum_{n=-\infty}^{\infty} I_k J_n\left(kr_k\right) \mathrm{e}^{in\left(\frac{\pi}{2}-\theta_k+\beta\right)} + \sum_{n=-\infty}^{\infty} A_n^k Z_n^k H_n\left(kr_k\right) \mathrm{e}^{in\theta_k} \\ &+ \sum_{\substack{j=1 \\ \neq k}}^{N} \sum_{n=-\infty}^{\infty} A_n^j Z_n^j \sum_{m=-\infty}^{\infty} J_m\left(kr_k\right) H_{n+m}\left(kR_{jk}\right) \mathrm{e}^{im(\pi-\theta_k)} \mathrm{e}^{i(n+m)\alpha_{jk}}. \end{aligned} \tag{37}$$

After substituting $-n$ for n in the summation of the first term and $-m$ for m in the final term, Bessel function identities may be applied and the above equation simplified to

$$\begin{aligned} \phi\left(r_k, \theta_k\right) =& \sum_{n=-\infty}^{\infty} I_k J_n\left(kr_k\right) \mathrm{e}^{in\left(\frac{\pi}{2}-\beta+\theta_k\right)} + \sum_{n=-\infty}^{\infty} A_n^k Z_n^k H_n\left(kr_k\right) \mathrm{e}^{in\theta_k} \\ &+ \sum_{m=-\infty}^{\infty} \left[\sum_{\substack{j=1 \\ \neq k}}^{N} \sum_{n=-\infty}^{\infty} A_n^j Z_n^j H_{n-m}\left(kR_{jk}\right) \mathrm{e}^{i(n-m)\alpha_{jk}} \right] J_m\left(kr_k\right) \mathrm{e}^{im\theta_k}. \end{aligned} \tag{38}$$

To solve for the unknown coefficients A_n^j, the body boundary condition for the rigid, impermeable surfaces of the N cylinders,

$$\frac{\partial \phi}{\partial r_k} = 0 \quad \text{on} \quad r_k = a_k, \quad k = 1, \ldots, N, \tag{39}$$

is applied to (38). Following some algebra and integration with respect to θ_k, this produces

$$\begin{aligned} A_m^k H_m^{'}(ka_k) + \sum_{\substack{j=1 \\ \neq k}}^{N} \sum_{n=-\infty}^{\infty} A_n^j Z_n^j H_{n-m}(kR_{jk}) \, \mathrm{e}^{\mathrm{i}(n-m)\alpha_{jk}} &= -I_k \mathrm{e}^{\mathrm{i}m\left(\frac{\pi}{2}-\beta\right)} \\ \text{for} \qquad k &= 1, \ldots, N, \\ \text{and} \quad -\infty &< m < \infty. \end{aligned} \tag{40}$$

This infinite system of equations may be truncated from $-M < m < M$ to produce an $N(2M+1)$ system of equations in $N(2M+1)$ unknowns. In this manner, the unknown coefficients A_n^j may be found through a linear algebraic solution.

The expression in brackets from (38) may then be substituted for through (40). After some algebra, this may be simplified as

$$\begin{aligned} \phi(r_k, \theta_k) &= \sum_{n=-\infty}^{\infty} A_n^k \left[Z_n^k H_n(kr_k) - H_n^{'}(ka_k) J_n(kr_k) \right] \mathrm{e}^{in\theta_k} \\ \text{if} \;\; r_k &< R_{jk} \quad \measuredangle j, \end{aligned} \tag{41}$$

which is a simple formula for the local velocity potential near any cylinder.

Following the above first order diffraction computation, the free surface elevation may be found from (10) above as

$$\eta(x, y, t) = \mathrm{Re}\left\{ A\phi(x, y) \, \mathrm{e}^{-\mathrm{i}\omega t} \right\}. \tag{42}$$

From this, the local modification to the incident wave amplitude due to diffraction is then

$$\frac{|\eta(x, y, t)|}{A} = |\phi(x, y)|. \tag{43}$$

As the non-dimensionalised component of the velocity potential with depth and time dependence removed, this variable $\phi(x, y)$ will be referred as the diffraction coefficient to further emphasize its modification of incident wave amplitude.

Figures 2.3, 2.4, and 2.5 demonstrate the application of this method to problems involving arrays of circular cylinders. These figures correspond to example calculations presented by Linton & Evans (1990) and show excellent agreement with their work to within plotting accuracy. Using the same notation, the variable h represents the spacing between the cylinder centres. Solid circles denote the cylinder positions. Key contours are labelled with magnitude in terms of the amplification modifying the incident wave. For example, a contour labelled 1 indicates no modification to the incident wave amplitude along that line, while a value of 1.5 corresponds to a 50% increase in amplitude. Figure 2.3 shows results for an array of four cylinders arranged at the vertices of a square, which is typical of offshore platform configurations. As indicated in the caption, incident waves are approaching from the bottom left corner of the figure (i.e. heading $\beta = \frac{\pi}{4}$radians). In contrast, Figure 2.4 shows the contours surrounding a group of eight cylinders in two parallel rows, and the accompanying Figure 2.5 displays the detail in the immediate vicinity of the upper right-hand cylinder from the same case. In both of these, incident wave approach from the bottom right corner of the figure with heading $\beta = \frac{3\pi}{4}$radians.

2.3.2 Focused wave groups

As the more complex nonlinear interactions between waves at different frequencies are not accounted for, the above first order diffraction theory is simple to apply to the case of focused wave groups. This is accomplished by linear superimposition of the diffracted wave field for each wavenumber component of the incident wave. Combining (30) and (42) above, the free surface elevation due to the scattering of an incident focused wave group can be calculated through

$$\eta\left(x,y,\tau\right)=\frac{\alpha}{\sigma^{2}}\sum_{n}C_{n}\,\mathrm{Re}\left\{\phi_{n}\left(x,y\right)\mathrm{e}^{-\mathrm{i}\left(k_{n}X+\omega_{n}\tau\right)}\right\}, \tag{44}$$

where $\tau = t - t_0$ and $X = x - x_0$, with the focus occurring in the y-plane at (x_0, y, t_0). The heading β is assumed to be zero and the diffraction coefficient for the n^{th} spectral component is ϕ_n.

However, keeping the amplitude of each spectral component fixed, a random phase angle ς_n may be included in (44) above to calculate the free surface elevation for an imperfectly focused wave group. This is then

$$\begin{aligned}\eta\left(x,y,\tau\right) &= \frac{\alpha}{\sigma^{2}}\sum_{n}C_{n}\,\mathrm{Re}\left\{\phi_{n}\left(x,y\right)\mathrm{e}^{-\mathrm{i}\left(k_{n}X+\omega_{n}\tau-\varsigma_{n}\right)}\right\}\\ &= \frac{\alpha}{\sigma^{2}}\sum_{n}C_{n}\,\mathrm{Re}\left\{\phi_{n}\left(x,y\right)\mathrm{e}^{-\mathrm{i}\left(k_{n}X+\omega_{n}\tau\right)}\mathrm{e}^{\mathrm{i}\varsigma_{n}}\right\},\end{aligned} \tag{45}$$

such that $0 \leq \varsigma_n \leq 2\pi$ and $\left|e^{\mathrm{i}\varsigma_n}\right| = 1$.

It is reasonable to suggest that there exists a value of this phase angle ς_n such that the velocity potential $\phi_n(x,y)$ for each component reaches its maximum value $|\phi_n(x,y)|$ at the same instant in time. This phase angle is

$$e^{\mathrm{i}\varsigma_{n}}=\frac{\left|\phi_{n}\left(x,y\right)\right|}{\phi_{n}\left(x,y\right)}, \tag{46}$$

which, applied to (45) above, produces

$$\eta(x,y,\tau)=\frac{\alpha}{\sigma^2}\sum_n C_n \operatorname{Re}\left\{\left|\phi_n(x,y)\right| \mathrm{e}^{-\mathrm{i}(k_n X+\omega_n \tau)}\right\}. \tag{47}$$

If the point of computation is then assumed to be the focus point, with $x = x_0$ and $t = t_0$ such that $\tau = 0$, (47) may be written as

$$\eta_m(x,y)=\frac{\alpha}{\sigma^2}\sum_n C_n \left|\phi_n(x,y)\right|. \tag{48}$$

This expression allows the computation of the maximum possible free surface elevation at a given point (x, y) for an incident focused wave group (of fixed amplitude components but arbitrary phasing) with linear diffraction. Equation (48) is, to the author's knowledge, as yet unpublished.

The validity of the above method for computing a diffracted focused wave group is demonstrated in Figures 2.6 through 2.18. The majority of the figures contain three subplots showing results for sections parallel to the x-axis as annotated (e.g. $y = 0$, h, and $2h$ in Figure 2.6). However, indicating the cylinder positions for identical geometry cases, plan views of the contours of η_m are interspersed within these sectioned figures. Figures 2.6 through 2.18 encompass varying geometries while maintaining $\frac{a}{h} = 0.5$ as in the above cases of Linton & Evans (1990). Incident focused wave groups are based on JONSWAP spectra with 120 wavenumber components and $\Delta k = \frac{k_p}{20}$. The wave spectra have been scaled such that the maximum free surface elevation for the undisturbed extreme crest from (30) is unity (i.e. $\eta_d^*(x_0, t_0) = 1$).

The solid lines and contour lines in Figures 2.6 through 2.17 indicate the maximum free surface elevation η_m as computed through (48). Thus, a value of 2 would indicate a maximum free surface elevation of twice the incident focused wave group, while 0.5 would indicate half of the incident elevation. Dotted lines represent the free surface elevation $\eta(x)$ at the instant of focus for an extreme wave crest (a NewWave event) focused at points representing integer or half integer values of $\frac{x}{h}$ as computed through (44).

Figures 2.6, 2.7, and 2.8 provide results for a single cylinder ($N = 1$) centred at the origin. Figure 2.9 provides a contour plot in plan view for the same incident wavenumber as the adjacent Figure 2.8 ($k_p h = 2\pi$ corresponding to $\frac{h}{\lambda_p} = 1$). Although having no physical meaning for the single cylinder case, h has been set at $h = 2a$ to allow for direct comparison with the multiple cylinder cases which follow. For this relatively simple single cylinder case, the focused wave group extreme crests do achieve the maximum free surface elevation (i.e. the dotted lines are, in general, tangent to the solid line). However, as the geometry becomes more complex and the importance of interaction effects between cylinders grows, this will no longer be the case.

Although the incident waves are parallel to the x-axis ($\beta = 0$), Figures 2.10, 2.11, and 2.12 have cylinders ($N = 4$) centred at the corners of a square with side length $2h$ and rotated through $\frac{\pi}{4}$ radians (i.e. cylinders centred at $(-\sqrt{2}h, 0)$, $(0, \sqrt{2}h)$, $(\sqrt{2}h, 0)$, and $(0, -\sqrt{2}h)$). Again, the contour plot of Figure 2.13 shows the geometry in plan view for the same case as the adjacent Figure 2.12. This rotated geometry is such that the case is comparable to Figure 2.3. Here a discrepancy between diffracted extreme crests and maximum free surface elevation becomes apparent, particularly for the shortest wavelength (highest wavenumber) plot of Figure 2.12 with $k_p h = 2\pi$. This difference is most clear in the upper subplots along the centreline and between the cylinders ($y = 0, \frac{x}{h} = 0$), where the incident extreme wave crest has been shifted upstream a distance of approximately $-0.1h$ and achieves an elevation that is some 50% of the maximum.η_m at that point.

Figures 2.14, 2.15, and 2.16 return to the square configuration of Figure 2.3, with two cylinders upwave and two downwave of the origin, but with incident wave again parallel to the x-axis ($\beta = 0$). With a plan view of the configuration, Figure 2.18 displays the contour plot equivalent to Figure 2.16. Discrepancies between diffracted extreme crests and maximum free surface elevations are most apparent in these figures. The largest differences may be noted in the upper subplots, plotting the centreline section along $y = 0$, and these differences are perhaps most apparent for the highest wavenumber case of Figure 2.16 with $k_p h = 2\pi$.

Finally, plotted along the plane $y = 0$ for the identical case as Figure 2.16, the three subplots of Figure 2.17 provide dashed lines for the wave groups achieving the maximum free surface elevation. These dashed lines are the free surface elevation η for a phase shifted focused wave group from (45) with phase specified through (46) to achieve the maximum free surface elevation. The upper plot is directly comparable to the upper plot of Figure 2.16, with wave groups focused to obtain maximum value at all integer values of $\frac{x}{h}$. It is clear that the phase-modified wave groups of Figure 2.17 obtain the maximum free surface elevation, while the unmodified groups of Figure 2.16 do not. The centre plot compares one such phase-modified diffracted wave group (dashed line) with the unmodified diffracted wave group (dotted line) focused at $\frac{x}{h} = 0$. Again, it is clear that the dashed line, extending above the dotted line to reach the maximum free surface elevation, is tangent to the solid line. The lower plot compares the undisturbed incident wave forms for these phase-modified and unmodified cases. It is clear that the dotted line of the unmodified focused wave group is symmetric about its maximum, while the phase-modified dashed line represents a more complex incident wave form with lower undisturbed peak value.

2.3.3 Random wave statistics

The diffraction of a focused wave group has been treated above as a deterministic event, in which the diffraction of the group is computed through the sum of diffracted components of fixed amplitude. However, returning to the extreme value statistics of random seas, the maximum expected free surface elevation may be characterised in terms of the energy in the spectrum and the number of observed waves. Assuming that all large observed events conform to a Rayleigh distribution (see Dean & Dalrymple 1991 for a complete derivation), the maximum expected incident free surface elevation η_i is

$$\eta_i = \sqrt{2\ln(N)\sum_n S(\omega_n)\ \triangle\omega}. \tag{49}$$

where N is the number of observed waves.

If the effects of diffraction due to the presence of a large structure are taken into account, the maximum expected diffracted free surface elevation η_d at a point (x, y) is then

$$\eta_d(x, y) = \sqrt{2\ln(N)\sum_n |\phi_n(x, y)|^2 S(\omega_n)\ \triangle\omega}. \tag{50}$$

It should be noted that the weighting of the diffraction coefficient ϕ_n is squared in this instance as it now modifies the energy density spectrum S (in units of m^{2}s), which has a squared relationship with the amplitude spectrum. This squared diffraction coefficient is consistent with the work of Eatock Taylor and Sincock (1989), who examined the mean square free surface elevation for random seas in the presence of a TLP structure (see Chapter 1 for a more complete description).

The effect of this spectral diffraction relative to the maximum undisturbed free surface elevation may then be computed through

$$\frac{\eta_d(x, y)}{\eta_i} = \sqrt{\frac{\sum_n |\phi_n(x, y)|^2 S(\omega_n)\ \triangle\omega}{\sum_n S(\omega_n)\ \triangle\omega}}. \tag{51}$$

An identical result may be obtained through the comparison of mean square free surface elevation. This implies that (51) also represents the diffracted modification to such random sea characteristics as root mean square free surface elevation and significant wave height, as calculated based on the incident wave spectrum.

In addition, through this computation of the effects of diffraction on an incident spectrum, the average shape of the largest diffracted wave measured at a point in the vicinity of a structure may be computed from the diffracted spectrum as

$$\eta_{dm}\left(x,y,\tau\right)=\frac{\alpha}{\sigma^2}\sum_n C_n\,\mathrm{Re}\left\{\left|\phi_n\left(x,y\right)\right|^2\mathrm{e}^{-\mathrm{i}\left(k_n x_0+\omega_n\tau\right)}\right\}. \tag{52}$$

This differs from the above discussion of the diffraction of incident focused wave groups in that the amplitude components of the spectrum are now assumed to be random and modified by the presence of the structure.

Figures 2.19, 2.20, and 2.21 demonstrate the computation of (51) for cases identical to those of Figures 2.9, 2.13, and 2.18 respectively. Again, the incident wave spectra are JONSWAP spectra of 120 wavenumber components with $\Delta k=\frac{k_p}{20}$.

Examining the sensitivity of the result to the discretisation in wavenumber, Figures 2.22 and 2.23 plot the contours of $\frac{\eta_d}{\eta_i}$ for the same geometry and peak wavenumber as Figure 2.21. However, the incident JONSWAP spectra have been computed with 60 wavenumber components (half of the original 120) and $\triangle k=\frac{k_p}{10}$. Testing the outcome for all the wavenumber values of Figure 2.21, the starting values of wavenumber are varied from $k_1=\frac{\triangle k}{2}$ and $\triangle k$ in Figures 2.22 and 2.23 respectively. It is apparent from comparing the three figures that, while the computation is sensitive to the spectral components chosen, a slight shift in the discretisation will not drastically effect the outcome.

This result is further supported by Figure 2.24, plotting the modification due to diffraction $\left|\phi_n\left(x,y\right)\right|^2$ versus the nondimensionalised wavenumber $\frac{kh}{\pi}$. Values are computed for three points along the line $x=0$, with the solid, dotted, and dashed lines indicating values at $y=0$, h, and $2h$ respectively. It is clear from this plot that any wavenumber discretisation must be sufficiently fine to capture the complex nature of variations in scattering at any one point. The varying minima of the three lines in Figure 2.24 are also of interest, such as the zero or near zero values for $\left|\phi_n\left(0,0\right)\right|^2$ (the solid line) at $kh\approx 0.8, 1.9, 3.4$, and 7.5. These minima indicate wavenumbers at which the incident and scattered waves effectively cancel each other due to destructive interference.

In comparison to the former contour plots of maximum free surface elevation from (48), the spectral diffraction modification plots from (51) are very similar. However, even for the relatively simple single cylinder case of Figure 2.19, there are some slight differences (note, for example, the somewhat larger contour at $\frac{\eta_d}{\eta_i}=0.4$ downwave of the cylinder in Figure 2.9 as compared to Figure 2.19).

For the more complex multiple cylinder geometries, differences between the two sets of figures are more notable, with diffracted spectral modification plots showing considerably larger and higher amplification regions. In Figure 2.20 the contours upwave of the cylinders at $\frac{\eta_d}{\eta_i} = 1.2$ are much more extensive than those of 2.13; and the runup on the centreline and downwave cylinders extends to $\frac{\eta_d}{\eta_i} = 2.2$ and 2 respectively, while the corresponding locations in Figure 2.13 experience $\frac{\eta_d}{\eta_i} = 2$ and 1.8. Similarly, Figure 2.21 displays upwelling along the centreline ($y = 0$) and runup at the downwave cylinders approximately 20% above that of Figure 2.18 (i.e. $\frac{\eta_d}{\eta_i} = 1.4$ as compared to $\eta_{mp} = 1.2$). Figures 2.25 and 2.26 demonstrate these differences more clearly by plotting the contours of $\frac{\eta_d}{\eta_i} - \eta_{mp}$ in the vicinity of the structure. It should be noted that there are no negative values in these results, indicating that the diffracted spectral modification yields a consistently higher modification relative to the diffracted focused wave group. The largest differences here are on the order of 0.2 (20% of the incident wave), typically occurring near the upwave and downwave cylinders in Figure 2.25. In Figure 2.26 the largest differences lie primarily along the lines of symmetry ($y = 0$ and $x = 0$) and in runup on the downwave cylinders .

The relative increased effects of diffraction shown in Figures 2.19, 2.20, and 2.21 in comparison with Figures 2.9, 2.13, and 2.18 are due to inherent differences in the computational methods. As (48) assumes the presence of an extreme focused wave group event, it treats the incident wave as a composition of several frequency components with fixed amplitude as dictated by focused wave group theory. This incident wave represents one extreme event from the undisturbed incident spectrum, and the diffraction of its wavenumber components is treated individually. In contrast, (51) computes the effect of diffraction on the incident wave spectrum and effectively produces a new random field at each point in the vicinity of a structure. This has the effect of modifying the underlying spectral statistics and any wave elevations computed from the spectrum, which may or may not represent extreme wave events. Thus, statistical elevations computed from the diffracted spectrum would be expected to show more amplification relative to corresponding diffracted focused wave groups.

2.4 Conclusions

The preceding chapter has yielded two primary results, namely:

(1) Existing potential-based theory has been reviewed for incident regular waves and focused wave groups, and the linear diffraction of these events has been considered.

(2) First order diffraction theory has been extended and studied in depth for the case of focused wave groups and random seas incident on an array of bottom mounted circular cylinders.

2.4.1 Review of existing theory

First order potential flow theory for incident regular waves has been presented as applicable for small amplitudes relative to wavelength. In addition, focused wave group theory has been reviewed as a somewhat more realistic incident wave condition. Based on the most probable shape of a large event from a wave spectrum, this extreme wave theory provides a very steep wave form for subsequent analysis.

Reviewing the linear diffraction theory of Linton & Evans (1990), the scattering of incident regular waves from arrays of vertical, bottom mounted circular cylinders has been computed. This multiple cylinder, first order diffraction analysis has been extended to the case of an incident focused wave group through the method of Eatock Taylor & Wu (1997), who computed the diffraction of focused wave groups from a single cylinder.

2.4.2 Extension of linear diffraction

Through the generalisation of first order focused wave group diffraction theory, a simplified expression has been derived for the maximum free surface elevation η_m at any point due to a given incident focused wave group. Due to the phasing of the scattered waves from the cylinders, this η_m is not necessarily achieved by an incident extreme wave crest but may be realised by an incident wave group which is somewhat out of focus. This method is applicable to a deterministic incident focused wave group chosen to correspond to a given incident wave spectrum. The amplitude components of this focused focused wave group are assumed to be fixed, and the effect of scattering from the cylinder array is computed through linear diffraction. It is also possible to compute the velocity potential and linear kinematics (related to the free surface elevation but not presented herein) for the focused wave group event achieving this maximum free surface elevation at a given point.

Returning to the concept of a random sea, the method of Eatock Taylor & Sincock (1989) has been applied to compute the effects of diffraction on the incident spectral components. This differs from the above result in that the energy in each spectral component is treated as variable, and a modification to this energy is computed through first order diffraction theory. This method may then be used to calculate statistics ($\frac{\eta_d}{\eta_i}$) for extreme surface responses consistent with an incident random wave field of known spectrum at a given point in the vicinity of a structure; this is also the local enhancement of root mean square free surface elevation and significant wave height. While this spectral method produces results similar to those for the diffraction of focused wave groups, significant differences do exist as the two methods differ in their treatment of extreme events.

In summary, two new methods for determining extreme design events have been presented. The first of these methods incorporates the effects of linear diffraction on a given incident focused wave group with fixed amplitude components as determined by the incident wave spectrum. In contrast, the latter computes a modification to the incident wave spectrum itself, enhancing or reducing the energy in the incident components. From this modified spectrum, statistics of surface elevation including the diffracted field at various points in the vicinity of a structure may then be computed.

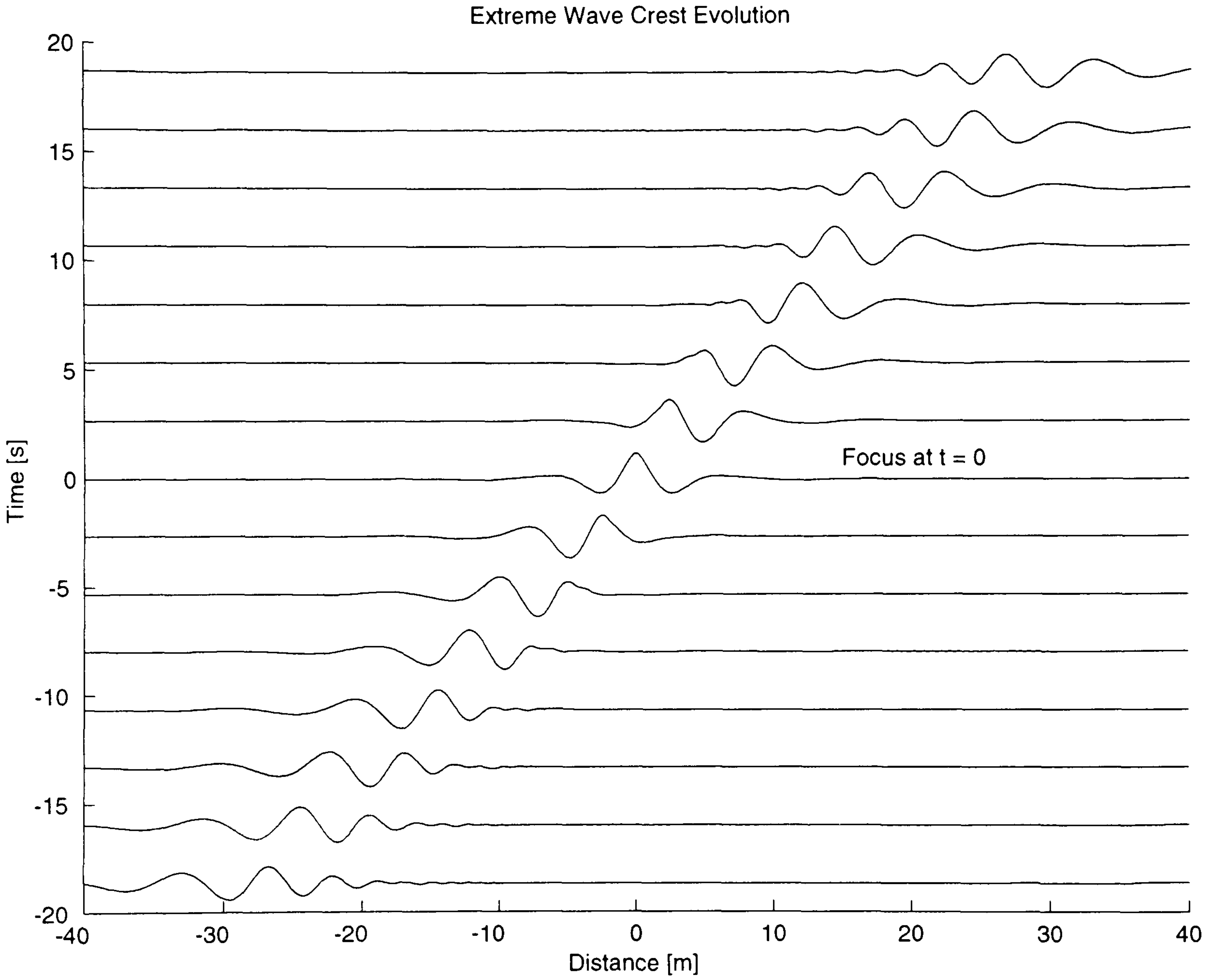

Figure 2.1. Evolution of a linear focused wave group

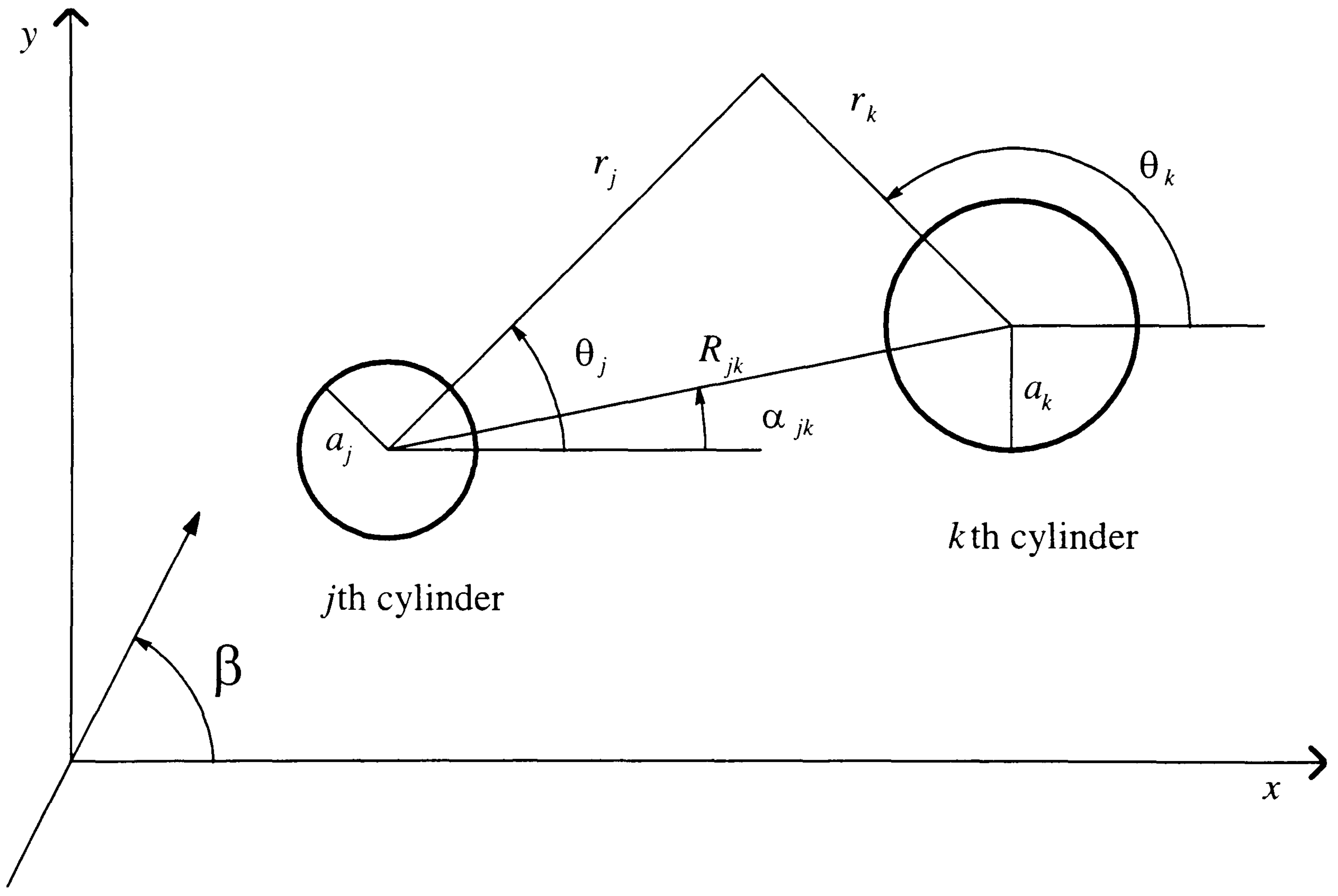

Figure 2.2. Multiple cylinder coordinate system definition

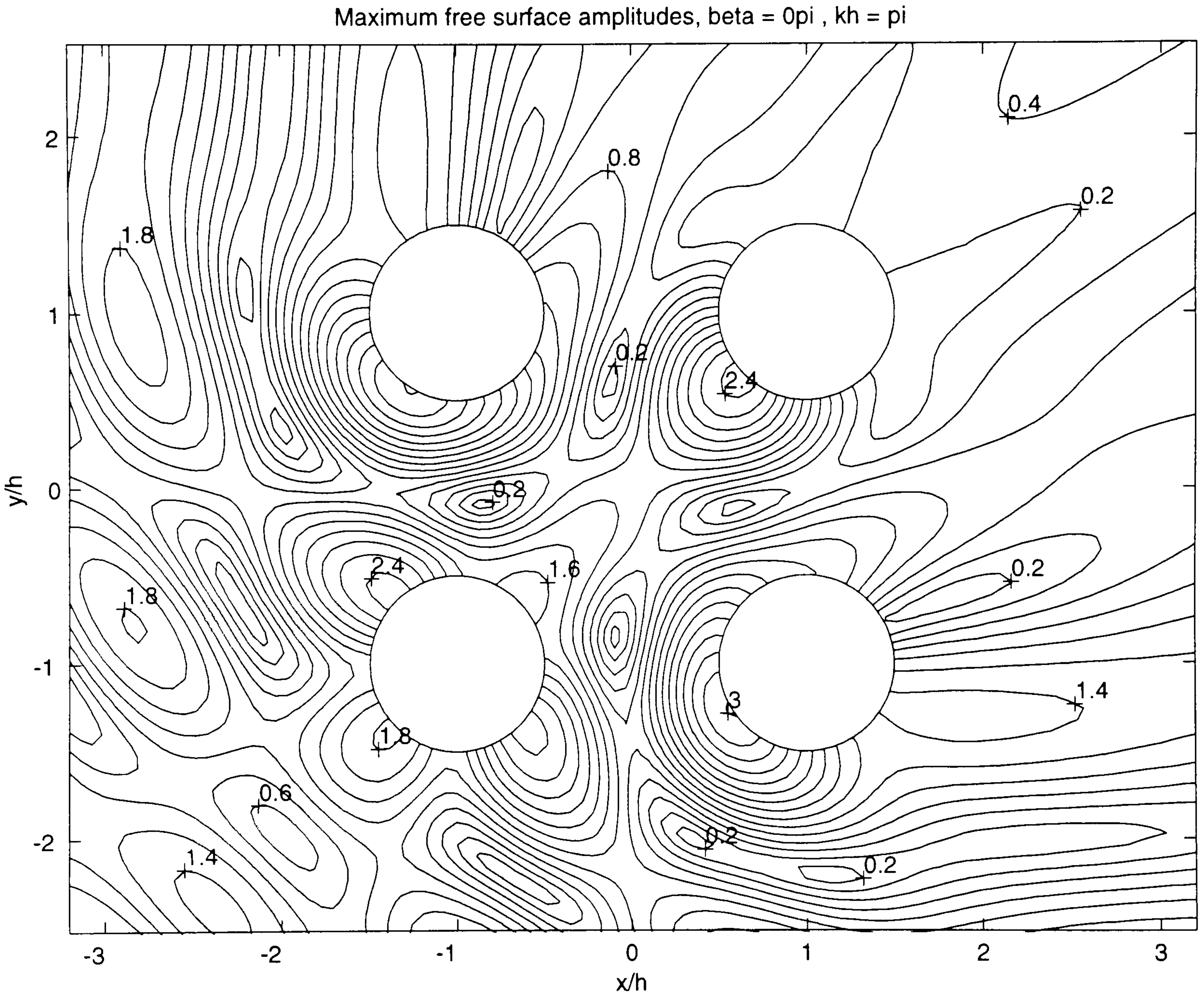

Figure 2.3. Maximum free surface amplitudes; $\beta = \frac{1}{4}\pi,\ kh = \pi,\ \frac{a}{h} = 0.5$; corresponds to Figure 6 in Linton & Evans (1990)

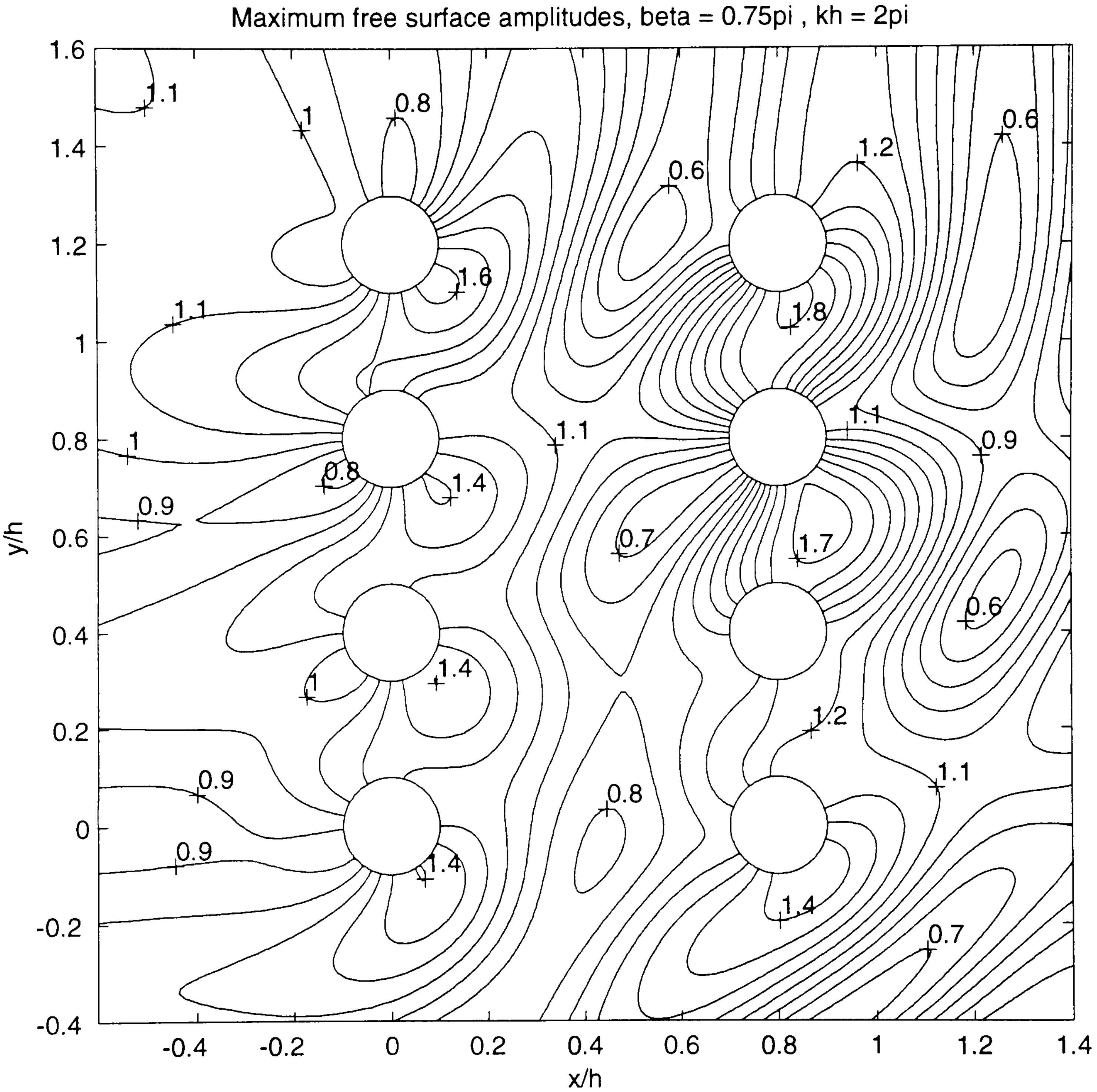

Figure 2.4. Maximum free surface amplitudes; $\beta = \frac{3}{4}\pi$, $kh = 2\pi$, $\frac{a}{h} = 0.1$; corresponds to Figure 10 in Linton & Evans (1990)

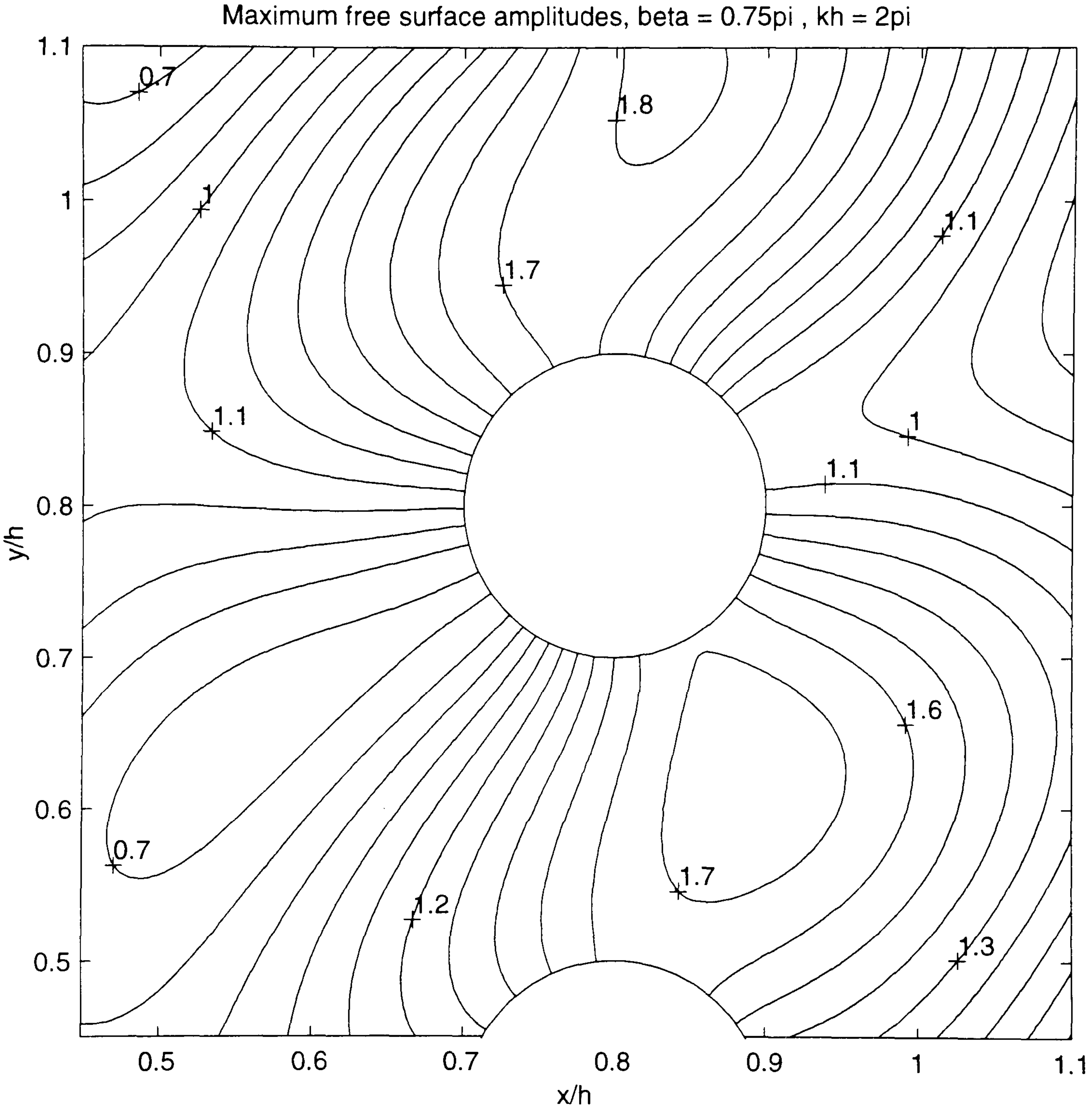

Figure 2.5. Detail of the maximum free surface amplitudes in the vicinity of the cylinder centred at $(0.8h, 0.8h)$ in the preceding figure; corresponds to Figure 11 in Linton & Evans (1990)

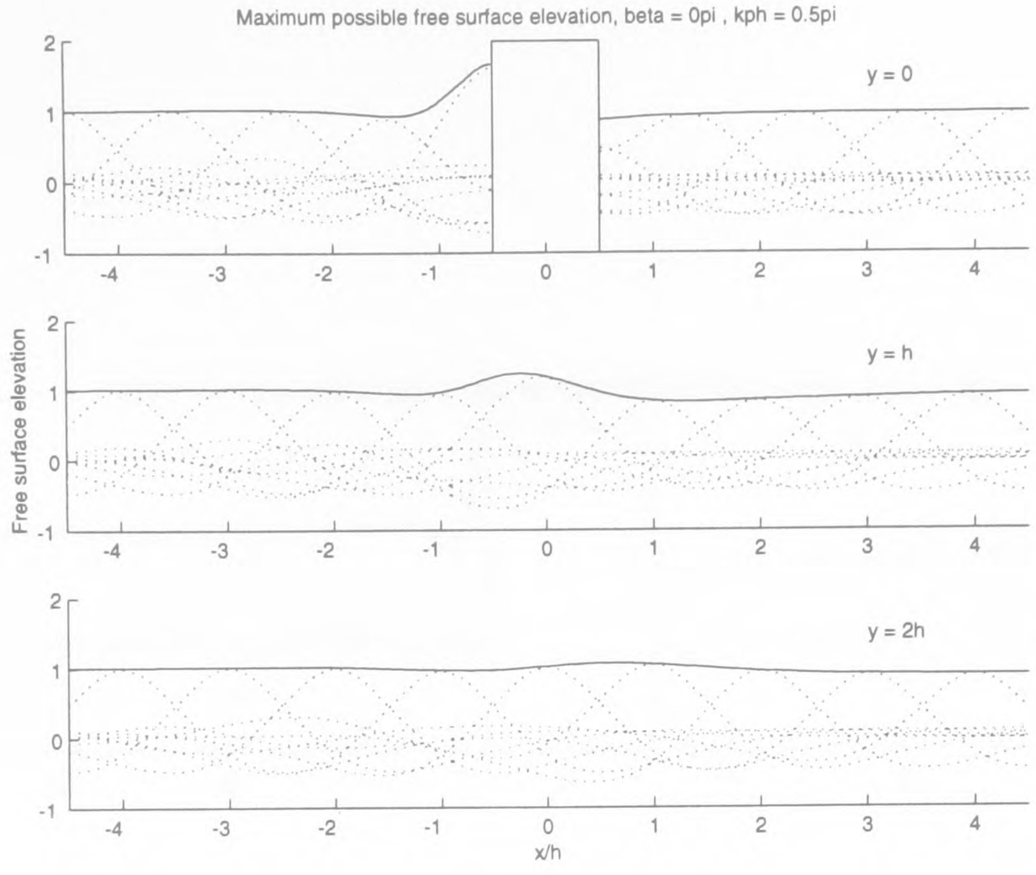

Figure 2.6. Maximum free surface elevation; $N = 1,\ \beta = 0,\ k_p h = \frac{\pi}{2},\ \frac{a}{h} = 0.5$

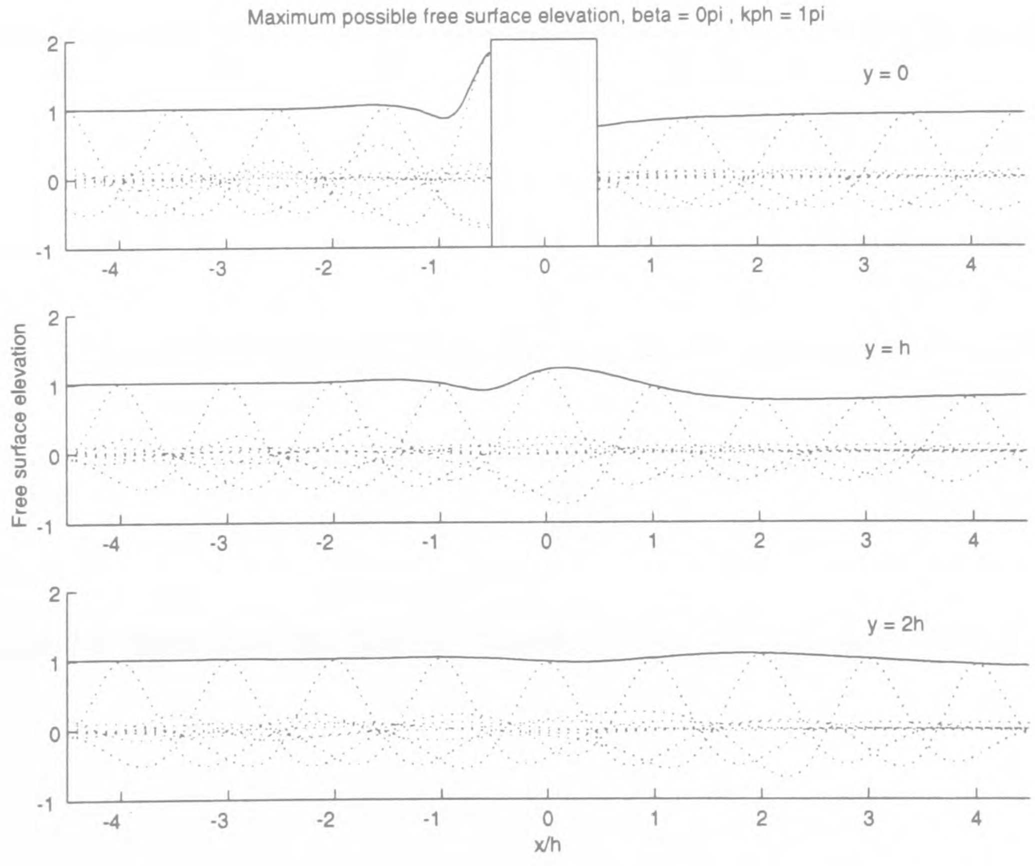

Figure 2.7. Maximum free surface elevation; $N = 1,\ \beta = 0,\ k_p h = \pi,\ \frac{a}{h} = 0.5$

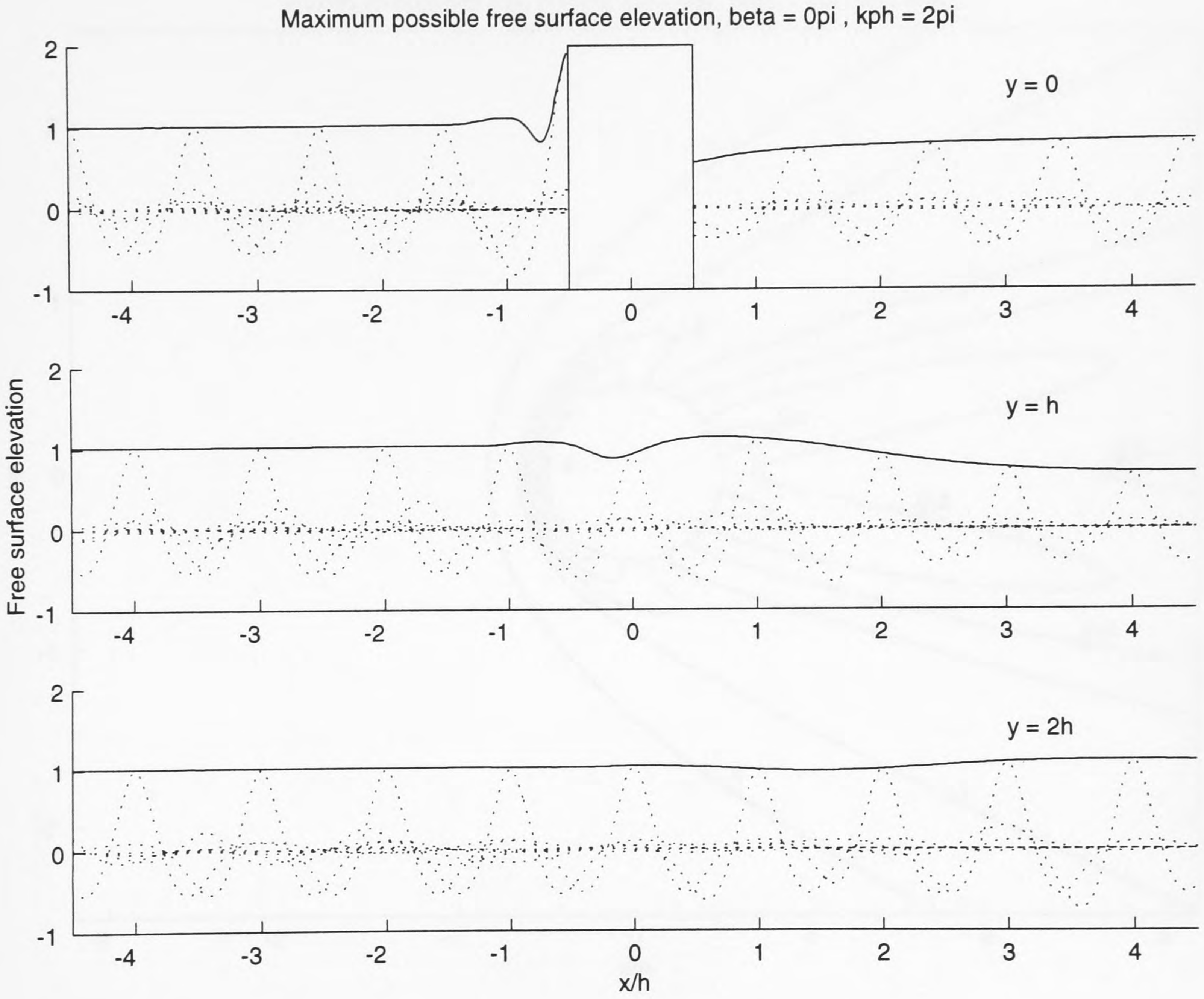

Figure 2.8. Maximum free surface elevation; $N = 1,\ \beta = 0,\ k_p h = 2\pi,\ \frac{a}{h} = 0.5$

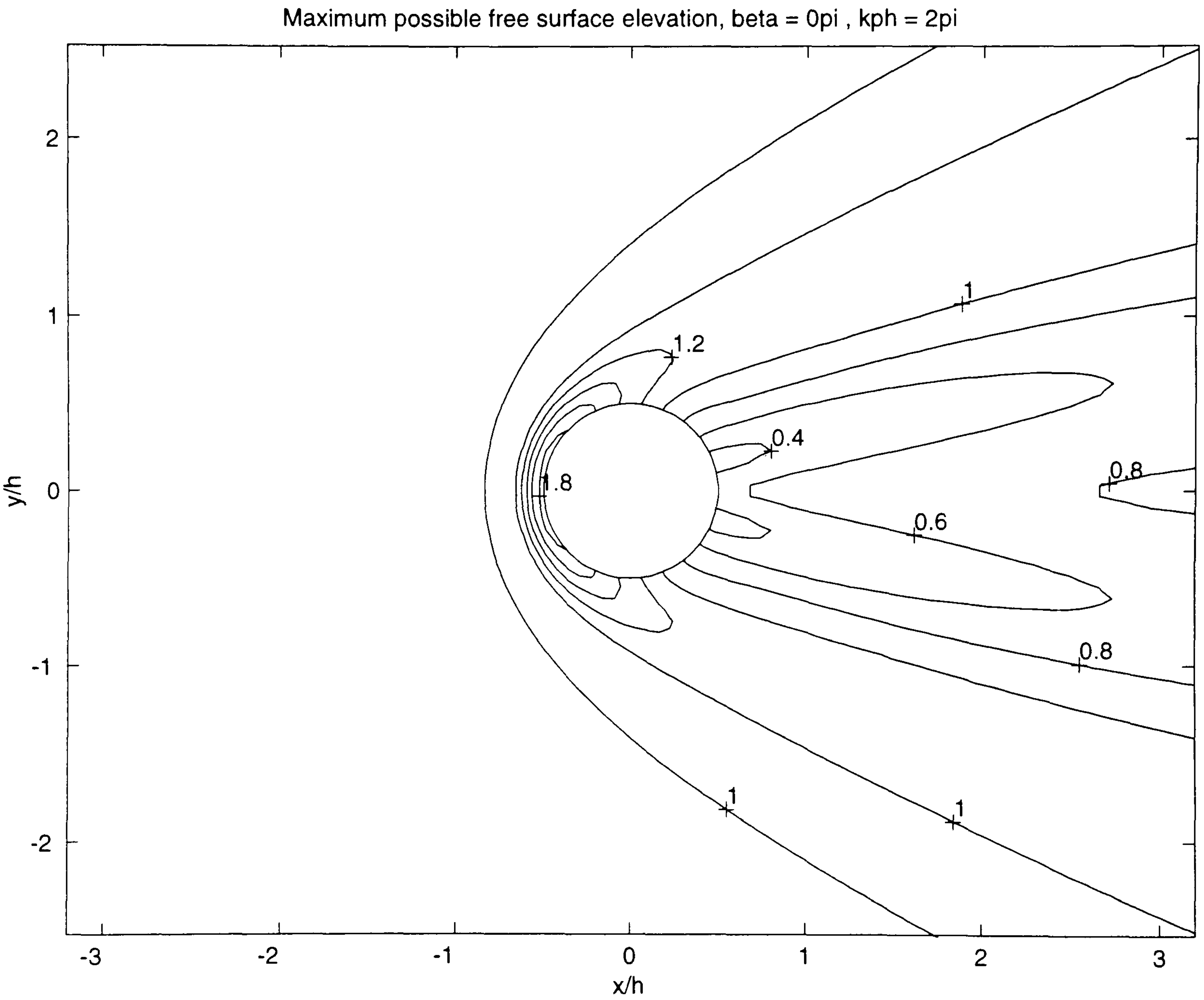

Figure 2.9. Contours of maximum free surface elevation; $N = 1$, $\beta = 0$, $k_p h = 2\pi$, $\frac{a}{h} = 0.5$

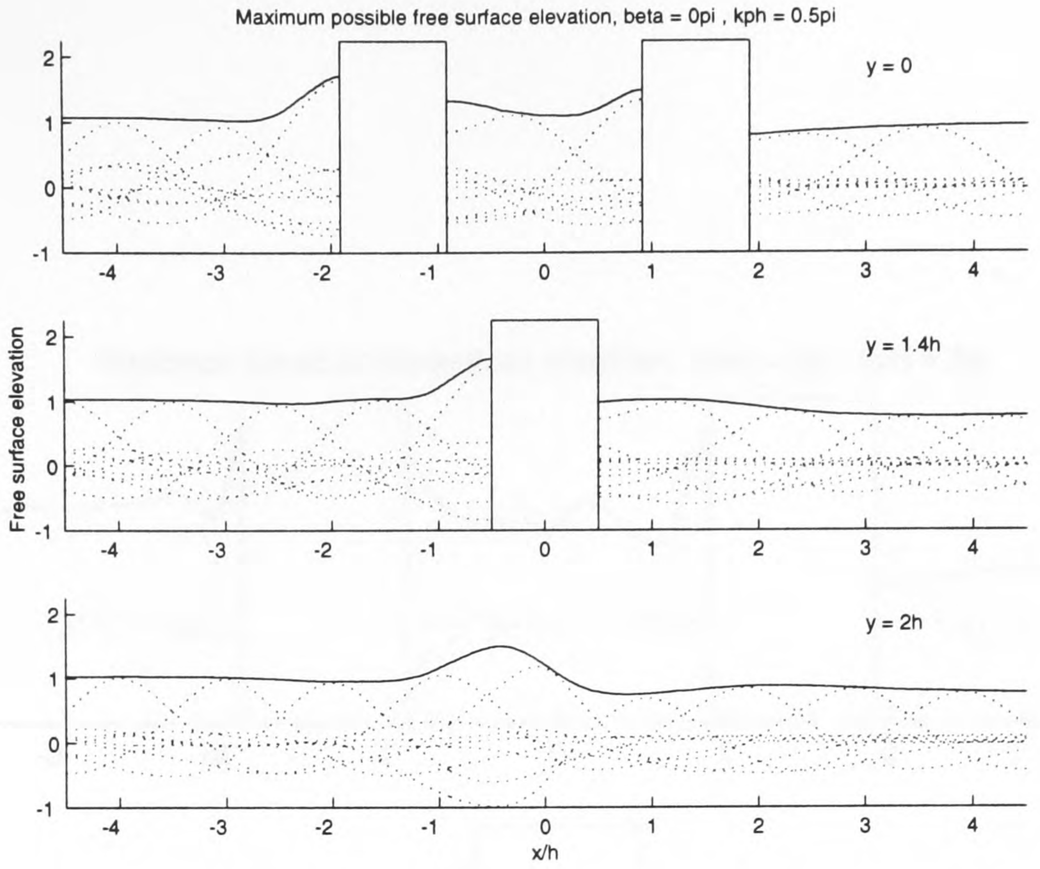

Figure 2.10. Maximum free surface elevation; $N = 4,\ \beta = 0,\ k_p h = \frac{\pi}{2},\ \frac{a}{h} = 0.5$

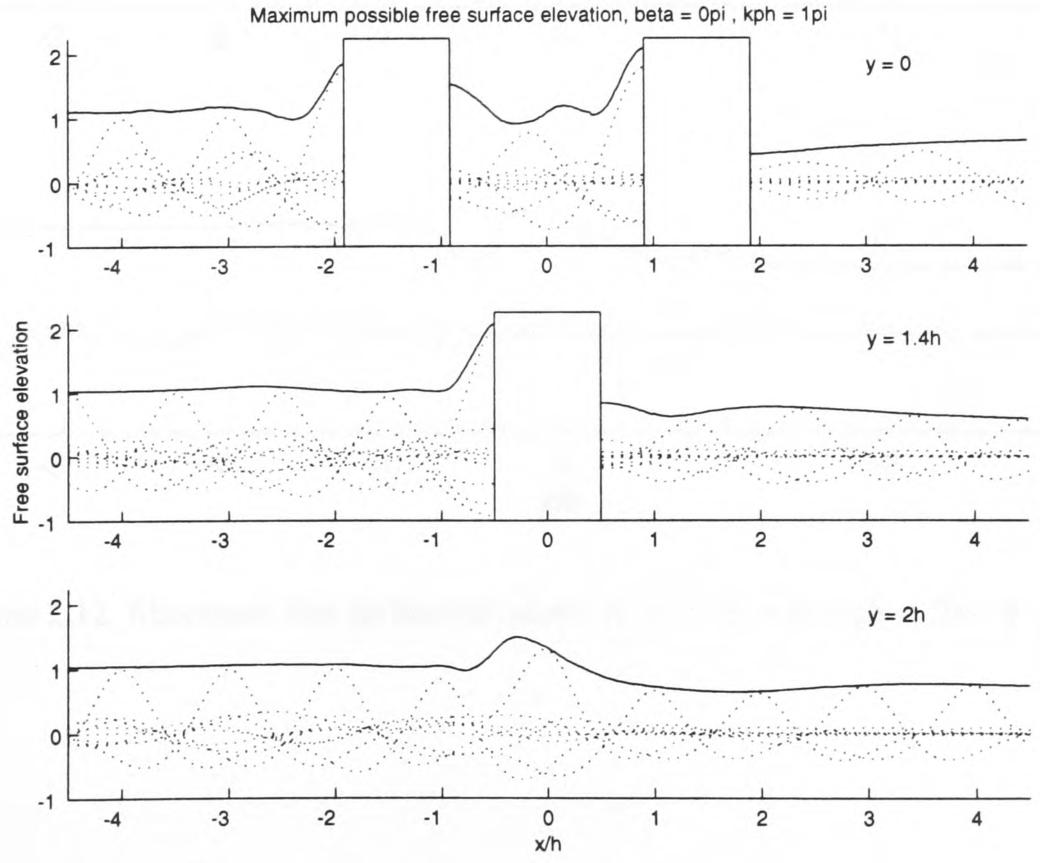

Figure 2.11. Maximum free surface elevation; $N = 4,\ \beta = 0,\ k_p h = \pi,\ \frac{a}{h} = 0.5$

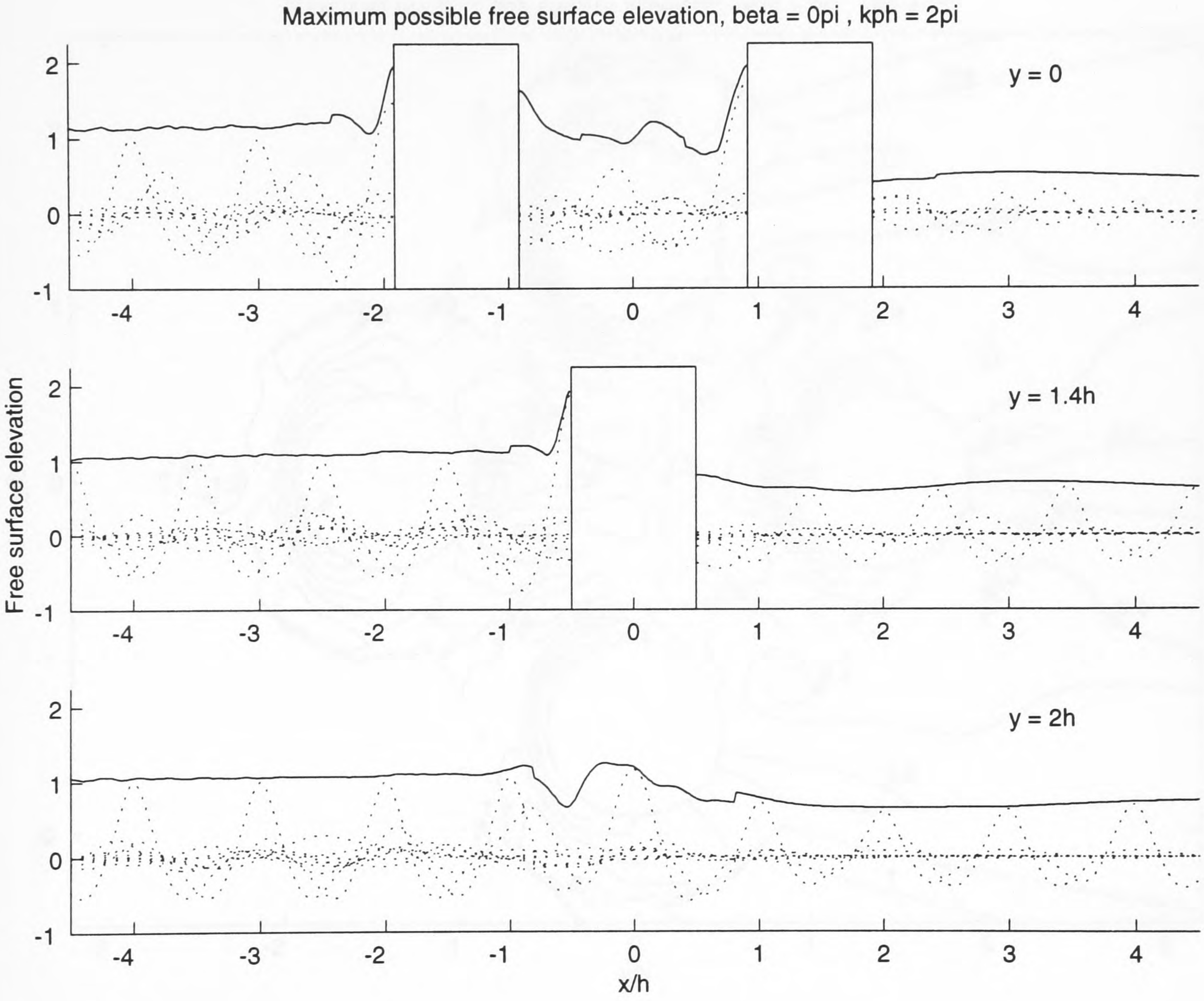

Figure 2.12. Maximum free surface elevation; $N = 4,\ \beta = 0,\ k_p h = 2\pi,\ \frac{a}{h} = 0.5$

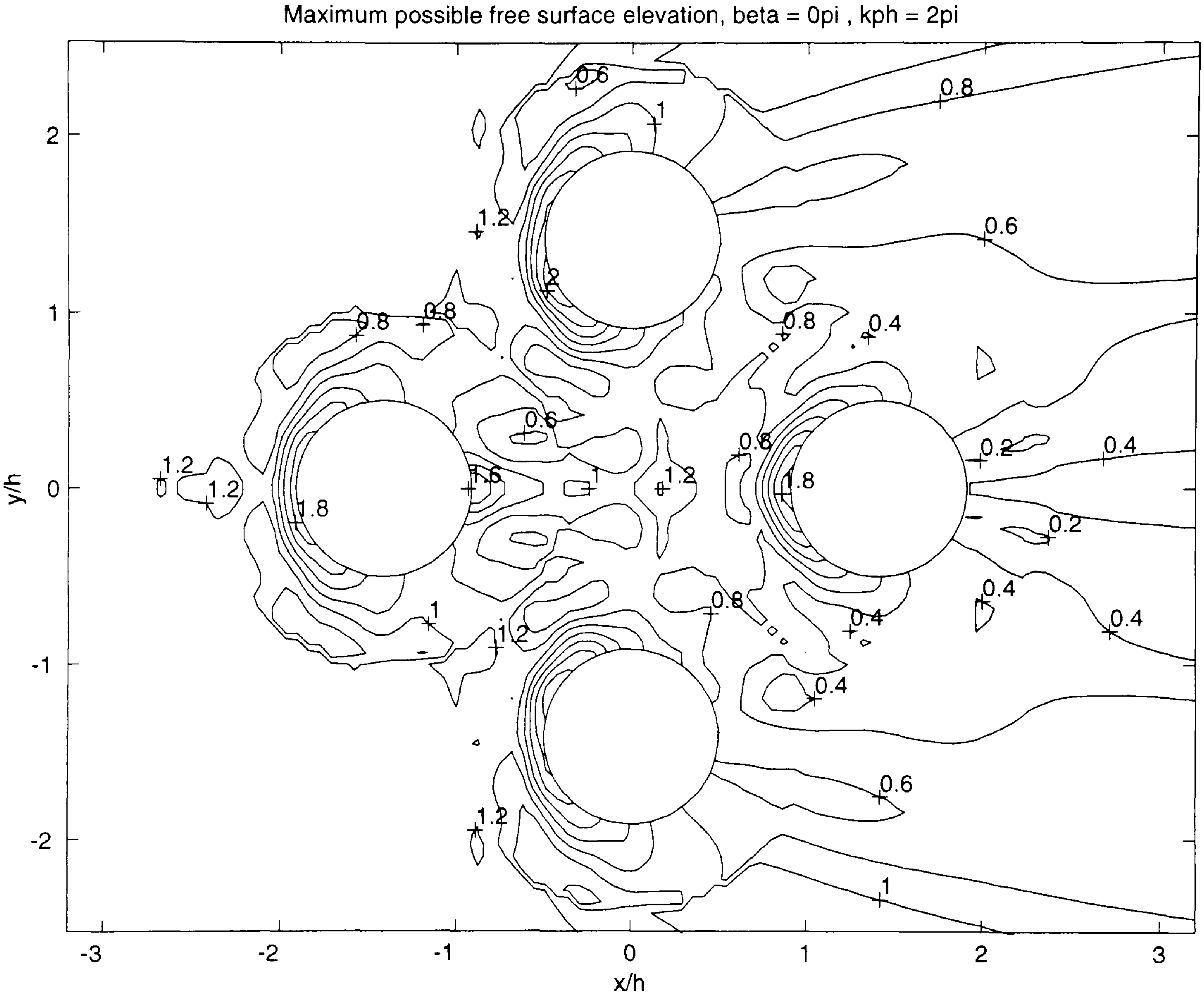

Figure 2.13. Contours of maximum free surface elevation; $N = 4$, $\beta = 0$, $k_p h = 2\pi$, $\frac{a}{h} = 0.5$

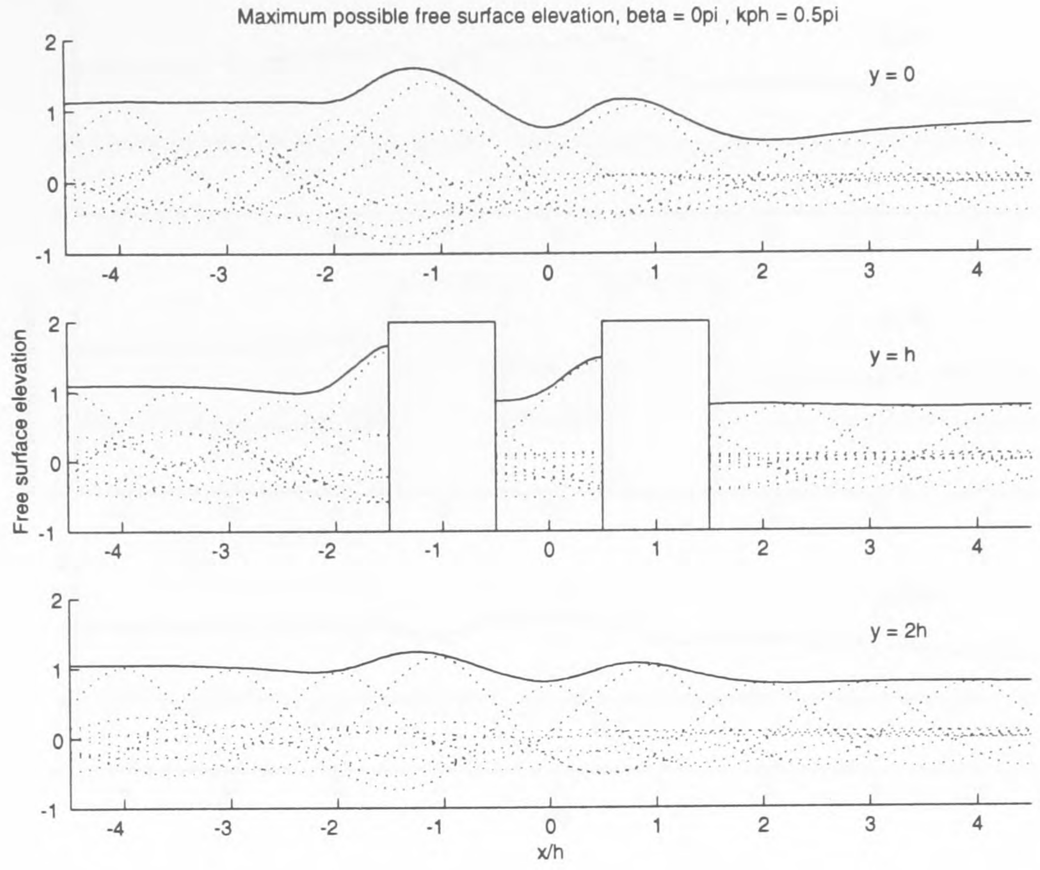

Figure 2.14. Maximum free surface elevation; $N = 4,\ \beta = 0,\ k_p h = \frac{\pi}{2},\ \frac{a}{h} = 0.5$

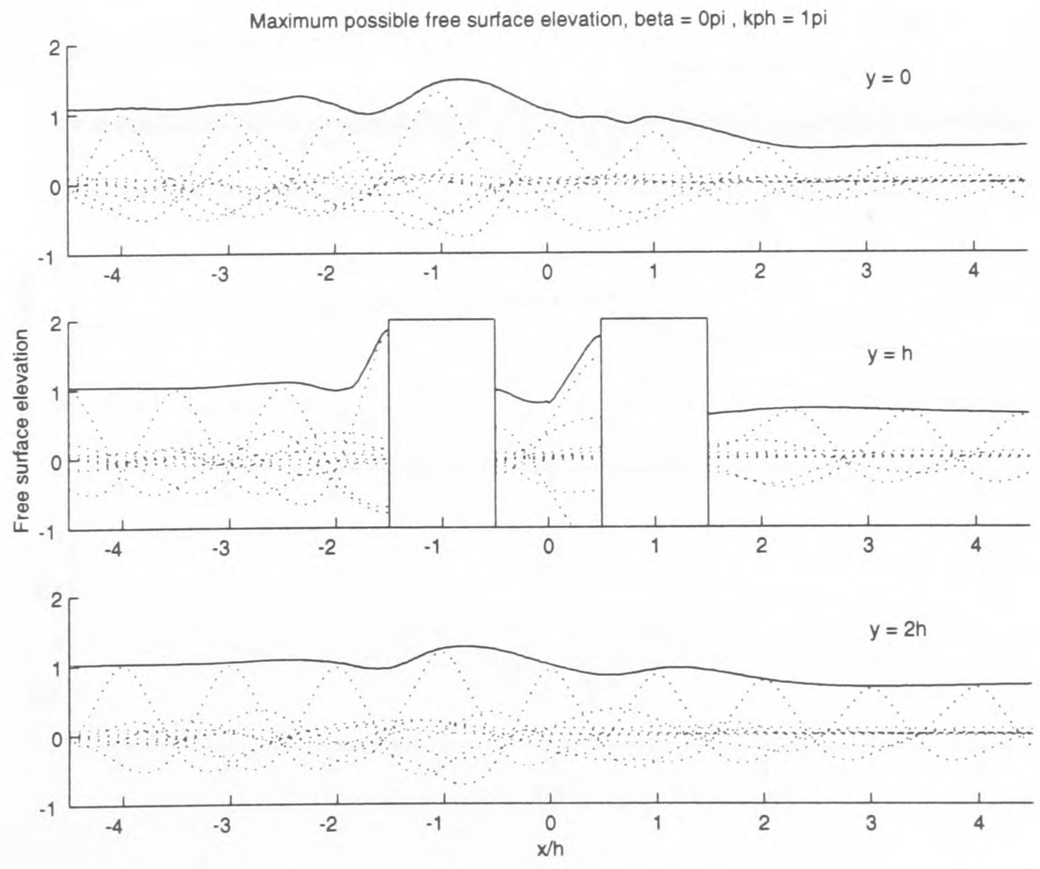

Figure 2.15. Maximum free surface elevation; $N = 4,\ \beta = 0,\ k_p h = \pi,\ \frac{a}{h} = 0.5$

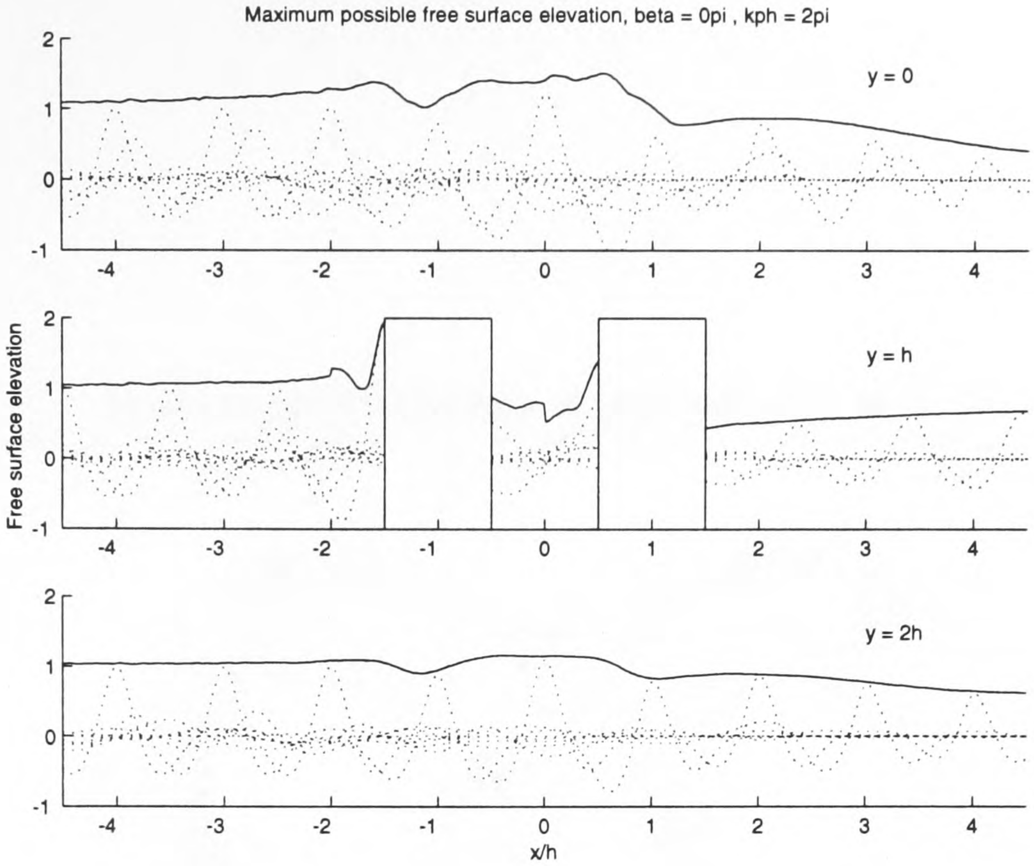

Figure 2.16. Maximum free surface elevation; $N = 4,\ \beta = 0,\ k_p h = 2\pi,\ \frac{a}{h} = 0.5$

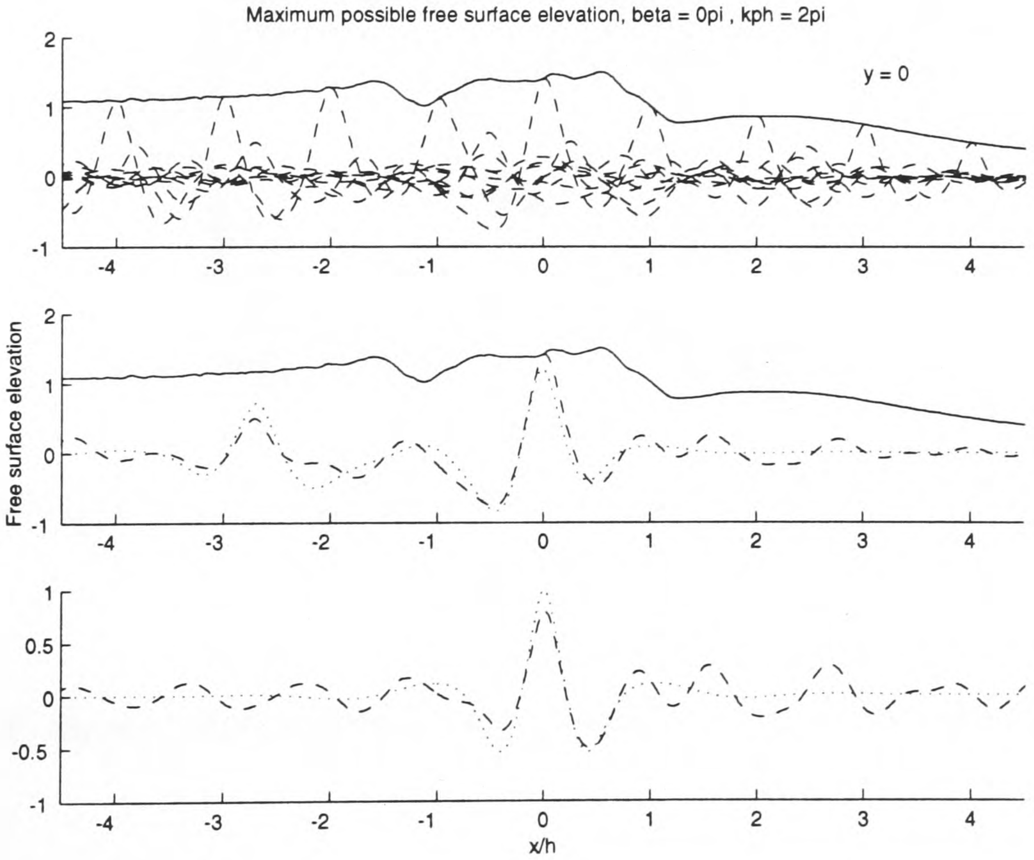

Figure 2.17. Maximum free surface elevation and varying incident wave forms; $N = 4,\ \beta = 0,\ k_p h = 2\pi,\ \frac{a}{h} = 0.5$

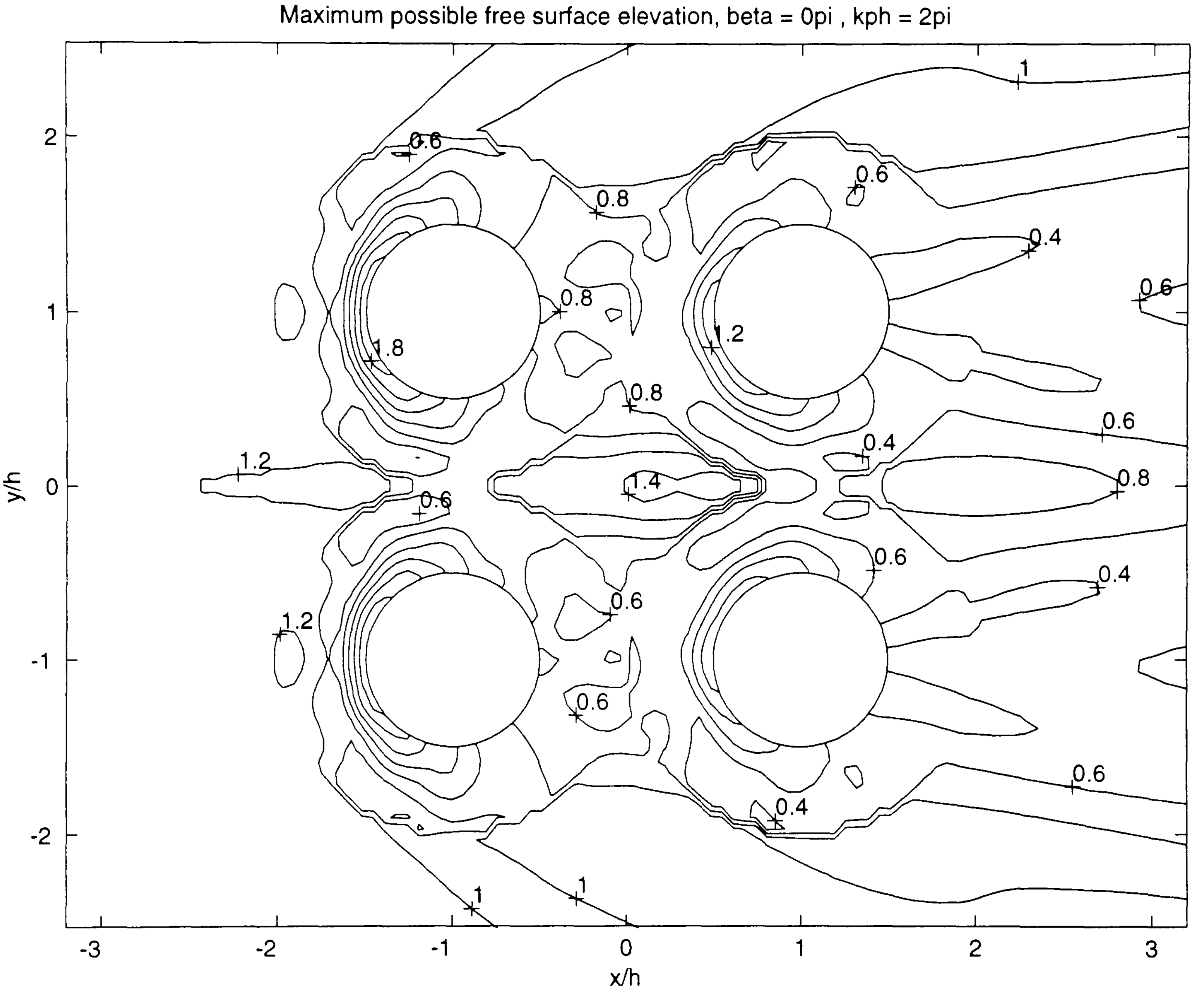

Figure 2.18. Contours of maximum free surface elevation; $N = 4$, $\beta = 0$, $k_p h = 2\pi$, $\frac{a}{h} = 0.5$

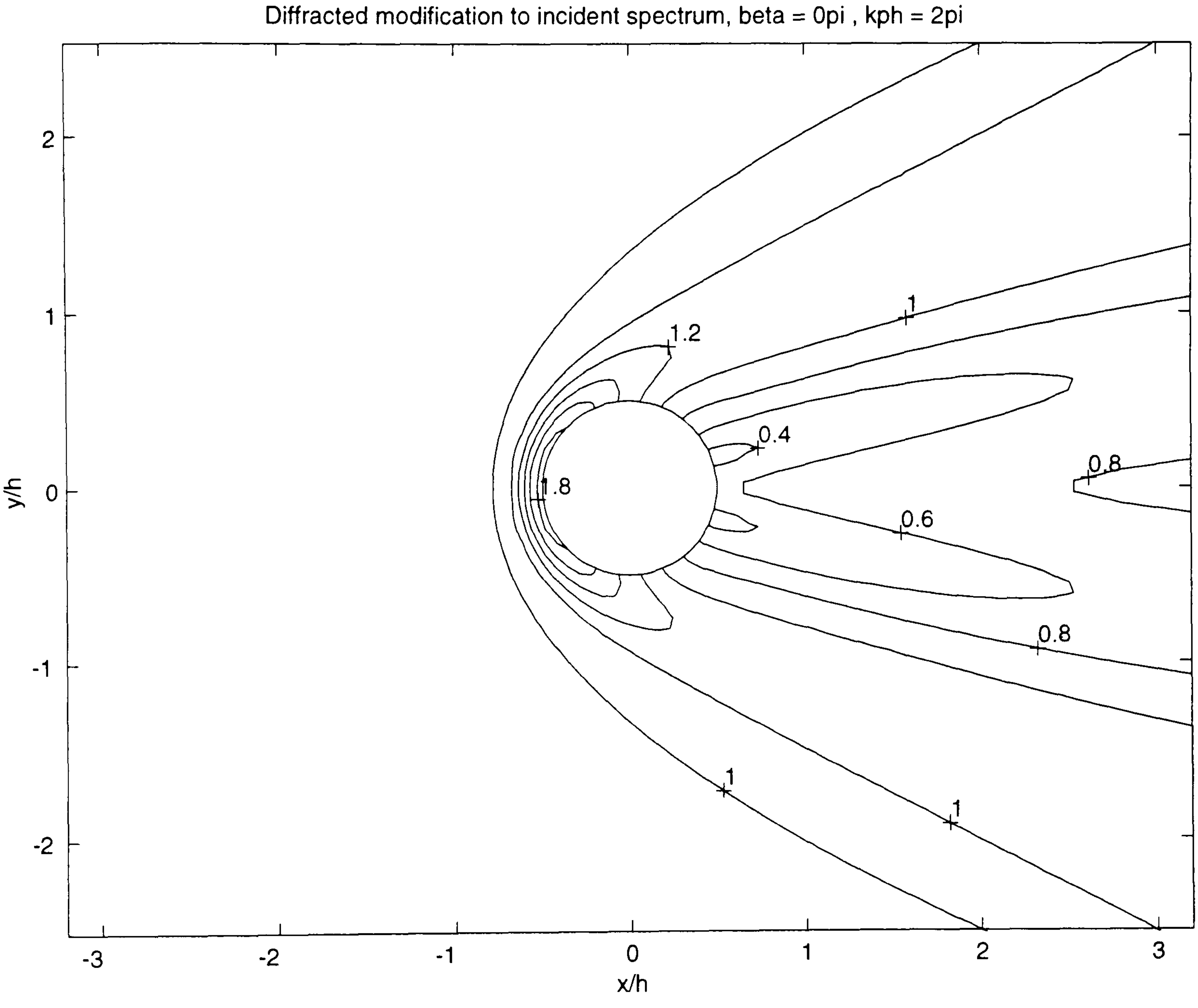

Figure 2.19. Diffracted modification to incident wave spectrum; $N = 1$, $\beta = 0$, $k_p h = 2\pi$, $\frac{a}{h} = 0.5$

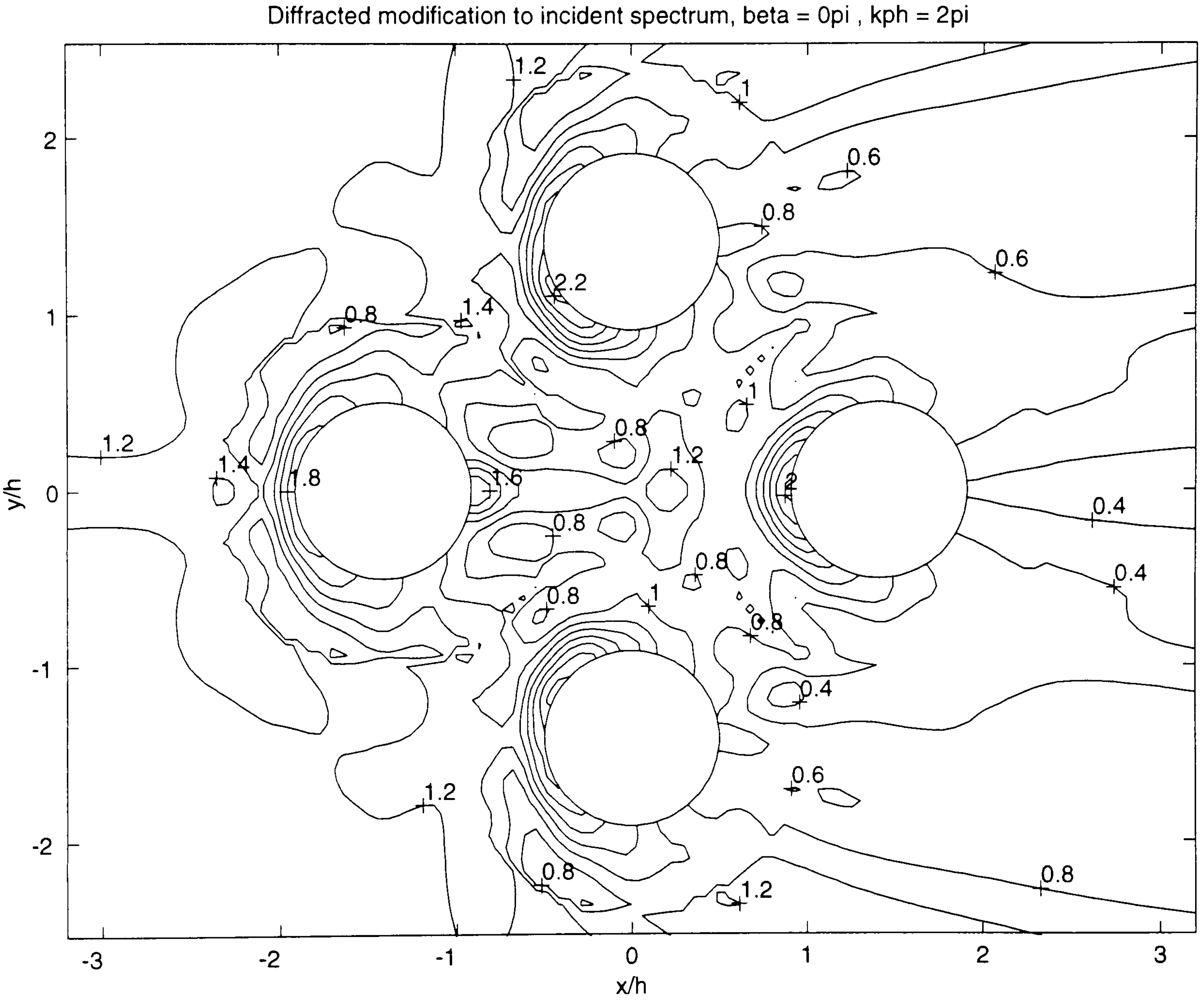

Figure 2.20. Diffracted modification to incident wave spectrum; $N = 4$, $\beta = 0$, $k_p h = 2\pi$, $\frac{a}{h} = 0.5$

Diffracted modification to incident spectrum, beta = 0pi , kph = 2pi

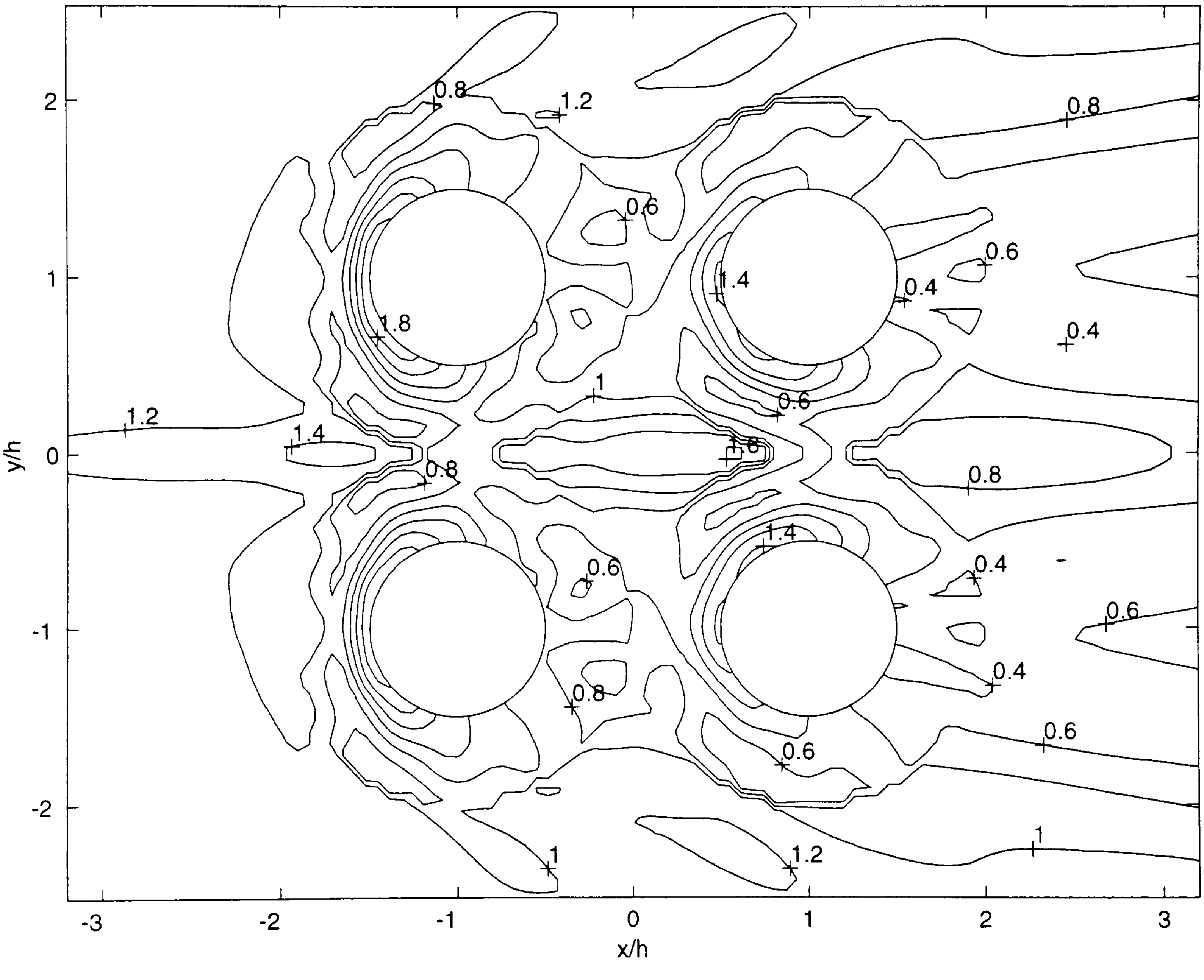

Figure 2.21. Diffracted modification to incident wave spectrum; $N = 4,\ \beta = 0,\ k_p h = 2\pi,\ \frac{a}{h} = 0.5$

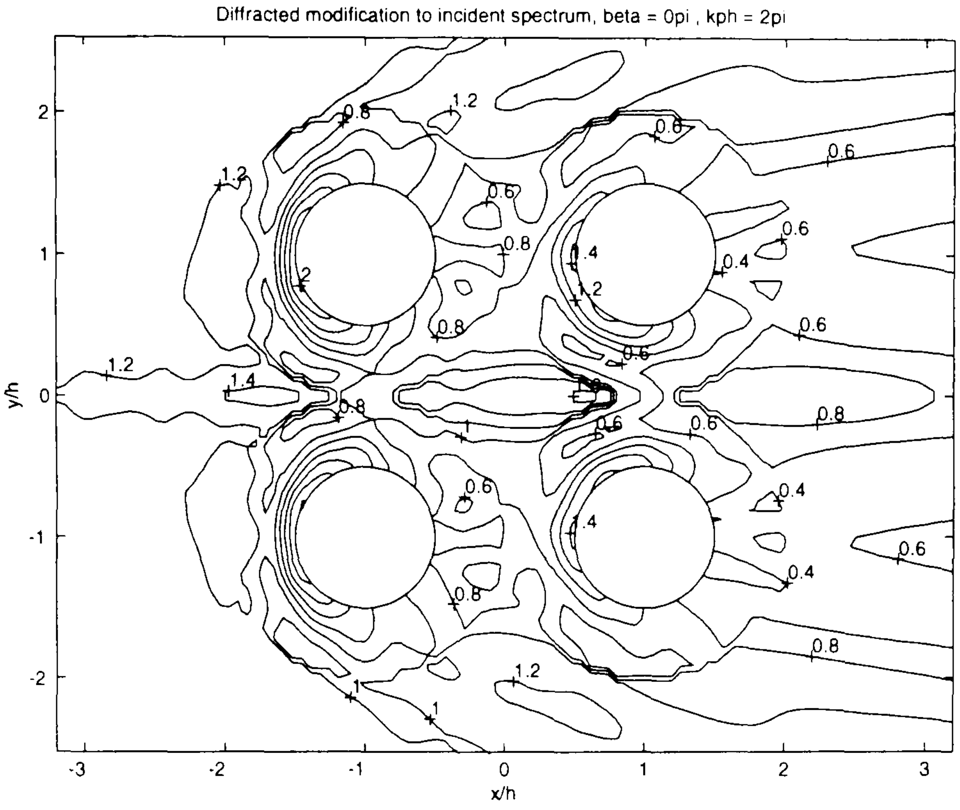

Figure 2.22. Diffracted modification to incident wave spectrum; 60 wavenumber components, $\triangle k = \frac{k_p}{10}$, $k_1 = \frac{\triangle k}{2}$; $N = 4$, $\beta = 0$, $k_p h = 2\pi$, $\frac{a}{h} = 0.5$

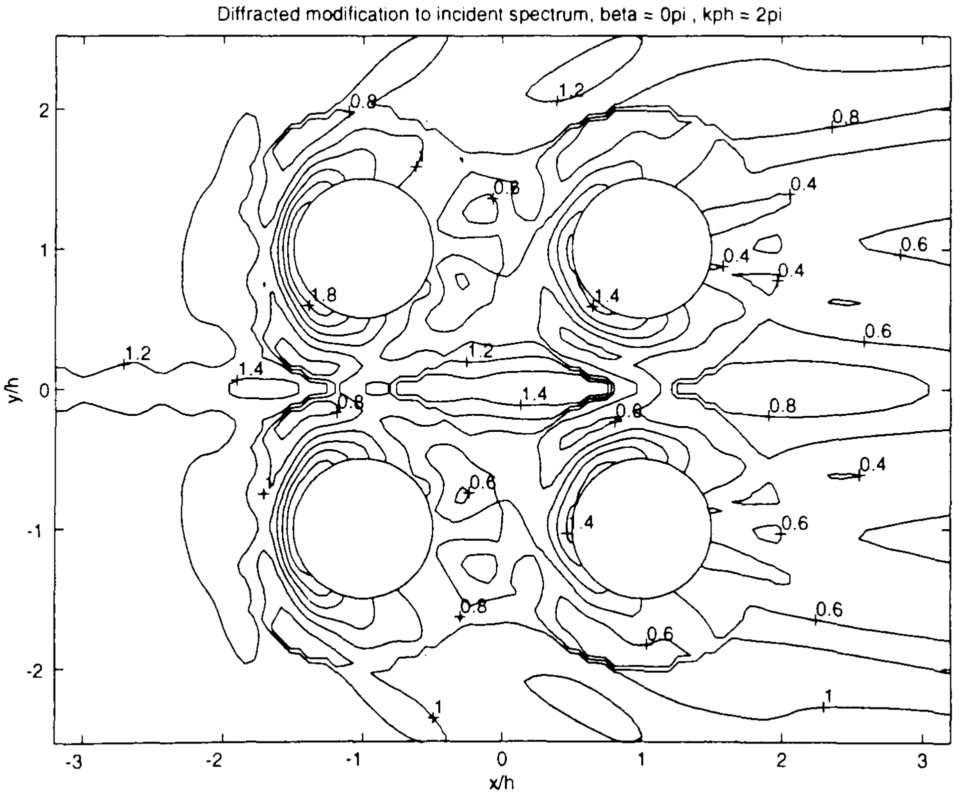

Figure 2.23. Diffracted modification to incident wave spectrum; 60 wavenumber components, $\triangle k = \frac{k_p}{10}$, $k_1 = \triangle k$; $N = 4$, $\beta = 0$, $k_p h = 2\pi$, $\frac{a}{h} = 0.5$

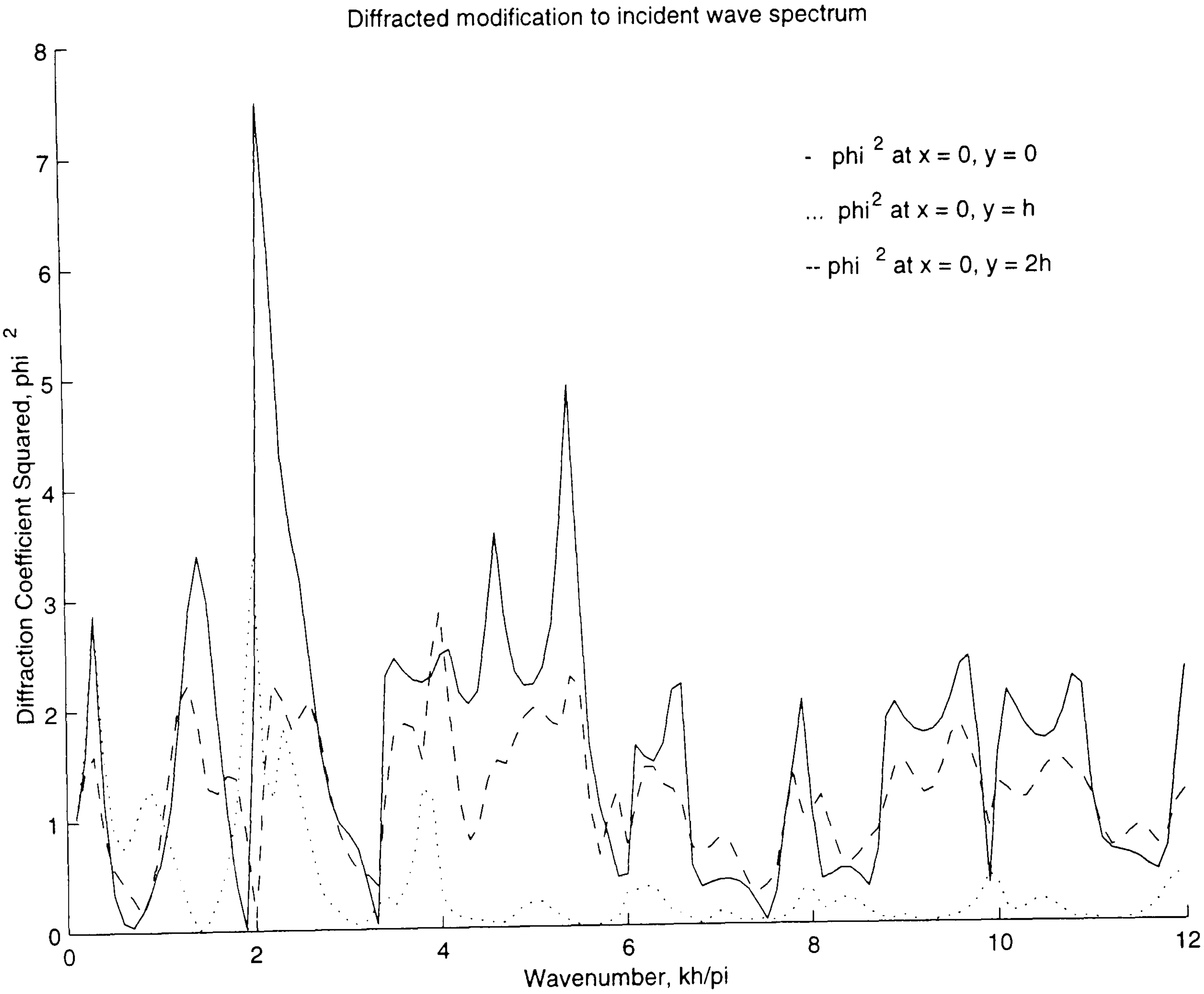

Figure 2.24. Diffracted modification to incident wave spectrum at points as annotated; $N = 4$, $\beta = 0$, $k_p h = 2\pi$, $\frac{a}{h} = 0.5$

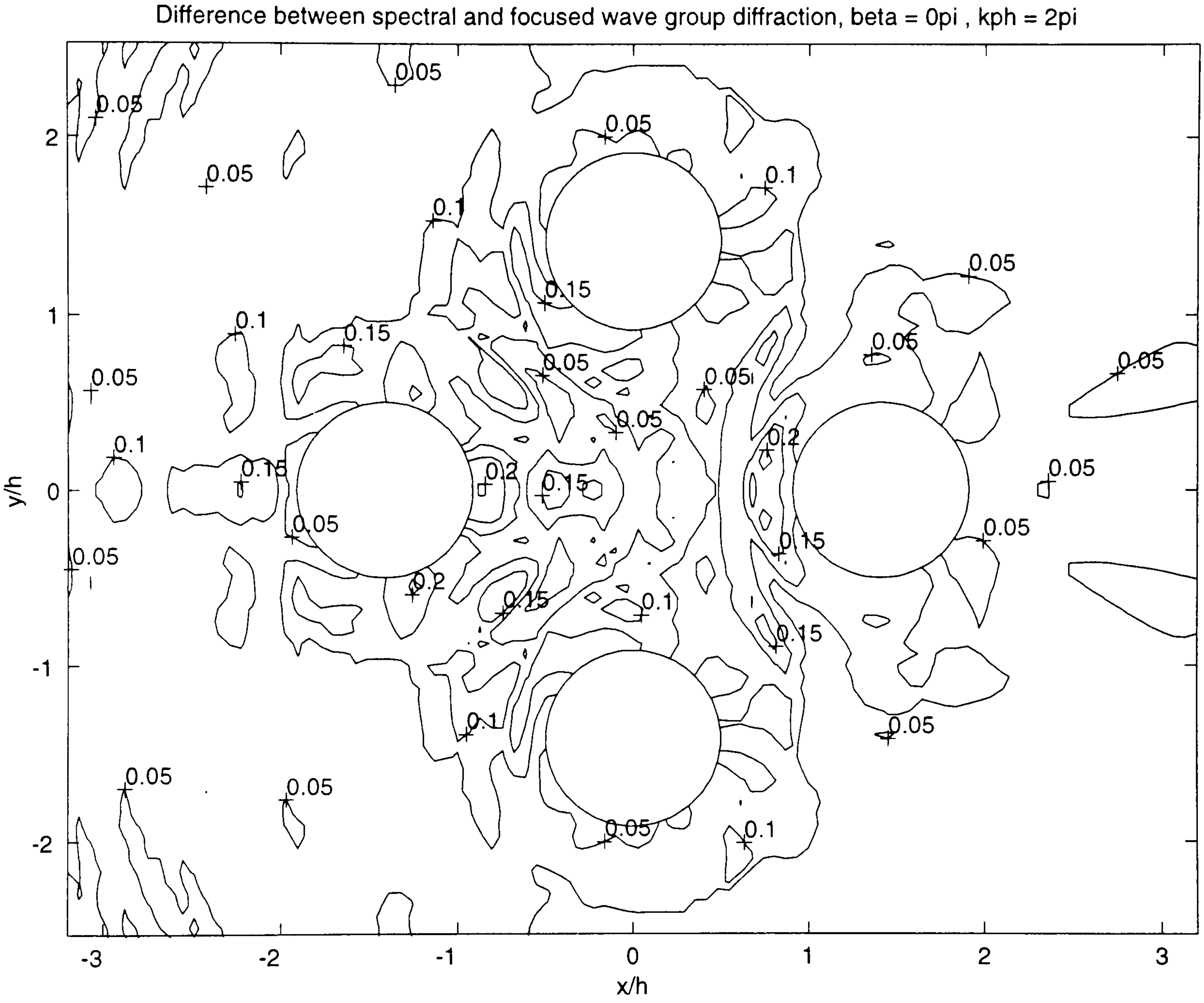

Difference between spectral and focused wave group diffraction, beta = 0pi , kph = 2pi

Figure 2.25. Difference between spectral and focused wave group diffraction $\frac{\eta_d}{\eta_i} - \eta_m$; $N = 4$, $\beta = 0$, $k_p h = 2\pi$, $\frac{a}{h} = 0.5$

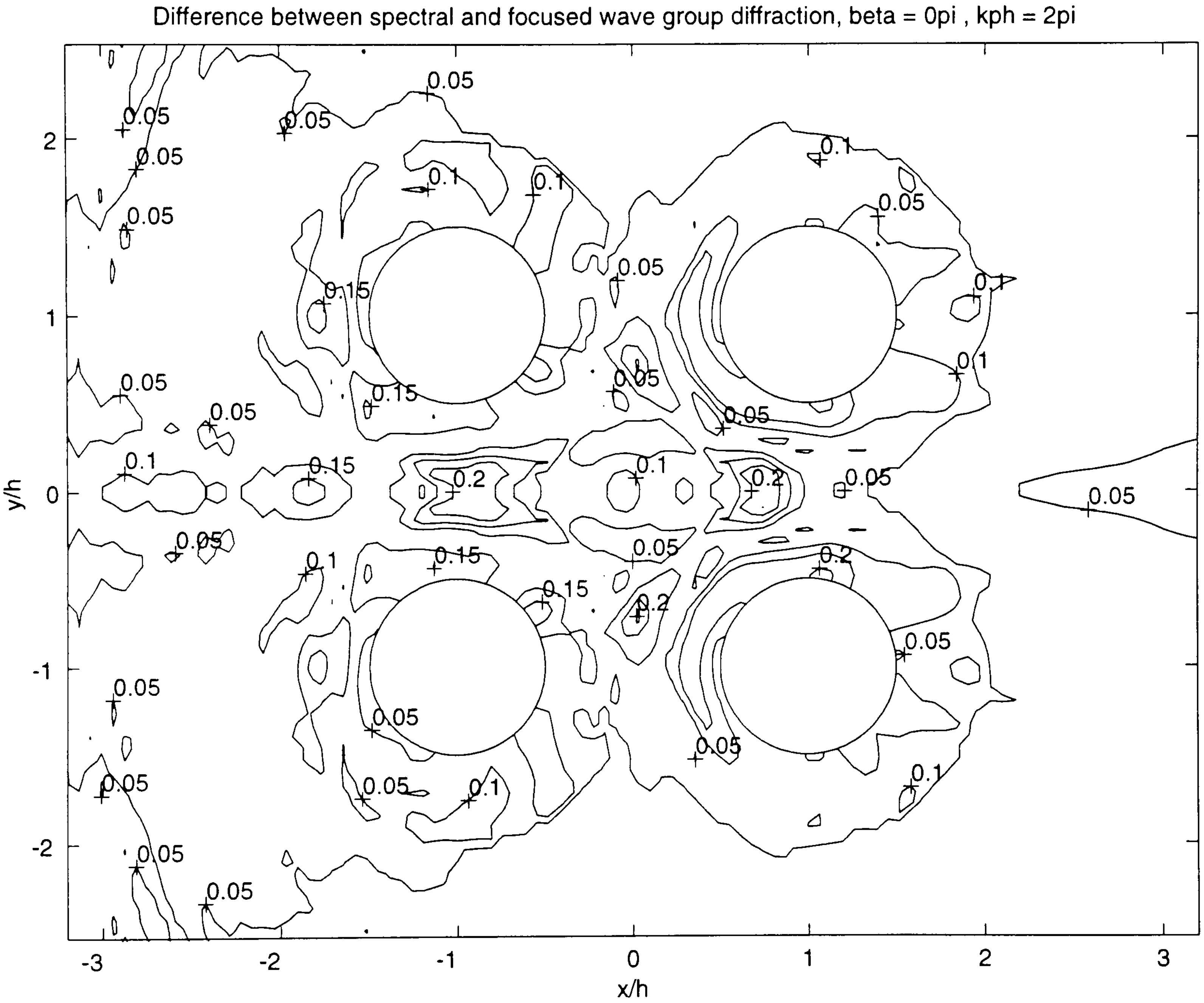

Figure 2.26. Difference between spectral and focused wave group diffraction $\frac{\eta_d}{\eta_i} - \eta_m$; $N = 4$, $\beta = 0$, $k_p h = 2\pi$, $\frac{a}{h} = 0.5$

Chapter 3
Nonlinear Theory for Focused Wave Groups

3.1 Introduction

As discussed in Chapter 1, the Creamer nonlinear transform (CNT) is a nonlinear transform for steep surface waves on deep water ($kd \rightarrow \infty$, but effectively applicable for $kd \geq 1.5$), and formulated by Creamer *et al.* (1989). Operating on a linear (first order) representation of the free surface in the spatial domain $\eta_L(x)$, the transform produces a nonlinear free surface and velocity potential in terms of their equivalent wavenumber components. Following these calculations, associated horizontal and vertical fluid velocities may be calculated on the free surface.

The following chapter details the formulation of the CNT and its application to linear waves, both regular waves and focused wave groups, as discussed by Taylor & Ohl (1999b). As a convention, the time of occurrence and position of highest free surface elevation for a focused extreme event will be at $x = 0, t = 0$. Subsequently, the recent work of Taylor, Ohl, & Sauvee (1999) on the specific application of the transform to focused wave groups is presented. This includes comparisons between local structure and kinematics on the free surface as predicted by the CNT and results calculated using a fully nonlinear uni-dimensional numerical wave tank (NWT) produced by Bateman, Swan & Taylor (1999a) at Imperial College, London. Beginning from the initial conditions of a free surface and velocity potential in space and through a pseudo-spectral method, their method restricts the water wave problem to equations on the free surface and simulates the time evolution of the surface wave. Results produced by this method for steep multi-directional waves are given by Bateman, Swan & Taylor (1999b).

Finally, analysing focused wave groups as produced by this NWT, subsequent work of Taylor & Ohl (1999a) is presented. This demonstrates the effectiveness of the CNT at identifying bound wave components of focused wave groups over short time scales and shows that it is incapable of reproducing long time scale evolution due to resonant wave-wave interactions.

3.2 Linear Focused Wave Groups

As discussed in Chapter 1, a focused wave group (also known as an extreme or freak wave) occurs when the numerous frequency components of a random sea come into phase and coincide. From the derivation of Chapter 2 and for uni-directional seas, the linear free surface η_L in the vicinity of such an extreme event may be written as

$$\eta_L\left(x,t\right) = \frac{\alpha}{\sigma^2}\sum_n C_n \operatorname{Re}\left\{\mathrm{e}^{\mathrm{i}(k_n x - \omega_n t)}\right\}, \tag{53}$$

where $C_n = (S_n \bigtriangleup \omega_n)$, and k_n and ω_n are the n^{th} wavenumber and radian wave frequency components of the random sea, respectively. The height of the extreme event is α, while σ is the standard deviation of the surface power spectrum $S_n = \frac{A_n^2}{2\triangle\omega}$, where A_n is the amplitude of the n^{th} component.

In Chapter 2, Figure 2.1 demonstrates the time evolution of a linear focused wave group. Proceeding from the lower left to the upper right of the plot, the wavenumber components of the group come into focus and form an extreme wave crest at $t = 0$ and $x = 0$. After this time the components rapidly defocus, with longer wavelength components overtaking those with shorter wavelength.

In contrast, Figure 3.1, displays the fully-nonlinear time evolution of a focused wave group computed by the NWT of Bateman *et al.* (1999a). In this deep water simulation the domain has been discretised into 512 spatial points (from $x = -22.5$ m to 22.5 m) and 256 wavenumber components. As an initial condition, the input spectrum is a linear JONSWAP spectrum with peak wavenumber $k_p = 5\ \mathrm{m}^{-1}$ ($T_p = 0.90$ s) and designed to focus 20s after the beginning of the run. The extreme event in this case is very close to breaking, with $\alpha k_p = 0.3$ on a linear basis. Due to nonlinear wave-wave interactions, the time of focus (here $t = 0$) occurs ~ 1.4 s before the prediction of linear theory, indicating that the wavenumber components are not obeying linear dispersion, as discussed by Taylor & Vijfvinkel (1998). In comparison with Figure 2.1 from Chapter 2, the nonlinear free surface at the time of focus has a more complex profile, including a shoulder just upwave of the crest. This results from wavenumber components close to the peak of the spectrum focusing before those in the high wavenumber tail.

3.3 Creamer Nonlinear Transform (CNT)

Given the spatial representation of a linear free surface $\eta_L\left(x\right)$, the nonlinear free surface elevation and associated velocity potential on the free surface may be obtained through the following

$$\hat{\eta} = \frac{1}{|k|}\int \mathrm{e}^{-\mathrm{i}kx}\left[\mathrm{e}^{\mathrm{i}k\eta_{LH}(x)} - 1\right] dx \tag{54}$$

and

$$\hat{\phi}_s = \frac{1}{|k|}\int \mathrm{e}^{-\mathrm{i}k[x-\eta_{LH}(x)]}\phi'_{sLH}(x)\; dx, \tag{55}$$

where $\hat{\eta}$ and $\hat{\phi}_s$ are the complex spectral components of the free surface and velocity potential for wavenumber k. This calculation requires η_{LH}, the Hilbert transform of the free surface, and $\phi'_{sLH} = u_{sLH}$, the Hilbert transform of the linear approximation to the horizontal velocity at the surface. Involving a 90° phase shift of the standard linear quantities, the Hilbert transform changes a cosine to a sine and a sine to a negative cosine. The necessary Hilbert transformed quantities may be calculated in the wavenumber domain as

$$\hat{\eta}_{LH} = \mathrm{i}\hat{\eta}_L \quad \text{and} \quad \hat{\phi}'_{sLH} = \mathrm{i}\hat{\phi}'_{sL} = \mathrm{i}\hat{u}_{sL}. \tag{56}$$

The presence of the wavenumber k in both the kx and $k\eta_{LH}$ terms of (54) and (55) above indicates that spatial FFTs may not be used for the calculation. However, for a discretised domain of N points in space and separated by distance $\triangle x$, they may be approximated by the following numerical integrals:

$$\hat{\eta} \approx \frac{1}{k}\sum_{n=1}^{N} \mathrm{e}^{-\mathrm{i}kx_n}\left[\mathrm{e}^{\mathrm{i}k\eta_{LH}(x_n)} - 1\right] \triangle x \tag{57}$$

and

$$\hat{\phi}_s \approx \frac{1}{k}\sum_{n=1}^{N} \mathrm{e}^{-\mathrm{i}k[x_n-\eta_{LH}(x_n)]}\phi'_{sLH}(x_n) \triangle x. \tag{58}$$

where k is both real and positive.

Plots of free surface elevation versus distance, Figures 3.2 and 3.3 demonstrate application of the above equations to both regular waves and focused wave groups. Dashed lines represent the linear free surface elevation, while solid lines represent the nonlinear CNT output. It is clear from both figures that the nonlinear crests are higher and steeper, while the nonlinear troughs are shallower and less steep. However, it is also important to note from Figure 3.2, for regular waves with different steepness from $Ak = 0.1$ to 0.3, that steeper linear free surfaces produce greater nonlinearity after the CNT has been applied.

Figures 3.4 and 3.5 show further application of the CNT to linear focused wave groups of varying steepness ($Ak_p = 0.1$, 0.2, and 0.3). The left hand side of each figure (3.4a and 3.5a) plots free surface elevation versus distance, while the right side (3.4b and 3.5b) plots free surface elevation versus time. As the CNT operates in the wavenumber and distance domains, these time histories have been produced by time stepping the linear free surface and applying the CNT to linear elevation $\eta_L(x)$ at every time interval. While Figure 3.4 presents an extreme crest as before, Figure 3.5 presents an extreme zero crossing event ($\eta(x = 0, t = 0) = 0$) which, for the linear free surface, is skew symmetric. This has been produced from the Hilbert transform of the extreme crest, effectively replacing the cosine terms with sine terms, and demonstrates the broad application of the CNT to all linear free surfaces.

Again, as for the previous case of regular waves, the steeper linear input generates even more nonlinear output. In addition, the spatial plots of Figures 3.4a and 3.5a are clearly twice as localised than the corresponding temporal plots of Figures 3.4b and 3.5b. This may be observed by analysing the decay of the group relative to increasing distance and time from the focus. In space, a distance of two wavelengths ($2\lambda = 4\pi \approx 12.5$ m for $k = 1$) is sufficient to obtain free surface elevation near to still water level. However, in the free surface elevation time history, a time interval of at least four wave periods ($4T \approx 8$ s for $k = 1$) is necessary to obtain a similar effect. This is a result of contrasting rates of decay for the wavenumber and frequency spectra. While the high frequency tail of a JONSWAP spectrum decays according to

$$S(\omega) \sim \omega^{-5}, \tag{59}$$

the energy distribution can be described in terms of either frequency or wavenumber as

$$S(\omega)\ d\omega = S(k)\ dk. \tag{60}$$

For wave on deep water ($\omega = \sqrt{kg}$), this leads to an equivalent wavenumber spectral tail of

$$S(k) \sim k^{-3}. \tag{61}$$

As the tail of the wavenumber spectrum decays more slowly than that of the frequency spectrum, the resulting extreme event is more compact in space over long scales and sharper or more rapidly varying at the central crest over short scales.

3.3.1 Local structure

It is clear that, from the above equations, a nonlinear free surface and velocity potential may be computed from a linear free surface. However, given a nonlinear free surface spatial profile η_{target}, it is also possible to compute a linear free surface which, through the CNT, reproduces the original free surface profile. This inverse transform

(ICNT) requires the following method for n iterations:

(1) An initial linear CNT input η_L is guessed.

(2) The CNT is applied to the guess η_{Ln} through (57) above to compute a nonlinear free surface η_n.

(3) The error is computed as $\eta_{\text{error}} = \eta_{\text{target}} - \eta_n$.

(4) Assuming that the error is linear in nature, a new linear CNT input is calculated as $\eta_{Ln+1} = \eta_{Ln} + \eta_{\text{error}}$, and the process is repeated from step 2 above.

This ICNT described above is stable and convergent and may be computed until a suitable tolerance is achieved (i.e. η_{error} is less than some prescribed value). For a nonlinear crest, if the equivalent trough case is available (produced, for example, by a NWT run with an inverted initial condition), a good initial linear guess for step 1 may be computed by subtracting the trough from the crest and dividing by two. In contrast, a guess for the nonlinear trough may be computed by subtracting the crest from the trough such that

$$\eta_{L1\text{crest}}(x) = \frac{\eta_{\text{crest}}(x) - \eta_{\text{trough}}(x)}{2} \quad \text{and} \quad \eta_{L1\text{trough}}(x) = \frac{\eta_{\text{trough}}(x) - \eta_{\text{crest}}(x)}{2}. \tag{62}$$

This initial computation has the effect of removing all even order non-resonant wave-wave interactions (2nd, 4th, etc.). However, if both a crest and trough condition are not available, the nonlinear free surface itself is a sufficiently good initial guess to begin the computation.

Figure 3.6 demonstrates the accuracy of this method for matching the nonlinear free surface using this method for a focused wave group crest (3.6a) and trough (3.6b) at the instant of focus. The crest for this case is identical to that of Figure 3.1, while the trough has been produced by effectively inverting the initial free surface which produces the crest. A dotted line represents the free surface elevation as computed by the NWT, which is matched exactly (and obscured) by the solid line of the Creamer free surface after only $n = 5$ iterations of the ICNT ($\eta_{\text{error}}(0) < 0.005\eta_{\text{target}}(0)$ at the focus point). The linear input η_{L5} is represented by the dashed line, which exhibits lower, broader crests and deeper, steeper troughs. Notably, the aforementioned shoulder upwave of the crest and the corresponding dip upwave of the trough are both well matched by the CNT, demonstrating the effectiveness of this method for analysing highly nonlinear events.

For the same above focused wave group crest and trough, Figure 3.7 reproduces the time evolution at the point of focus. This is accomplished by shifting the individual wavenumber components of $\eta_{L5}(x, t = 0)$ based on linear dispersion. The CNT is then applied to the equivalent $\eta_{L5}(x, t = t_1)$, and $\eta_5(x = 0, t = t_1)$ is selected. This process is repeated at every time step.

Beginning from the moment of focus as described above, $\eta(t = 0)$ is very accurate; but, as expected, the accuracy decreases steadily with increases in absolute time. In Figure 3.7a the crest is reproduced very accurately between the limits of $t \pm 0.25$ s from the moment of focus. There are slight but significant errors in the trough before the extreme event ($t \approx -0.5$ s) and the smaller crest after the extreme event ($t \approx +1$ s). Similar results are found for the extreme crest of Figure 3.7b, although the large crests occurring before and after the event ($t \approx -0.5$ s and $t \approx +0.3$ s) are more closely reproduced than the troughs of Figure 3.7a. However, considering the gross nature of the dispersion assumption and the particularly steep case presented, it is worth noting that the accuracy in both the crest and trough is quite good.

3.3.2 Kinematics

As derived by Creamer *et al.* (1989) from the equations of motion, the horizontal and vertical velocities on the free surface, u_s and v_s, at any point x may be calculated through

$$u_s(x) = \frac{\phi'_s(x) - \dot{\eta}(x)\,\eta'(x)}{1 + [\eta'(x)]^2} \quad \text{and} \quad v_s(x) = \frac{\dot{\eta}(x) - \phi'_s(x)\,\eta'(x)}{1 + [\eta'(x)]^2}, \tag{63}$$

where ϕ'_s is the derivative of the velocity potential on the free surface with respect to distance along the surface and $\dot{\eta}$ and η' are the derivatives of the free surface elevation with respect to time and distance. As the free surface and velocity potential on the free surface have been computed in the wavenumber domain, the amplitude spectra of their spatial derivatives may be computed from

$$\hat{\eta}' = ik\hat{\eta} \quad \text{and} \quad \hat{\phi}'_s = ik\hat{\phi}_s. \tag{64}$$

However, the amplitude spectrum of the time-derivative of the free surface must be evaluated through the time-derivative of (54),

$$\frac{\partial}{\partial t}\hat{\eta} = \int \mathrm{i}\dot{\eta}_{LH}(x)\,\mathrm{e}^{\mathrm{i}k[\eta_{LH}(x) - x]}\,dx, \tag{65}$$

where $\dot{\eta}_{LH}$ is the time-derivative of the Hilbert transform of the linear free surface.

For the crest and trough cases of Figure 3.6, Figures 3.8 and 3.9 demonstrate the accuracy of the CNT in reproducing the velocity potential on the surface and the associated kinematics for highly nonlinear events. Again, the dots represent the NWT data, while the solid line represents the CNT quantities. Results for the crest are in

Figures 3.8a, 3.9a&c while the trough results are in Figures 3.8b, 3.9b&d.

The highly nonlinear velocity potential is very accurately reproduced, while the corresponding horizontal and vertical velocities on the free surface are also very good. However, given accurate free surface elevation and velocity potential, this last result may be expected. The horizontal velocity for the crest (Figure 3.9a) is predicted to within 0.25% at the point of focus, although the error at the equivalent point for the trough (Figure 3.9c) is approximately 6.5%. In addition, the complex shoulder features are also reproduced.

3.4 Global Nonlinearity

Demonstrating the application of the CNT for the analysis of nonlinear wave-wave interactions, the following section continues with a more in depth analysis of the fully nonlinear NWT data, as produced by Bateman *et al.* (1999a). As before, the principal condition investigated will be that of the very steep focused wave group produced from a linear JONSWAP spectrum, with peak wavenumber $k_p = 5$ m^{-1} ($T_p = 0.90$ s) and $\alpha k_p = 0.3$ on a linear basis. A second focused wave group of half that steepness, with $\alpha k_p = 0.15$ on a linear basis, is also analysed for comparison purposes. While further evidence is presented for the inability of the CNT to reproduce long time scale evolution of irregular seas, the amplitude and phase variations present within these complex processes are studied in depth and the CNT is shown to be useful at identifying and removing bound wave structure.

Through the process presented above for Figure 3.7, the CNT may approximate the time evolution of a nonlinear surface through the linear dispersion of the linear free surface. Figure 3.10 utilizes this process for the time evolution of a focused wave group, with free surface elevation versus distance plotted at $t = -15$, 0, and $+15$ s in (a), (b), and (c), respectively. The focused wave group analysed is the same as previously discussed, with $\alpha k_p = 0.3$ ($k_p = 5$ m^{-1}) on a linear basis. The dashed and dotted line represents the NWT data while the solid line shows results from the CNT as applied at the moment of focus and time evolved to produce surfaces at long time intervals before and after the moment of focus.

Figure 3.10 demonstrates the presence of nonlinear interactions during the time evolution of the free surface. At $t = -15$ s the free surface predicted by the CNT is reasonably similar in amplitude and phase relative to the NWT results, with longer wavelength components moving to overtake shorter wavelength components. However, at a long time following the extreme event in Figure 3.10c, the fully nonlinear computation of the NWT yields a further large crest significantly higher than any present in the free surface predicted by the CNT. This discrepancy can only be explained by the presence of resonant wave-wave interactions, which are not simulated by the Creamer transform, operating in the spatial domain at every instant in time.

As discussed above, the CNT accurately represents the bound wave structure present for a linear free surface. Adding greater complexity to the free surface profile and kinematics of nonlinear waves, bound waves are essentially higher order components of an incident wave at a given wavenumber, with celerity equivalent to the first order component. As derived to third order by Kinsman (1965), bound waves may be identified in the classical Stokes perturbation expansion for finite amplitude regular waves as

$$\eta_{\text{Stokes}}(x) = a\cos(kx) + \frac{1}{2}ka^2\cos(2kx) + \frac{3}{8}k^2a^3\cos(3kx)\,. \tag{66}$$

In the context of focused wave groups and random seas in general, energy at twice the peak spectral frequency or wavenumber (equivalent to that for second order bound waves) arises from the similar non-resonant interaction of linear component pairs. Two linear frequency components (ω_1, k_1) and (ω_2, k_2) may then generate a higher order component at $(\omega_1 + \omega_2, k_1 + k_2)$, moving at the celerity of the linear components from which it was generated. For linear components near the peak of the spectrum, the non-resonant interaction generates energy at approximately $(2\omega_p, 2k_p)$. The application of the CNT to this problem is demonstrated in Figure 3.11, comparing the amplitude spectra at the time of focus for the NWT output (the solid line) to the linear CNT input (the dashed line). Identifying and removing the bound wave structure, the ICNT has reduced the amplitude of higher wavenumber components ($\frac{k}{k_p} > 2$) in the tail of the linear spectrum, which is now comparable to the tail of the original linear input spectrum.

However, for time evolution of a nonlinear free surface, the CNT assumes that the underlying motion of the principal wave components is governed by linear dispersion. This assumption does not allow for the possibility of resonant wave-wave interactions, which may generate components with frequency and wavenumber near the original linear components. For example, three distinct frequency components near the spectral peak could interact to produce energy at $(\omega_1 + \omega_2 - \omega_3, k_1 + k_2 - k_3)$, which is then near to the spectral peak at (ω_p, k_p) (i.e. the new energy is resonating with the components from which it originated). These resonant interactions allow energy to pass from one component to another of similar frequency and wavenumber in a random sea and are the subject of the following investigation.

3.4.1 Time evolution of wavenumber spectra

In the formation of a steep crest, focused wave group spectra exhibit significant alteration. Two cases contrasted here are the previously discussed wave group, with a linear steepness of $\alpha k_p = 0.3$, and an event of half that linear steepness, $\alpha k_p = 0.15$. This half-steepness focused wave group is produced from an initial linear spectrum of identical shape but with less energy than the former case and therefore generating significantly less nonlinear interaction.

Plotted as absolute amplitude versus non-dimensionalised wavenumber, Figures 3.12 and 3.13 demonstrate the nonlinear time evolution of wave spectra for the steep and half-steep focused wave groups, respectively. The dashed lines represent the spectra at $t = -7.5$ s, well before the moment of focus, which evolve to the dashed and dotted line at the focus ($t = 0$) and subsequently the solid line ($t = +7.5$ s). For the steep wave of Figure 3.12 there is a significant transfer of energy away from the spectral peak ($\frac{k}{k_p} = 1$) as the group evolves. This is accompanied by a broadening of the spectrum at the focus time, with energy shifting to lower wavenumbers ($\frac{k}{k_p} < 0.7$), second order ($1.5 < \frac{k}{k_p} < 2.5$), and higher wavenumber components in the tail of the spectrum. Beyond the focus time at $t = +7.5$ s the spectrum does not return to the original profile, with the highest amplitude components evolving to wavenumbers below the original spectral peak ($\frac{k}{k_p} \approx 0.95$). Although there is some decrease in the spectral tail ($\frac{k}{k_p} > 2.5$), several peaks are still present at higher wavenumbers. In stark contrast to this, Figure 3.13 displays much weaker nonlinearity, with the spectrum at $t = +7.5$ s regaining many of the characteristics of the original spectrum. However, there is still significant higher order energy present at the focus time, and some of this is retained in a peak at $\frac{k}{k_p} \approx 2.25$.

For spectral time evolution long after the focused event, Figure 3.14 compares the spectra at the focus (dashed and dotted line) with those at $t = +7.5$ s (dashed line) and $t = +15$ s (solid line). The high wavenumber tail ($\frac{k}{k_p} > 2.5$) clearly returns to close to the initial linear input, while significant change is still present near the spectral peak, which has shifted slightly to still lower wavenumber and become higher and more narrow. This is representative of the longer wavelength component's (lowest wavenumber) reluctance to defocus following the extreme event, as demonstrated in Figures 3.1 and 3.10.

3.4.2 Time evolution of wavenumber components

Tracking changes in amplitude for individual wavenumber components over time, Figures 3.15 and 3.16 demonstrate the shift of energy between modes for the steep and half steep focused wave group cases ($\alpha k_p = 0.3$ and 0.15, respectively). The difference in scales must be noted, with the steeper crest plotted over a longer time interval and a higher maximum amplitude, as the less steep case exhibits significantly less overall change with time. Wavenumber components have been selected as representative of the overall behaviour and labelled with the non-dimensionalised wavenumber.

In all of the time histories of Figures 3.15 and 3.16, there is a significant change in amplitude during formation of the extreme crest ($t = 0$). This is most clear in Figure 3.15, in which all wavenumber components decrease in amplitude apart from the component near $2k_p$ ($\frac{k}{k_p} = 2.0039$), which exhibits a large peak at the focus time. This change is very rapid, occurring over a time scale of ~2 s (~$2T_p$), after which the amplitudes return to their long term trends. As observed previously in Figure 3.12, this is characteristic of a transfer of energy away from the spectral peak to higher wavenumbers and enhancement of the spectral tail. Occurring near the moment of focus, these localised changes may be related to the convergence of fluid towards an extreme crest as identified by McIver & Peregrine (1981), who noted that energy moving from a wavenumber component returns to that component if no breaking occurs.

For the steeper crest of Figure 3.15, considerable long term amplitude variation is present in the three components close to the spectral peak. For the lowest of these ($\frac{k}{k_p} = 0.8086$), there is a long term transfer of energy into the component, while the component at the peak ($\frac{k}{k_p} = 1.0020$) shows a continuous energy loss until well after the focus event ($t \approx 12.5$ s). This is consistent with the shift of the spectral peak to lower wavenumber and general broadening of the spectrum. In contrast, the component just above the spectral peak ($\frac{k}{k_p} = 1.1953$) undergoes little variation until the focus time, after which it steadily gains energy. This behaviour is in agreement with the development of the peak near $\frac{k}{k_p} \approx 1.2$ a long time after the focus event ($t = 15$ s) in Figure 3.14. However, below the spectral peak, the wavenumber component $\frac{k}{k_p} = 0.5977$ gains energy up to the focus time, after which it gradually returns to its initial value.

Short term oscillations (again on the order of $2T_p$) exist not just at the focus time, but over large lengths of the record for all the components. These are most visible in the dashed line of $\frac{k}{k_p} = 2.0039$ in Figure 3.15, which plots the amplitude of this component from the NWT. Comparing these short term oscillations, peaks in this $2k_p$ component correspond to troughs in the lower wavenumber components, supporting the principle of energy transfer between modes. At this wavenumber, strong contributions from both the 2nd harmonic of the spectral peak and the free waves are expected, which are the source of non-resonant interactions. The solid line that plots roughly through these oscillations is the locally linear component amplitude as identified by the ICNT, demonstrating the identification and removal of non-resonant interactions. However, the solid line still follows the underlying large scale trends, showing a factor of 4 change at $\sim 4T_p$.

In contrast with the steep crest case, the smaller amplitude crest of Figure 3.16 exhibits considerably less amplitude variation over long time scales and the short term $2T_p$ oscillations are entirely absent. This may be expected from the 3rd order nature of the resonant interactions, with a cubic dependence on wave steepness. However, some amplitude variation at the time of focus is present, with a similar effect to that noted above and previously observed by McIver & Peregrine (1981).

3.4.3 Phase speed time evolution

As with the amplitude changes of individual wavenumber components, the phase of the component may be determined from the complex result of an FFT at each time step. Defining the linear phase speed of wavenumber component k as

$$c_0 = \sqrt{\frac{g}{k}}, \tag{67}$$

a local estimate of the phase speed may be calculated through

$$\frac{c}{c_0} = \frac{\triangle\theta}{\triangle t}\frac{1}{\sqrt{gk}}, \tag{68}$$

where $\triangle t$ is the time interval and $\triangle\theta$ is the change in phase angle. Plotting non-dimensionalised phase speed computed with a 1s moving average, Figures 3.17 and 3.18 present the same individual wavenumber components for the identical focused wave group cases analysed above. The dashed lines trace the linear value ($\frac{c}{c_0} = 1$), while the solid lines follow the values computed through (68). Although the lower steepness cases are again plotted over a shorter time scale, it should be noted that all plots share identical vertical axes, with the exception of both of the lower plots ($\frac{k}{k_p} = 2.0039$) in Figures 3.17 and 3.18 and the upper plot ($\frac{k}{k_p} = 0.5977$) in Figure 3.18, all of which have greater ranges of celerity modification near the focus time.

For the steeper case ($\alpha k_p = 0.3$) of Figure 3.17, there is a continuous rise in phase speed (between 1 and 2%) for the three components near the spectral peak until the wave begins to focus. The nature of the behaviour near the focus time is discussed further below. As this extreme wave represents a solitary wave group on deep water, this modification may be explained as per Taylor and Haagsma (1994), who demonstrated that the nonlinear interaction of wavenumber components near a spectral peak can approximate the formation of an envelope soliton, for which the celerity is

$$\frac{c}{c_0} = 1 + \frac{1}{4}(ak)^2 . \tag{69}$$

Approximating the local wave steepness throughout as $ak \approx 0.25$, the estimated phase speed increase is ~1.5% for the terms near the spectral peak, which is very similar to that observed in Figure 3.17. In comparison, for the less steep case of Figure 3.18, celerity is much closer to linear for the wavenumber components near the spectral peak. As for the long term amplitude modifications discussed previously, the reduced higher order interactions may be expected for the less nonlinear, lower amplitude case. In addition, for the wavenumber components at $\frac{k}{k_p} = 0.5977$ and 2.0039, there is little or no long term increase in celerity beyond that expected for the linear case.

In all of the plots, there is a significant local change in celerity of duration $\sim 2T_p$ near the focus time ($t = 0$). For the lowest wavenumber components in both plots ($\frac{k}{k_p} = 0.5977$), a significant rise in celerity is recorded shortly before the focus, with a decrease just afterwards. For the components near the spectral peak in Figure 3.17 there is a drop in celerity at the focus time. However, for the lower steepness case of Figure 3.18, celerity decreases for all the wavenumber components shortly after the focus time.

Finally, well after the focus time at $t \approx 6$ s, there is a strong local increase to approximately $1.4c_0$ for $\frac{k}{k_p} = 2.0039$ in the steeper wave case. As shown in the corresponding Figure 3.15, this increase in celerity occurs as the amplitude of this wavenumber component decreases near to zero. With wavenumber near to $2k_p$, this may be assumed to be a bound wave component. Thus, the large loss of free wave energy at $t \approx 6$ s may be assumed to leave only bound wave energy, with celerity approximately equal to that of the peak wavenumber components.

The celerity near this time could then be computed as

$$\frac{c}{c_0} = \frac{\sqrt{\frac{g}{k_p}}}{\sqrt{\frac{g}{2k_p}}} = \sqrt{2}, \quad \text{or} \quad c = \sqrt{2}c_0 \approx 1.4c_0. \tag{70}$$

3.5 Conclusions

The nonlinearity of steep focused wave groups and applications of the Creamer nonlinear transform to these events have been investigated with the following results:

(1) Given a nonlinear free surface spatial profile, the CNT has been shown to accurately predict fully nonlinear kinematics at the free surface.

(2) The utility of the CNT for predicting the time evolution of a nonlinear free surface has been investigated, and its range of validity have been clearly defined.

(3) The CNT has been used to study the long time scale evolution of focused wave groups and has proved useful as a tool for identifying resonant and non-resonant wave-wave interactions.

3.5.1 Kinematics via CNT

Accurate prediction of maximum free surface elevation and the kinematics associated with a given free surface profile are essential for estimating the necessary air gap and dictating the overall design of offshore structures. Based on a spatial representation of a linear free surface profile, the CNT reproduces much of the local nonlinearity of steep deep water waves, to include bound wave structure for focused wave groups. In addition, nonlinear kinematics on the free surface may also be computed which compare well with fully nonlinear NWT calculations. For one such highly nonlinear case (a focused wave group with $Ak_p = 0.3$), the peak horizontal velocity has been predicted to within 0.25% at the instant of focus. As such, the CNT has been shown to be an accurate starting point for the design of offshore structures.

3.5.2 Nonlinear time evolution

In order to calculate the time evolution of a given free surface, fully nonlinear NWT schemes require both the free surface elevation and the velocity potential on the free surface as functions of time. In contrast, the CNT requires only a linear estimation of the free surface elevation as a function of distance and the direction of motion of the waves. From this linear free surface profile, the CNT can estimate both an equivalent nonlinear free surface and the associated kinematics, including the velocity potential on the free surface. It has also been shown that the time evolution of these quantities may be accurately calculated over short periods. One possible use for the CNT may then be to provide free surface elevation and velocity potential values to be used as starting points for fully nonlinear NWT simulations.

Reproducing a given nonlinear free surface spatial profile requires complete spatial information at an instant in time. However, practical measurements are made at stationary positions, such as the location of a resistance wave probe, where free surface elevation is recorded as a function of time. The CNT has been demonstrated to provide accurate results for localised space to time transformations of free surface elevation. This implies that the equivalent time to space transformation is also possible, such that measurement of the free surface time history at a fixed point may be transformed into accurate prediction of the local kinematics through the CNT.

However, slow cumulative interactions between wave components occur, decreasing the accuracy of linear dispersion with increasing time. These long term effects have been shown in numerical simulations (Taylor and Vijfvinkel 1998) and observed in experiments (Baldock *et al.* 1996). Although the CNT accurately simulates the bound wave structure and kinematics, reliance on linear dispersion for time evolution of the free surface renders it inaccurate over long time scales. This demonstrates the need for a method of computing such long time scale interactions between wave components.

3.5.3 Resonant wave-wave interactions

As discussed above, the non-resonant wave-wave interactions leading to trough-crest asymmetry are reproduced accurately by the CNT, and application of an inverse CNT has proved useful in identifying these bound wave components for focused wave groups. However, resonant wave-wave interactions, modifying both the amplitude and celerity of individual wavenumber components over time, must still be accounted for over long time scales for waves of high steepness. As the CNT operates in the wavenumber and spatial domains, it is incapable of simulating these resonant interactions and predicting the time evolution of an irregular sea. While these long time scale effects have been noted herein for the case of a focused wave group extreme crest, Taylor and Vijfvinkel

(1998) observed the same effects for an inverted focused wave group, producing an extreme trough. This indicates that these wave-wave interactions are indeed resonant, occurring at odd-order in the Stokes perturbation expansion.

Furthermore, for uni-directional deep water waves, one important observation made here is the reluctance of localised wave groups to defocus following the formation of an extreme crest. In the experimental context of long wave basins (flumes or channels), this result suggests that statistics for tall crests at different points along the channel will not be consistent. This work demonstrates that very steep focused wave groups are reluctant to defocus for as long as 17 wave periods after the extreme event (15 s at $T_p = 0.9$ s). This time interval is comparable to that required for wave groups to travel the complete length of very long channels. Thus, even for basins in which the wave paddle is driven by a random signal, a greater number of extreme events might be expected at points further downstream.

Again, the work presented herein has been for uni-directional wave groups on deep water only. Similar focused wave groups on intermediate water depth have shown weaker resonant wave-wave interactions (Taylor & Vijfvinkel 1998), although the bound wave structure observed was more pronounced (greater trough-crest asymmetry). Equivalent effects in a realistically spread sea on deep water have also been shown to be much weaker (Johannessen & Swan 1998). Thus, this may indicate that large time scale wave-wave interactions are of interest only for laboratory wave basins, or it may simply place some constraints on the formation of 'freak' or 'rogue' waves at sea.

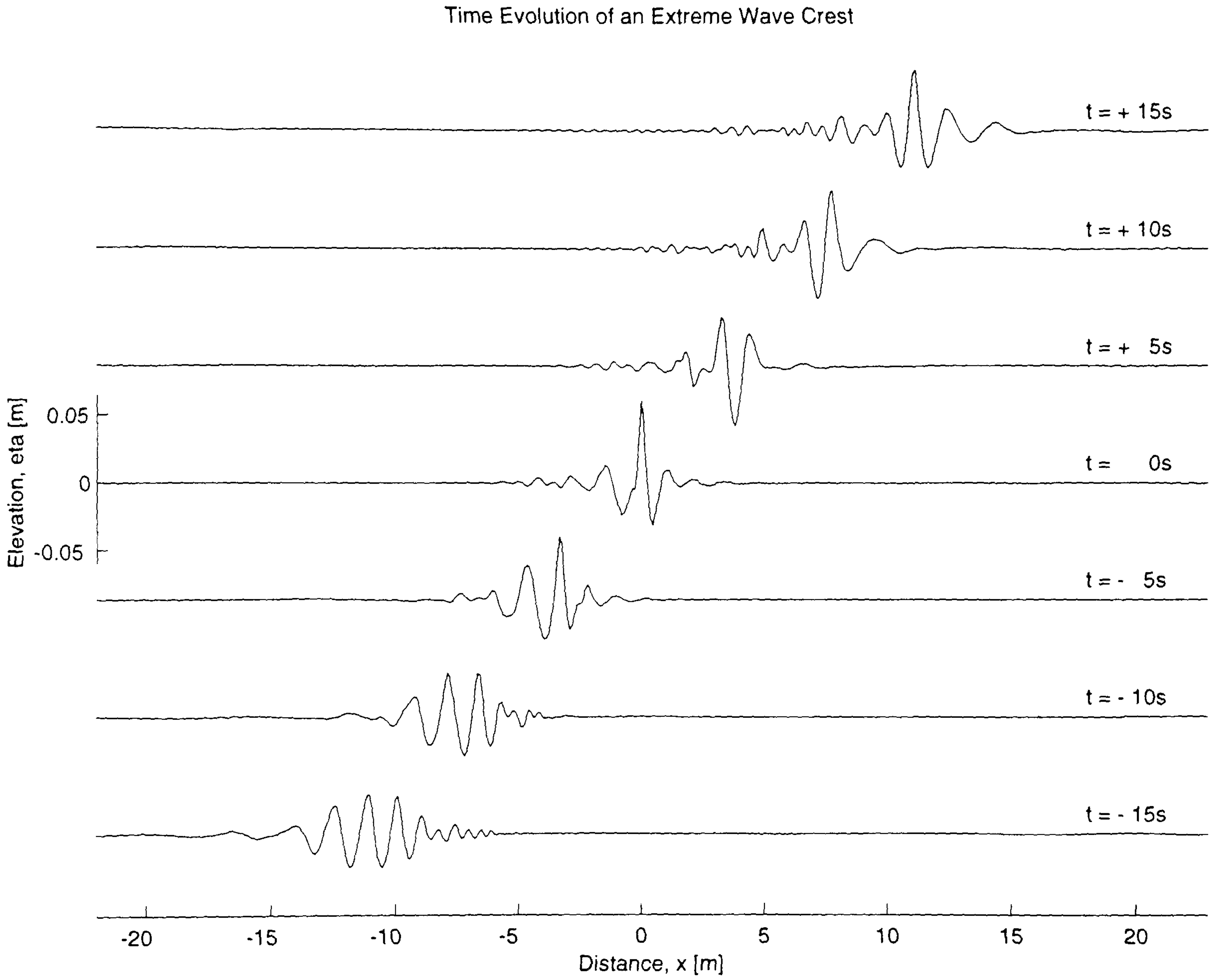

Figure 3.1. Nonlinear evolution of a focused wave group; from the NWT of Bateman & Swan (1999)

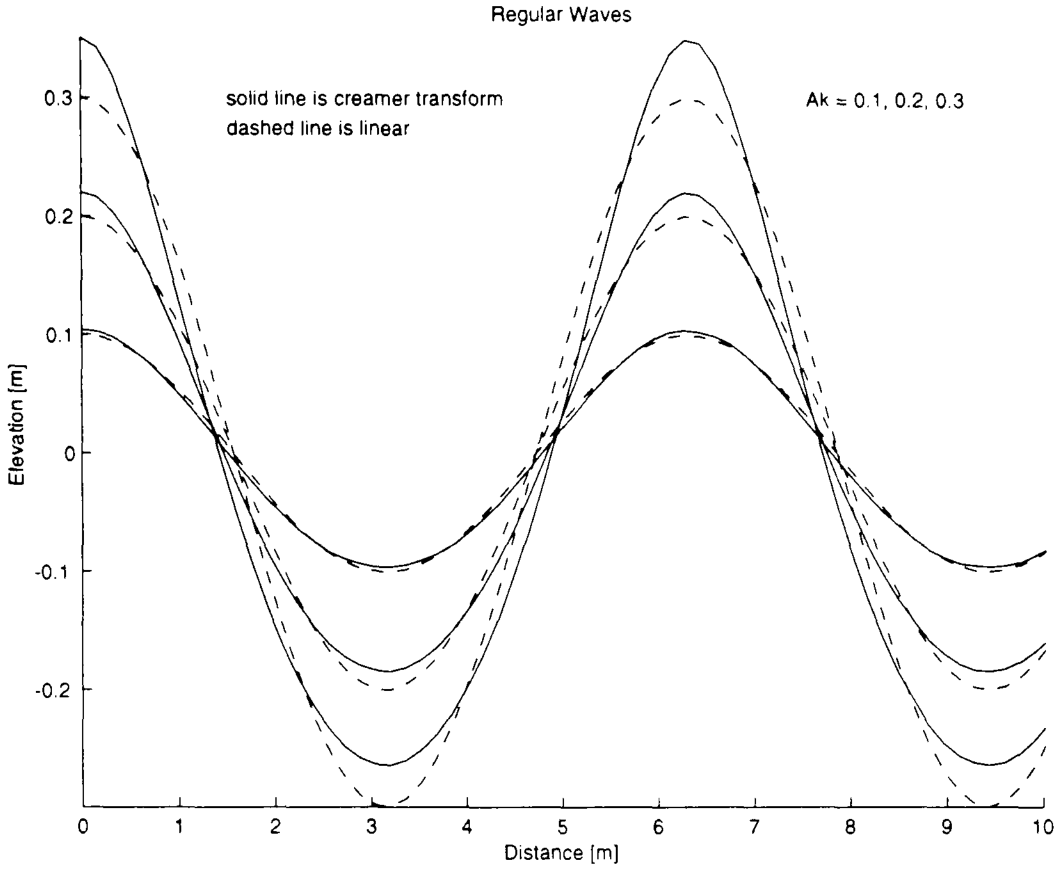

Figure 3.2. Free surface elevation versus distance for linear regular waves and the CNT results; $Ak = 0.1, 0.2$, and 0.3

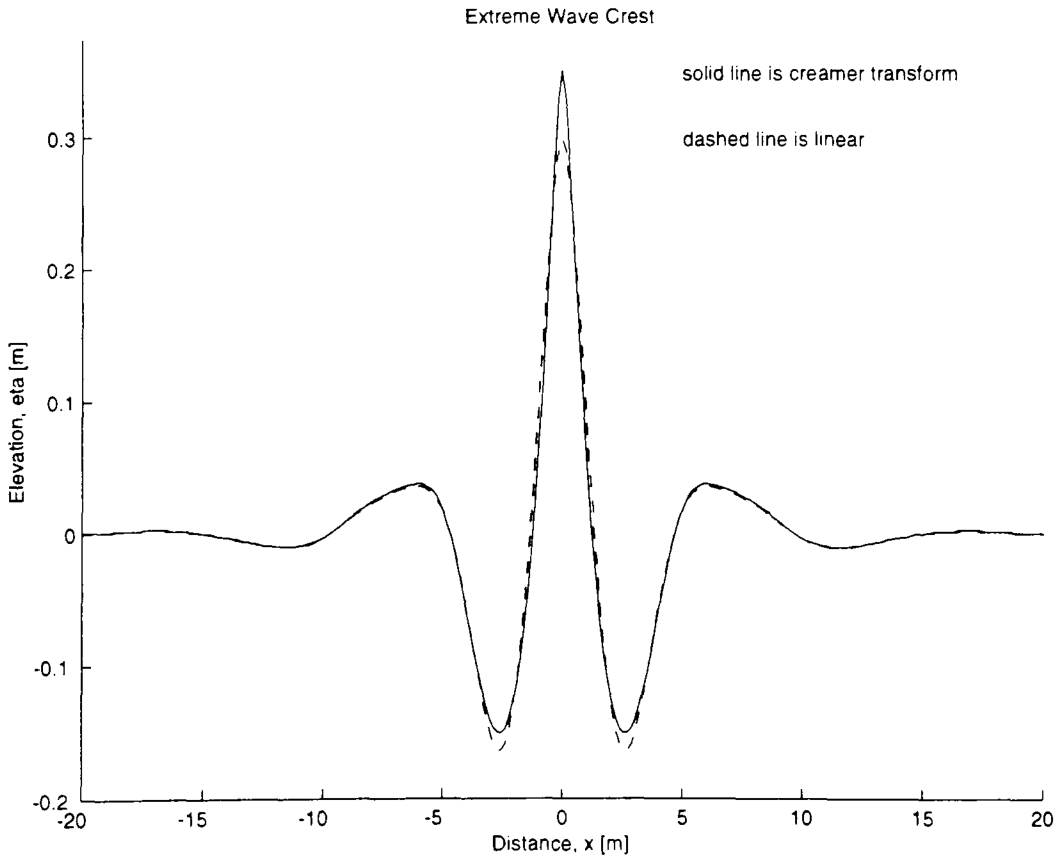

Figure 3.3. Free surface elevation versus distance for a linear focused wave group and the CNT result; $Ak_p = 0.3$

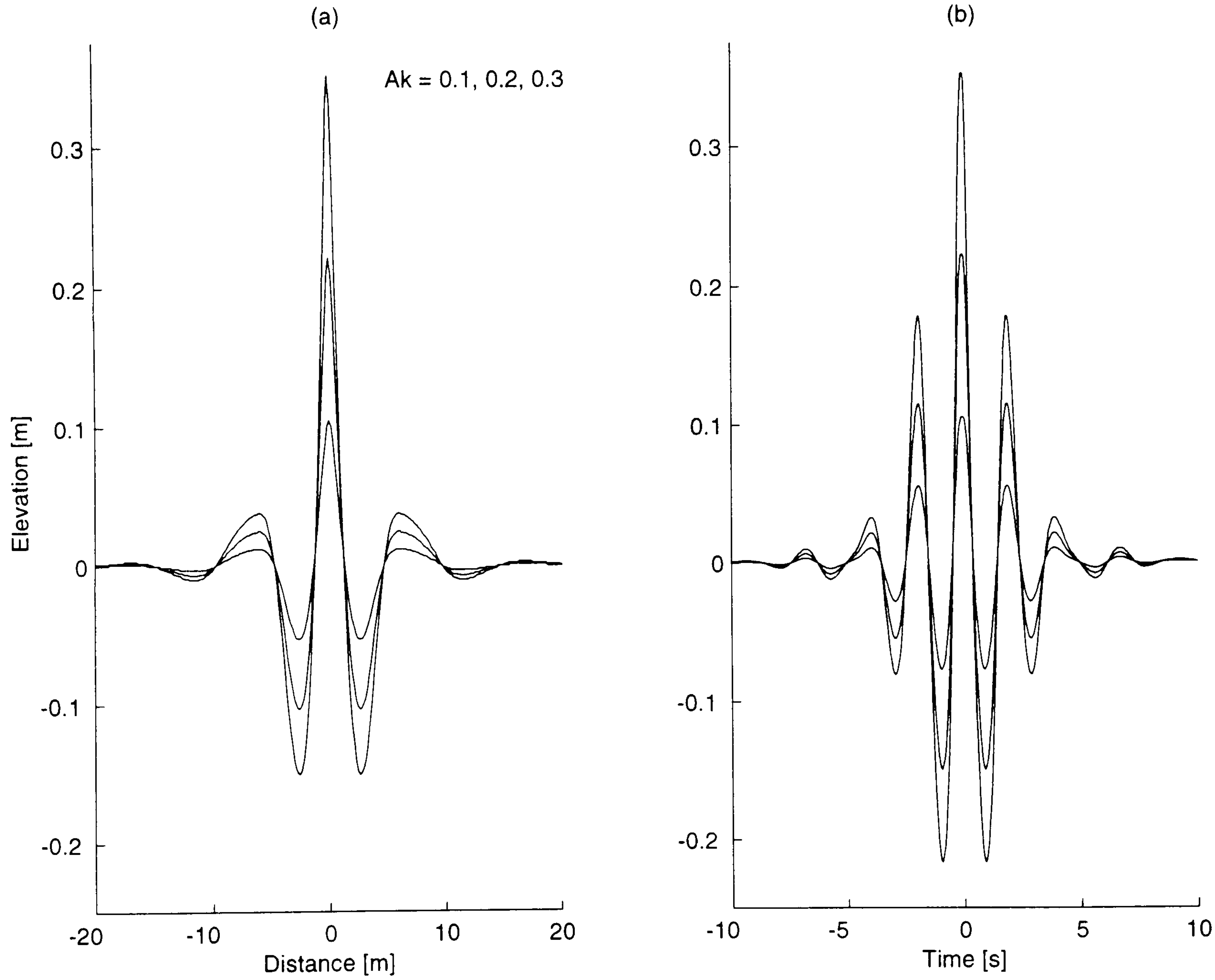

Figure 3.4. Free surface elevation versus distance (a) and time (b) for focused wave group crests; $Ak_p = 0.1$, 0.2, and 0.3

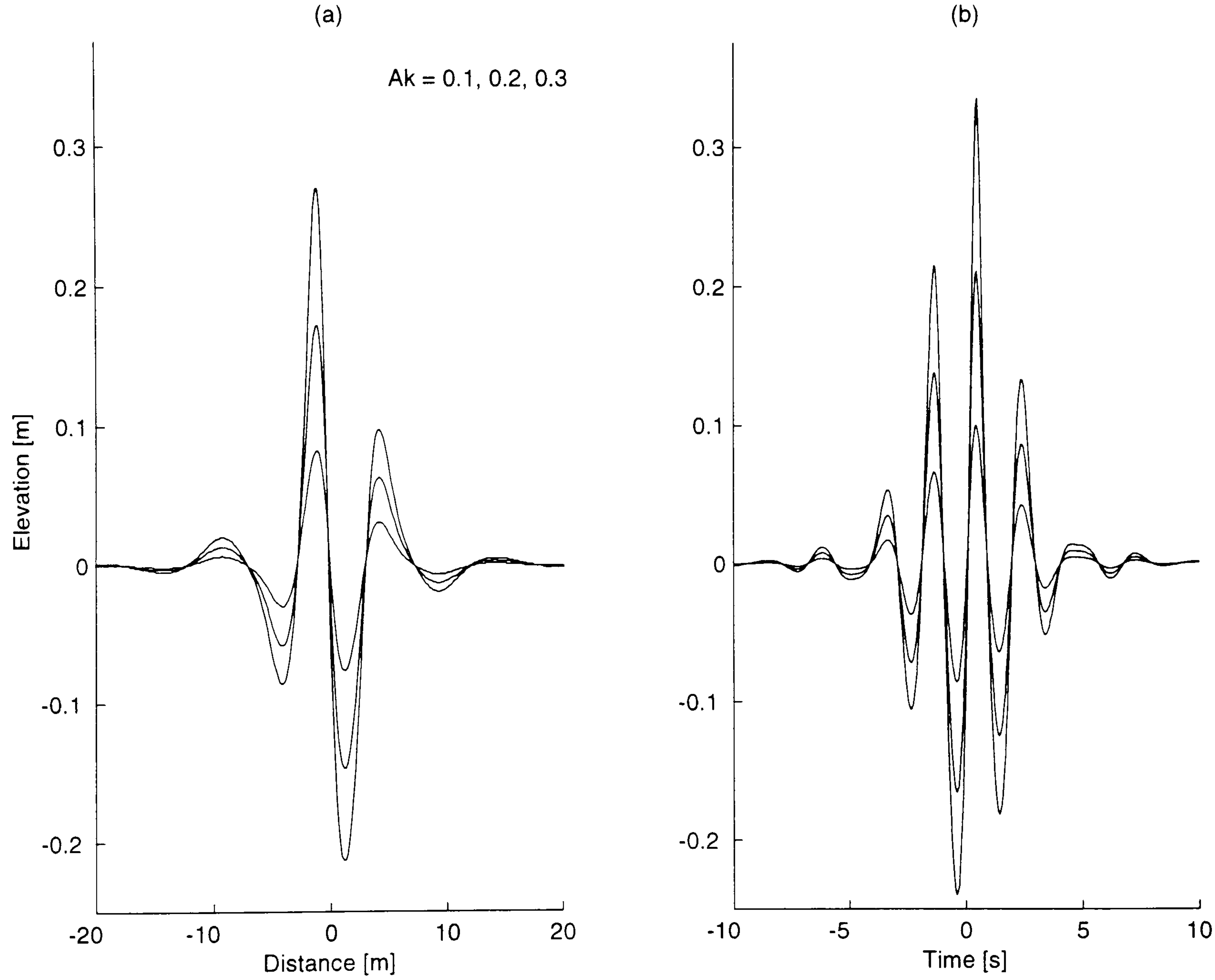

Figure 3.5. Free surface elevation versus distance (a) and time (b) for focused wave group skew symmetric events; $Ak_p = 0.1, 0.2$, and 0.3

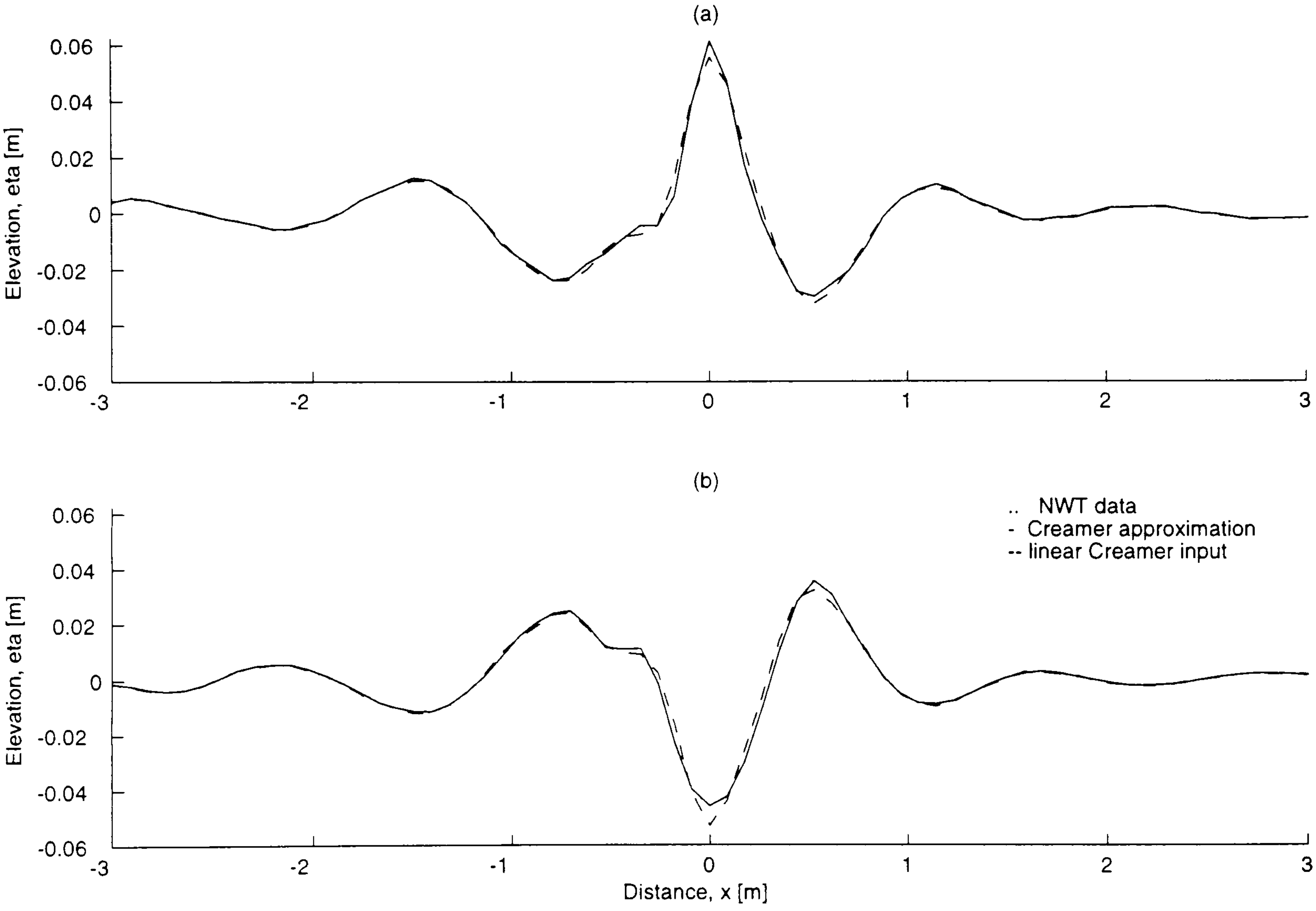

Figure 3.6. Free surface elevation versus distance for a focused wave group crest (a) and trough (b) for $\alpha k_p = 0.3$

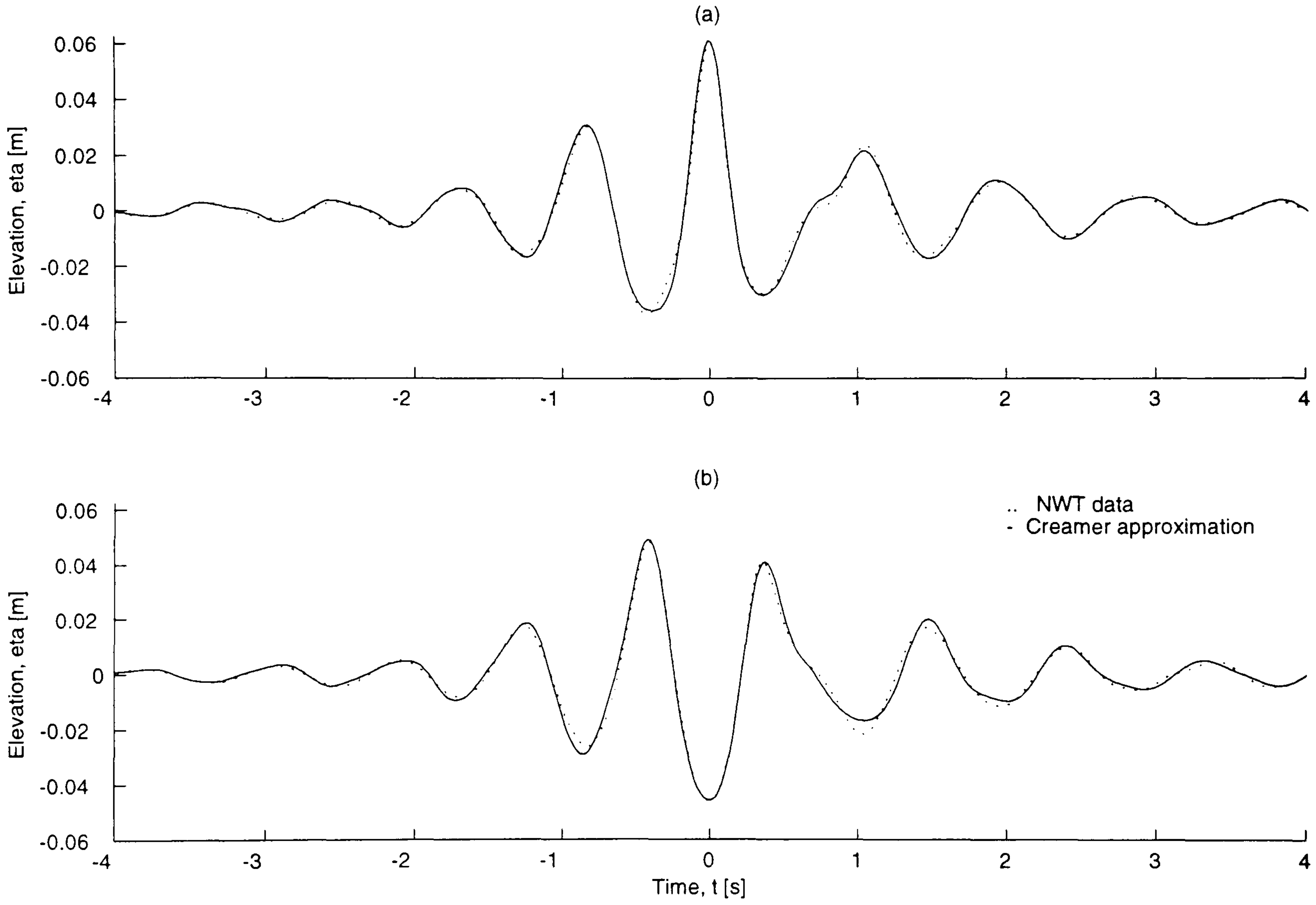

Figure 3.7. Free surface elevation versus time for a focused wave group crest (a) and trough (b) for $\alpha k_p = 0.3$

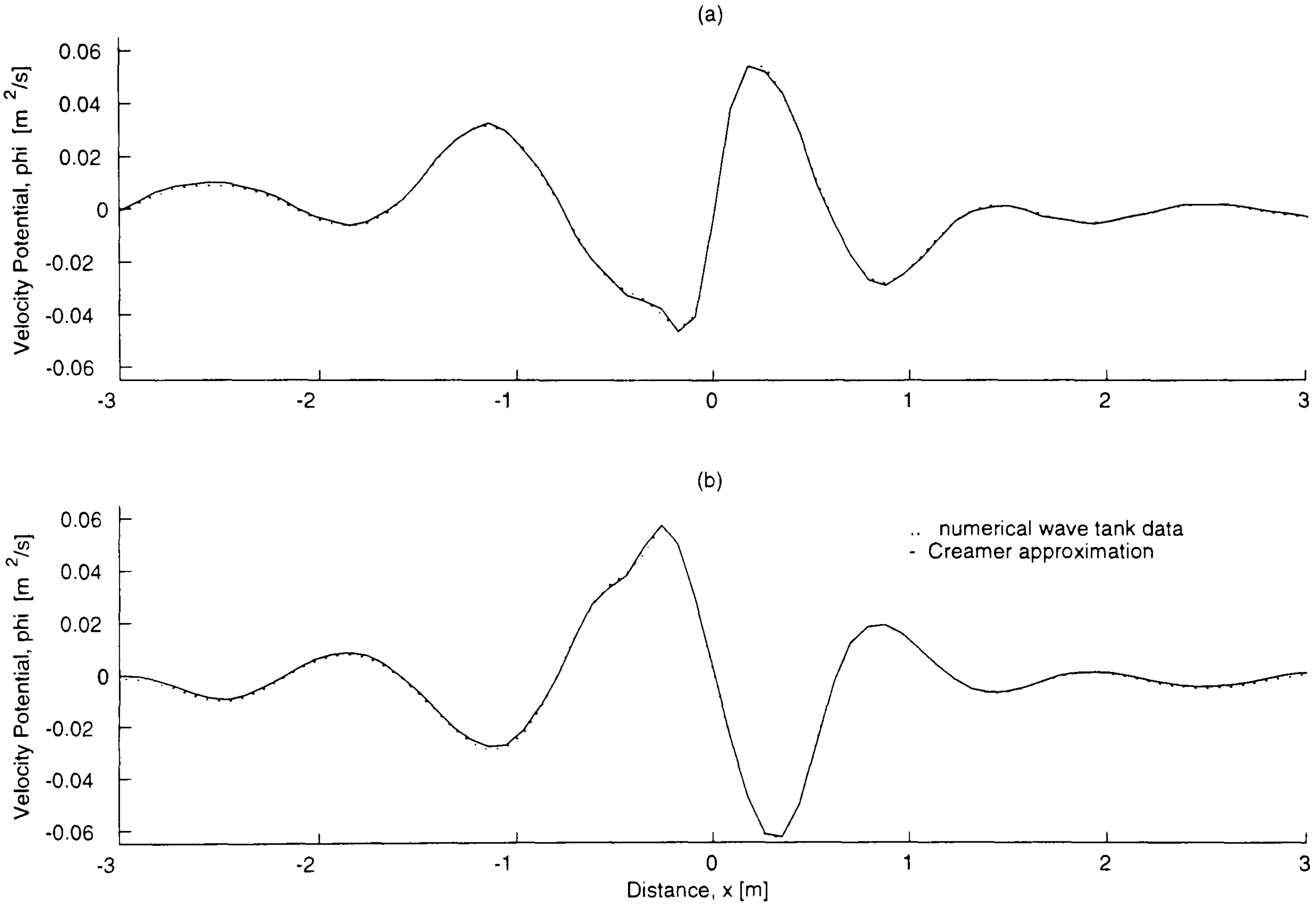

Figure 3.8. Velocity potential on the free surface versus distance for a focused wave group crest (a) and trough (b) for $\alpha k_p = 0.3$

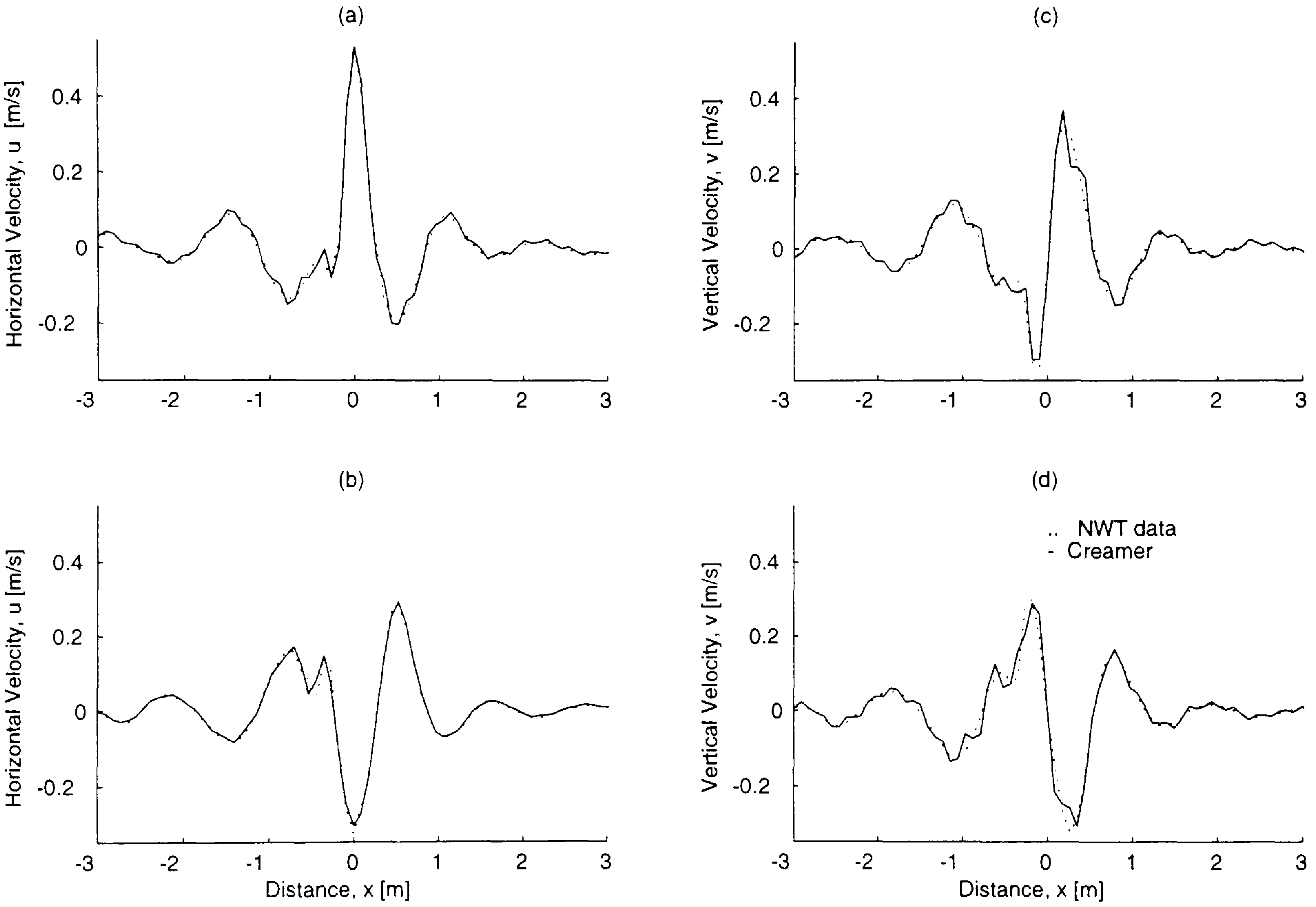

Figure 3.9. Horizontal and vertical velocity on the free surface versus distance for a focused wave group crest (a) & (c) and trough (b) & (d) for $\alpha k_p = 0.3$

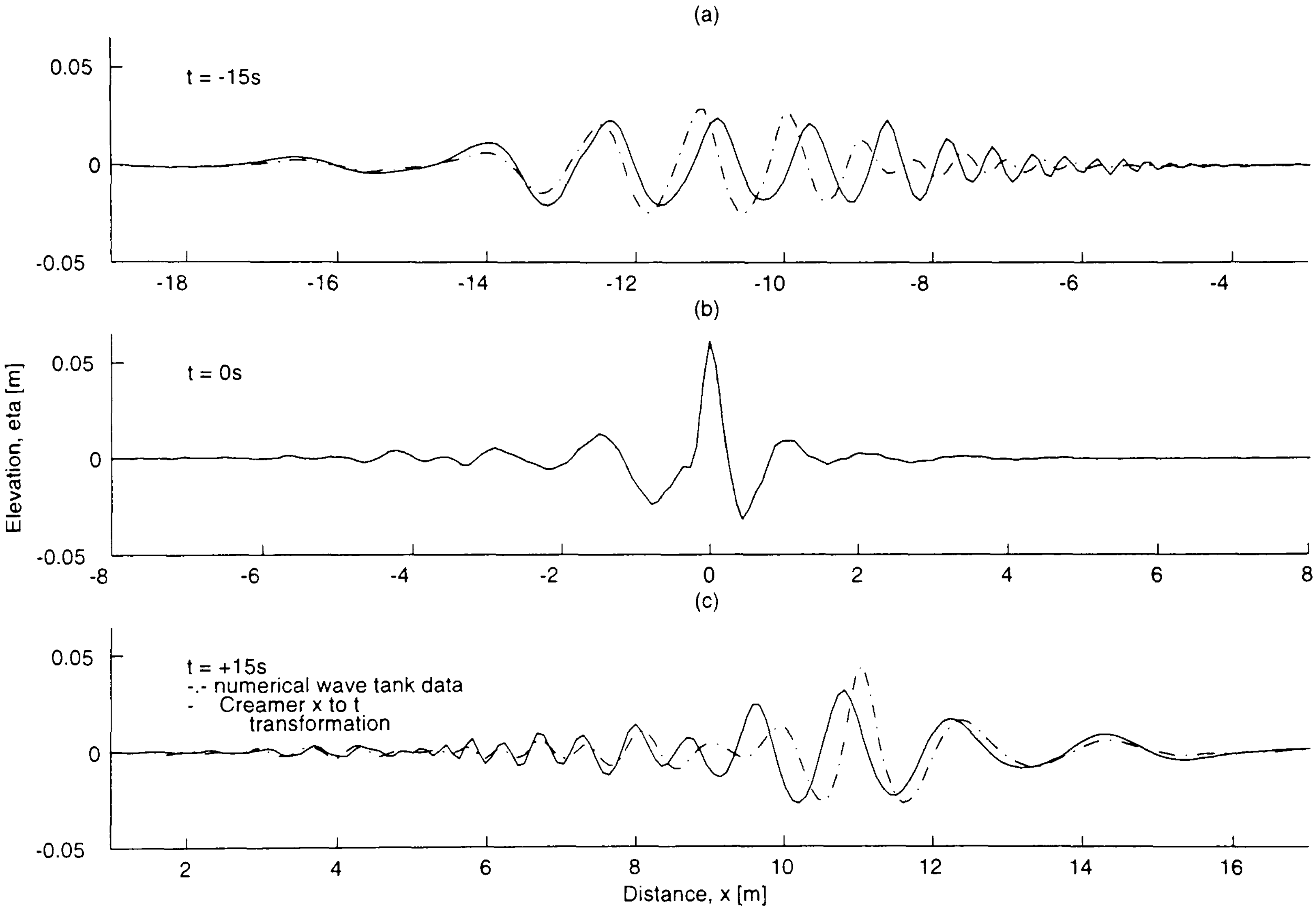

Figure 3.10. Free surface elevation versus distance for a focused wave group crest at times $t = -15, 0$, and 15 s for $ak_p = 0.3$

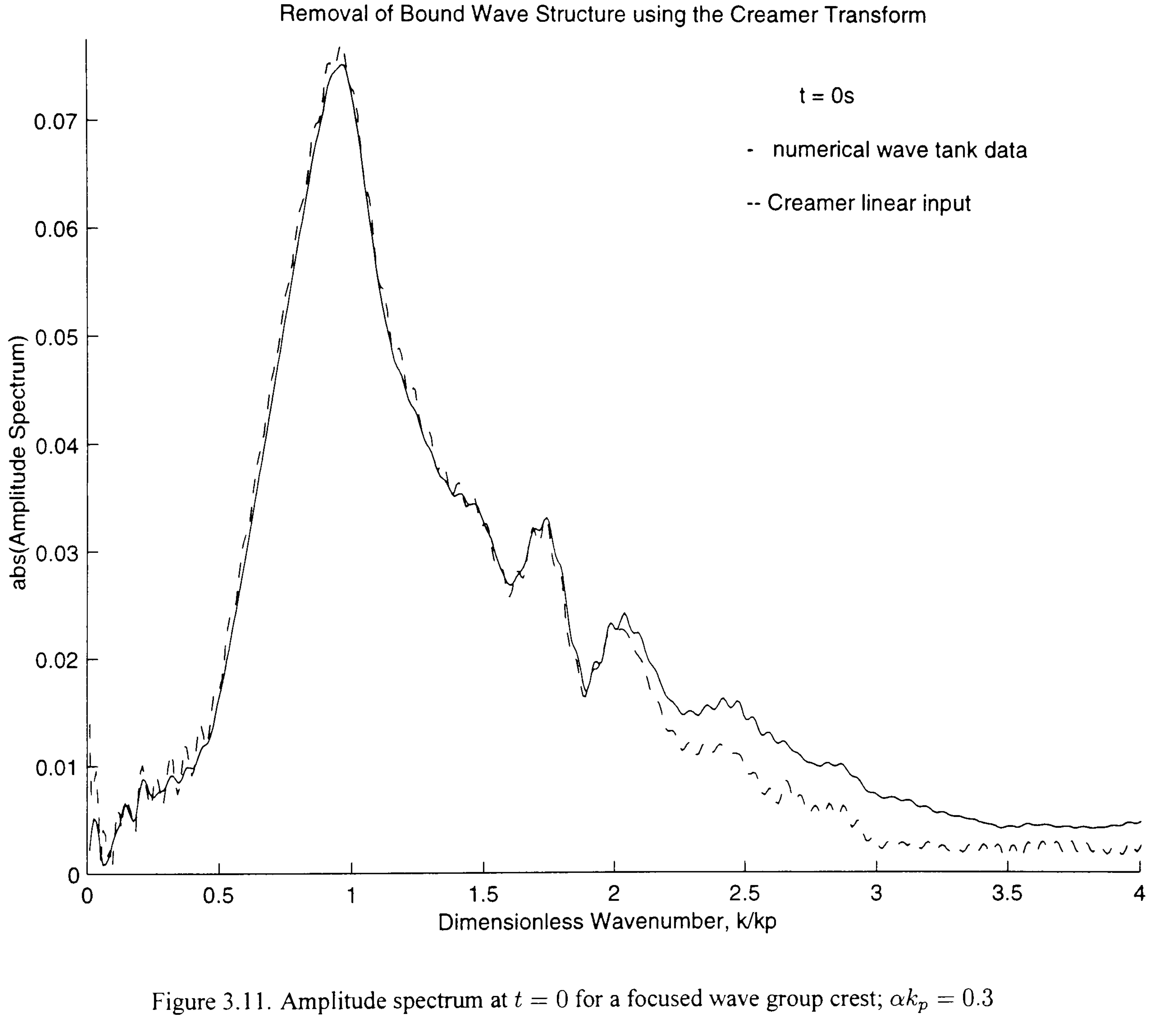

Figure 3.11. Amplitude spectrum at $t = 0$ for a focused wave group crest; $\alpha k_p = 0.3$

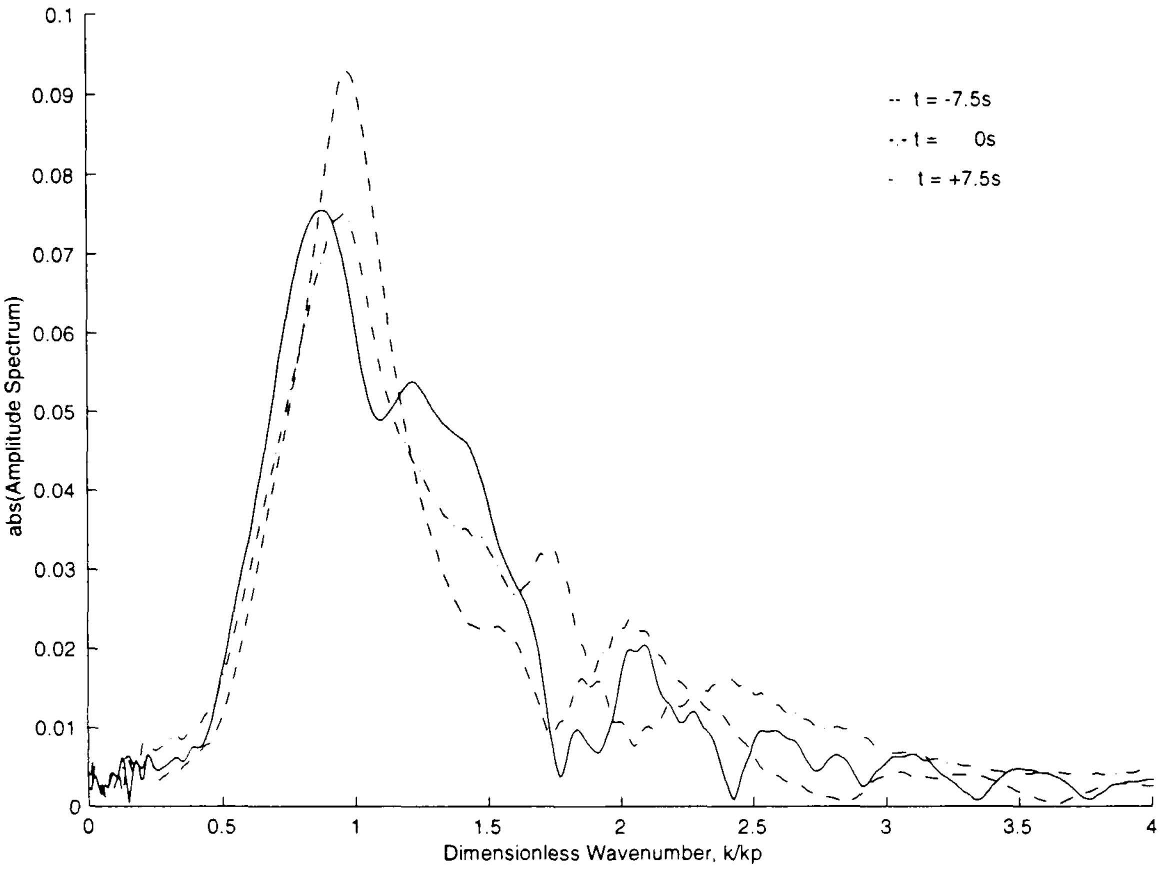

Figure 3.12. Amplitude spectrum time evolution ($t = -7.5$, 0, and +7.5 s) of a focused wave group crest for $\alpha k_p = 0.3$

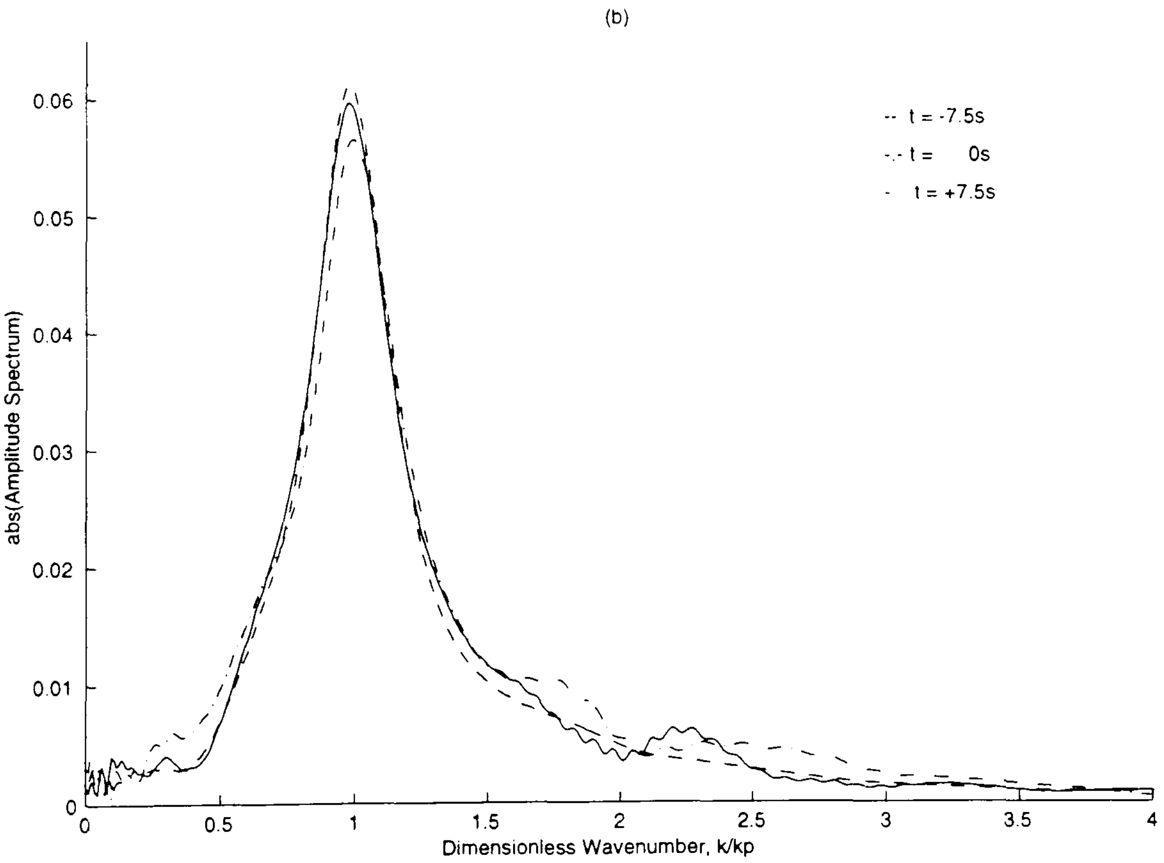

Figure 3.13. Amplitude spectrum time evolution ($t = -7.5$, 0, and +7.5 s) of a focused wave group crest for $\alpha k_p = 0.15$

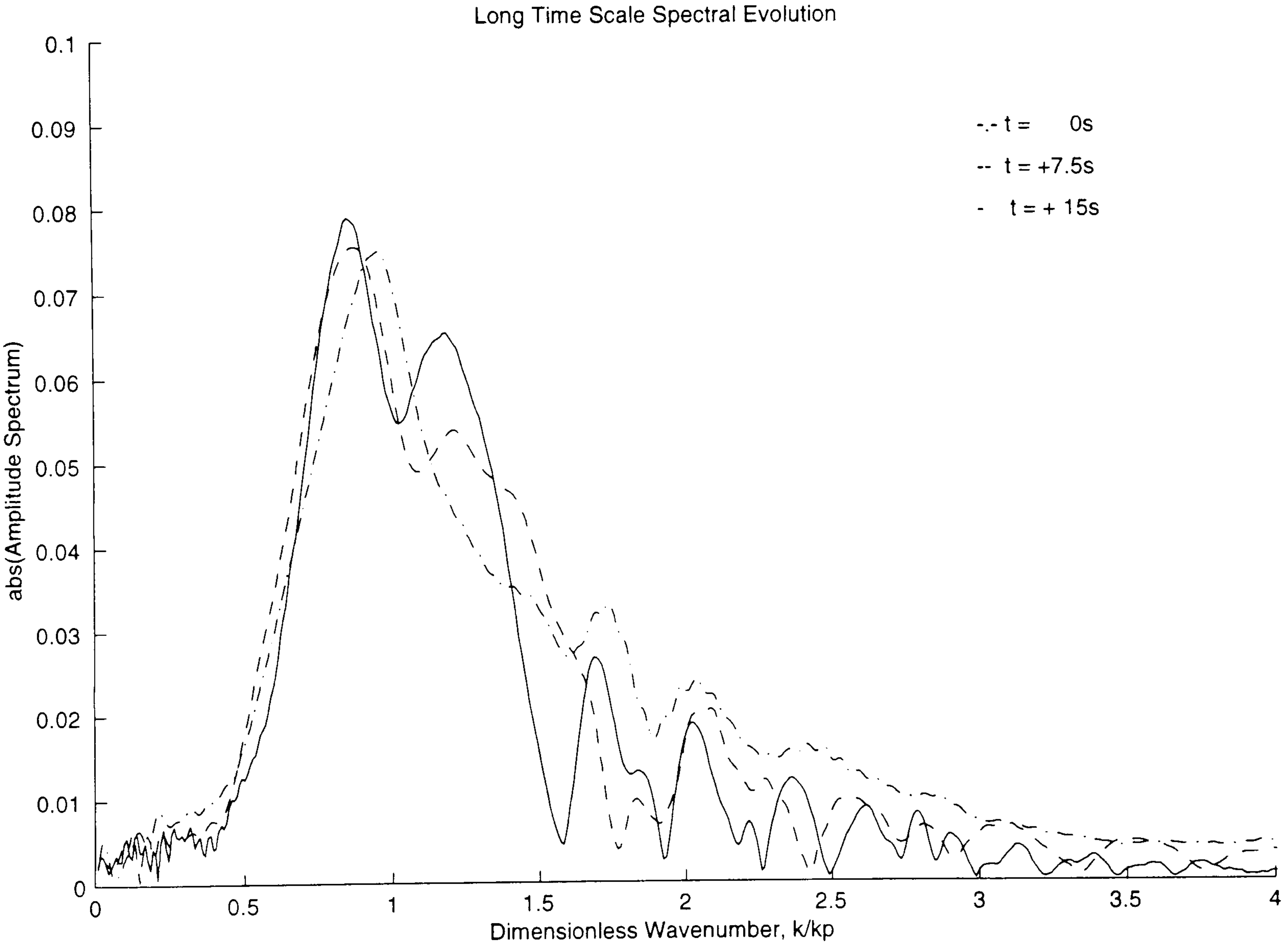

Figure 3.14. Amplitude spectrum time evolution ($t = 0$, $+7.5$, and $+15$s) of a focused wave group crest for $\alpha k_p = 0.3$

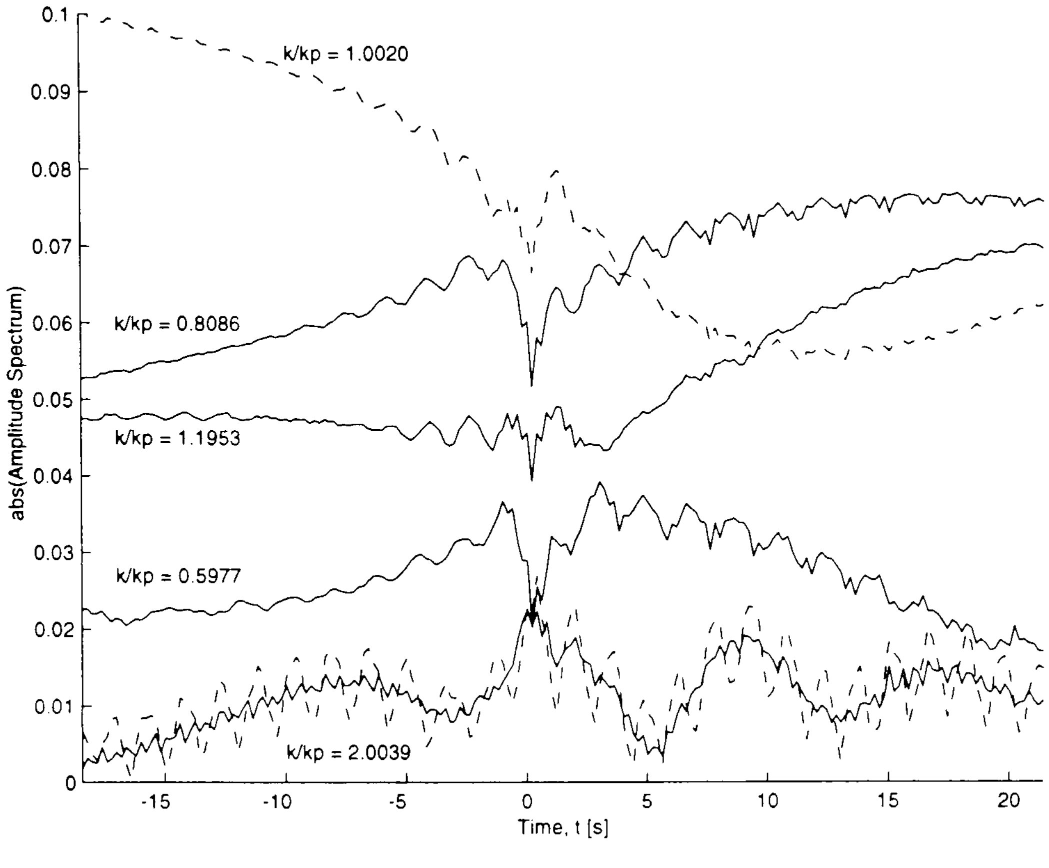

Figure 3.15. Long time scale amplitude variation of individual wavenumber components for $\alpha k_p = 0.3$; for the component at $\frac{k}{k_p} = 2.0039$ a dashed line indicates NWT output and a solid line indicates linear CNT input

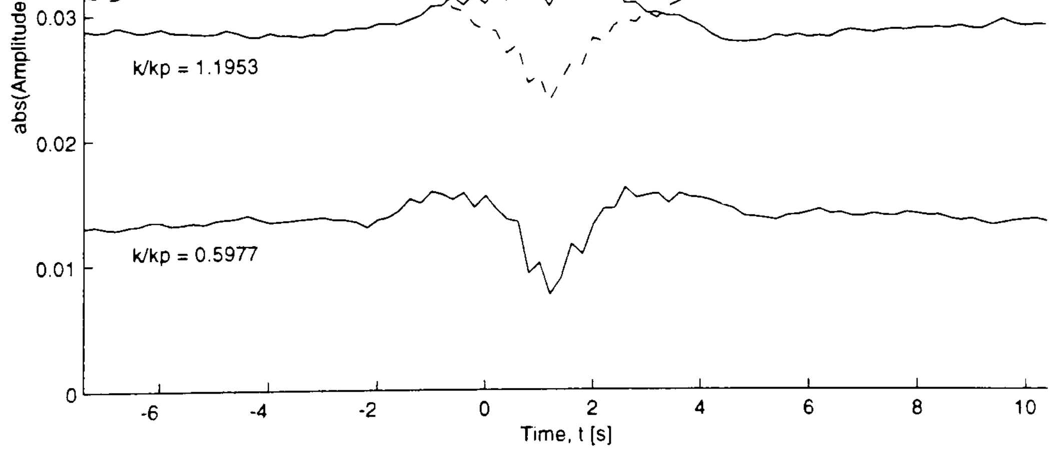

Figure 3.16. Amplitude variation of individual wavenumber components for $\alpha k_p = 0.15$

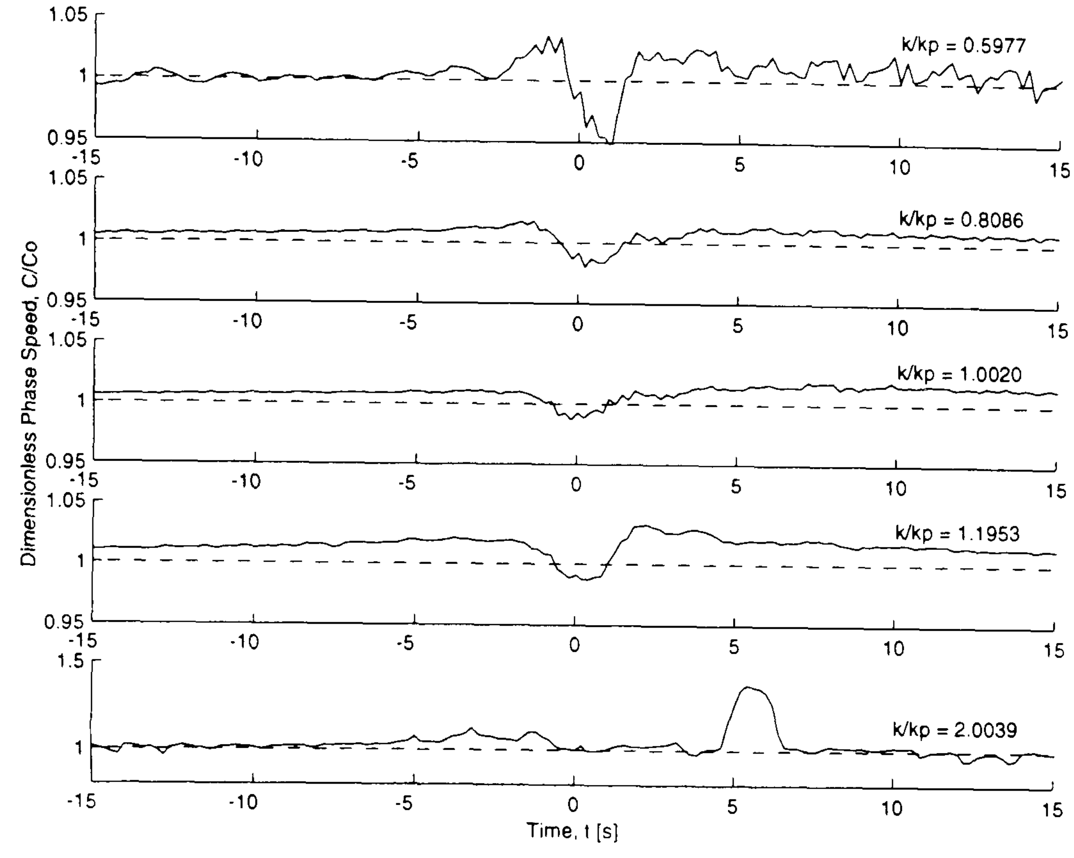

Figure 3.17. Long time scale phase speed variation of individual wavenumber components for $ak_p = 0.3$

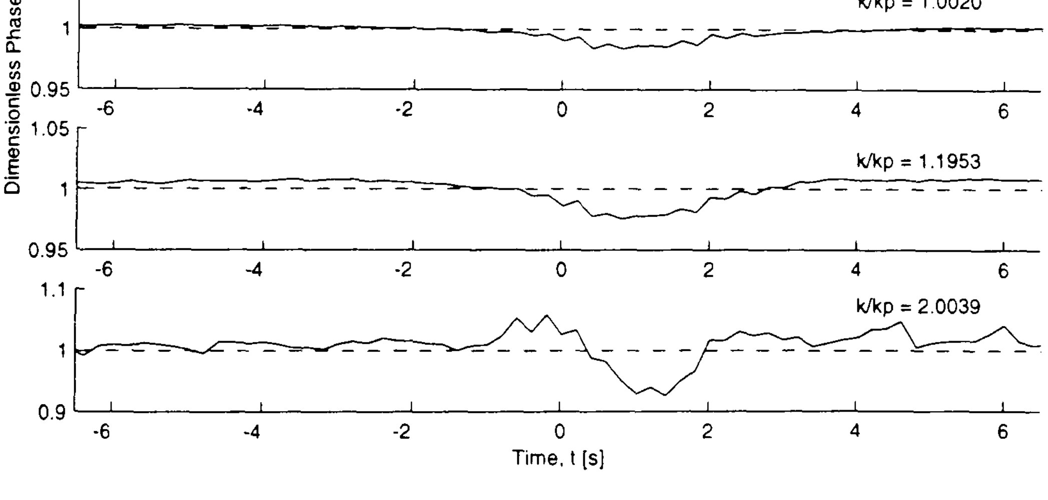

Figure 3.18. Phase speed variation of individual wavenumber components for $ak_p = 0.15$

Chapter 4
Wave Diffraction Experiments

4.1 Introduction

The experimental setup of multicylinder diffraction tests is discussed in detail in this chapter. Testing occurred over a 2 week period in September 1998 in the Offshore Wave Basin at HR Wallingford Ltd. Both regular and irregular incident waves were produced in 104 individual tests on the multicylinder model.

Discussion begins with a presentation of the overall objectives of the experiments, followed by a description of the test apparatus, including construction and installation. Relevant schematic diagrams are presented, as well as the test matrix detailing the frequencies selected and locations of wave probe measurements. Testing procedures and the data acquisition method are also described. Results from these experiments are discussed in Chapters 5 & 6 for regular and irregular waves, respectively.

4.2 Objectives

The principal objective of these experiments was to examine the free surface elevation in the vicinity of a multicylinder model. The model geometry selected was a square array of four ($N = 4$) bottom mounted vertical cylinders of uniform circular cross-section. The simplified geometry of the model and the examination of free surface elevation allow for relatively straightforward comparison with alternative theoretical and numerical data. A range of incident regular wave frequencies and steepness values was tested to provide a large sample of data for comparison. In addition, some irregular wave tests were conducted to examine the effects of various wave spectra.

As discussed in Chapter 1, experiments involving single bottom mounted cylinders have been conducted for comparison to first and second order analytical diffraction theory (Kriebel 1992) as well as NWT methods (Mercier & Niedzwecki 1994 and Park *et al.* 1999). More complex arrays of columns have also been tested, such as truncated cylinders in a TLP model and tapering cylinders from a GBS (Owen & Padilla Perez 1987 and Swan *et al.* 1997). However, the most common measurements made in such tests are forces or moments on the structure, which are integrated effects of the pressure distribution, as opposed to the free surface elevation that may be directly related to the velocity potential and so can represent a more thorough test of computational methods. In addition, the single cylinder structures tested have limited applicability within the offshore industry due to their relatively simple geometry, while the testing of scale TLP or GBS model structures makes the application of theoretical and numerical methods difficult.

4.3 Description

4.3.1 HR Wallingford offshore wave basin

Model testing was conducted in the three-dimensional offshore wave basin at HR Wallingford. As shown in Figure 4.1, this facility has a plan area of 25 m $\times$ 25 m and operates with a working depth of 2 m. The 80 computer controlled individual paddles at the basin's upstream end are capable of generating either regular or irregular waves with directional spreads of up to $\pm 45°$. However, only uni-directional waves were analysed in these experiments, with the incident wave ray (a vector perpendicular to the wave crests and pointing in the direction of wave advance) perpendicular to the wave paddles. At the downstream end of the basin is a beach to prevent significant reflection of wave energy. Not shown in Figure 4.1 is a moveable bridge running across the basin parallel to the wavemaker. Approximately 2 m in width, the bridge is supported on wheeled tracks at the basin's edge and may be moved up to the centre to provide access to the deck of the model structure or positioned away for observation during testing. The placement of video cameras (discussed further below) at the side of the wave basin is indicated by the appropriate symbols.

As indicated in Figure 4.1, the model was placed in the centre of the wave basin, where the origin $(x = 0, y = 0)$ is identified for reference purposes. The x-axis is taken as parallel to the incident wave direction (the longitudinal direction), while the y-axis is perpendicular to the incident wave direction and parallel to the wave paddles (the transverse direction).

4.3.2 Diffraction model

The diffraction model comprised a square array of four bottom mounted vertical circular cylinders and was fabricated at HR Wallingford from standard 406 mm (16 in) diameter steel pipe ($\rho \approx 7850\ \frac{\mathrm{kg}}{\mathrm{m}^3}$) with thickness 6.35 mm (0.25 in). Figures 4.2a & b provide plan view and side elevation schematics of the model. As shown, the cylinders are arranged at the corners of a square, with centre to centre distance equal to twice the cylinder diameter and gap between cylinders of one cylinder diameter. The air gap between the mean still water level and the deck structure supporting the wave probes was selected to be 450 mm, which was assumed to be higher than the diffracted free surface elevation for any of the incident waves to be considered.

Due to the large mass of each cylinder (approximately 1150kg), the model was designed to be assembled inside the basin. The lower cylinder ends were welded to individual bases. This allowed them to be bolted in place on a larger template, designed to rest on the basin bottom and obtain a watertight seal. The template featured a hole at the centre of the array which mated with a pin at the wave basin centre ($x = 0, y = 0$). In addition, two subsequent holes on the periphery of the template allowed the model to be positioned in two configurations. The first configuration, hereafter referred to as heading 0°, is that presented in Figure 4.2, with two cylinders upstream and two downstream. The second configuration, hereafter referred to as heading 45°, is with one cylinder upstream (centre along $y = 0$), one downstream (centre along $y = 0$), and two along the transverse centreline of the wave basin (centres along $x = 0$). It should be noted that use of the terminology 0° and 45° heading is for the purposes of standardized reference only and bears no relation to the mathematical term heading (represented by the symbol β), which is the angle between the incident wave ray and the x-axis (see Chapter 2).

4.3.3 Resistance wave probes and deck structure

A total of 13 channels were available for wave probe measurements, allowing the use of one permanently fixed wave probe (hereafter referred to as the reference probe or probe 0) at ($x = -114\,\text{mm}, y = 3500\,\text{mm}$) and 12 moveable wave probes in the vicinity of the model structure.

To allow for measurement of the free surface in the vicinity of the model, a wave probe support system was developed to be attached to the model itself. Mounted to the top of the cylinders, the deck structure contained a matrix of positions for the wave probes to be attached. This deck structure and 16 wave probes (4 more than necessary to allow for the possibility of damage) were fabricated in the Department of Engineering Science workshop at the University of Oxford.

Figure 4.3 provides both plan view (a) and side elevation (b) schematics of the wave probe support structure, as described above. Two 10 mm thick Perspex sheets measuring 1000 mm × 1000 mm provided the base for the deck. These sheets were designed to rest on top of the cylinders, with edge deflections minimized through a welded framework of square cross-section (25 mm × 25 mm) RS steel tubing. The steel tubing was screwed to the Perspex along the perimeter of the two sheets.

A matrix of 15 mm diameter holes for the wave probes was drilled into the Perspex. A plan view of these positions is given in Figure 4.4, which gives dimensions along the x- and y-axes for the hole locations. Making use of the longitudinal symmetry present in both headings, the matrix of possible wave probe locations ran along the basin centre in transverse and longitudinal directions, as well as upstream and downstream of the cylinder centres. Aluminium mounting blocks (100 mm × 25 mm × 50 mm), positioned at intervals of 120° around the cylinder positions were used to secure the deck to the cylinders. Threaded holes in the centre of the mounting blocks allowed the use of bolts to accurately position and secure the deck structure for both 0° and 45° headings. The orientation of the deck structure with respect to the model in the 0° and 45° headings is presented in Figures 4.5a and b. The dashed circles indicate the cylinder positions, while dashed lines drawn between the cylinder centres are for reference purposes only.

The wave probes were designed for minimum deflection along the length of the probe and to be secured rigidly in the deck structure. To accommodate the 450 mm air gap (see Figure 4.2), the probes were constructed of 3.2 mm diameter (16 gauge) stainless steel tube in 900 mm lengths, ensuring measurement of the lowest troughs. Figures 4.6a, b, & c display side elevation and plan view schematics of the wave probes. The lower ends of the stainless steel tubes were sealed by welding and imbedded in a nylon block (18 mm × 6 mm × 7 mm) to maintain the 12 mm separation, while the upper ends were soldered to 4 mm electrical plugs for interfacing with the connections at HR Wallingford. The interfacing system for rigidly fixing the wave probes in the deck structure was constructed from nylon, with M4 nylon bolts to adjust the height of the steel tubes. A third M4 bolt was run through the centre of the nylon to tighten a rubber O-ring, providing a tight seal in the 15 mm holes of the deck structure. With this central bolt loose, the wave probes could then be moved freely between holes of the matrix. When tightened, the bolt would then hold the probe securely in any of the positions.

4.3.4 Video camera use

Video cameras were positioned as indicated in Figure 4.1 to provide views from the upstream and downstream end of the wave basin as well as between the cylinders. The signals from the cameras were fed into a split screen television, allowing both camera angles to be viewed simultaneously. This made it possible to follow the progression of a wave as it approached the model, reached the cylinders, and progressed further downstream. Recordings were made on SONY U-matic cassettes for the duration of all the tests.

4.4 Experimental Procedures

Following model installation in the 0 degree heading configuration and the subsequent filling of the basin, the wave probes were individually calibrated. A series of tests over a range of frequencies, pre-calibration regular wave tests (PRWT), were then performed to identify frequencies of interest for the final test matrix as well as regions of significant upwelling and runup for wave probe placement. Following these PRWT, a reasonable test matrix was developed to examine the effects of varying both frequency and steepness for regular and irregular incident waves for both model headings. Testing then began for the 0 degree heading case, during which the wave probes were placed in two separate configurations. Following these tests, the model was rotated through 45°, and the same series of incident regular and irregular waves was tested, again with two wave probe configurations. After the model tests, the deck structure supporting the wave probes was fixed in place on the basin bridge at the identical location as atop the model. The basin was then emptied for model removal and subsequently refilled for a repetition of the tests, producing equivalent regular and irregular wave results for an empty wave basin. Due to time constraints, the incident waves were not calibrated prior to testing with the model present. The target regular wave heights and spectral shapes are then not exactly equivalent to those measured during the empty tank testing (see Chapter 5).

4.4.1 Model installation

Prior to the model testing, the wave basin was fully drained to allow for model installation. The template was then placed in position at the basin centre and oriented in the 0 degree heading configuration. The steel cylinders were individually lifted into the basin and bolted upright to the template. After the basin was refilled, lead ballast was placed on the template and a submersible pump was used to fill the cylinders with water, greatly increasing the mass of the cylinders and increasing the overall stability of the structure. The deck structure supporting the wave probes was then installed from the water via an inflatable raft, with assistance from the basin bridge. The deck structure was positioned on top of the cylinder array as indicated in Figure 4.5a, and the bolts in the aluminium locating blocks were tightened securely to ensure rigid and accurate positioning.

4.4.2 Wave probe calibration

Following model installation, probes 1-12 were connected to the free surface measurement equipment and calibrated individually by comparing signals at 0 mm, 50 mm, and 100 mm in the basin. All probes were found to have linear responses, with the lowest value of R for the linear regression 0.999916.

4.4.3 Pre-calibration regular wave tests (PRWT)

The experimental testing began with the PRWT, testing the model (heading 0°) in regular waves covering a range of wave frequencies. The aim of the PRWT was to allow for direct observation of runup and upwelling effects in the vicinity of the model. From this, frequencies of waves inciting significant response could then be identified for inclusion in the test matrix, and regions of extreme upwelling and runup could be noted for the placement of wave probes. These initial tests were numbered 1 through 18 (0001 through 0018 in the video as above), with the test frequencies selected to produce a range of values of ka, the wavenumber multiplied by the cylinder radius. The relevant test parameters, to include incident wave frequency and height, are listed in Table 4.1. It is important to note that the parameters listed are the inputs to the wave basin controlling mechanisms and do not constitute measured values. This is most important in the case of wave height H, which may or may not correspond to the true height produced by the wave paddles.

4.4.4 Test matrix

From observations made during the PRWT, it was concluded that the highest frequency waves ($ka > 0.4$) showed the most significant free surface disturbances. In addition, this disturbance was in some way related to the ratio of incident wavelength to cylinder diameter or spacing (as discussed in Chapter 1). A test matrix was then constructed to analyse the effects of varying incident wave frequency based on the ratio of wavelength to cylinder diameter ($\frac{\lambda}{D}$). However, also of importance is the ratio of wavelength to cylinder spacing (taken as the distance between the centres of the most upstream and most downstream cylinders), which is $\frac{\lambda}{S_0}$ and $\frac{\lambda}{S_{45}}$ for the 0° and 45° heading configurations.

For ease of notation, the three basin configurations, with the model at 0° and 45° heading and with the model removed from the basin, were designated $b1$, $b2$, and $b3$, respectively. The six regular wave frequencies selected for testing were labelled f_r1 through f_r6. For each of these frequencies, two separate values of steepness were chosen, one near to breaking with wave heights $H_r1a - 6a$ and the other half as steep with wave heights $H_r1b - 6b$ ($\frac{\lambda}{H_ra} = 12$, $kA_a = 0.262$ and $\frac{\lambda}{H_rb} = 24$, $kA_b = 0.131$). In addition, three irregular waves (from JONSWAP spectra) were selected and designated with peak frequency $f_i1 - 3$ and significant wave height $H_s1 - 3$. In this manner, a complete test condition may then be designated with a single character string, such as $b2f_r3H_r3b$, which indicates a test of the model in the 45 degree heading configuration, regular wave frequency 3, and regular wave height $3b$ (the lower steepness).

The resulting test matrices for regular and irregular waves is displayed in Table 4.2. Any values omitted are due to the repetition of a frequency It is important to note that all values in the test matrix related to wavenumber or wavelength have been computed through the linear dispersion equation (see Chapter 1). In addition, all values in the table represent inputs to the wave generation equipment and not measurements made following the tests (see Chapter 5).

4.4.5 Wave probe configurations

Wave probes were placed in the matrix of holes in the deck structure in order to best measure the interaction effects of wave scattering from the four cylinders. The chosen positions were based upon observations made during the PRWT. The two probe configurations for each model heading were designated A and B for the 0 degree heading and C and D for the 45 degree heading. With 12 movable wave probes and the reference probe, this provided a total of 13 wave probes in each probe configuration, with 25 distinct measurement positions for each model heading. The reference probe (probe 0) position was constant for the duration of the experiments.

The relevant probe positions are listed in Table 4-3 in Cartesian coordinates with the origin at the model centre and the positive x direction away from the wavemaker as indicated in Figure 4.1. The probes are referenced according to probe configuration and probe number(i.e. B9 is wave probe 9 in configuration B for the 0 degree heading case). For the empty tank regular wave tests, the probes were placed in configuration D; but, for the empty tank irregular wave tests, probes were placed in all four configurations A, B, C, and D. However, for configuration C during the empty tank tests, the bracing used to support the deck structure necessitated the shifting of probes C10, C11, and C12 a distance of 50 mm towards the wavemaker (i.e. -50 mm in the x direction; moving them to the next available hole in the matrix).

4.4.6 Model rotation

Following all the tests in the 0 degree heading configuration, the wave probes and deck structure were removed from the model. To provide buoyancy, the lead ballast on the locating plate was removed and a submersible pump emptied the cylinders of water. A crane fixed to a beam over the tank centre was then used to lift the model, which was rotated through 45°. Rotating about the central hole in the template, the model was properly aligned through a hole in the periphery of the template. The lead ballast was then replaced, the cylinders were again filled with water, and the deck structure and wave probes were replaced in the 45 degree heading configuration as shown in Figure 4.5b.

4.4.7 Deck structure bracing and model removal

After completion of all model testing, the wave basin bridge was moved to the basin centre and the wave probe deck structure was fixed to it. This allowed the positioning of wave probes in the empty tank in the exact positions as with the model in the basin. The basin was then drained, the model was disassembled and removed, and the empty tank tests were conducted.

4.4.8 Settling time and data acquisition

Between tests a settling time of approximately 30 to 45 minutes was allotted to allow for the damping of any standing waves in the basin. This settling time ensured that waves left over from initial tests would not invalidate subsequent tests, provided accurate measurement of the still water level, and allowed the wave probes to be zeroed prior to the start of each test. During the regular wave tests, data acquisition began when the wave paddles were first activated and continued until the input to the paddles ceased, a total duration of 100 wave periods (i.e. 125 seconds of data for the highest regular wave frequency of $f = 0.8000$ Hz, $T = 1.25$ s). During the irregular wave tests, data acquisition began approximately two minutes following the start of the wave paddles, after which time a fully-developed sea state was assumed to be present in the wave basin. Data acquisition was then continued to record 2^9 (512) peak wave periods (i.e. 640 seconds of recorded data for $f_p = 0.8000$ Hz).

Measurements of free surface elevation by the wave probes were recorded at a rate of 40 measurements per wave period for the regular wave tests, corresponding to a sampling rate of $40f$ (i.e. sampling at 32 Hz for $f = 0.8000$ Hz). In contrast, the sampling rate for the irregular wave tests was set so as to record 2^{14} (16384) data points for each test (i.e. sampling at 25.6 Hz for the 640s record at $f_p = 0.8000$ Hz). Data were stored in individual files for each wave probe, with 13 data files per test recording the measurements from start to finish of the data acquisition period in a single column.

4.5 Potential Errors and Limitations

It is important to note possible errors that might result in poor measurements as well as the overall experimental limitations.

4.5.1 Potential Errors

Possible errors in the data could result from either the presence of undesirable disturbances in the wave basin or motion of the wave probes. Undesirable disturbances in the wave basin could be caused by residual energy from previous testing due to insufficient settling time or the slow accumulation of reflected energy due to incomplete damping from the beach. Any motion of the wave probes could be due to direct stimulation by incident waves or indirectly through motion of the model and deck structure as caused by wave forces. However, none of the above sources of error were observable during the testing, and the data collected are believed to be of high quality.

4.5.2 Experimental Limitations

Furthermore, limitations should be noted with regard to the measurement of the free surface during particularly violent events. The resistance wave probes utilized in the experiments depend on a continuous free surface between the rods in order to register an elevation reading. Due to the spacing between rods (12 mm distance centre to centre as shown in Figure 4.6), it is reasonable to suggest that any spray or foam generated for waves of high steepness would not have been recorded. In addition, the wave probes and associated data collection equipment are capable of registering only one distinct elevation per time interval, thus assuming that the free surface is single valued.

Test \#	f [Hz]	ω $[\frac{\mathrm{rad}}{\mathrm{s}}]$	k $[\frac{\mathrm{rad}}{\mathrm{m}}]$	ka	λ [m]	$\frac{\lambda}{D}$	H [m]
0001	0.407	2.555	0.739	0.150	8.50	20.9	0.26
0002	0.485	3.049	0.985	0.200	6.38	15.7	0.32
0003	0.549	3.450	1.232	0.250	5.10	12.6	0.31
0004	0.583	3.663	1.379	0.280	4.56	11.2	0.29
0005	0.604	3.797	1.478	0.300	4.25	10.5	0.28
0006	0.625	3.925	1.576	0.320	3.99	9.82	0.27
0007	0.644	4.048	1.675	0.340	3.75	9.24	0.26
0008	0.663	4.167	1.773	0.360	3.54	8.73	0.26
0009	0.682	4.282	1.872	0.380	3.36	8.27	0.25
0010	0.699	4.394	1.970	0.400	3.19	7.85	0.25
0011	0.717	4.503	2.069	0.420	3.04	7.48	0.25
0012	0.734	4.610	2.167	0.440	2.90	7.14	0.24
0013	0.750	4.713	2.266	0.460	2.77	6.83	0.24
0014	0.766	4.815	2.365	0.480	2.66	6.54	0.24
0015	0.774	4.865	2.414	0.490	2.60	6.41	0.24
0016	0.782	4.914	2.463	0.500	2.55	6.28	0.24
0017	0.790	4.963	2.512	0.510	2.50	6.16	0.24
0018	0.798	5.012	2.562	0.520	2.45	6.04	0.24

Table 4.1. Frequencies used for pre-calibration regular wave tests (PRWT)

Test	f [Hz]	ω $[\frac{\mathrm{rad}}{\mathrm{s}}]$	k $[\frac{\mathrm{rad}}{\mathrm{m}}]$	ka	λ [m]	$\frac{\lambda}{D}$	$\frac{\lambda}{S_0}$	$\frac{\lambda}{S_{45}}$	H [m]	γ
f_r1H_r1a	0.8000	5.03	2.58	0.524	2.44	6.00	3.00	2.70	0.2032	
f_r1H_r1b									0.1016	
f_r2H_r2a	0.7838	4.93	2.47	0.503	2.54	6.25	3.13	2.82	0.2117	
f_r2H_r2b									0.1058	
f_r3H_r3a	0.7686	4.83	2.38	0.483	2.64	6.50	3.25	2.93	0.2201	
f_r3H_r3b									0.1101	
f_r4H_r4a	0.7542	4.74	2.29	0.465	2.74	6.75	3.38	3.04	0.2286	
f_r4H_r4b									0.1143	
f_r5H_r5a	0.7406	4.65	2.21	0.449	2.84	7.00	3.50	3.16	0.2371	
f_r5H_r5b									0.1185	
f_r6H_r6a	0.7277	4.57	2.13	0.433	2.95	7.25	3.63	3.27	0.2455	
f_r6H_r6b									0.1228	
f_i1H_s1	0.8000	5.03	2.58	0.524	2.44	6.00	3.00	2.70	0.1300	2.0
f_i2H_s2	0.7686	4.83	2.38	0.483	2.64	6.50	3.25	2.93	0.1400	2.0
f_i3H_s3	0.7406	4.65	2.21	0.449	2.84	7.00	3.50	3.16	0.1400	2.0

Table 4.2. Test matrix for regular and irregular waves

Probe	x [mm]	y [mm]
A0	-114	3500
B0	-114	3500
B10	-1150	0
B9	-1050	0
B8	-950	0
B7	-850	0
B6	-750	0
B5	-650	0
B4	-550	0
B3	-450	0
A12	-350	0
A11	-250	0
A10	-150	0
A9	-50	0
A8	50	0
A7	150	0
A6	250	0
A5	350	0
A4	450	0
B12	-765	-407
B11	-665	-407
B2	-150	-407
B1	-50	-407
A3	50	-407
A2	100	-407
A1	150	-407

Probe	x [mm]	y [mm]
C0	-114	3500
D0	-114	3500
C9	-350	0
D6	-300	0
C8	-250	0
D5	-200	0
C7	-150	0
D4	-100	0
C6	-50	0
C5	0	0
C4	50	0
D3	100	0
C3	150	0
D2	200	0
C2	250	0
D1	300	0
C1	350	0
C12	-325	-575
C11	-275	-575
C10	-225	-575
D12	220	-575
D11	320	-575
D10	370	-575
D9	420	-575
D8	470	-575
D7	520	-575

Table 4.3. Wave probe positions for 0 degree (A & B) and 45 degree (C & D) headings

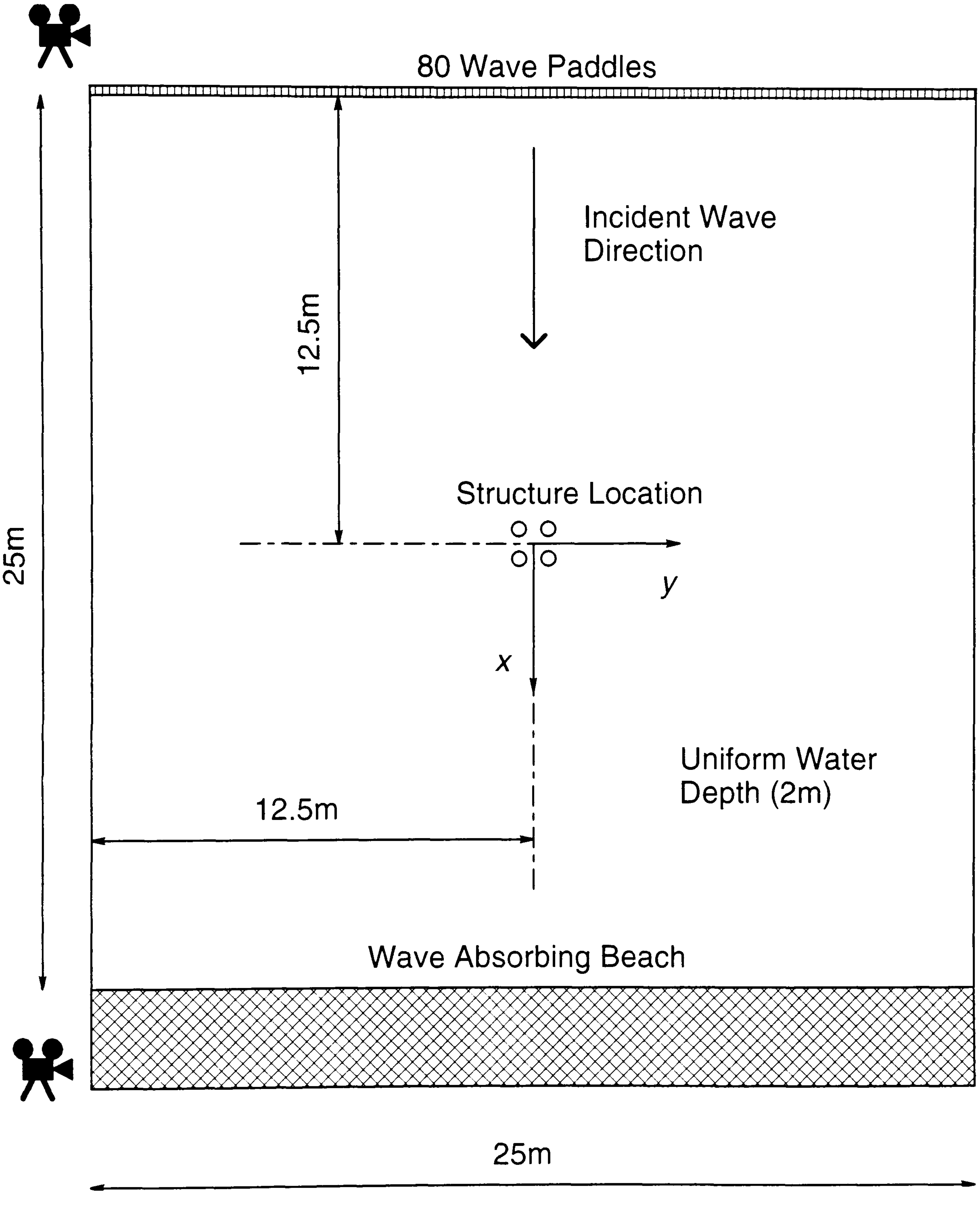

Figure 4.1. Schematic diagram of the wave basin with the location of the model structure indicated

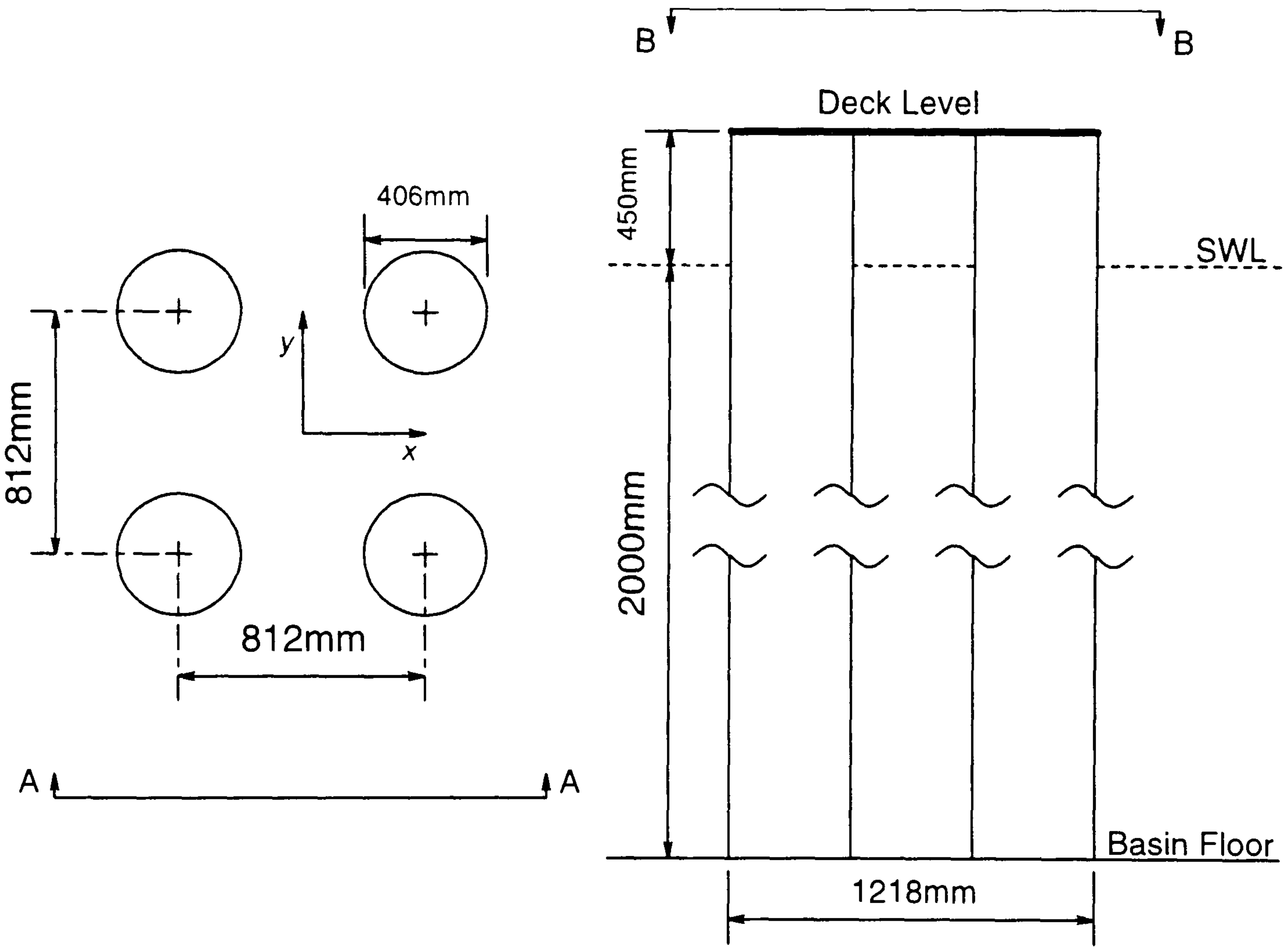

Plan View (B-B)
(a)

Side Elevation (A-A)
(b)

Figure 4.2. Schematic diagram of the model structure in plan view (a) and side elevation (b)

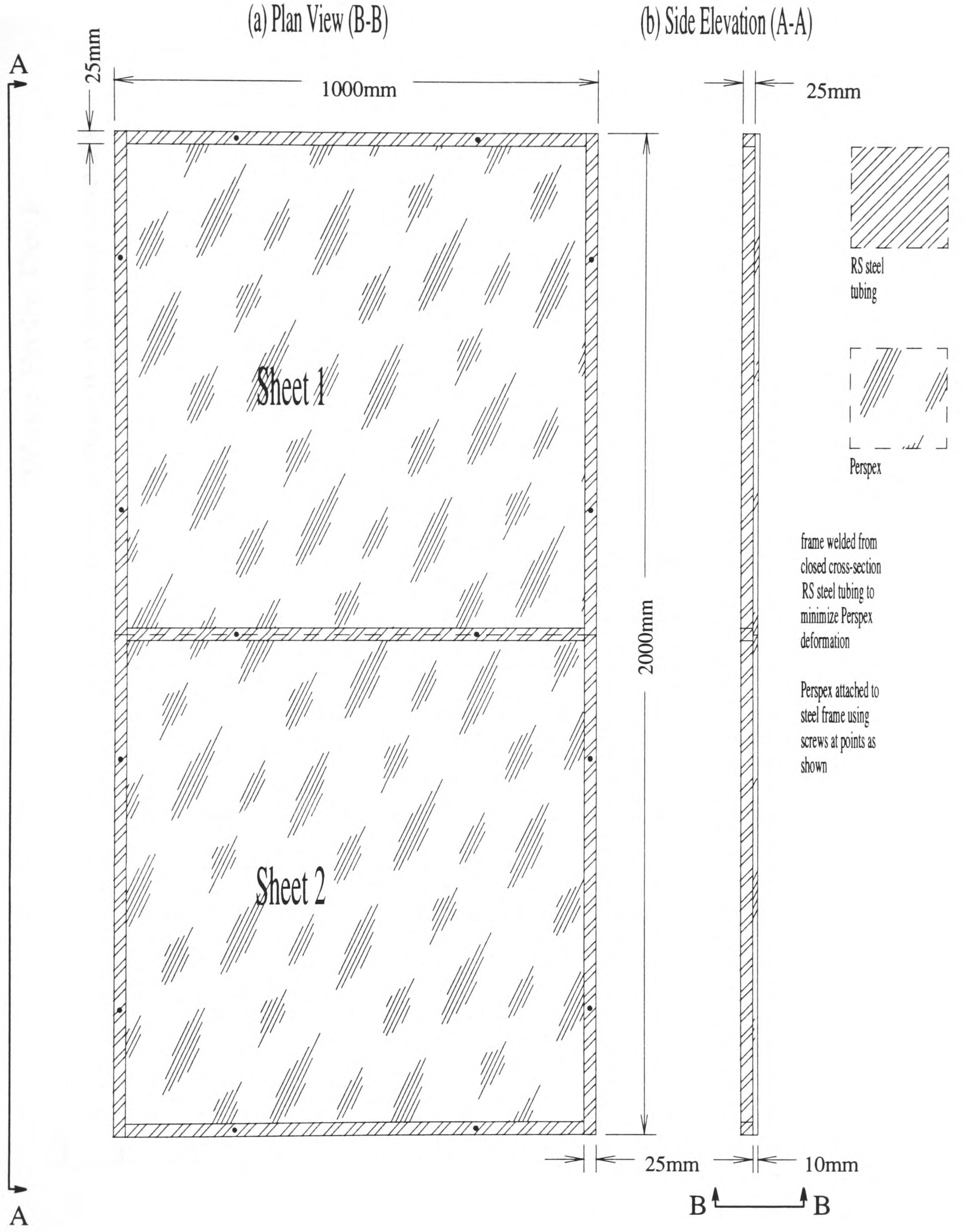

Figure 4.3. Schematic diagram of the deck structure supporting the wave probes in plan view (a) and side elevation (b)

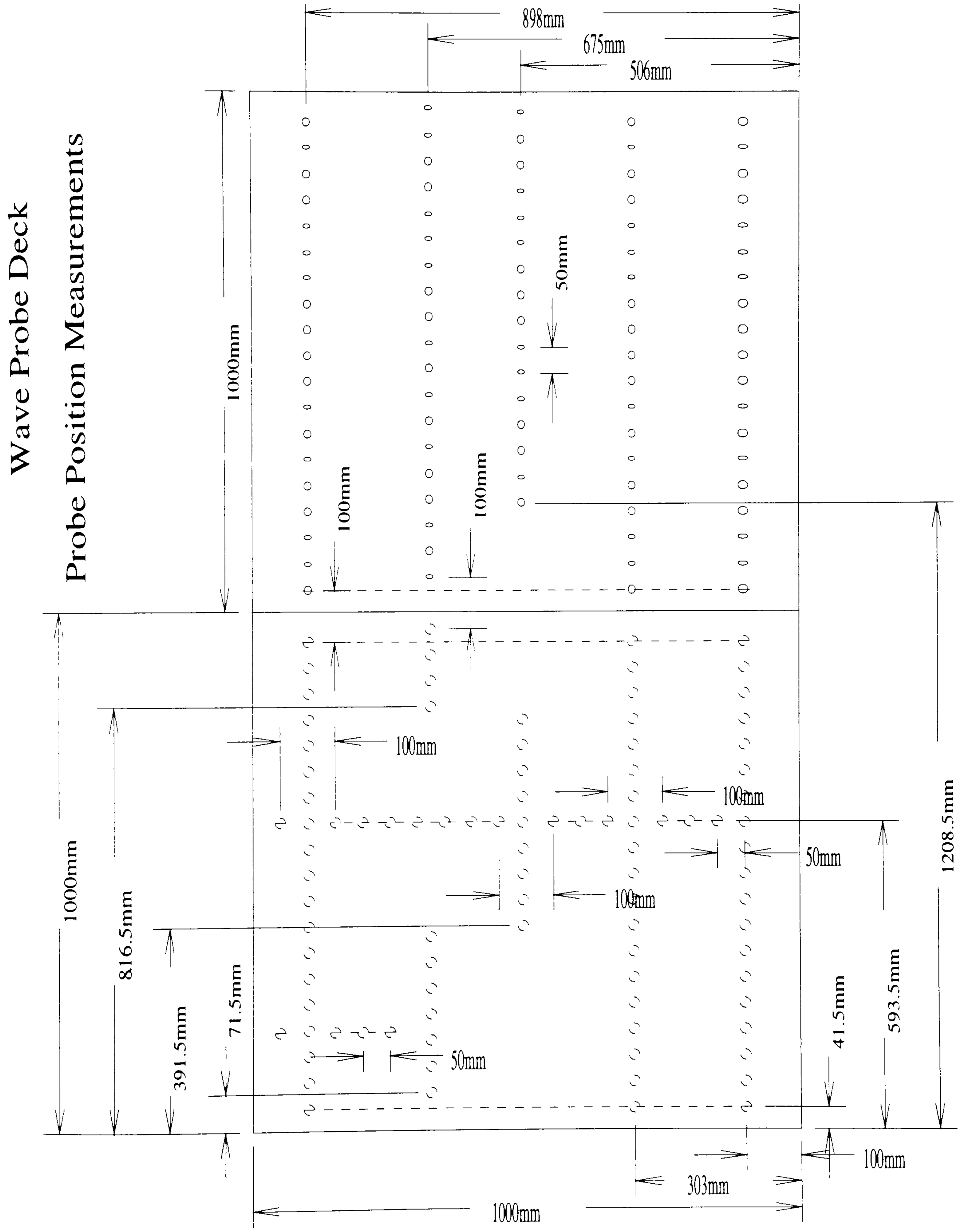

Figure 4.4. Schematic diagram of the deck structure in plan view showing the matrix of holes for wave probes and relevant dimensions

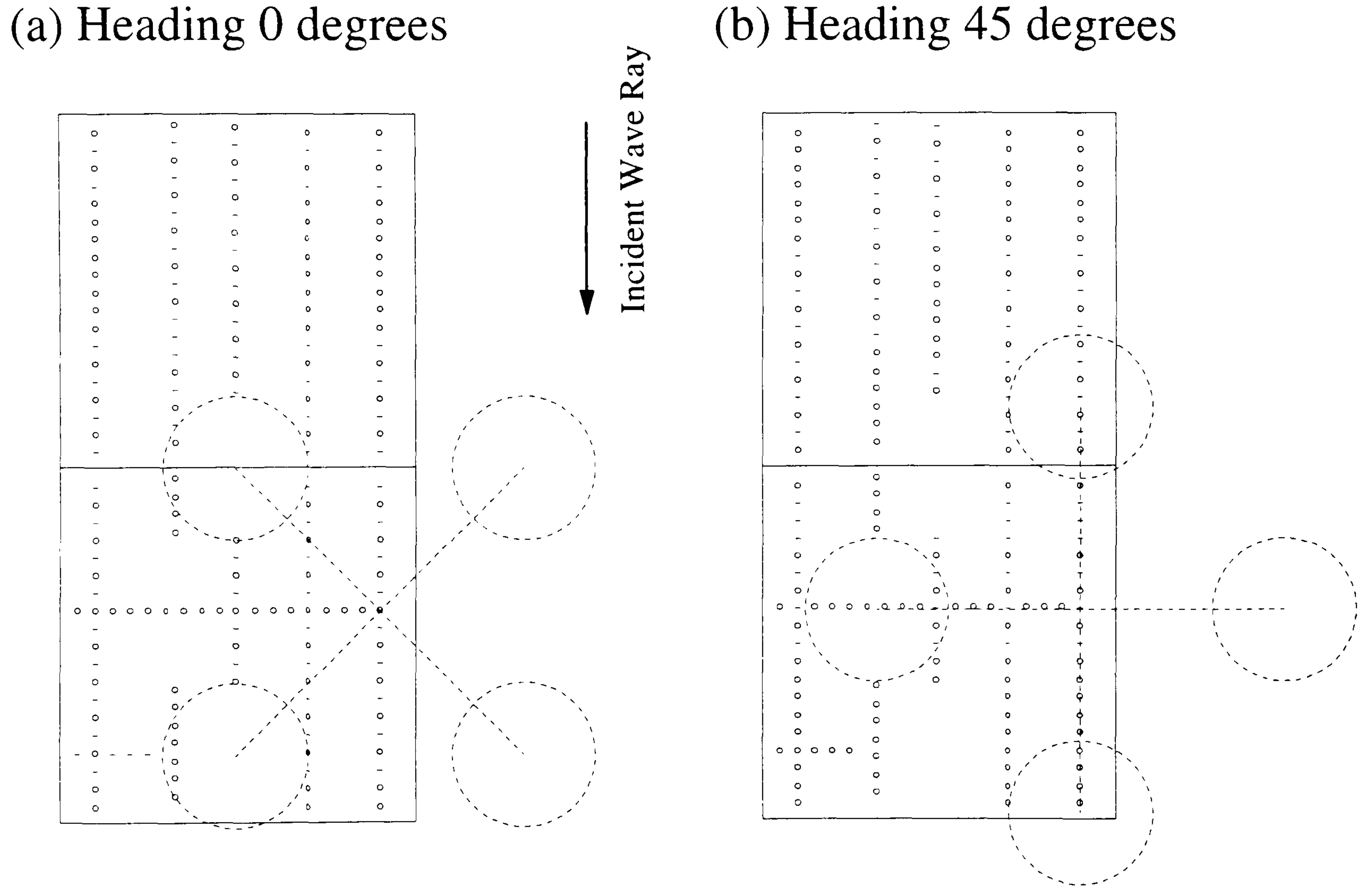

(a) Heading 0 degrees

(b) Heading 45 degrees

Figure 4.5. Schematic diagram of the deck structure showing 0° (a) and 45° (b) heading configurations

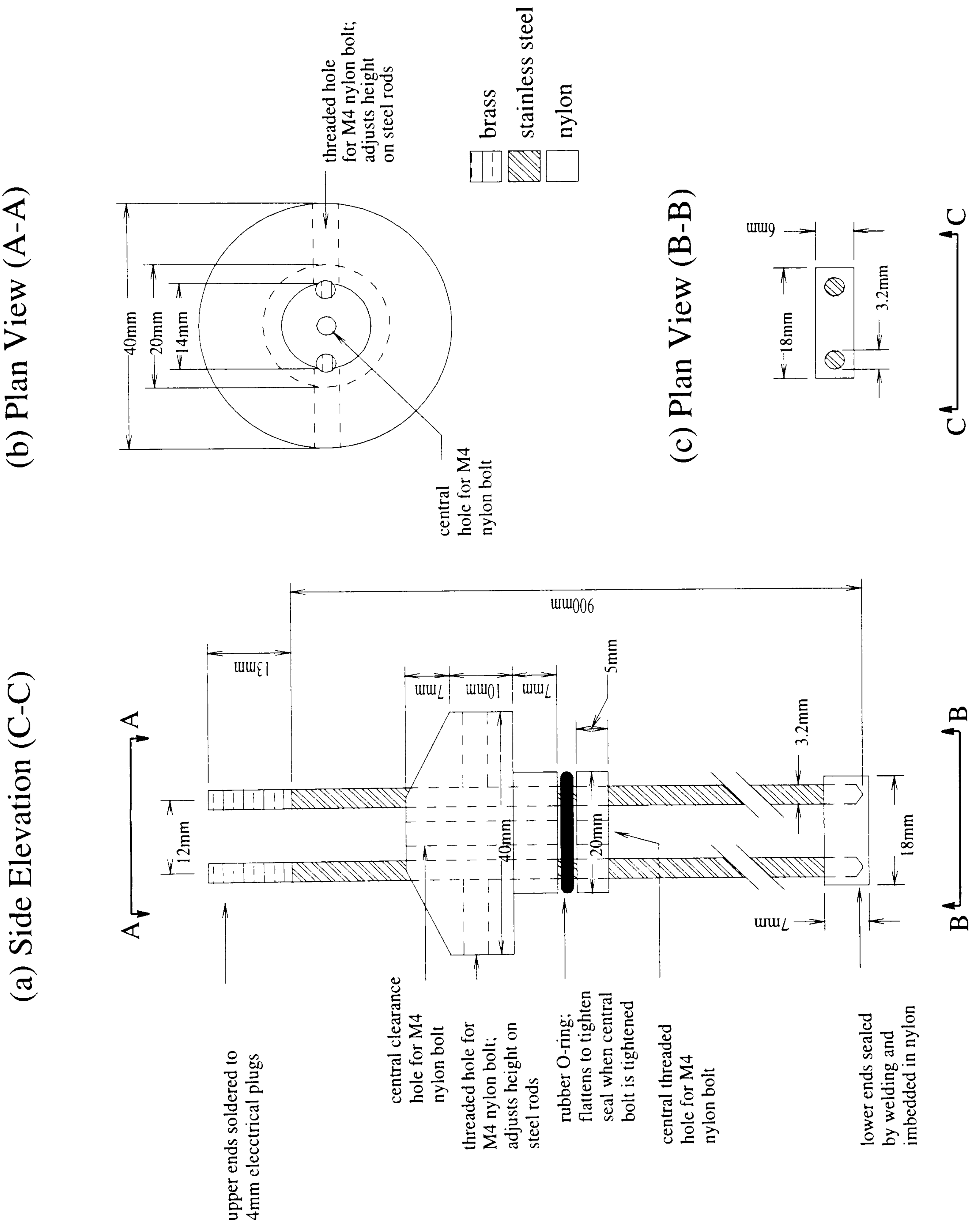

Figure 4.6. Schematic diagram of the wave probe side elevation (a) and plan views (b & c)

Chapter 5
Regular Wave Results

5.1 Introduction

The data analysis from multicylinder diffraction experiments carried out at HR Wallingford (discussed in Chapter 4) is described in detail, and the results are compared, where appropriate, to those from analytical diffraction theories (presented in Chapter 2). Results from the regular wave tests are discussed with reference to linear and second order diffraction theory.

As described in Chapter 4, the heading β used in both model configurations is zero in mathematical terms. However, for ease of description, the first model configuration (with two cylinders upstream and two downstream) will be referred to as heading 0°; and the second model configuration (with one cylinder upstream, two abeam the tank centre, and one downstream) will be designated as heading 45°.

In the following discussions, cylinders are distinguished as upwave and downwave in both heading cases and as offset for the centreline cylinders of the 45° heading cases. The upwave and downwave cylinder edges are referred to as the front and rear faces, respectively. The terms inboard and outboard are used to describe direction toward and away from the centre of the model, respectively. In contrast, longitudinal and transverse describe general orientation parallel and perpendicular to the incident wave ray, respectively.

5.2 Video Observations

As discussed in Chapter 4, video cameras mounted on tripods at the side of the wave basin were used to record all of the tests conducted at HR Wallingford. Two cameras were used, one placed upwave and the other downwave of the model. The camera angles chosen are detailed in the plan drawings of Figures 5.1 and 5.2, which are discussed further below. Both signals were fed into a single split screen television, with the upwave camera in the upper half of the screen and the downwave camera in the lower half of the screen. Taken from a particularly violent event observed in the video, examples of this split screen view are displayed in the still pictures of Figures 5.3 and 5.4. The significance of these two figures is discussed further below.

Videos of the regular wave tests are used primarily for qualitative analysis to provide a general description of the wave scattering processes. Such a general description is presented first, with subsequent presentation of comparable theoretical results in the form of contour plots. The qualitative video observations are then compared with the theoretical contour plots.

5.2.1 Qualitative video observations

Discussion of video observations is divided according to wave heading. The overall observed process is first discussed based upon the lower steepness cases, as these involve less spray and foam and are thereby easier to characterise. The behaviour, however, shows significant effects of nonlinearity. Simplistic plan drawings in Figures 5.1 and 5.2 provide a reference to these general processes. Cylinder positions are clearly defined with thick line circles; arrows indicate the direction of the incident wave and any scattered liquid flow; arcs show the presence of radiating waves; and ellipses and partial ellipses are at the locations of upwelling and runup on the cylinders.

This overview of the video observations is then followed with a description of the time evolution of a wave approaching the model. Finally, differences between the behaviour due to changes in wavelength and the higher steepness cases are discussed.

5.2.1.1 Heading 0°

During the 0° heading tests, the behaviour of the free surface is primarily characterized by a large upwelling at the centre of the model, beneath the deck structure. This event causes the radial flow of liquid from the centre of the model. As illustrated in Figure 5.1, this upwelling and subsequent radial flow generates far field radiating waves as well as large sites of increased wave amplitude upwave and to either side of the model.

As a wave approaches the model, its amplitude visibly increases just upwave of the model as it meets a stream of fluid being expelled upwave from the model centre. The amplitude again increases at the point of runup at the upwave cylinder front faces. Subsequently, as the wave proceeds beneath the deck structure, a massive upsurge is observed at the model centre. This central upsurge is accompanied by upwelling to either side of the model, approximately 2.5 diameters from the model centre. As the central mound of water collapses, liquid moves outward radially from beneath the structure. This results in a high frequency radiating wave at two or three times the incident frequency; and, as previously mentioned, a stream is forced upwave to interact with the next incoming wave.

More specifically, as the wavelength of the incident wave increases (decreasing frequency), the two primary locations of upwelling (at the model centre and just upwave of the model) move progressively and substantially upwave. As incident wave steepness increases, the overall observed processes are similar, but there is significant enhancement in the overall violence of the aforementioned upwelling and radiation events. There is a large amount of foam and spray generated by the central upwelling at higher steepness, but the free surface does not contact the lower deck structure, and the spray generated by upwelling and runup does not extend appreciably above the deck level. In addition, at higher steepness, the liquid being expelled upwave appears to break as it meets the incoming incident wave.

5.2.1.2 Heading 45°

Again, the most visible event during the 45° heading tests is massive upwelling, and possible formation of a clapotis (a large reflected wave resembling a standing wave), at the model centre. This upwelling generates radiating waves, but liquid expulsion from the centre does not appear as dramatic as that observed during the 0° heading tests described above. Figure 5.2 indicates the centre upwelling as well as the principal regions of runup, observed at the front and rear faces of the offset and downwave cylinders.

Upwave of the model, the incident wave remains undisturbed until the upwave cylinder is reached and runup amplification occurs. Passing the upwave cylinder, runup amplification occurs again at the front face of the offset cylinder. Again, large upwelling occurs as the wave proceeds beneath the deck structure and appears to be the direct source of far field waves radiating away from the model at two or three times the incident wave frequency. This amplified wave progresses towards the downwave cylinder, where significant runup occurs, while expelling fluid between the offset and downwave cylinders. This stream of fluid causes large runup both at the rear faces of the offset cylinders and, as the incident wave passes the downwave cylinder, at the rear face of the downwave cylinders.

The timing of observed events at the model centre varies somewhat with the incident wave frequency. At the highest two frequencies, $f = 0.8000$ and 0.7838 Hz, runup at the front face of the downwave cylinder occurs shortly before runup at the rear face of the offset cylinders. With increasing wavelength, runup at the offset begins to precede that at the downwave cylinder. As above for the 0° heading, the location of the maximum centre upwelling moves steadily upwave with increasing wavelength (decreasing frequency). Again, with higher steepness the centre upwelling and runup at the cylinders produces large amounts of spray and foam, but the free surface does not make contact with the deck structure, and the spray does not extend appreciably or consistently above the deck (except in one case discussed further below).

In addition, with increasing wavelength the location of maximum runup at the rear face of the offset cylinder shifts steadily further away from the model centre. This shift is more noticeable in the higher steepness cases, in which this runup occurs directly downwave at $f = 0.8000$ Hz but swings steadily outboard to approximately 45° at $f = 0.7227$ Hz.

Finally, there is a notable increase in the overall violence of the process, to include the centre upwelling and runup at the offset cylinder's rear face, at $f = 0.7542$ Hz. For the higher steepness case at this frequency, spray generated by front face runup on the downwave cylinder rises to approximately 20 cm above the deck. Figures 5.3 and 5.4, stills taken from the test video of this case, depict the maximum centre upwelling and spray as well as the runup and splashing on the downwave cylinder.

5.2.2 Contour plots of linear free surface amplitude

As a means of comparison with the video, contour plots of the local linear free surface amplitudes were produced through the analytical method described in Chapter 2 for a case identical to that of the experiments. These contour plots are presented here in Figures 5.5 to 5.10 for heading 0° and Figures 5.11 to 5.16 for heading 45°. Solid circles denote the cylinder positions. Key contours are labelled with magnitude in terms of the amplification modifying the incident wave. For example, a contour labelled 1 indicates no modification to the incident wave amplitude along that line, while a value of 1.5 corresponds to a 50% increase in amplitude. As before, discussion of these plots is separated according to heading.

5.2.2.1 Heading 0°

The principal features of the contour plots are broad regions of large upwelling upwave of the model and at the model centre. Between these peaks of upwelling, a region of diminished wave amplitude runs transversely between the two upwave cylinders, while small lobes of decreased amplitude exist outboard of the upwave cylinders. Significant runup is indicated at the front and rear faces of the upwave cylinders and at the front face of the downwave cylinders. Any modifications to the incident wave amplitude diminish greatly with increased distance away from the model, most particularly downwave, where very little modification is observed past the downwave cylinders.

With increasing wavelength and decreasing frequency, the upwave upwelling broadens longitudinally but decreases in height (by approximately 25%). In contrast, the centre upwelling remains reasonably constant at approximately 1.65 times the incident wave height. Both upwelling regions shift steadily upwave with increasing wavelength, while the diminished amplitude region between the upwave cylinders becomes less pronounced. Indeed, at $f = 0.7277$ Hz in Figure 5.10, virtually no modification of the incident wave amplitude occurs between the upwave cylinders.

5.2.2.2 Heading 45°

The contour plots feature a significant region of upwelling and runup throughout the centre of the model, to include runup at all inboard cylinder edges. In addition, some runup occurs at the front face of the upwave cylinder and at the rear face of the downwave cylinder. Notably, no major areas of diminished wave amplitude are observed apart from small lobes at the outboard edges of the offset cylinders and the transverse edges of the upwave cylinder, which are present only at the highest frequencies ($f = 0.8000$ and 0.7838 Hz in Figures 5.11 and 5.12).

At the higher frequencies, a small region of upwelling upwave of the model borders onto the runup at the front face of the upwave cylinder. In addition, the upwave cylinder is flanked by upwelling approximately 2.5 diameters from the cylinder centre, and runup is indicated at both the front and rear faces of the offset cylinder. With decreasing frequency and increasing wavelength, the upwelling and runup at the upwave cylinders diminish significantly in height and the flanking regions disappear entirely. Again, the strength of the centre upwelling remains reasonably constant, decreasing from approximately 1.65 to 1.55 times the incident wave amplitude with increasing wavelength. As in the 0° heading case described above, the position of maximum upwelling at the model centre shifts upwave with increasing wavelength. Finally, from an aesthetic perspective, the contour plots become somewhat symmetric at the lowest test frequencies ($f = 0.7406$ and 0.7277 Hz in Figures 5.15 and 5.16).

This symmetry is unique to these frequencies and is not present in contour plots at increasingly lower frequencies outside of the test range (not presented here).

5.2.3 Comparison of video observations with contour plots

For the most part, the global features which can be observed in the videos are very similar to those found in the contour plots. For the 0° heading cases, the extreme upwelling observed upstream and beneath the model correspond well with the first order theoretical predictions. This is also true for the runup at the front face of both upwave and downwave cylinders. However, the offset upwellings observed some 2.5 diameters to either side of the model are not predicted by the theory. It is possible that this offset upwelling is generated by a second or third order event related to energy radiation from the structure in the near field. Regions of diminished wave amplitude in the contour plots, such as the lobes outboard of the upwave cylinders and the region in between these two cylinders, are difficult to identify in the video. Similarly, at 45°, the locations of significant upwelling and runup at the model centre are predicted well by the theory. In addition, the runup sites at the upwave cylinder's front face and the downwave cylinder's rear face are as in the contour plots. Finally, the upwave shift of the global features in the contour plots of both cases is consistent with the video observations.

5.3 Data Manipulation

Measurements of the time variation of free surface elevation $\eta(t)$ were made at prescribed locations in the vicinity of the multicylinder model. The exact model configuration, wave tank description, and testing procedures are described in detail in Chapter 4. In the case of the regular wave tests, data from the tests with the model present were analysed to provide first, second, and third order free surface amplitudes at each wave probe position. These amplitudes were then compared to incident wave amplitudes as computed from empty tank tests.

5.3.1 Data record truncation

The initial data records from the regular wave tests begin at the start of the wavemaker motion and end approximately 2 minutes later. As such, they included an initial timespan during which full wave height had not been achieved as well as an end period during which reflected waves from the tank boundary opposite the wavemaker had arrived at the model. The usable middle section of the data was then identified by analysing complete time histories to determine the point after which waves had stabilized near their intended height and, subsequently, the point after which some reflection or other interference was visibly altering this sustained height. A FORTRAN program was then used to truncate the data into usable sections, as identified above. The truncated data was then loaded into MATLAB for further processing.

This data record truncation is illustrated in Figure 5.17, which contains the majority of three data records, and Figure 5.18, which provides more detail of the isolated segments. These figures plot free surface elevation versus time from wave probe locations near the tank centre; the three subplots contain traces from model tests at 0° and 45° headings as well as the empty tank tests; and the case presented is the lower steepness case at $f = 0.7542$ Hz. It is clear from Figures 5.17 and 5.18 that, by the start of the truncated data section, waves at the model centre have reached a steady state condition. While it is more difficult to discern the point at which reflections in the wave basin have disturbed this steady state condition, it is reasonable to suggest that this occurs after this truncated section.

5.3.2 Cubic spline

The existing truncated data consisted of approximately 13 wave periods and 550 points, the exact number varying slightly depending upon the test frequency of the data in question. To facilitate frequency analysis using FFT (Fast Fourier Transform) methods, it was necessary to have data with 2^N points spanning an integer number of wave periods. The MATLAB program SPLINE.M was then used to fit a cubic spline to the truncated data sets and obtain a fitted data set of 512 (2^9) points over 12 exact wave periods.

5.3.3 Frequency analysis and amplitude computation

FFTs of the fitted data were used to produce a frequency domain analysis for each wave probe. Spectral peaks at the incident frequency, double frequency, and triple frequency (frequencies equivalent to $f = f_i$, $2f_i$, and $3f_i$, where f_i is the incident wave frequency) were then separated by removing all spectral components other than those at or near the peak (within $0.25f_i$ above or below). Components at these frequencies will hereafter be referred to as first, second, and third order harmonics for the single, double and triple frequencies, respectfully. Inverse FFTs of the modified spectra produced time series plots of the separate components, from which a mean amplitude and standard deviation over the 12 wave periods could be computed.

5.3.4 Set up and set down

The magnitude of the set up and set down terms were calculated from the time histories of surface elevation. Given that the fitted data set discussed above encompasses an integer number of wave periods (12), the mean value of the entire set was calculated to compute the set up or set down at each probe position.

5.4 Data Presentation and Observations

To best represent the data, plots were made of computed experimental values versus the wave probe location. Plots of first, second, and third order amplitude values were produced for direct comparison with corresponding analytical theories. In addition, the set down or set up beneath the model was computed and plotted.

In the descriptions of observed phenomena, distinction is made between centreline plots (along the tank and model longitudinal centreline at $y = 0$), offset plots (to the side of the model at $y = -2a$ or $y \approx -2.83a$), and the location of the transverse centreline (along the tank and model transverse centreline at $x = 0$).

5.4.1 Definition of incident wave amplitude

In order to properly non-dimensionalise the data, the incident wave amplitude was taken to be the amplitude of the first order component of the incident wave as measured during the empty tank tests. Use of the empty tank tests to define the undisturbed incident wave ensured the removal of any far-field disturbances that may have been generated by the presence of the model.

Figure 5.19 is a plot of incident wave amplitude, A, versus the non-dimensional ratio of wavelength to cylinder radius, $\frac{\lambda}{a}$. The wavelength λ used here is the linear wavelength as computed from a linear dispersion relationship, and it is non-dimensionalised to accentuate the test frequency selection, based upon integer and half-integer values of $\frac{\lambda}{a}$ as discussed previously in Chapter 4. The '$\times$' and '$+$' symbols are used for the higher and lower amplitude cases, respectively, and represent the amplitude of the first order component of the incident wave as defined above. Use of this labelling convention ('$\times$' for higher and '$+$' for lower steepness) is maintained in subsequent figures. The standard deviations of amplitudes measured at separate probe positions was computed, and errorbars are drawn to a width of one standard deviation above and one below the computed amplitude. The dashed and dotted lines represent the target wave steepness values of $kA = 0.262$ and 0.131 (corresponding to $\frac{\lambda}{A} = 24$ and 48, respectively).

It is apparent from the graph that, although the waves used in the experiments were not calibrated prior to testing, the amplitudes observed are reasonably close to the target steepness. However, the deviation present in the higher steepness case is significant, particularly for the longest wavelength (and subsequently highest wave) of $\frac{\lambda}{a} = 14.5$.

5.4.2 Amplitude variation plots and linear theory comparison

As discussed in Chapter 4, wave probes were placed along the centreline of the model ($y = 0$) for both headings. However, for the 0° heading tests additional probes were placed along a line between the centres of the upwave and downwave cylinders (at $y = -2a$), while, for the 45° heading tests, probes were placed upwave and downwave of the cylinder abeam the tank centre (at $y \approx -2.83a$). For each test frequency, plots of amplitude versus position were made for the properly non-dimensionalised first, second, and third order components. Separated into six subplots for each discrete frequency and heading combination, the complete results are presented here in Figures 5.20 to 5.25 for heading 0° and Figures 5.26 to 5.31 for heading 45°. The three subplots on the left present first, second, and third order amplitudes (from top to bottom) as computed along the centreline of the tank, while the subplots on the right present the offset amplitude computations. As above, the '$\times$' and '$+$' symbols are used for the higher and lower amplitude cases, respectively, and solid lines are drawn to denote the cylinder positions.

Linear diffraction theory (as described in Chapter 2) was used to compute a theoretical prediction corresponding to the experimental results. This comparison is presented as the solid line in the upper two subplots of Figures 5.20 to 5.31.

Direct observations which can be made from Figures 5.20 through 5.31 are grouped herein according to heading and order, beginning with the 0° heading, first order plots and proceeding to the 45° heading, third order plots. Where possible, observed trends in the higher order plots are described with reference to the corresponding first order plot. In addition, regions or point locations of amplification are referred to as peaks, while regions of diminished amplitude are referred to as troughs. It should be kept in mind that use of these words bears no resemblance to the crests and troughs of waves as measured in the time or spatial domains.

5.4.2.1 Heading 0°: first order observations

With some notable exceptions, the comparison of experimental and theoretical results at first order is good. There is also little difference between results at lower and higher amplitudes.

For the centreline plots, the overall trends in both theory and experiment indicate two large peaks, one approximately four cylinder radii ($4a$) upwave of the model centre and the other directly beneath the model centre. At longer wavelengths (lower frequencies), both of these peaks shift slightly further forward and the upwave peak loses strength in relation to the central peak.

While the match between experiment and theory is close, there are notable differences in the location of the minimum amplitude, the magnitude of the upwave peak, and the profile of the offset plots. For all cases, the experimental result is approximately 5 cm downwave of the theoretical prediction. In addition, at higher amplitude the height of the upwave peak is significantly greater than the theory and the lower amplitude results for four of the six test frequencies, $f = 0.7838$, 0.7542, 0.7406, and 0.7277 Hz in Figures 5.21, 5.23, 5.24, and 5.25. In contrast, the lower amplitude upwave peak is the greatest only for $f = 0.8000$ Hz, the highest test frequency, as shown in Figure 5.20. In one extreme example (at $f = 0.7838$ Hz), the high amplitude result is approximately 25% greater than the low amplitude result and 50% greater than the prediction of first order theory.

Finally, the offset plots yield significant differences between the two experimental profiles as well as between theory and experiment. Differences between the values at higher and lower amplitudes are varying and hard to characterize. Both experimental profiles upwave of the model seem to correspond roughly to the theoretical prediction. However, between the cylinders, the theoretical profile is characterized by a positive slope from the rear face of the upwave cylinder to the front face of the downwave cylinder, while the experimental results exhibit more complex behaviour. For all frequencies and both amplitudes, the experimental results show a peak at the rear face, followed by a trough near the transverse centreline ($x \approx 0$), a further peak nearer to the downwave cylinder, and, finally, a trough at the front face of the downwave cylinder. Although the resolution of this profile is inadequate due to the wave probe spacing, it is apparent that the peak near the downwave cylinder shifts upstream as the wavelength increases (decreasing frequency).

5.4.2.2 Heading 0°: second and third order observations

At second and third order, the lower amplitude plots show significantly higher non-dimensional peaks. However, it is important to note that both the higher and lower amplitude plots follow similar trends in the location of peaks and troughs. Also, the maximum height of the second order peaks is significantly greater in the small wavelength (high frequency) cases, while the third order peaks are of similar maximum height at all frequencies.

For the centreline plots, the third order profiles exhibit more rapid variation than those at second order. In general, the second order profiles contain peaks corresponding to peaks and troughs in the first order profiles; and second order troughs occur at maximum slopes in the first order profiles. In contrast, third order peaks occur at locations of peaks and maximum slopes in the first order profiles, while third order troughs occur at the first order troughs and any gradual slopes or crest transition points (i.e. where a peak is transitioning to a slope, or vice versa). However, the largest third order peaks occur at the first order maximum slopes, with less significant third order peaks at the first order peaks. This behaviour can be clearly observed in Figures 5.24 and 5.25, where the largest third order peak occurs at $x \approx -0.25$ m, near the midpoint of the first order profiles shift from a trough to a peak. As the locations of second and third order peaks are dependent upon the first order profile, the peaks shift steadily upwave with increasing wavelength, as described above.

While the second and third order offset plots are more difficult to characterize in terms of any correspondence with the first order profiles, their behaviour is similar at most test frequencies, with a notable exception being the second order runup. At the upwave cylinder's front face, the second order profile shows a gradual decrease approaching the cylinder for three frequencies (f = 0.8000, 0.7838, and 0.7542 Hz in Figures 5.20, 5.21, and 5.23), but an increase is observed for the others (f = 0.7686, 0.7406, and 0.7277 Hz in Figures 5.22, 5.24, and 5.25). This seems to indicate some transition of response for the second order runup near these frequencies (f = 0.7686 and 0.7542 Hz). In contrast, the lower amplitude third order profiles consistently show a gradual increase approaching the upwave cylinder's front face at all test frequencies, while the higher amplitude third order profiles exhibit very low non-dimensional values.

In the offset plots between the cylinders, the second order amplitude profile peaks at the rear face of the upwave cylinder, dips to a trough near the transverse centreline ($x \approx 0$), then increases to peak again at the front face of the downwave cylinder. At third order, the profile exhibits a trough at the rear face of the upwave cylinder, rises to a peak near the transverse centreline, falls again into a trough, and finally peaks at the front face of the downwave cylinder. It is apparent that the third order transverse centreline peak either shifts upwave or broadens as the wavelength increases and frequency decreases. However, it is impossible to distinguish which of these two is occurring due to the wave probe spacing and, in particular, the lack of a probe at $x \approx 0$, where the third order transverse centreline peak might be expected at the lowest test frequencies (such as $f = 0.7277$ Hz in Figure 5.25). Finally, it is important to note that, in the offset cases, the higher amplitude plots show extremely low values, even in comparison with the corresponding centreline plots.

5.4.2.3 Heading 45°: first order observations

Again, with some exception, the comparison of experimental and theoretical results at first order is good and there is little difference between the lower and higher amplitude test cases. It is important to note that, unlike the 0° heading cases, the magnitude of the diffracted first order amplitude never drops below that of the incident wave amplitude (that is, none of the plotted first order values are lower than unity).

For the centreline plots, the overall trend in both theory and experiment indicates a general area of upwelling at the model centre between the upwave and downwave cylinders, with a slight peak in the vicinity of the downwave cylinder. As the wavelength increases (decreasing frequency), the amplitude profile becomes more uniform, with the peak shifting slightly upwave and virtually disappearing at the longest wavelengths. This upwave shift of the global feature is similar, though less extreme, to that observed in 0° heading case.

The trends of the higher and lower steepness cases are virtually identical; but the lower steepness yields a slightly higher upwelling at all the frequencies apart from the lowest ($f = 0.7277$ Hz in Figure 5.31), at which the higher frequency result exceeds the lower very slightly at the peak. The theoretical results also appear to be a better match for the lower steepness data at all the frequencies apart from $f = 0.7406$ Hz in Figure 5.30, where the higher steepness results are slightly better. While the overall magnitude of the centre upwelling is well matched by the theory, the subtle features are not exactly duplicated. This is particularly noticeable at the three highest frequencies, $f = 0.8000$, 0.7838, and 0.7686 Hz of Figures 5.26, 5.27, and 5.28. The experimental values rise slightly from the rear face of the upwave cylinder to a small peak, followed by a slight dip at $x \approx -0.2$ m. Subsequently, there is a steady rise in amplitude to a more extreme peak upwave of the downwave cylinder

($x \approx 0.2$ m), a more dramatic drop approaching the front face of the downwave cylinder, and a final increase in amplitude very near the front face.

Finally, the offset plots yield only slight differences between the theoretical and experimental results. The general trend is a slight increase in upwelling approaching the front face of the offset cylinder, followed by a slight decrease downwave of the rear face. The experimental results indicate a somewhat steeper increase approaching the front face, and a slight peak appears to exist just downwave of the offset cylinder (at $x \approx 0.45$ m) in certain cases. While there are some slight differences in the diffracted amplitudes at the two steepness values, these variations are not consistent nor are they frequency dependent.

5.4.2.4 Heading 45°: second and third order observations

As in the 0° heading cases above, the lower amplitude plots show significantly higher peaks. But, unlike the 0° heading cases, the trends in the location of peaks and troughs are not entirely consistent at second order and are significantly different at third order. In terms of magnitude, the height of the second order centre peak is reasonably consistent at all frequencies, while the runup at the downwave cylinder's front face is significantly greater at longer wavelength and lower frequency. Similarly, the heights of the third order peaks are greatly increased at longer wavelength. In addition, the experimental results vary greatly between the two steepness values, and the lower steepness cases will be treated first and more thoroughly as their behaviour is more consistent with that previously observed in the 0° heading cases.

Again, for the centreline plots at the lower steepness, the third order profiles exhibit more rapid variation than those at second order. Ignoring the aforementioned first order profile complexities and idealizing the profiles as peaking in the model centre and sloping down to the upwave and downwave cylinders, then the behaviour at second and third order may be explained more succinctly in terms of this idealized first order profile. Related to the first order profile, these second and third order profiles shift upwave slightly with increasing wavelength (decreasing frequency).

At lower steepness along the centreline, the second order profile has three peaks at the edges of both cylinders and in the model centre. When compared with the corresponding first order plots, the second order profiles exhibit amplification at both first order peaks and troughs, with second order troughs at any maximum slopes of the first order profile. It is important to note that the magnitude of the central peak seems reasonably constant at a value of 5 for most of the test frequencies. However, the second order runup at the downwave cylinder's front face exhibits an increase with increasing wavelength to a maximum of 10 at $f = 0.7277$ Hz in Figure 5.31.

From observations of the lower steepness case, the overall behaviour appears to be consistent with that observed previously in the 0° heading tests, with third order peaks corresponding to locations of peaks and maximum slopes of the first order profile and third order troughs at first order troughs and crest transition points (see above). These features can be most clearly observed in the plot at $f = 0.7838$ Hz in Figure 5.27, which even shows a peak at the front face of the downwave cylinder corresponding to the more detailed first order runup feature at this location. Again, the magnitude of the third order peaks is greater at the first order maximum slopes than at the first order peaks. At most of the frequencies, the predominance of third order peaks at the first order maximum slopes results in a third order profile largely dominated by two peaks, one just upwave and the other just downwave of the central first order peak.

In the offset plots at lower steepness, the second and third order profiles are, once again, more difficult to characterise in terms of those at first order. However, consistent patterns do exist and the global features adhere to the aforementioned trend of shifting upwave with increasing wavelength. At the highest frequency ($f = 0.8000$ Hz in Figure 5.26), the second order plot greatly resembles the first order, with peaks at the front and rear faces of the offset cylinder and gentle slopes away from the cylinder. As the frequency decreases, a trough appears downwave of the offset cylinder ($x \approx 0.5$ m at $f = 0.7686$ Hz in Figure 5.28) and, subsequently, a peak begins to develop further downwave as the trough shifts upwave at the lowest frequencies ($f = 0.7406$ and 0.7277 Hz in Figures 5.30 and 5.31). The general behaviour at third order is characterized by a gentle rise into a peak at the offset cylinder's front face. Downwave of the cylinder, the profile rises to a peak, drops into a trough ($x \approx 0.4$ m at $f = 0.8000$ Hz in Figure 5.26), and then rises again to a peak. Again, these global features shift significantly forward with increasing wavelength; the aforementioned third order trough, for example, shifts to $x \approx 0.3$ m at $f = 0.7277$ Hz in Figure 5.31.

At the higher steepness, the second and third order profiles are quite different for several cases and are often difficult to characterize in terms of the first order plots. At second order the higher steepness plots conform loosely to the above description at lower steepness with lower non-dimensionalised values at the peaks. However, as the wavelength increases in the centreline plots, and most notably at the lowest frequencies ($f = 0.7406$ and 0.7277 Hz in Figures 5.30 and 5.31), the second order profile transitions into a trough at the upwave cylinder's rear face, followed by a steady rise to a central peak, another trough, and a final rise to peak at the downwave cylinder's front face. The higher steepness third order profiles exhibit very low non-dimensionalised values and few large features when compared to the corresponding lower steepness cases. In the centreline plots, the primary feature of the third order plots is a shallow peak just downwave of the model centre at $x \approx 0.2$ m. However, in the offset plots the profiles are nearly uniformly low in amplitude and not easily described in terms of peaks, troughs, and slopes.

5.4.3 Far field radiation

Using the same data manipulation process described above, second and third order amplitudes were calculated for data taken at the reference gauge, located to the side of the model at $(x, y) = (-0.114\,\text{m}, 3.500\,\text{m})$. Any disturbance in the incident wave amplitude at this site can be taken as representative of the far field radiation produced by the model. Calculated second and third order amplitudes are presented here in Figures 5.33 and 5.34 for the 0° and 45° heading cases, respectively. For comparison to these, Figure 5.32 presents second and third order amplitudes of the undisturbed incident wave, computed as an average of amplitudes at each probe location during the empty tank tests. Non-dimensionalised second order amplitude is shown in the upper half of the figures, with non-dimensionalised third order amplitude in the lower half, and both are plotted against the incident wavelength to cylinder radius ratio.

These figures clearly show that the far field higher order components are significantly altered from what would be expected in the incident wave. The Stokes perturbation expansion would produce non-dimensionalised values of $\frac{1}{2}$ and $\frac{3}{8}$ at second and third order, respectively. This corresponds well with the incident wave analysis of Figure 5.32, although the third order components are somewhat larger than the $\frac{3}{8}$ expected value. While significant differences do exist between the two heading cases, both far field amplitude plots with the model present show amplification with respect to the empty tank results, and the lower amplitude results tend to exceed those of the higher amplitude. Some exceptions to this do exist, such as the second order amplitude at $\frac{\lambda}{a} = 14$ for the 45° heading, in which the higher steepness result exceeds the lower.

Perhaps the most obvious observation from Figures 5.33 and 5.34 is the contrast between the predominance of second order radiation in the 0° heading case and third order radiation in the 45° heading case. In addition, significant variation of radiated amplitude occurs with change in incident wavelength. This is particularly of interest at $\frac{\lambda}{a} = 13.5$, or $f = 0.7542$ Hz, which corresponds to a near-trapping event (discussed further below). At this wavelength for the smaller steepness, the 0° heading case exhibits a very clear maximum in far field radiation at both second and third order, while the 45° case exhibits a clear minimum in third order radiation and a relative minimum at second order. This is supported by observations made from the video, as discussed above, in which more radiation was clearly visible during the 0° heading case at this frequency in comparison to the 45° heading case.

5.4.4 Set down and set up

The set down or set up observed beneath the model (computed as previously discussed) is presented here in Figures 5.35 to 5.40 for heading 0° and Figures 5.41 to 5.46 for heading 45°. Separated into 2 subplots for each discrete frequency and heading combination, the left subplot presents set down or set up as computed along the centreline of the tank, while right subplot presents the offset set down or set up. Again, the '$\times$' and '$+$' symbols are used for the higher and lower amplitude cases, respectively, and solid lines are drawn to denote the cylinder positions. The solid and dotted lines are drawn in the left hand subplot only to aid the eye in distinguishing between the trends of the higher and lower amplitude cases.

As before in the case of free surface amplitudes, the plot will be discussed according to the heading, beginning with 0° and proceeding with 45°. Within the headings the centreline mean sea level profiles will be discussed first followed by the offset profiles.

5.4.4.1 Heading 0°: set down and set up observations

In the centreline plots for the 0° heading cases, there are two significant mean sea level peaks, one upwave of the model and a second near the model centre. This is indicative of significant set up at these locations, between which are set down troughs. These three global features occur at locations corresponding to the first order upwelling sites discussed above in Figures 5.20 to 5.25 and exhibit the same upwave shift behaviour with increasing wavelength and decreasing frequency. In the offset plots the mean sea level indicates set up both at the front face of the upwave cylinder and between the upwave and downwave cylinders. In addition, large set up is present at the runup sites on the downwave cylinder's front face for all frequencies and on the upwave cylinders front face for $f = 0.8000$ Hz in Figure 5.35.

Some systematic differences appear to exist between the higher and lower steepness cases. At the four lowest frequencies (from $f = 0.7686$ to 0.7277 Hz in Figures 5.37 and 5.40), the lower steepness downwave set up in the centreline plot is significantly higher (in non-dimensional terms) than that at the higher steepness. In contrast, at all frequencies apart from the highest at $f = 0.8000$ Hz in Figure 5.35, the upwave centreline set up is significantly higher for the higher steepness case.

At the near-trapping frequency $f = 0.7542$ Hz from Figure 5.38, it is interesting to note that the centreline plot indicates a maximum set down for the lower steepness case. As discussed before, this occurs at the location of the trough in the first order free surface amplitude profile as presented in Figure 5.23.

5.4.4.2 Heading 45°: set down and set up observations

For the 45° heading, all of the mean sea level profiles indicate virtually no set down. In contrast to the 0° heading case analysed above, the global set up features in the centreline plots correspond to those of the second order free surface amplitude profiles as presented previously in Figures 5.26 to 5.31. Like these amplitude profiles and most clearly visible in the lower steepness cases, these set up plots show peaks at the inboard cylinder edges and at the model centre with two troughs upwave and downwave of the centre. With increasing wavelength, as with results described above, the primary global feature of central setup shifts upwave in the centreline plots. Similarly, with peaks at the offset cylinder's front and rear faces, the offset mean sea level profiles follow the general trends of the second order amplitude profiles.

Again, some systematic differences exist between the lower and higher steepness cases. At the lower steepness, the central peak is more clearly defined at all frequencies, whereas at some frequencies, notably $f = 0.7838$ Hz in Figure 5.42, the higher steepness set up profile yields almost no peak between the cylinders. In addition, the value at the downwave cylinder's front face is consistently greater for the lower steepness cases.

The maximum set up indicated occurs on the front face of the downwave cylinder at the lowest test frequency ($f = 0.7277$ Hz in Figure 5.46) for the lower steepness case. This corresponds to the maximum second order runup observed previously at this frequency and steepness in Figure 5.31.

5.5 Conclusions

Several primary results have been recognised and are summarised here. These are:

(1) As incident wavelength is increased, there is a consistent upwave shift of the global features, including amplitude and mean sea level profiles.

(2) For the steeper incident wave cases and at some frequencies in the less steep cases, the observed behaviour is indicative of highly nonlinear breaking induced by diffraction.

(3) These diffraction processes are highly sensitive to small changes in incident wavelength, particularly in the vicinity of a near-trapping event.

5.5.1 Global features shift upwave with increasing wavelength

As predicted by first order theory, the global features produced by the wave scattering shift steadily upwave with respect to the body as the incident wavelength is increased. This prediction has been verified in observations made from the video as well as plots of free surface amplitude and mean sea level profiles, as presented above. In addition, excellent agreement has been shown between first order diffraction theory and the experimentally computed first order amplitudes, particularly for incident waves of low steepness.

5.5.2 Diffraction induced breaking

For the vast majority of the test cases, the first order theoretical predictions were found to match more closely the lower steepness incident wave cases. As this diffraction theory is based on the potential flow assumptions of small amplitude incident waves, the result is not particularly surprising. However, significantly higher peaks in the non-dimensionalised amplitude profile are observed in some of the cases. This could indicate some input of energy at the incident frequency from sources other than the first order scattered wave, such as higher order diffracted wave components. In addition, at higher steepness, the second and third order amplitude components were frequently far lower than those of the lower amplitude cases. Given the assumed higher nonlinearity of steeper waves, this result is somewhat counterintuitive.

One possible explanation for these observations is nonlinear breaking induced by diffraction. In this process, steep incident waves, already close to breaking for the steepest cases studied herein, interact with scattered waves from the structure. The resulting height of these superimposed waves is then too great to be supported given the incident wavelength. The incident and scattered waves then break and, in the generation of turbulence and foam, transfer energy to lower frequencies.

This process is observable to a certain extent in the videos produced during the testing. This diffraction induced breaking could explain the aforementioned breaking stream observed at the upwelling site upwave of the model in the 0° heading case. In addition, it would directly explain the vast amounts of spray and foam generated at the model centre during the higher steepness test cases.

5.5.3 Effects at near-trapping frequency

The geometry used in the 45° heading case is identical to a case studied by Malenica, Eatock Taylor, and Huang (1999). One of the cases studied in their paper is the near-trapping observed in the free surface amplitude profile for $ka = 0.468$. They observed that this non-dimensionalised frequency corresponds to near-trapping of the second order wave component (first order near-trapping occurring at $ka = 1.66$). This ka value differs by only 0.64% from the frequency studied here, $f = 0.7542$ Hz, which corresponds to $ka = 0.465$.

The three subplots in Figure 5.47 display a comparison of the experimental and theoretical results for first order amplitude, second order amplitude, and second order set down, respectively. As before, the solid line indicates the theoretical results, while the '$\times$' and '$+$' symbols represent the higher and lower steepness cases, respectively. The first order case has been presented previously in Figure 5.29 and discussed before, but it is worth noting that the theory gives a very close prediction of the experimental results.

In the second order plot, the global features of the free surface amplitude profile at near-trapping have been very well captured. In particular, the value of the central peak is very closely predicted, although the location of this predicted peak is approximately 4 cm too far upwave. However, the runup values at the cylinder edges are significantly over predicted. Possible explanations for this are as follows:

- Diffraction induced breaking disperses energy from this frequency component, as discussed above.
- The data record, truncated to contain only 12 steady-state waves, was of insufficient length to fully saturate

the near-trapping event.

- The sensitivity of the near-trapping phenomenon to small changes in ka.

Figure 5.17 demonstrates the effect of the data record truncation at this frequency. In the upper subplot, the pronounced second order disturbance clearly grows with time well after the end of the analysed data section. However, it is not clear that this increasing disturbance is related to increased saturation of the near-trapping mode as opposed to the build up of reflected energy within the wave basin.

The sensitivity to small changes in ka has been observed by Malenica, Eatock Taylor, and Huang (1999). In Figure 15 of their paper, they examined the frequency dependence of dimensionless runup in a square array of very similar geometry to that studied here ($\frac{a}{d} = 0.6$ as opposed to $\frac{a}{d} = 0.5$ analysed here, where a is the radius and $2d$ is the distance between cylinder centres). Both first and second order runup were found to exhibit very sharp peaks in response around near-trapping frequencies, with $\frac{\eta}{A}$ at first order increasing from 2 to 7.5 for a ka increase of only 0.05.

The theoretical profile of the second order set down and set up poorly represents the global features of the mean sea level. While the general magnitude and profile downwave of the upwave cylinder is well reproduced by the theory, the experimentally indicated peak at the model centre is not predicted. In addition, in the lower steepness case, the excessive peak at the front face of the downwave cylinder is not well matched. However, it must be kept in mind that these theoretical results are limited to the second order and do not include potential contributions from higher order components.

As previously mentioned in the discussion of far field radiation, significant variation in second and third order radiated wave amplitude is observed at this near-trapping frequency for both headings. This frequency corresponds to a wavelength to cylinder radius ratio of $\frac{\lambda}{a} = 13.5$ as displayed in Figures 5.33 and 5.34 above. For the 0° heading case, excitation at this wavelength generates a very clear maximum in both second and third order far field radiation. This is in stark contrast to the clear minimum in third order radiation and relative minimum in second order radiation observed in the 45° case. In addition, as discussed previously with regard to set up and presented in Figure 5.38, the mean sea level profile at this frequency shows a significant drop at the model centre for the 0° heading. This is particularly true for the lower steepness case relative to the set down at other frequencies. However, as shown in Figure 5.44, the 45° heading mean sea level profile shows a set up at the centre that is reasonably consistent with that at other frequencies.

These results are indicative of two widely differing responses at the near-trapping frequency for the two test geometries:

- For the 0° heading case, far field radiation is maximized for the 0° heading and is accompanied by a relative decrease in local mean sea level at the model centre.
- For the 45° heading case, far field radiation is minimized while a set up is maintained at the model centre.

This suggests general tendencies for energy dissipation and radial flow from the centre for the 0° heading cases at near-trapping, with a contrasting tendency to store energy and fluid at the centre for the 45° heading. This last statement echoes observations made from the videos, in which local radiation and fluid propagating from the model centre appeared far more significant in the 0° heading cases in relation to the 45° heading cases. Finally, given the sheltered geometry of the 45° heading case, this result is somewhat intuitive.

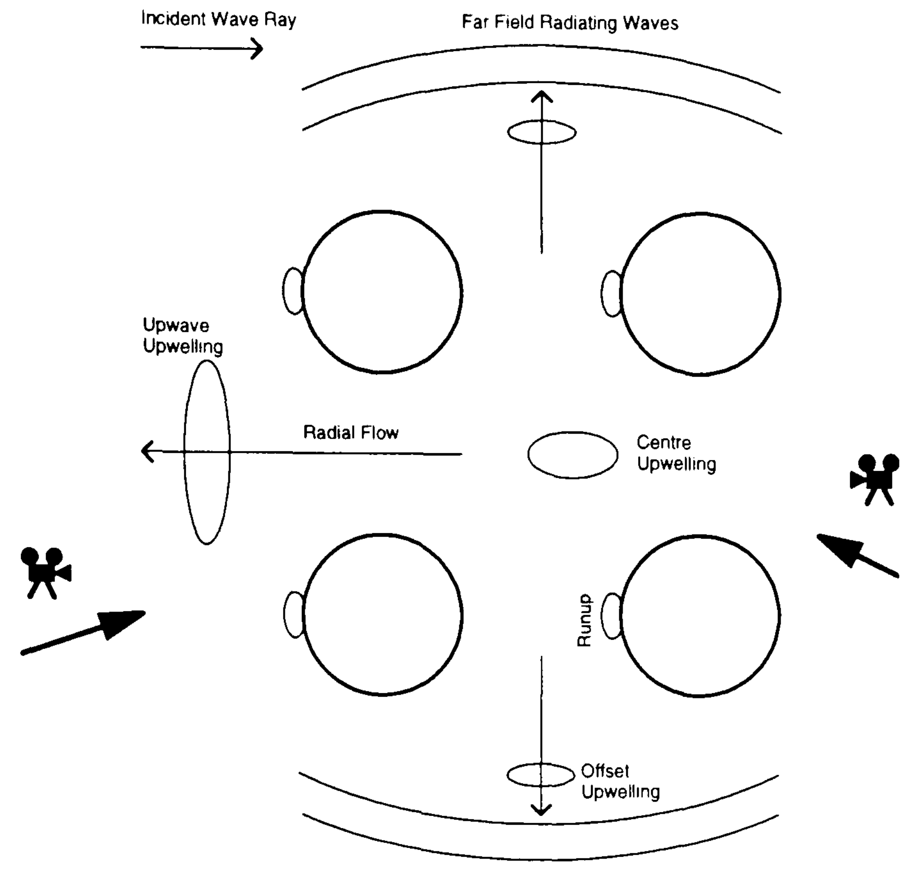

Figure 5.1. Diagram of general video observations with camera angles indicated; $\beta = 0°$

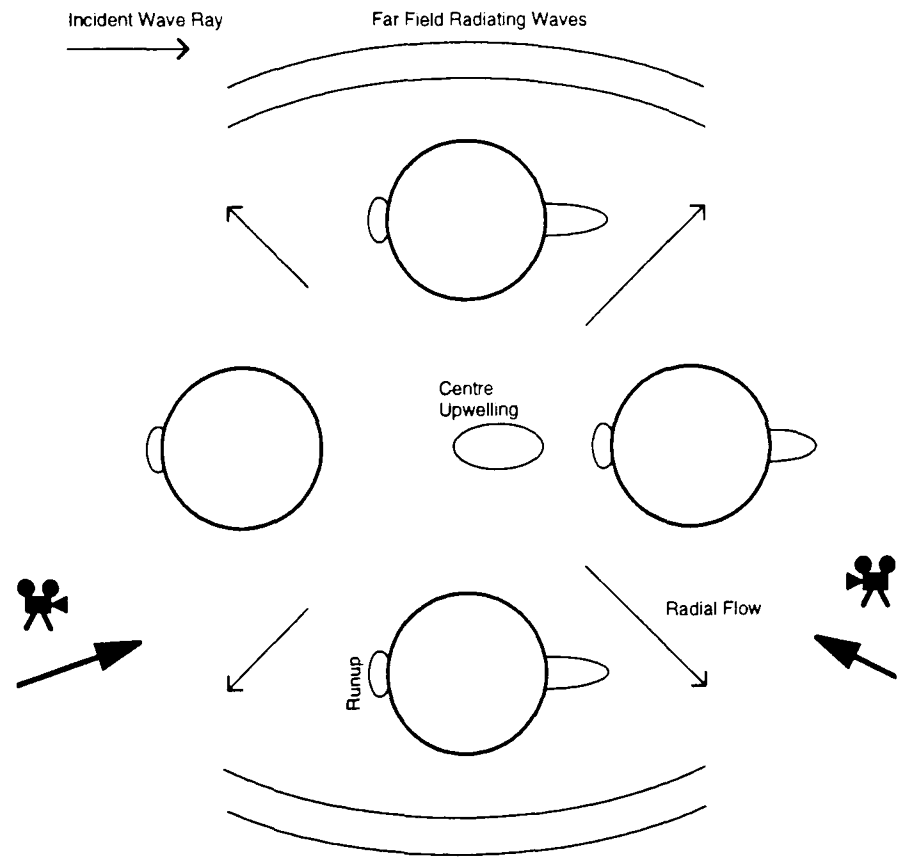

Figure 5.2. Diagram of general video observations with camera angles indicated; $\beta = 45°$

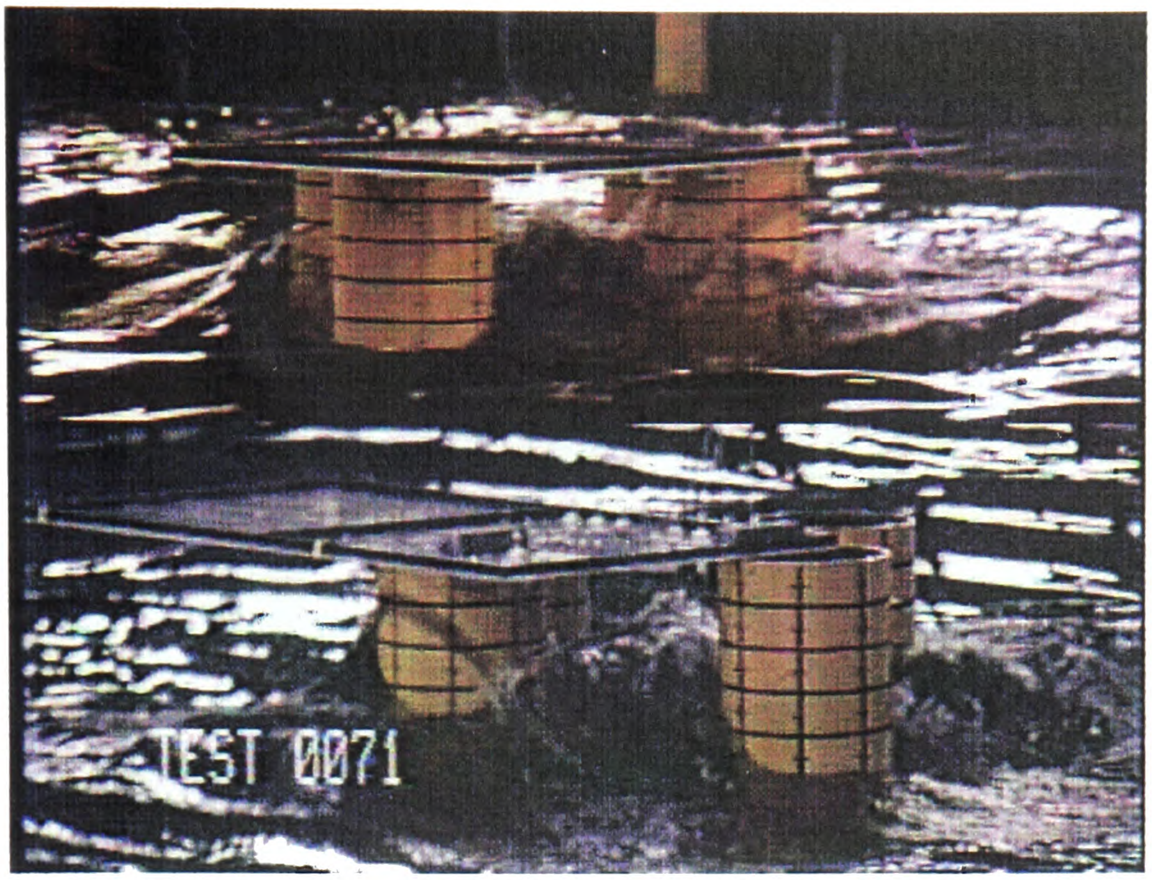

Figure 5.3. Maximum observed centre upwelling; $\beta = 45°$, $f = 0.7542$ Hz, largest steepness case

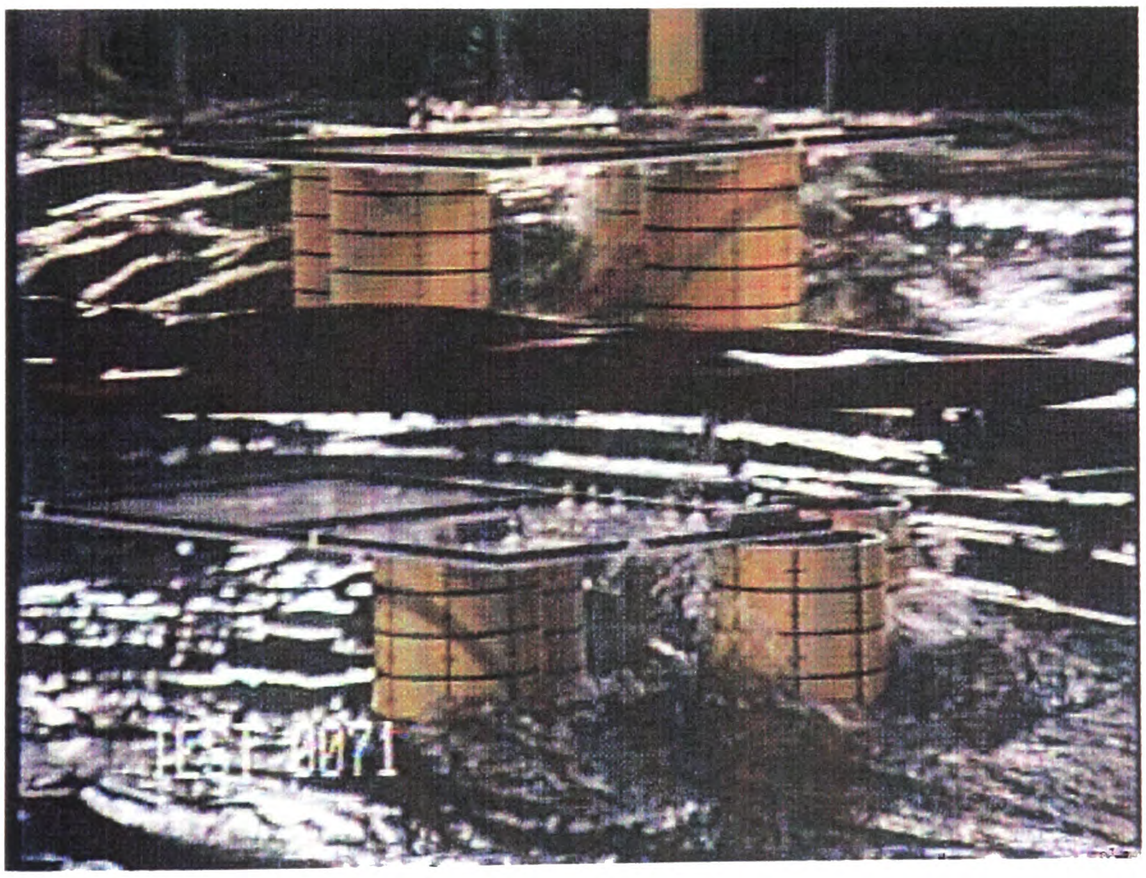

Figure 5.4. Maximum runup on downwave cylinder; $\beta = 45°$, $f = 0.7542$ Hz, largest steepness case

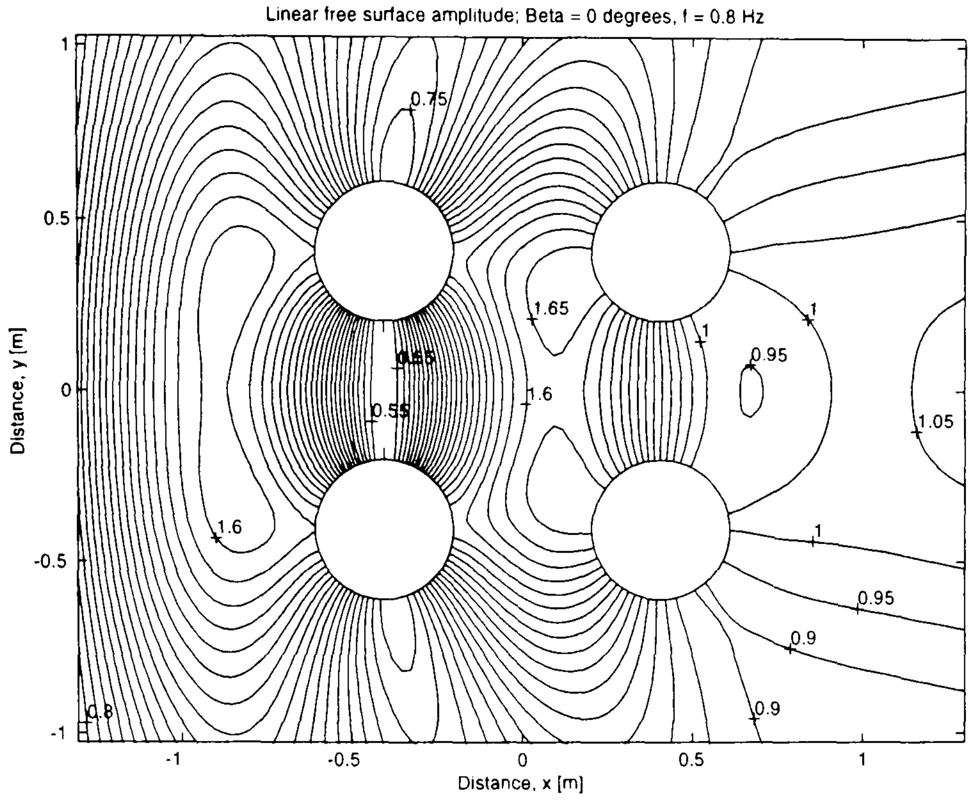

Figure 5.5. Linear free surface amplitude; $\beta = 0°$, $f = 0.8000$ Hz

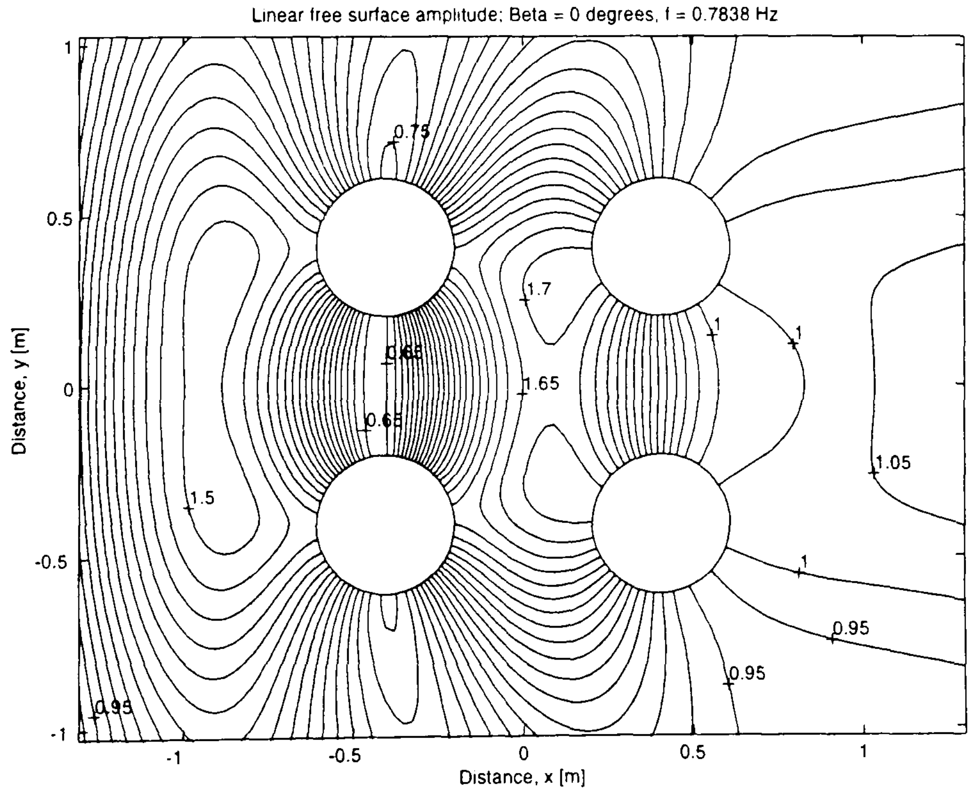

Figure 5.6. Linear free surface amplitude; $\beta = 0°$, $f = 0.7838$ Hz

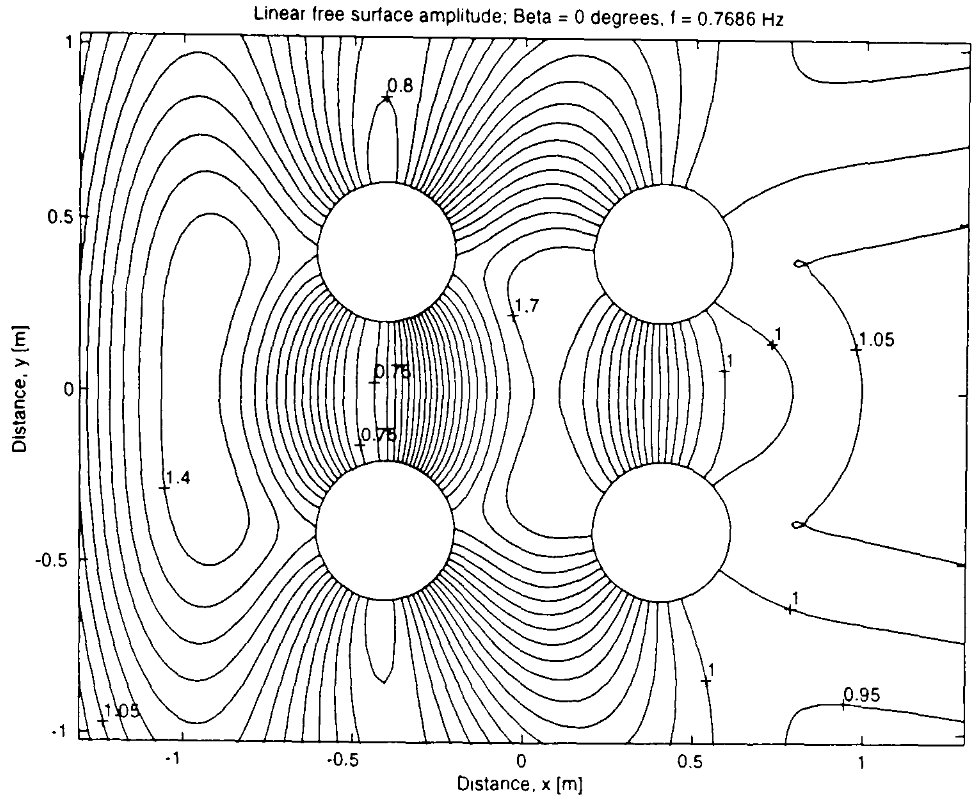

Figure 5.7. Linear free surface amplitude; $\beta = 0°$, $f = 0.7686$ Hz

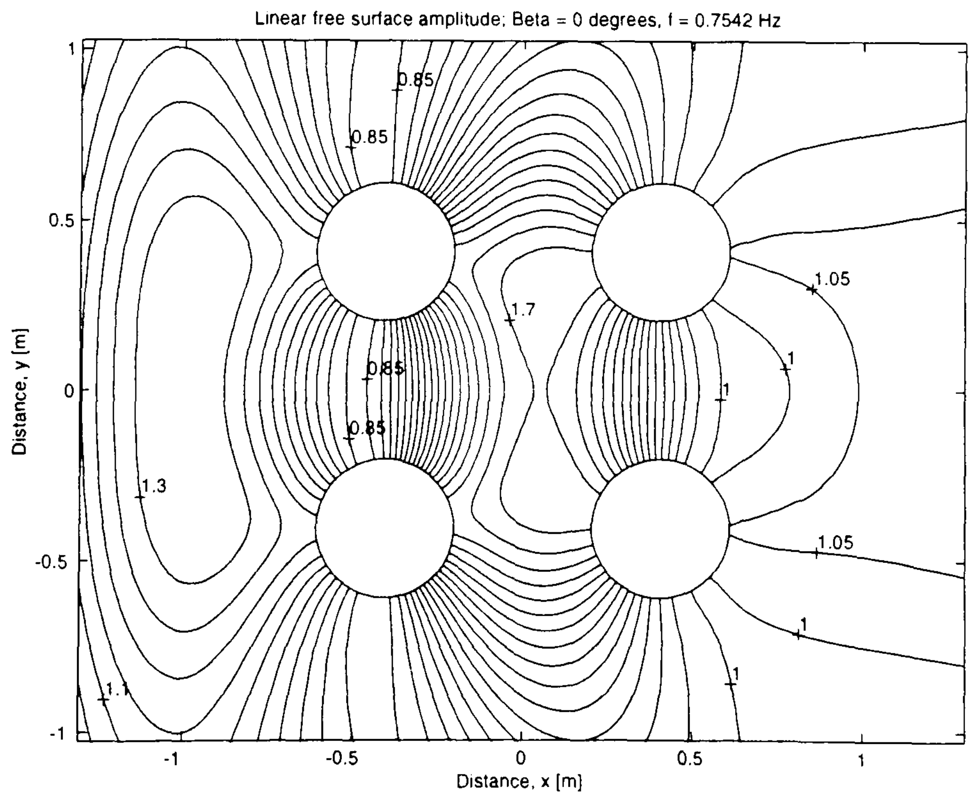

Figure 5.8. Linear free surface amplitude; $\beta = 0°$, $f = 0.7542$ Hz

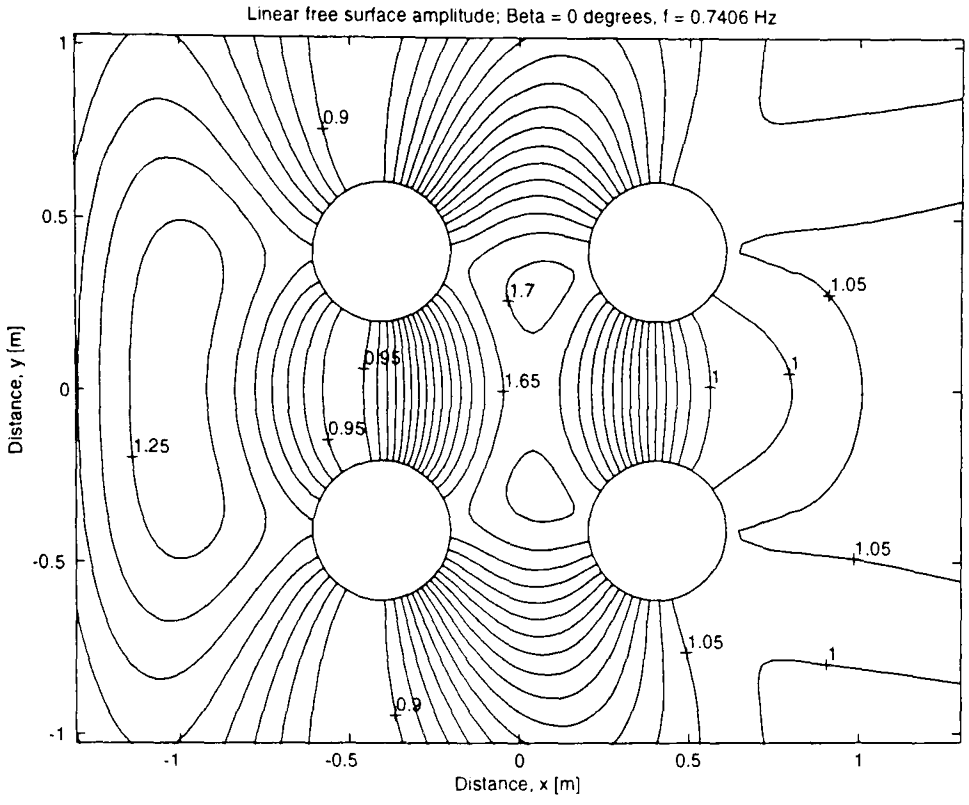

Figure 5.9. Linear free surface amplitude; $\beta = 0°$, $f = 0.7406$ Hz

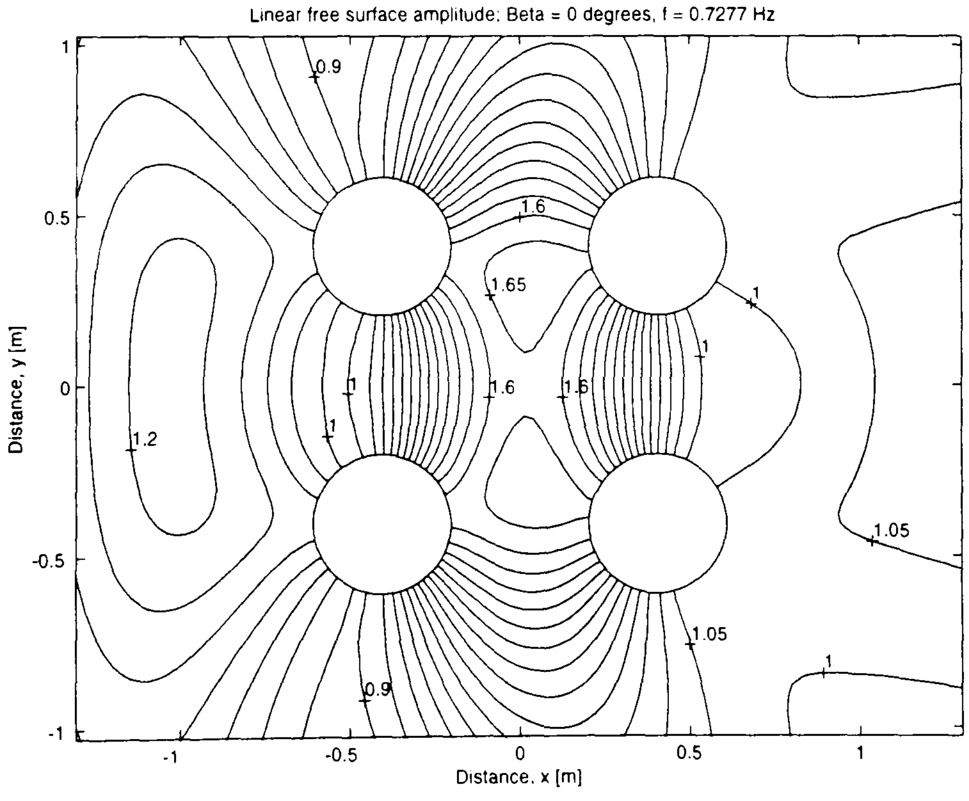

Figure 5.10. Linear free surface amplitude; $\beta = 0°$, $f = 0.7277$ Hz

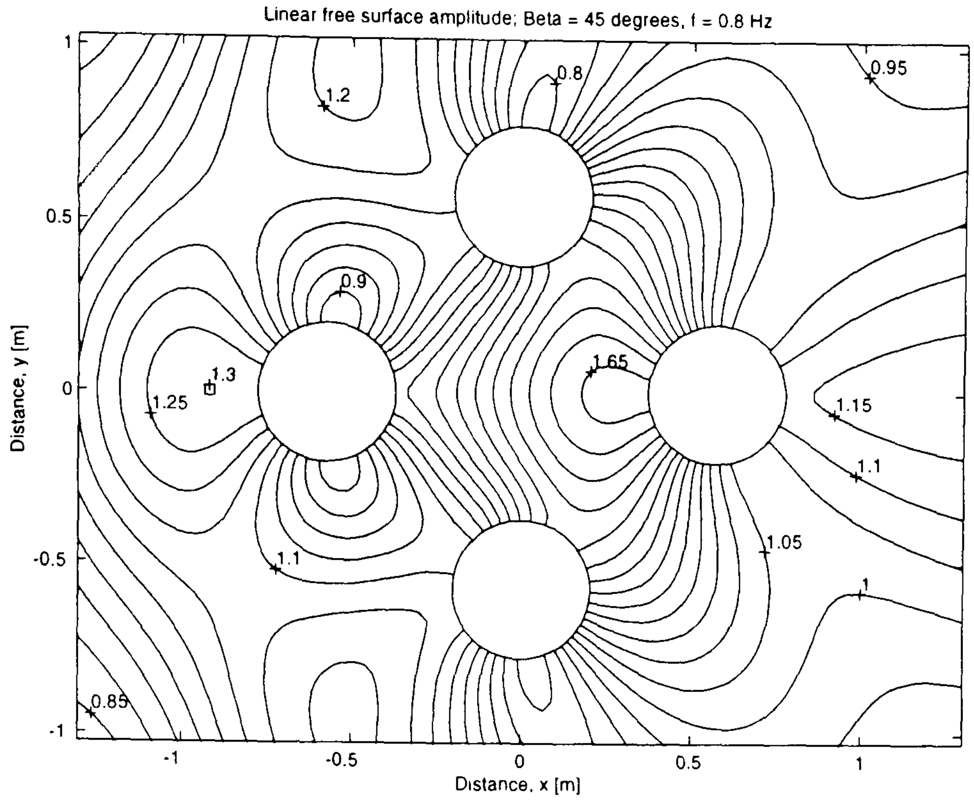

Figure 5.11. Linear free surface amplitude; $\beta = 45°$, $f = 0.8000$ Hz

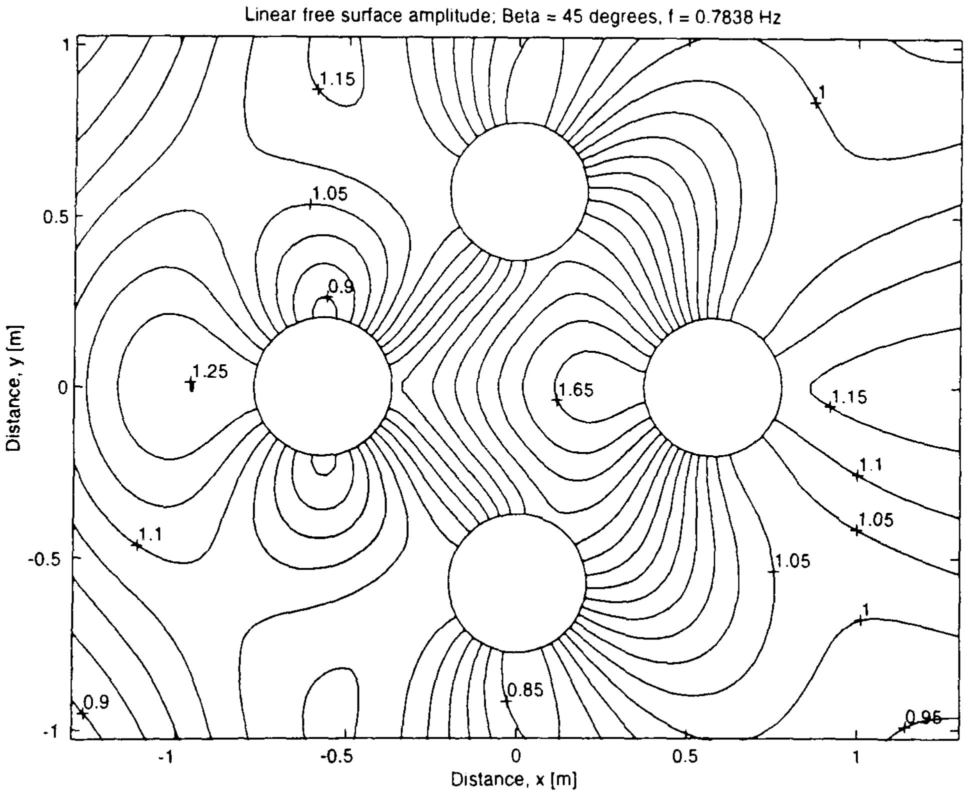

Figure 5.12. Linear free surface amplitude; $\beta = 45°$, $f = 0.7838$ Hz

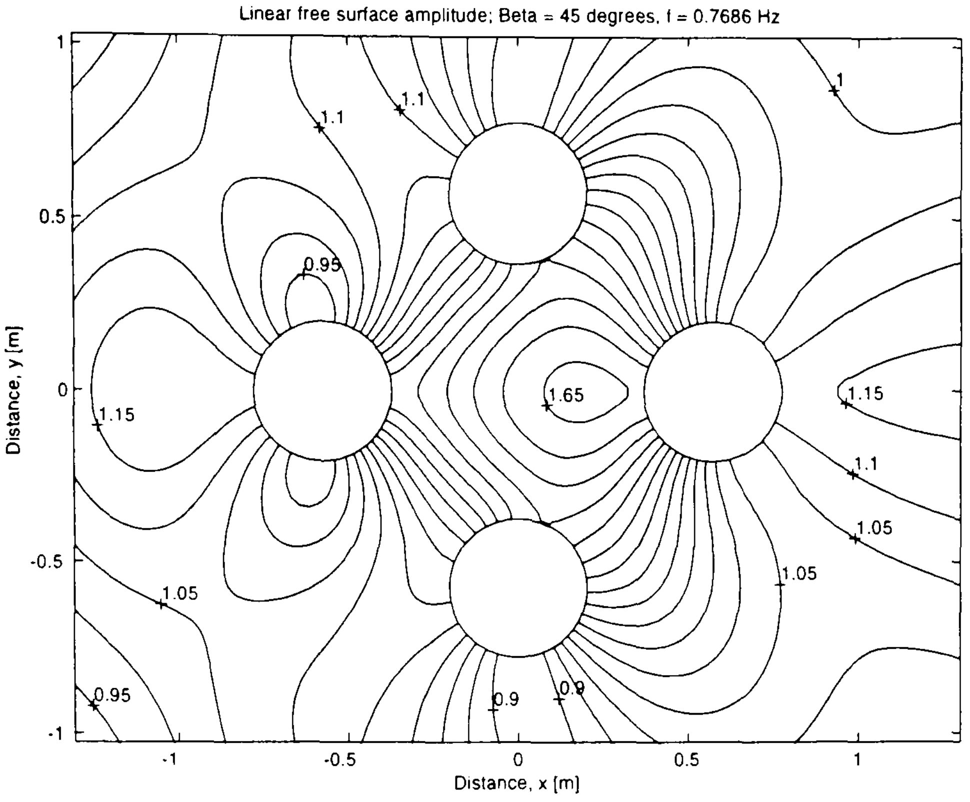

Figure 5.13. Linear free surface amplitude; $\beta = 45°$, $f = 0.7686$ Hz

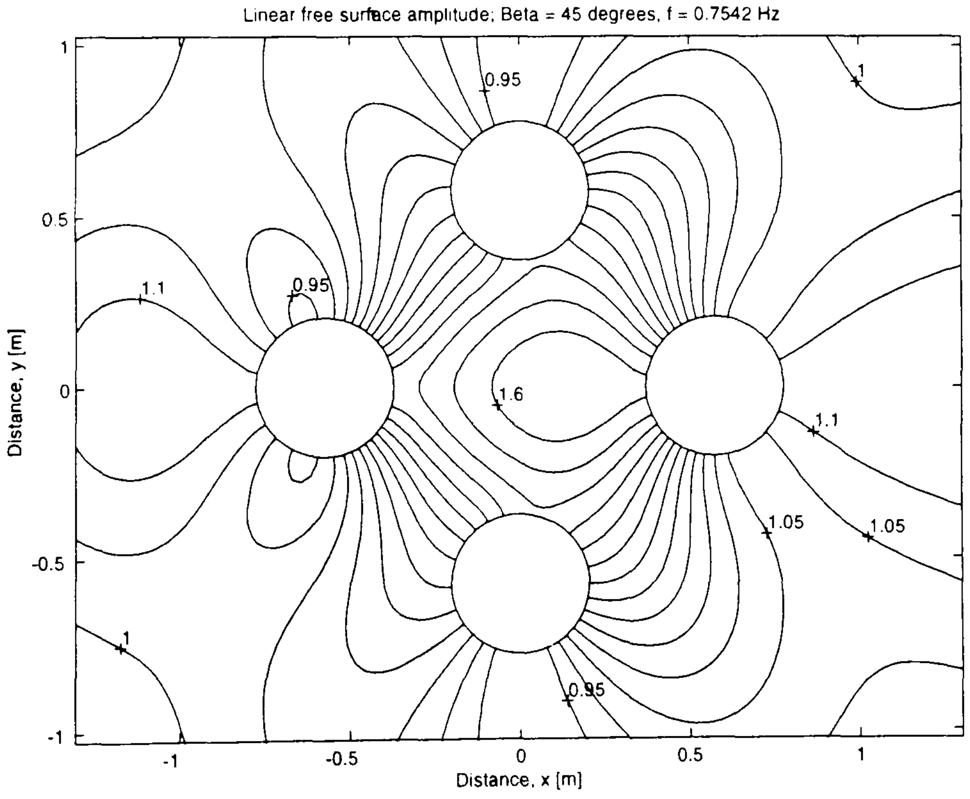

Figure 5.14. Linear free surface amplitude; $\beta = 45°$, $f = 0.7542$ Hz

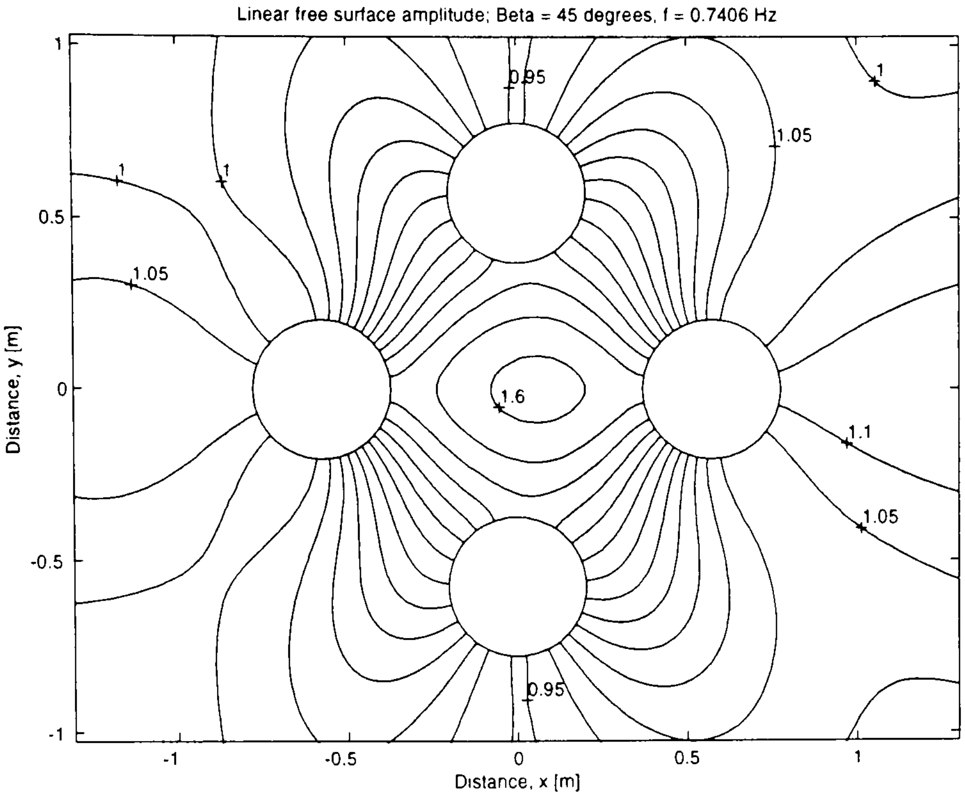

Figure 5.15. Linear free surface amplitude; $\beta = 45°$, $f = 0.7406$ Hz

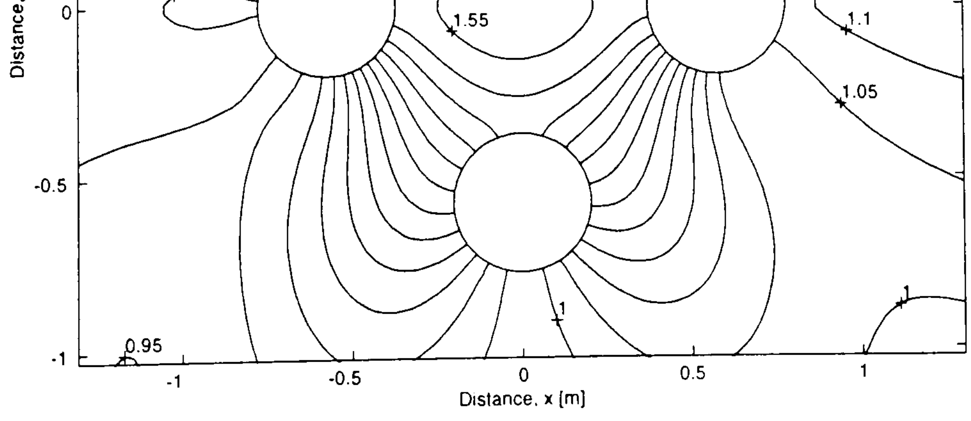

Figure 5.16. Linear free surface amplitude; $\beta = 45°$, $f = 0.7277$ Hz

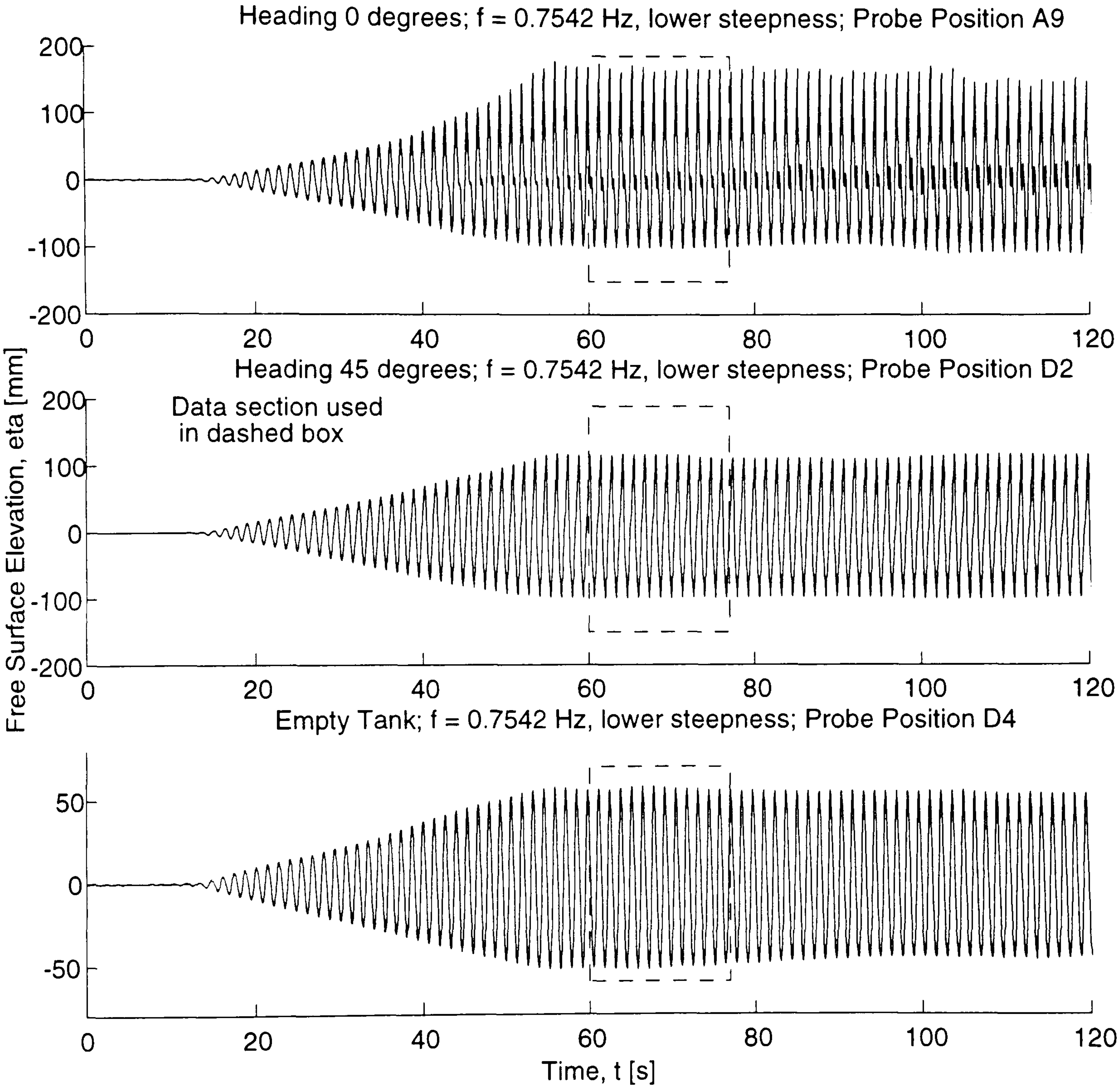

Figure 5.17. Free surface elevation vs. time for the entire data record; $\beta = 0^\circ, 45^\circ$ and the empty tank case, $f = 0.7542$ Hz, lower steepness case; from locations near the tank centre

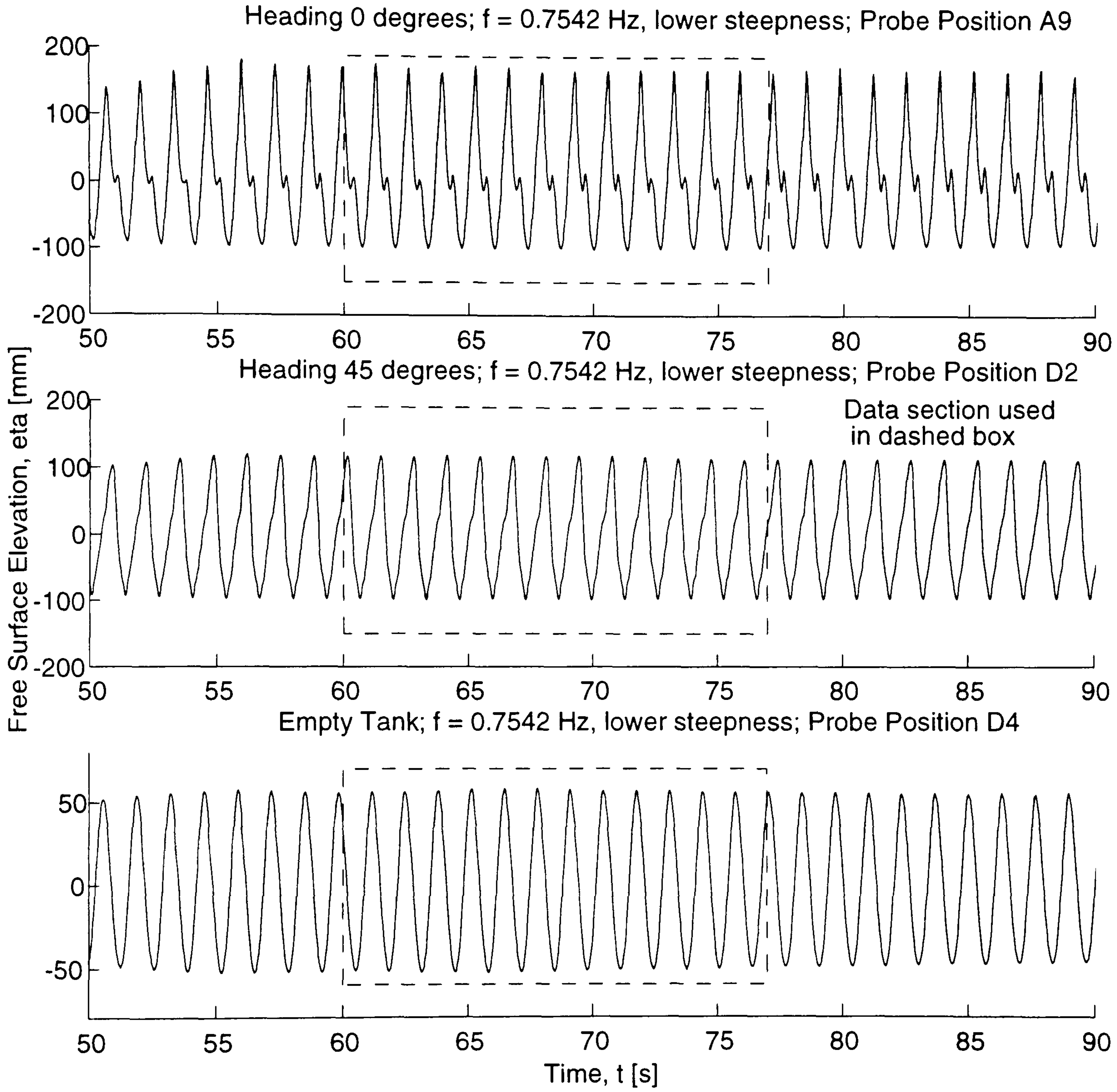

Figure 5.18. Free surface elevation vs. time for partial data record; $\beta = 0^\circ, 45^\circ$ and the empty tank case, $f =$ 0.7542 Hz, lower steepness case; from locations near the tank centre

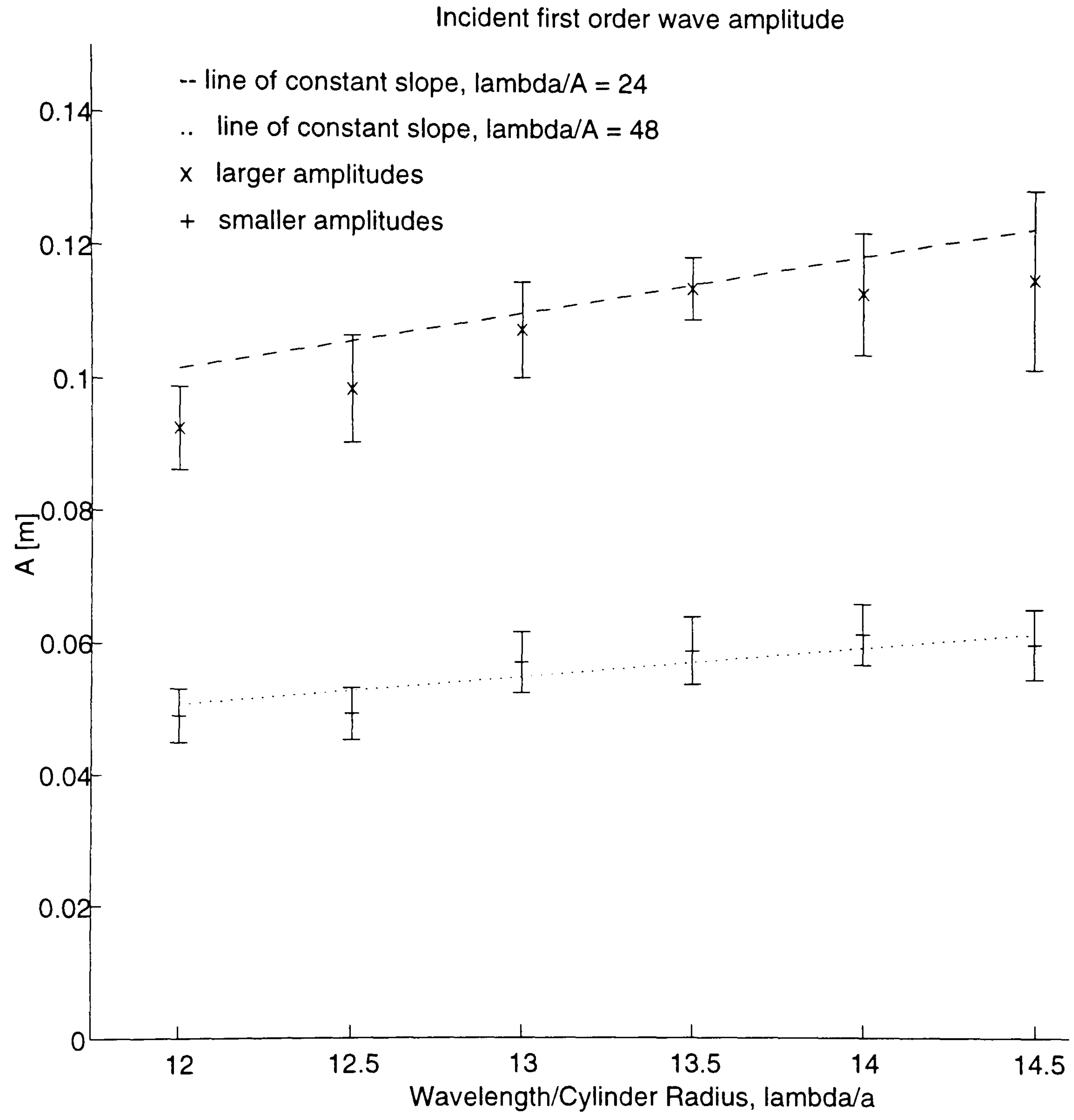

Figure 5.19. Incident amplitude definition; first order amplitude versus wavelength

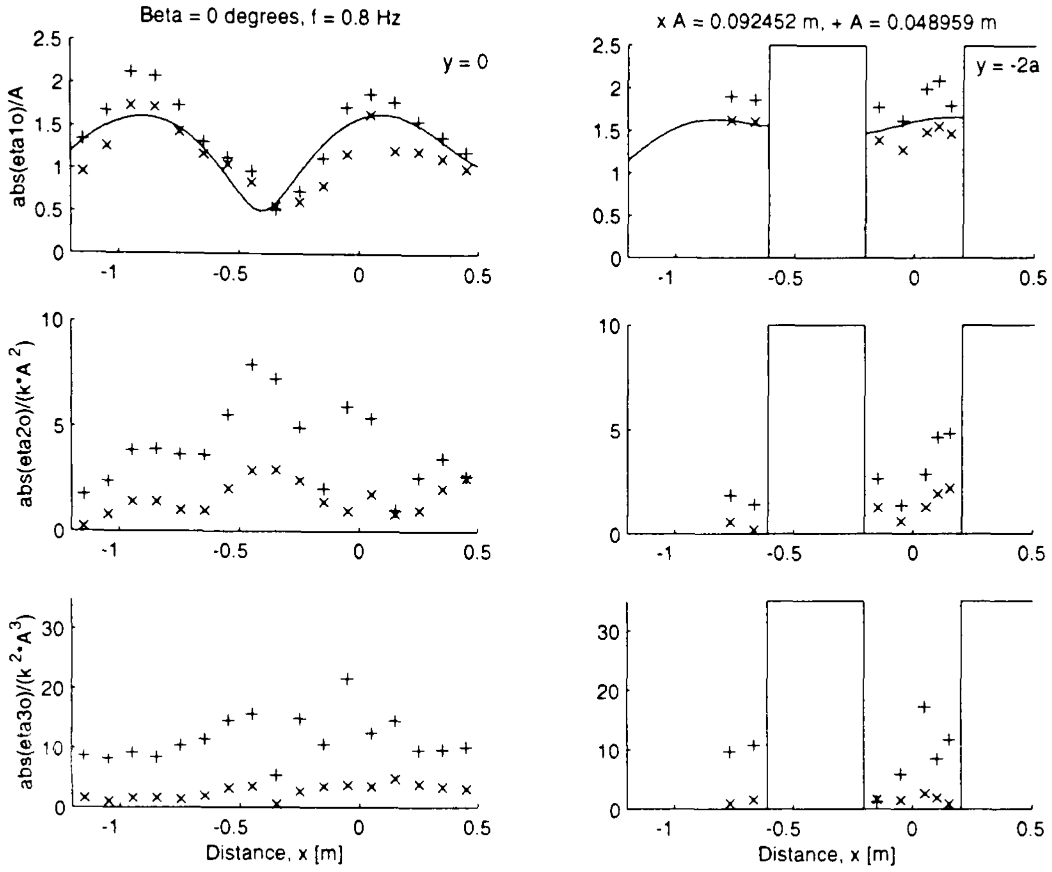

Figure 5.20. Amplitude versus position; $\beta = 0°$, $f = 0.8000$ Hz

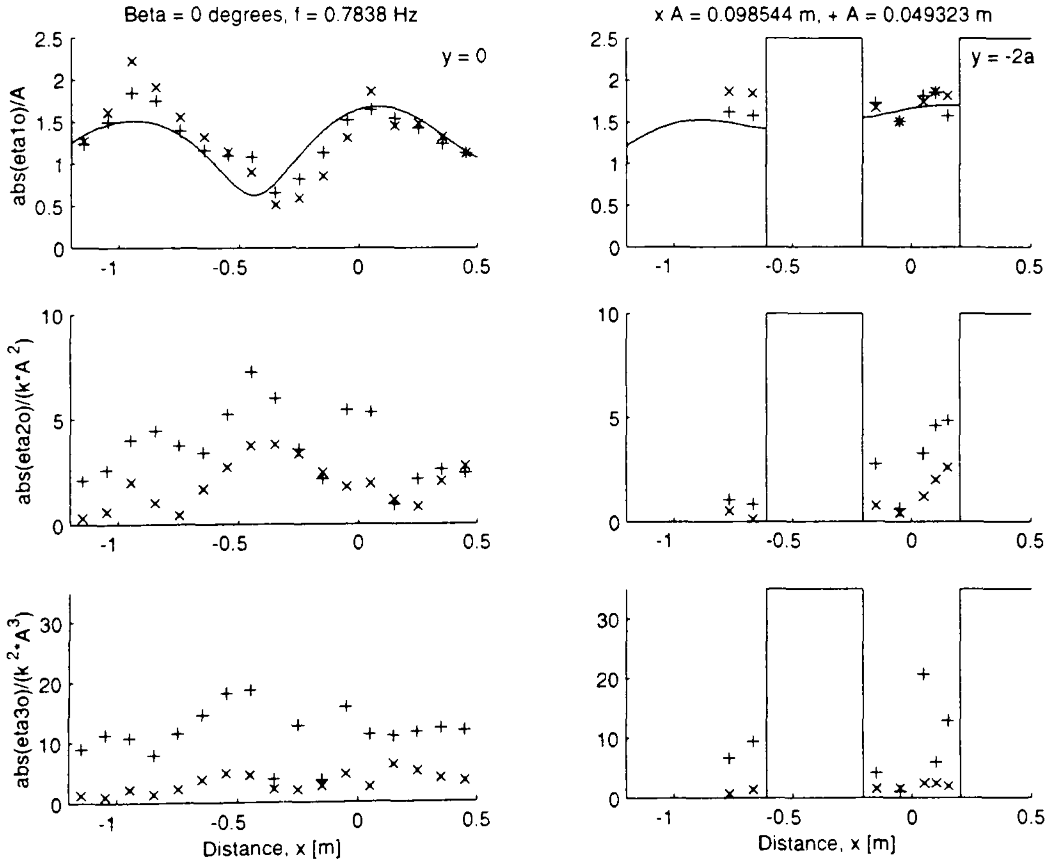

Figure 5.21. Amplitude versus position; $\beta = 0°$, $f = 0.7838$ Hz

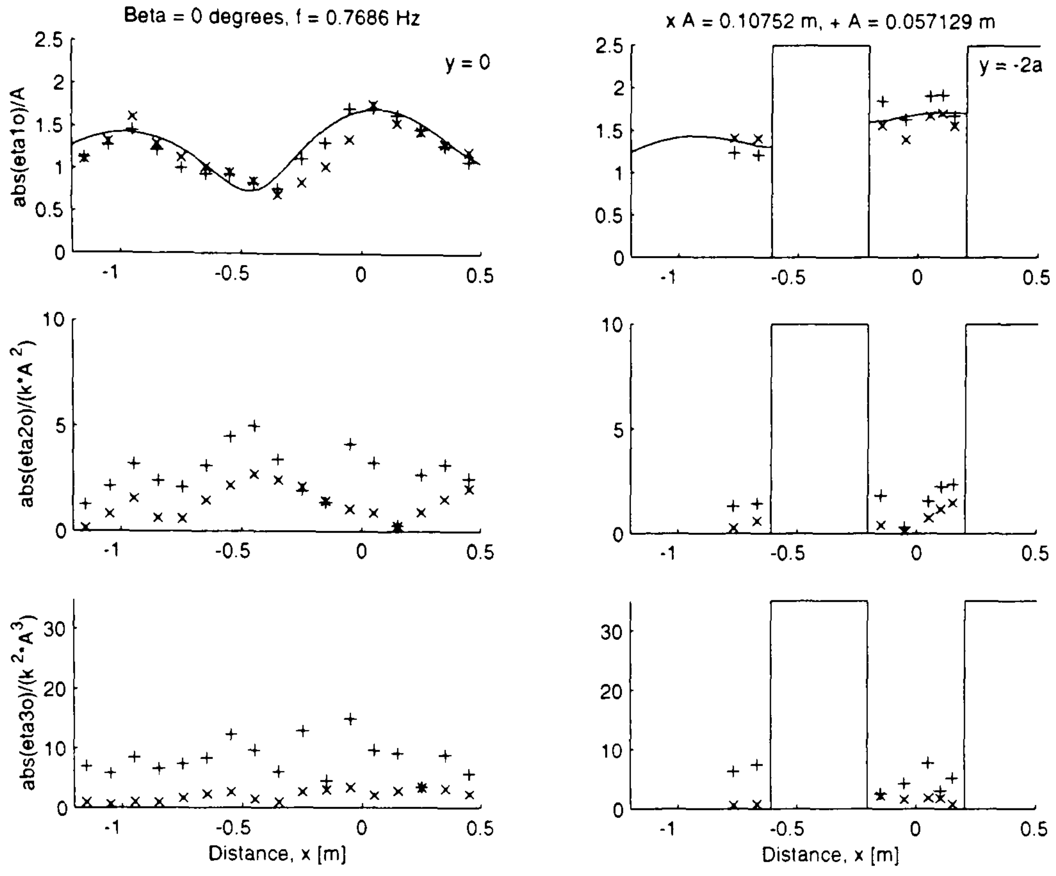

Figure 5.22. Amplitude versus position; $\beta = 0°$, $f = 0.7686$ Hz

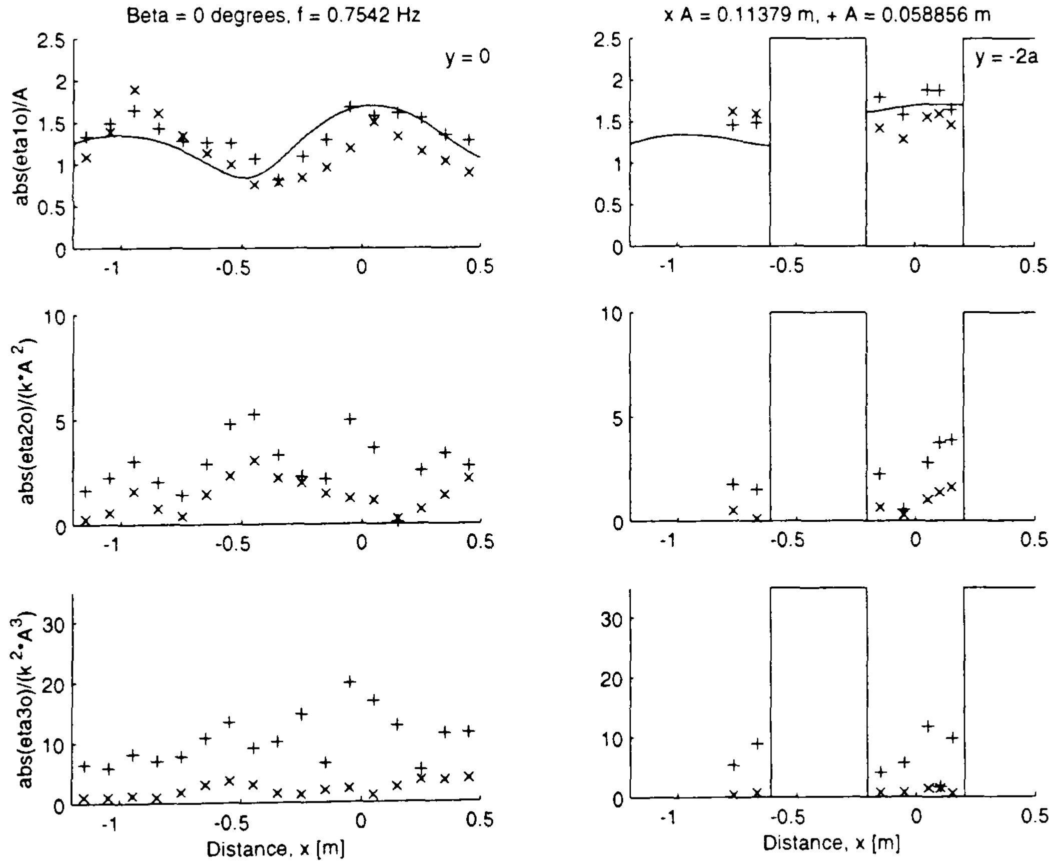

Figure 5.23. Amplitude versus position; $\beta = 0°$, $f = 0.7542$ Hz

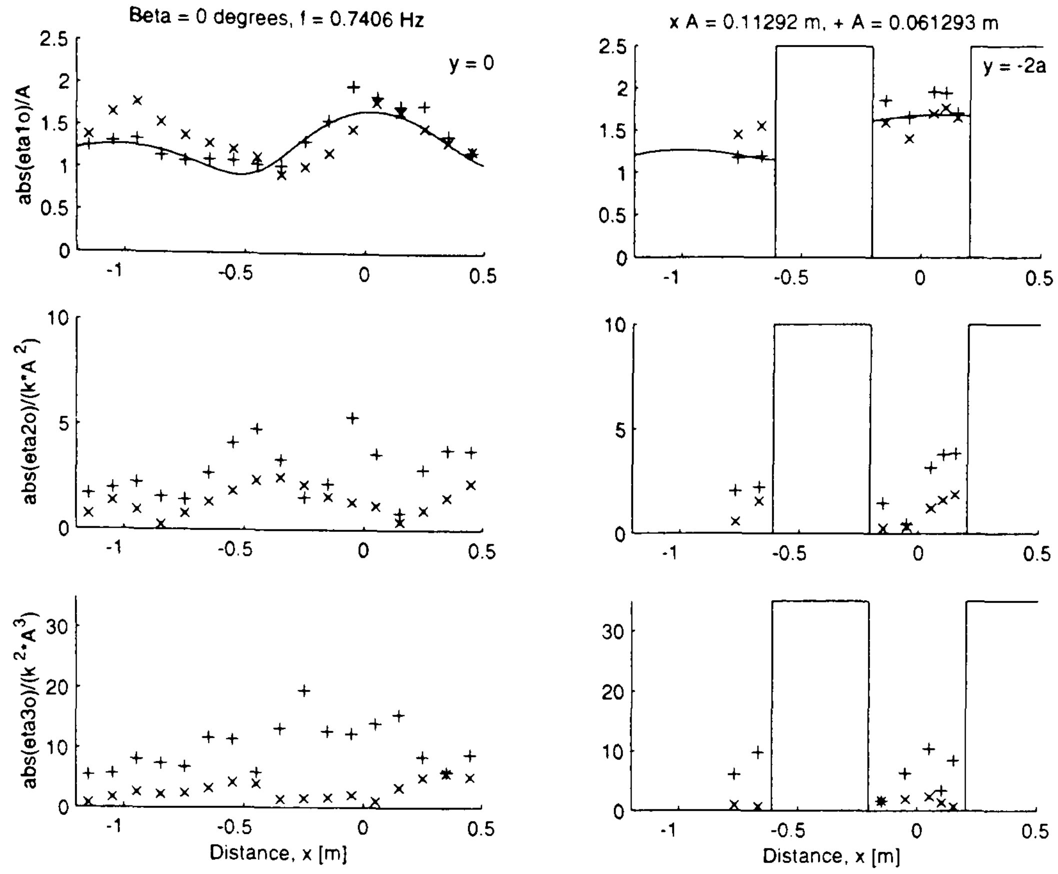

Figure 5.24. Amplitude versus position; $\beta = 0°$, $f = 0.7406$ Hz

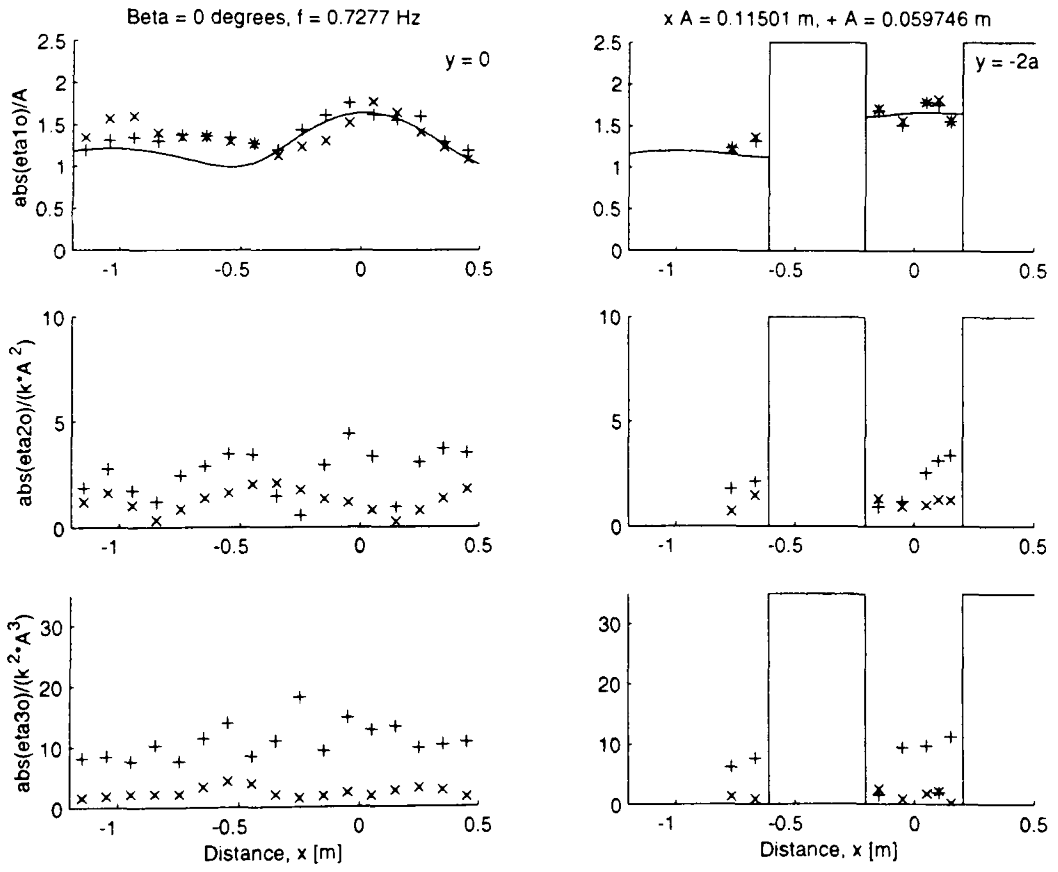

Figure 5.25. Amplitude versus position; $\beta = 0°$, $f = 0.7277$ Hz

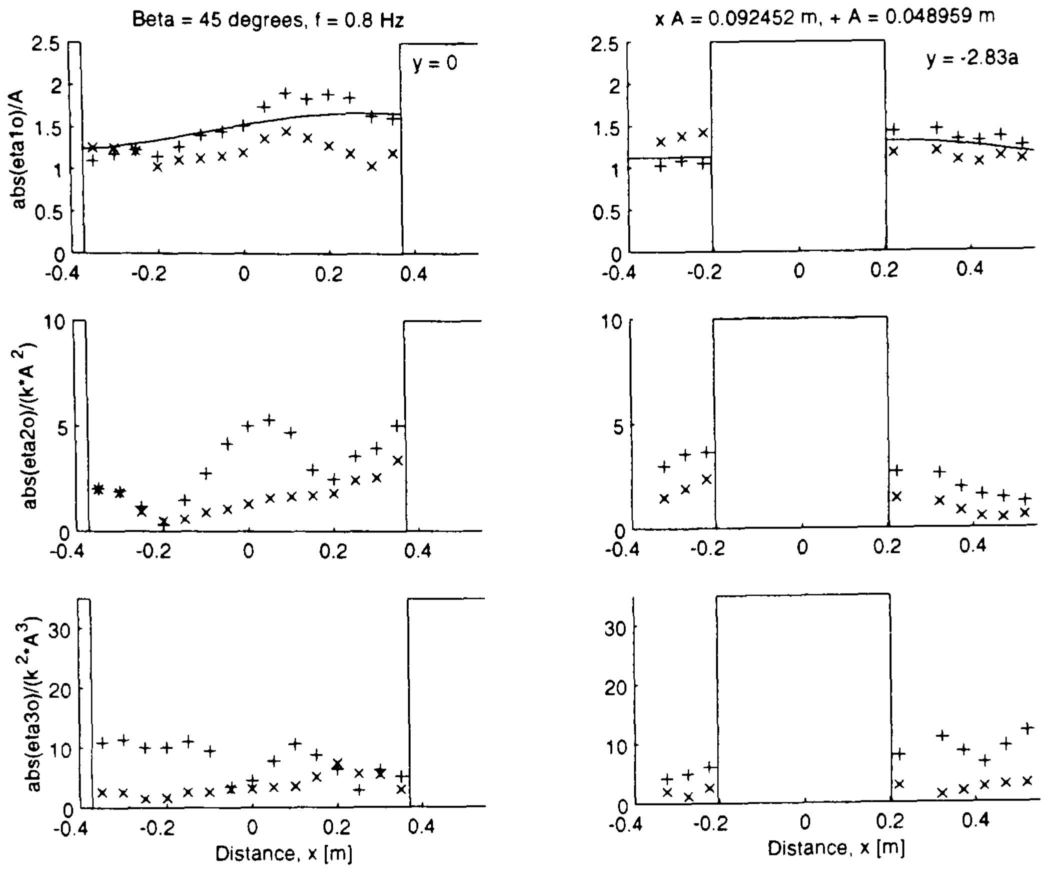

Figure 5.26. Amplitude versus position; $\beta = 45°$, $f = 0.8000$ Hz

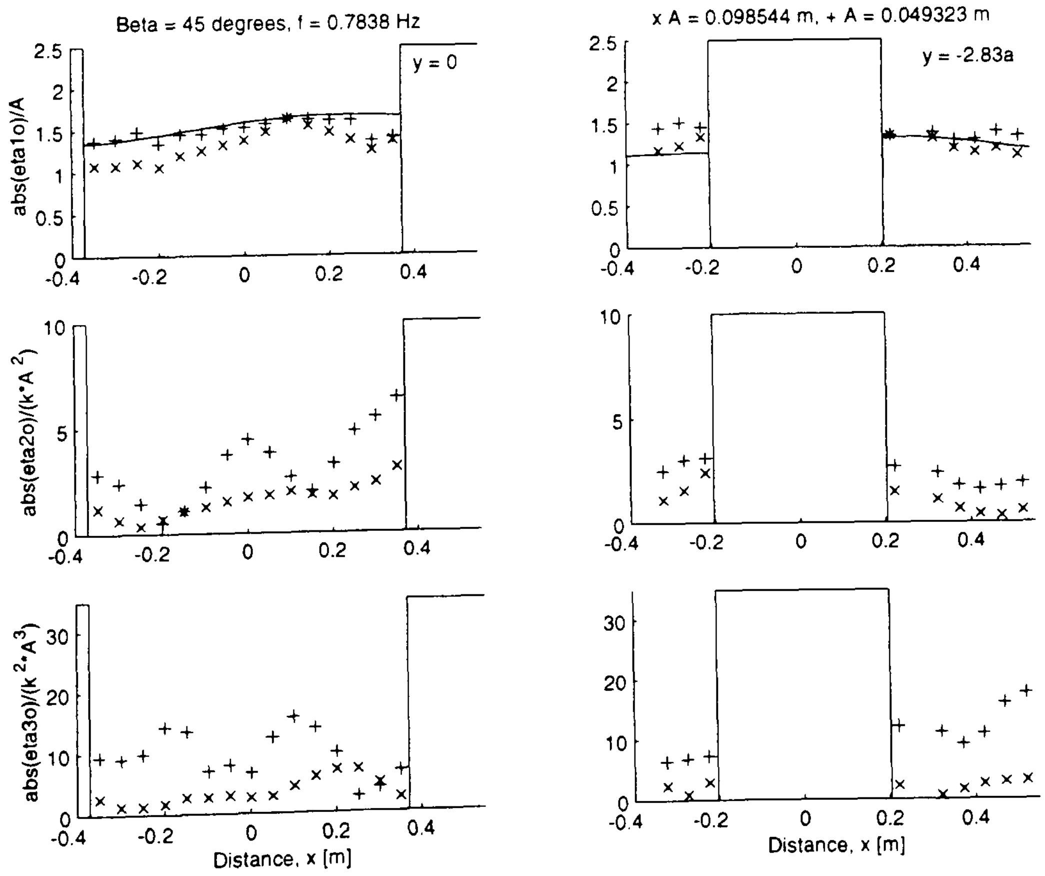

Figure 5.27. Amplitude versus position; $\beta = 45°$, $f = 0.7838$ Hz

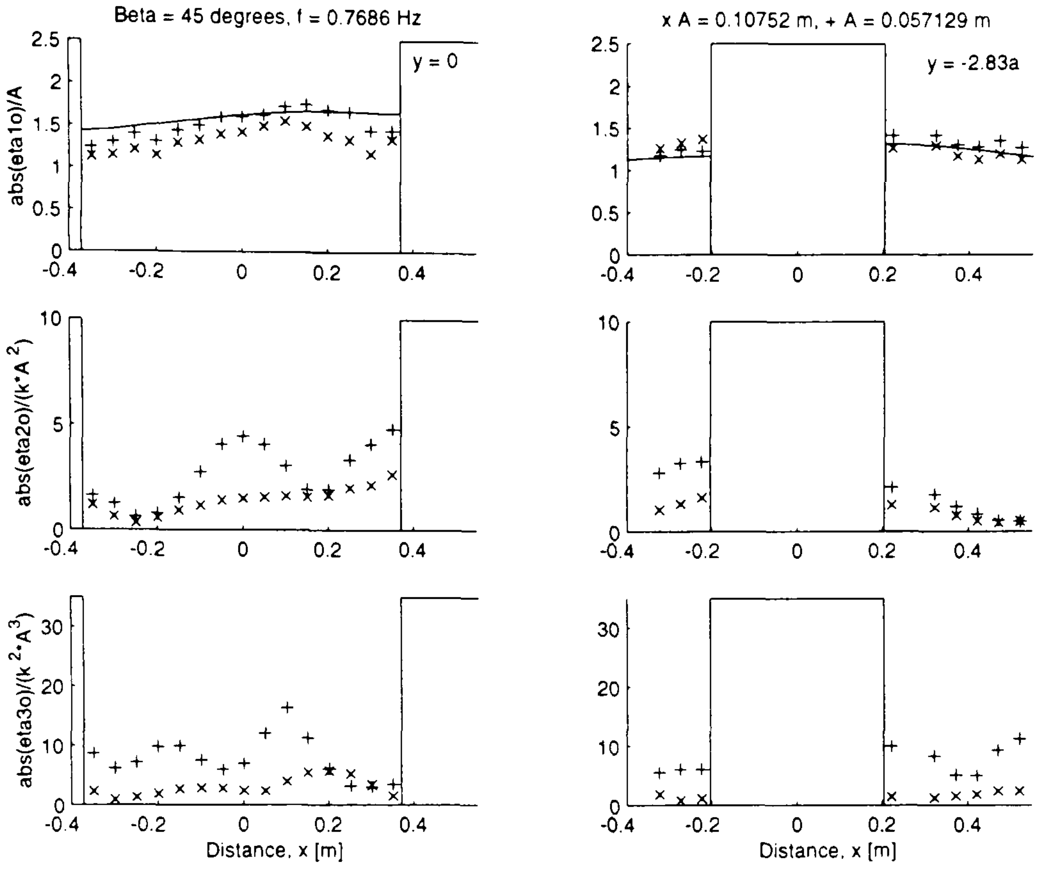

Figure 5.28. Amplitude versus position; $\beta = 45°$, $f = 0.7686$ Hz

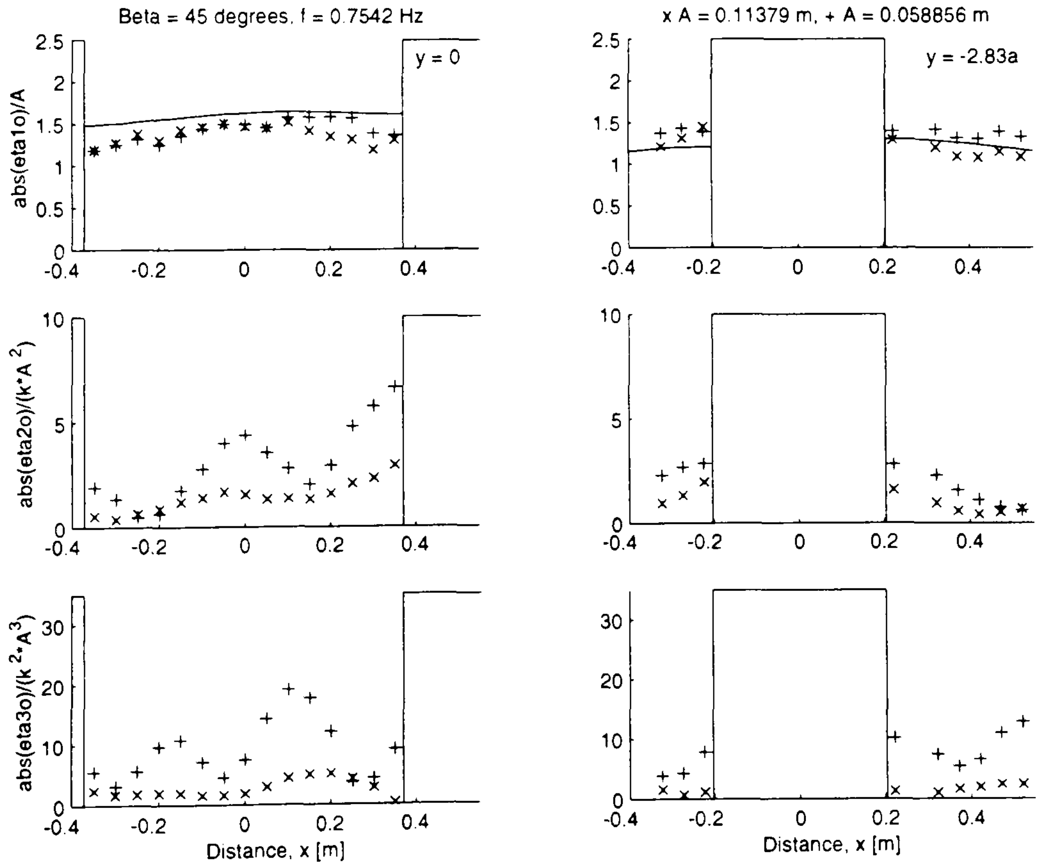

Figure 5.29. Amplitude versus position; $\beta = 45°$, $f = 0.7542$ Hz

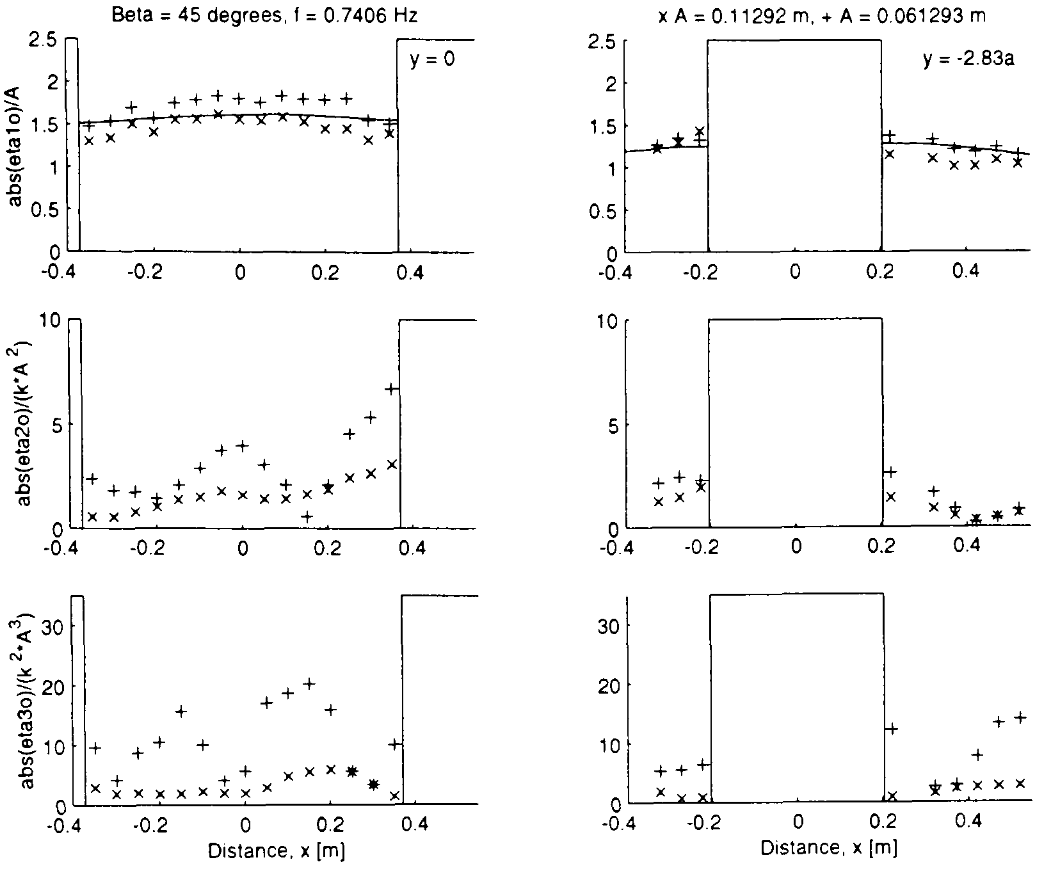

Figure 5.30. Amplitude versus position; $\beta = 45°$, $f = 0.7406$ Hz

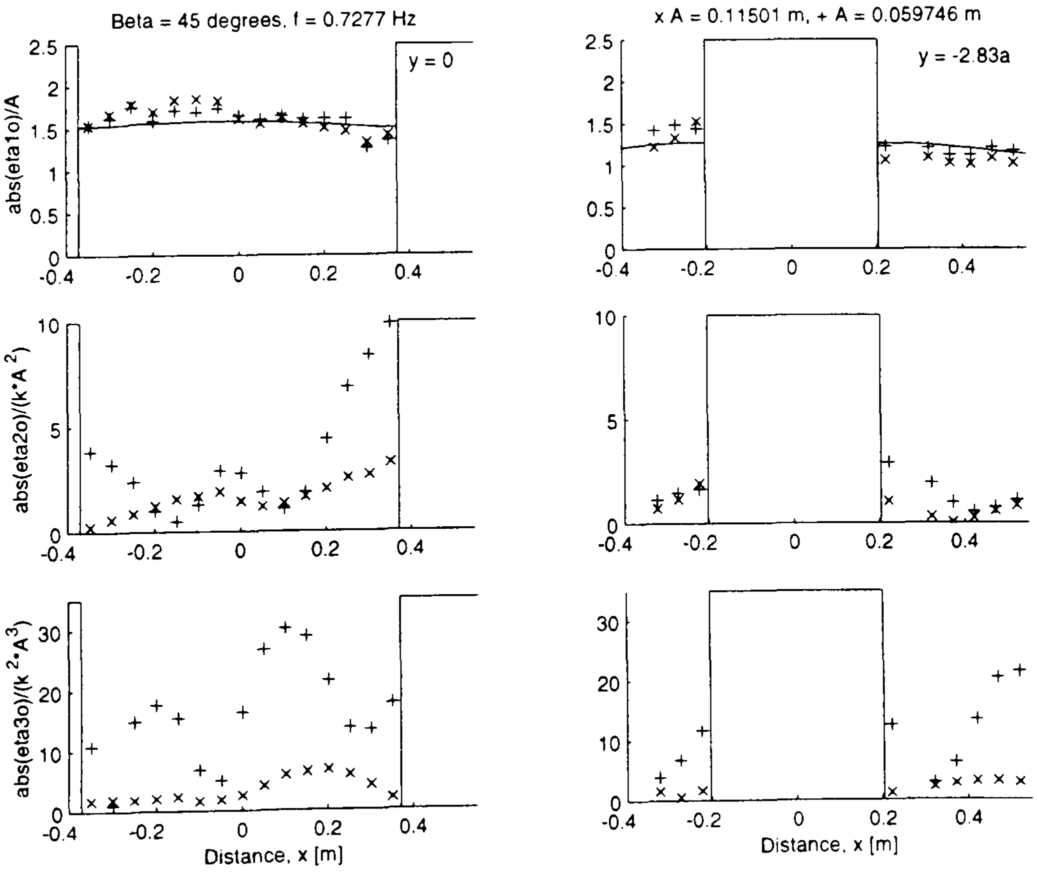

Figure 5.31. Amplitude versus position; $\beta = 45°$, $f = 0.7277$ Hz

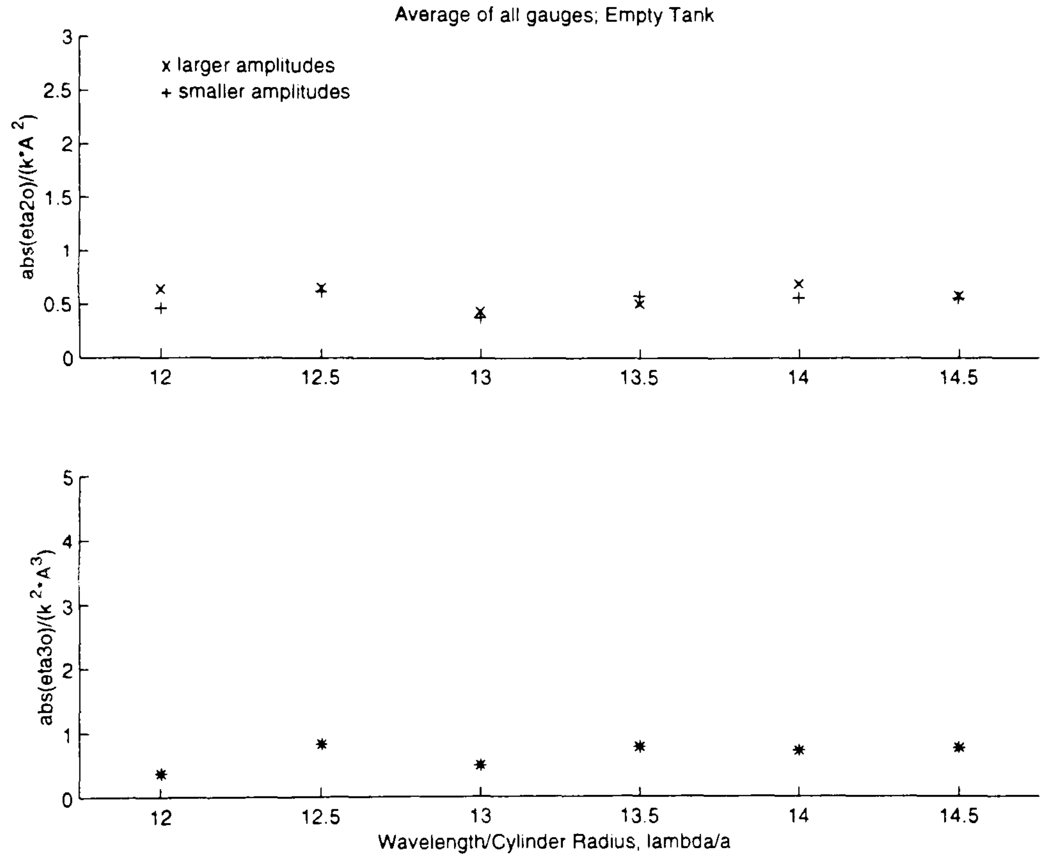

Figure 5.32. Second and third order amplitude versus nondimensionalised wavelength; empty tank

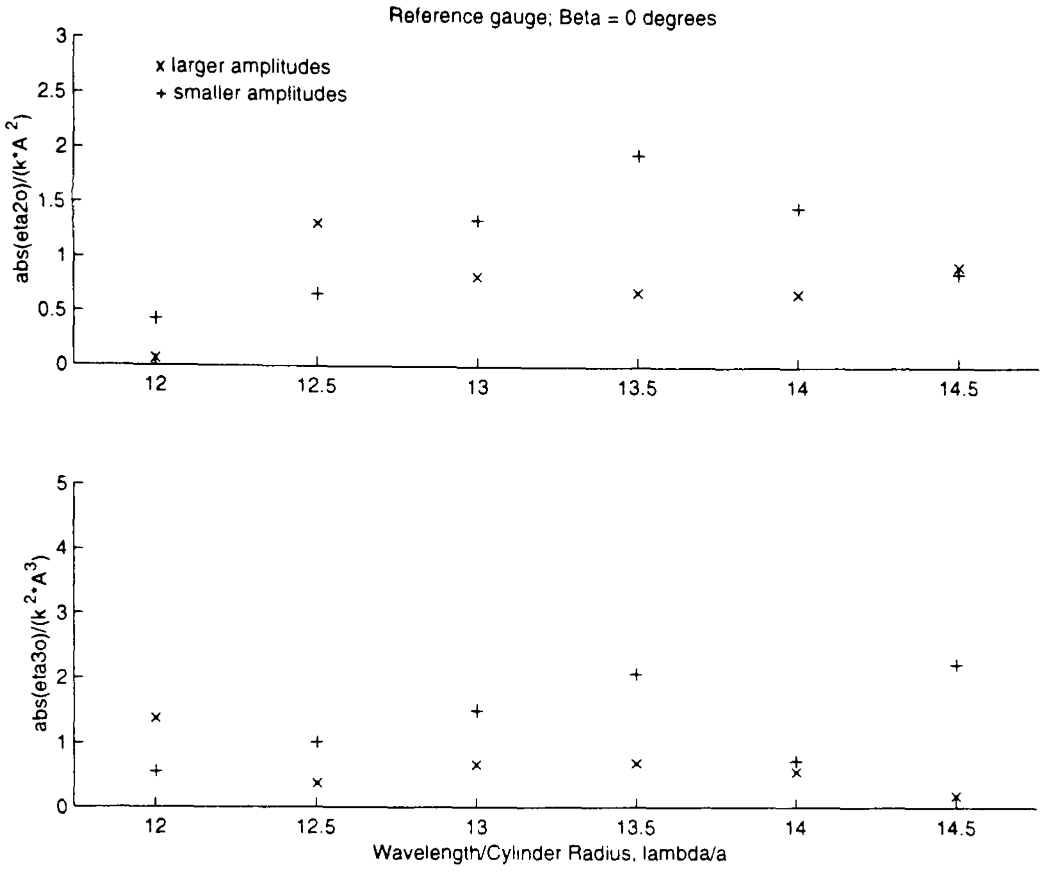

Figure 5.33. Second and third order amplitude versus nondimensionalised wavelength; $\beta = 0°$

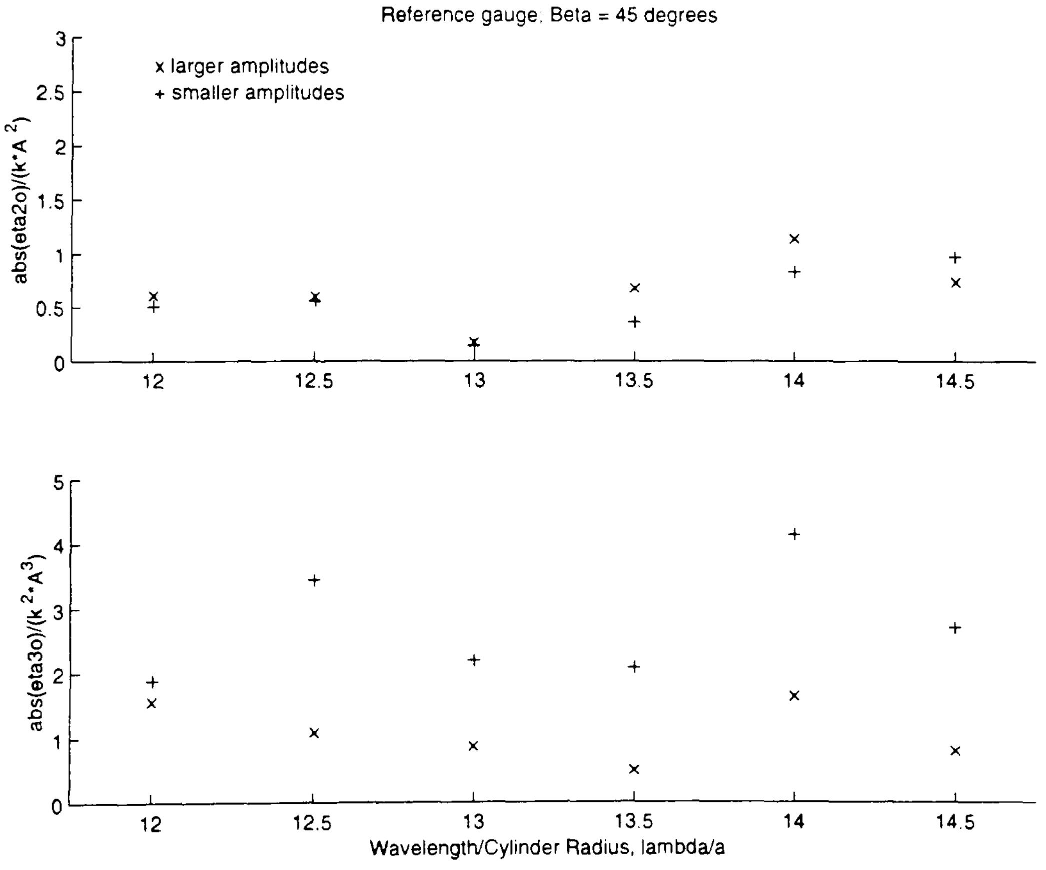

Figure 5.34. Second and third order amplitude versus nondimensionalised wavelength; $\beta = 45°$

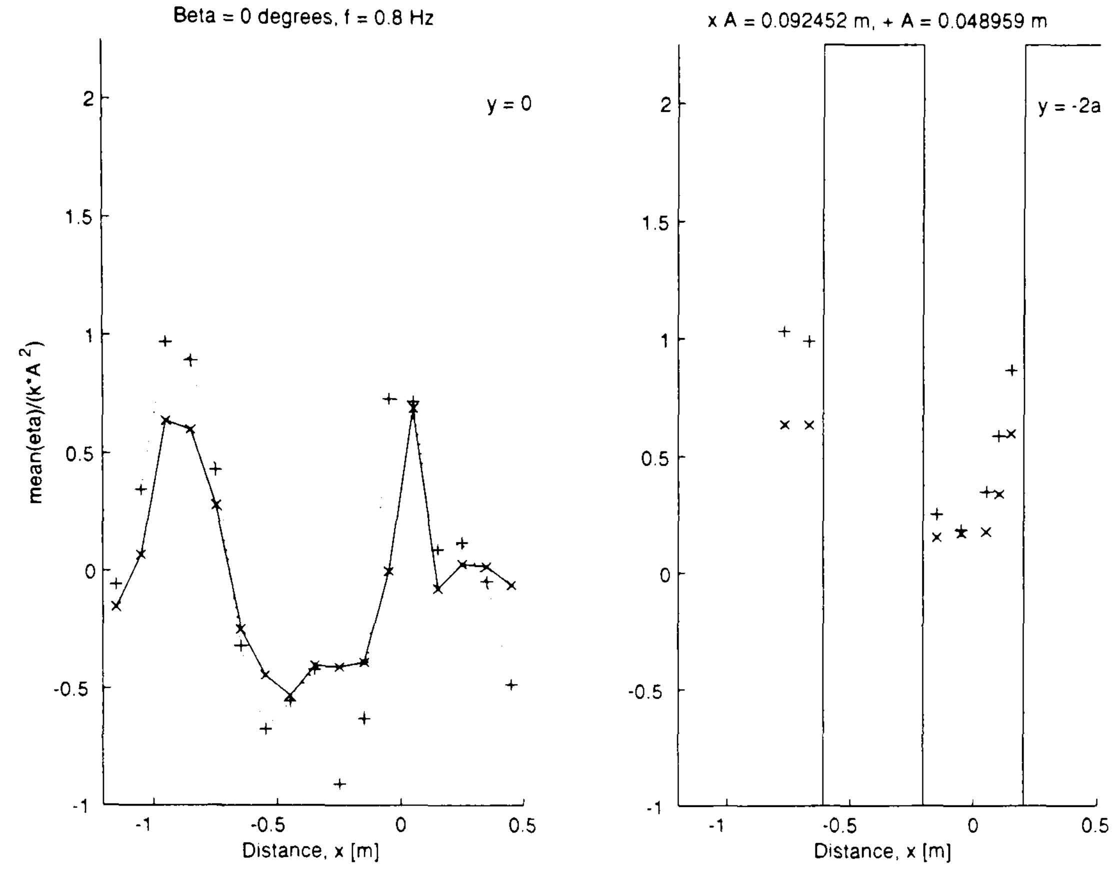

Figure 5.35. Set down versus position; $\beta = 0°$, $f = 0.8000$ Hz

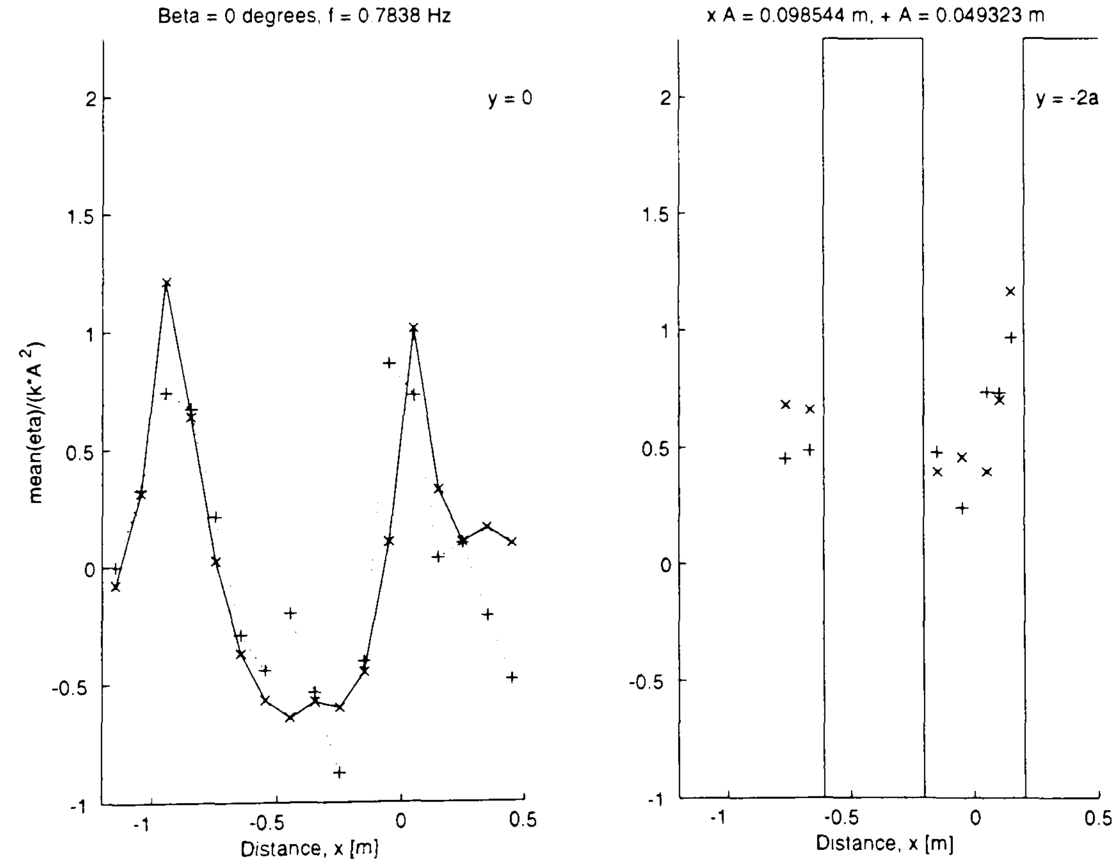

Figure 5.36. Set down versus position; $\beta = 0°$, $f = 0.7838$ Hz

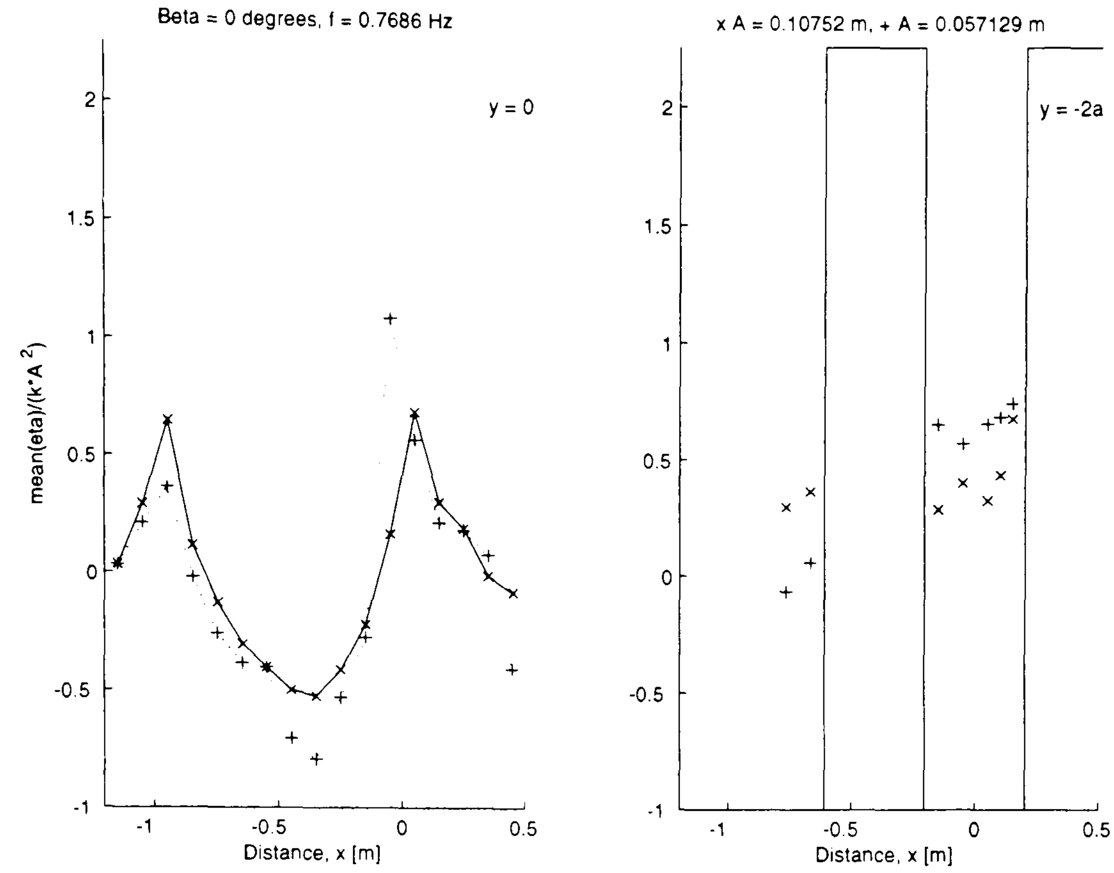

Figure 5.37. Set down versus position; $\beta = 0°$, $f = 0.7686$ Hz

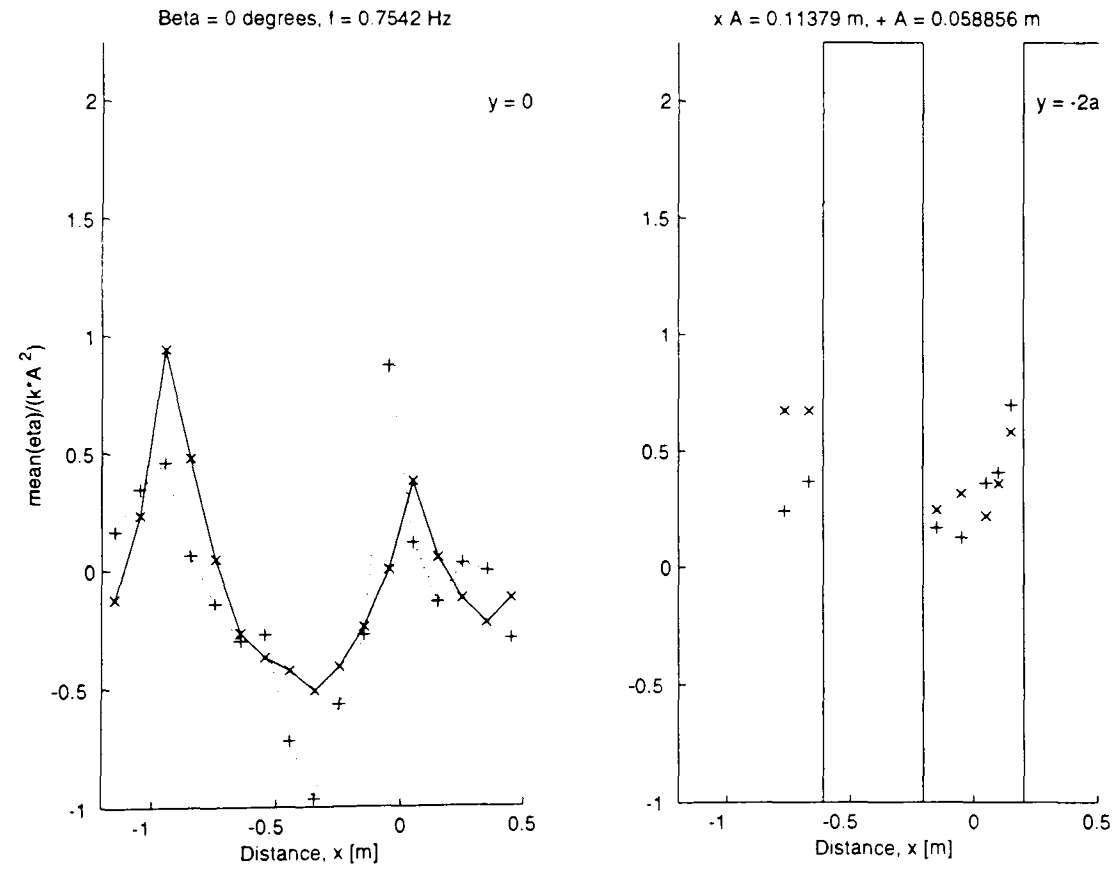

Figure 5.38. Set down versus position; $\beta = 0°$, $f = 0.7542$ Hz

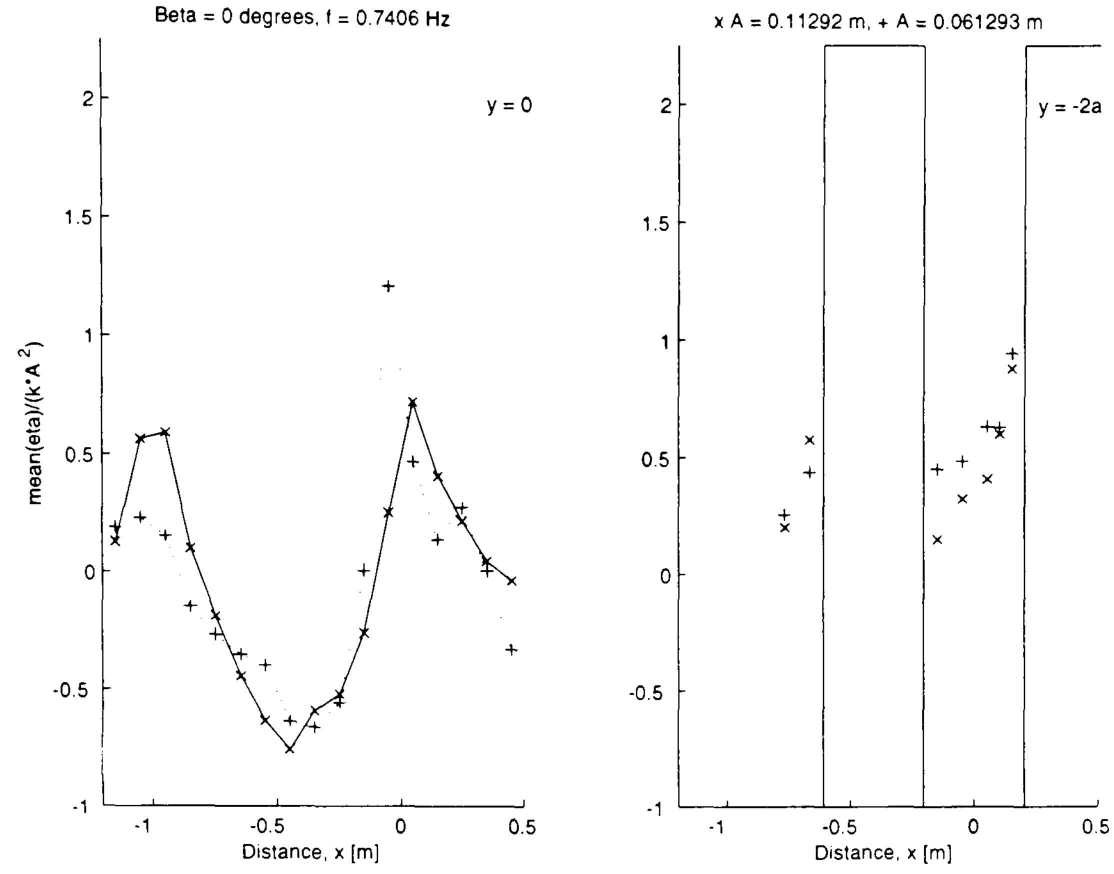

Figure 5.39. Set down versus position; $\beta = 0°$, $f = 0.7406$ Hz

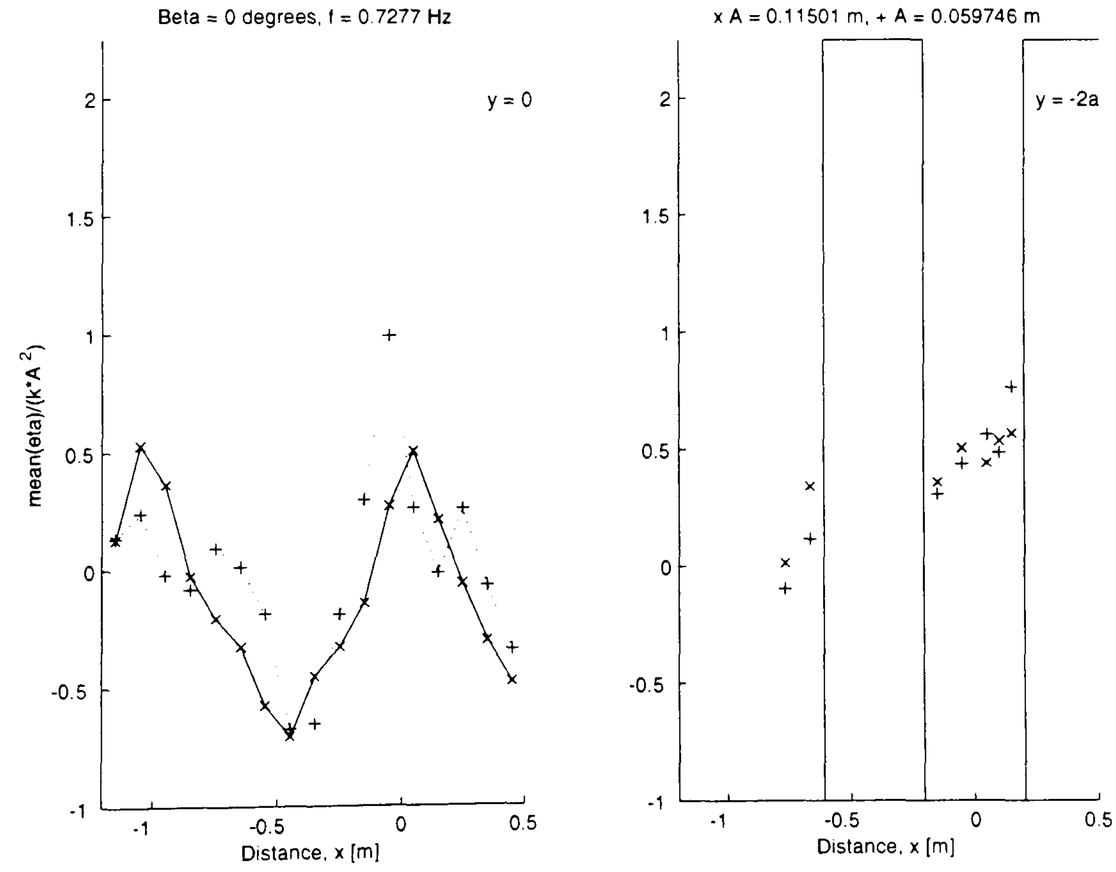

Figure 5.40. Set down versus position; $\beta = 0°$, $f = 0.7277$ Hz

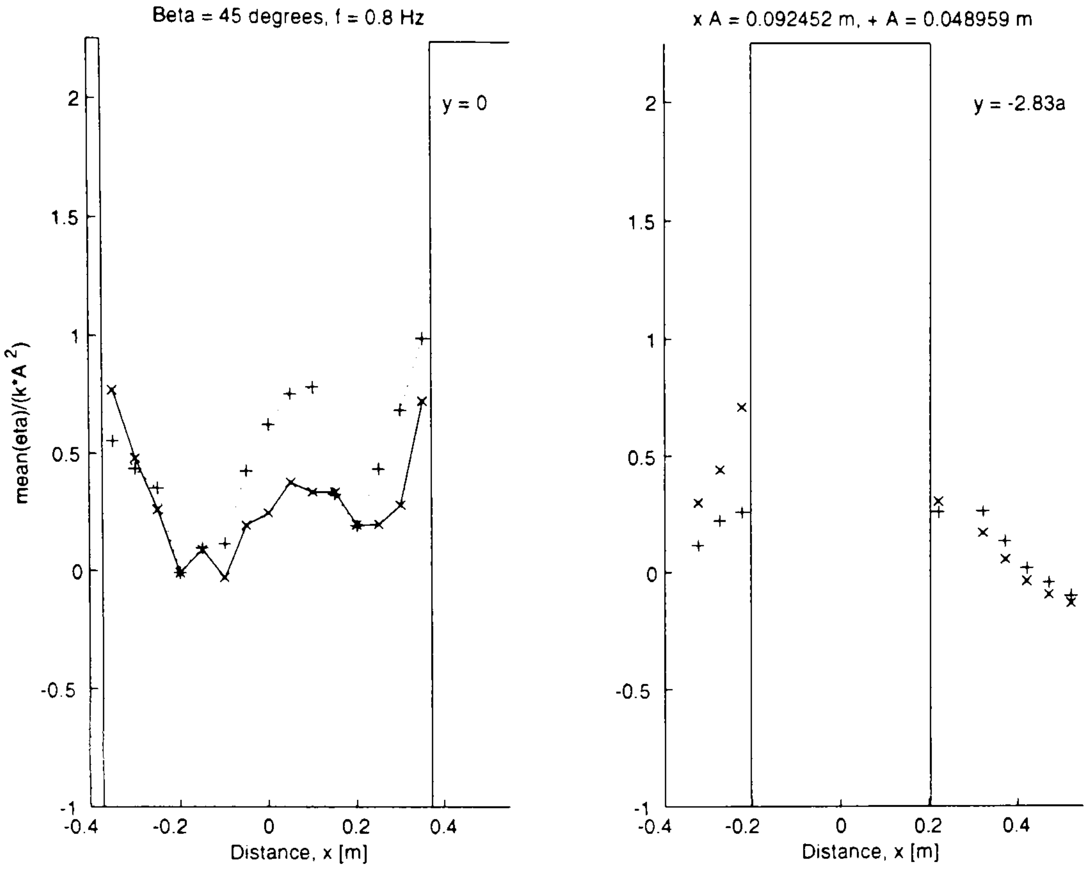

Figure 5.41. Set down versus position; $\beta = 45°$, $f = 0.8000$ Hz

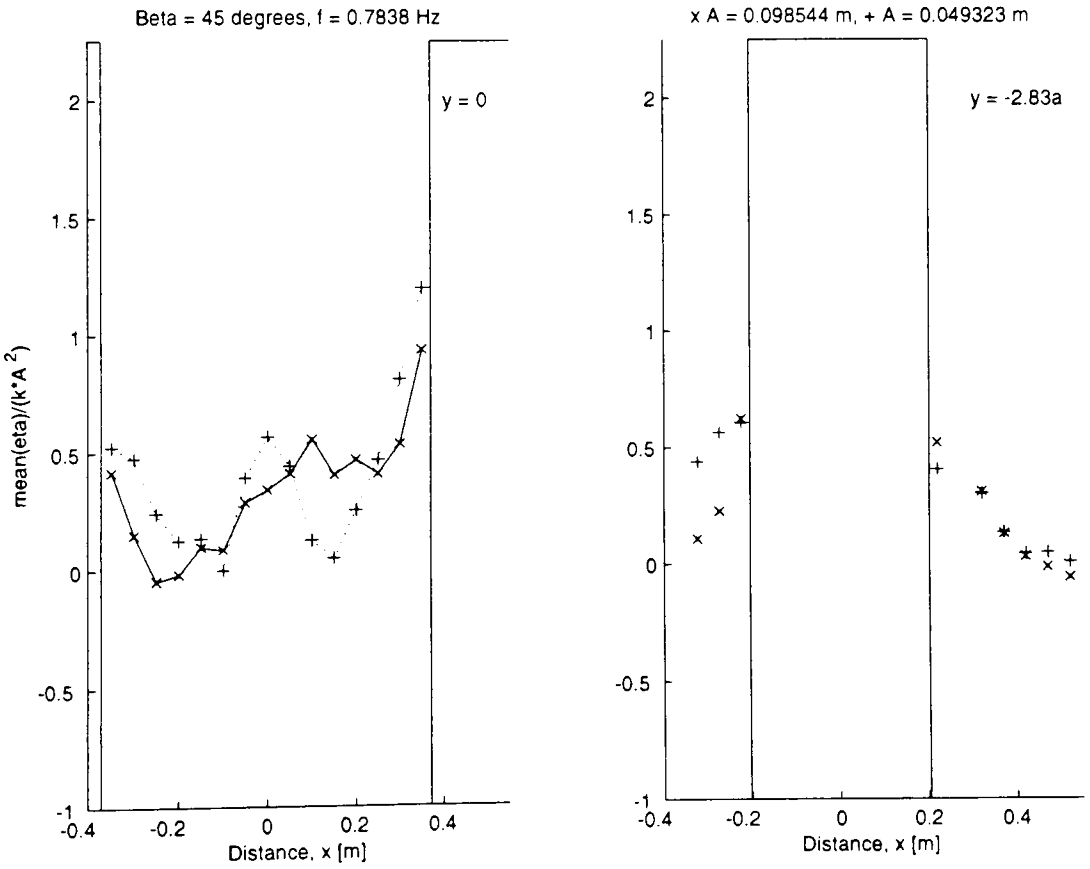

Figure 5.42. Set down versus position; $\beta = 45°$, $f = 0.7838$ Hz

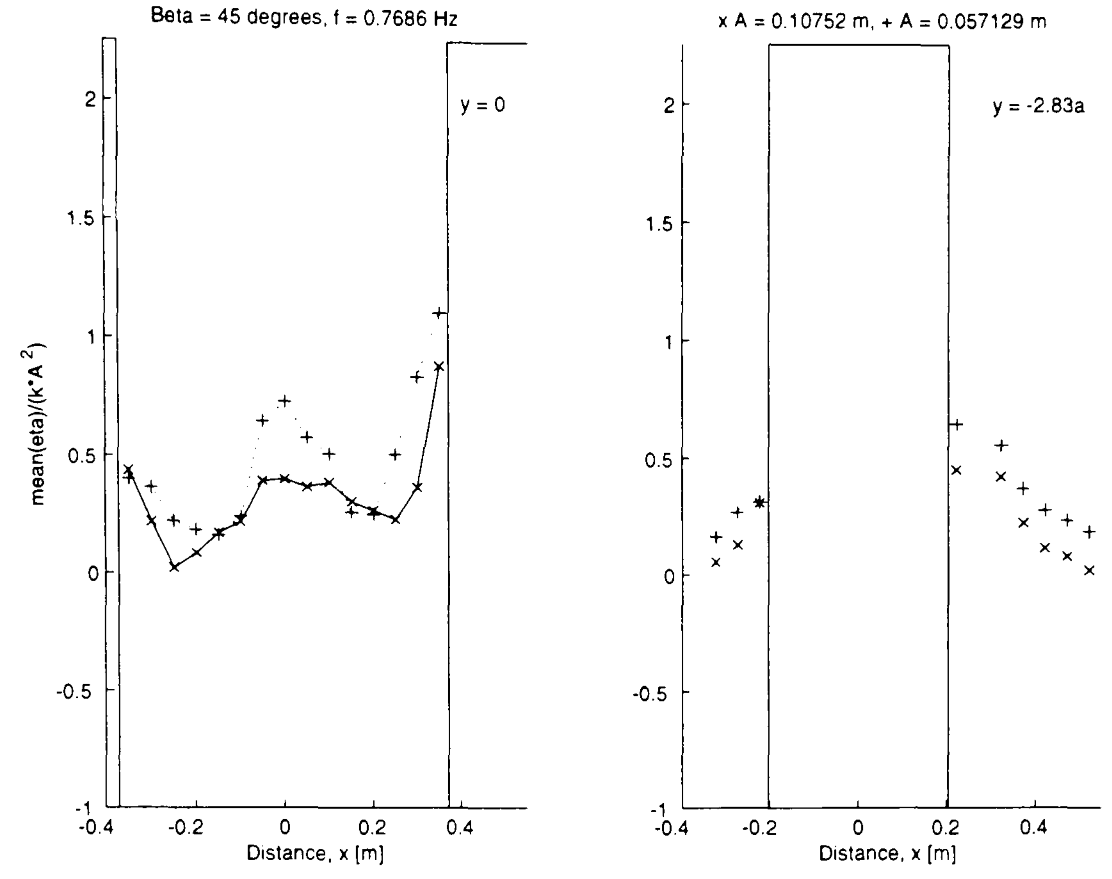

Figure 5.43. Set down versus position; $\beta = 45°$, $f = 0.7686$ Hz

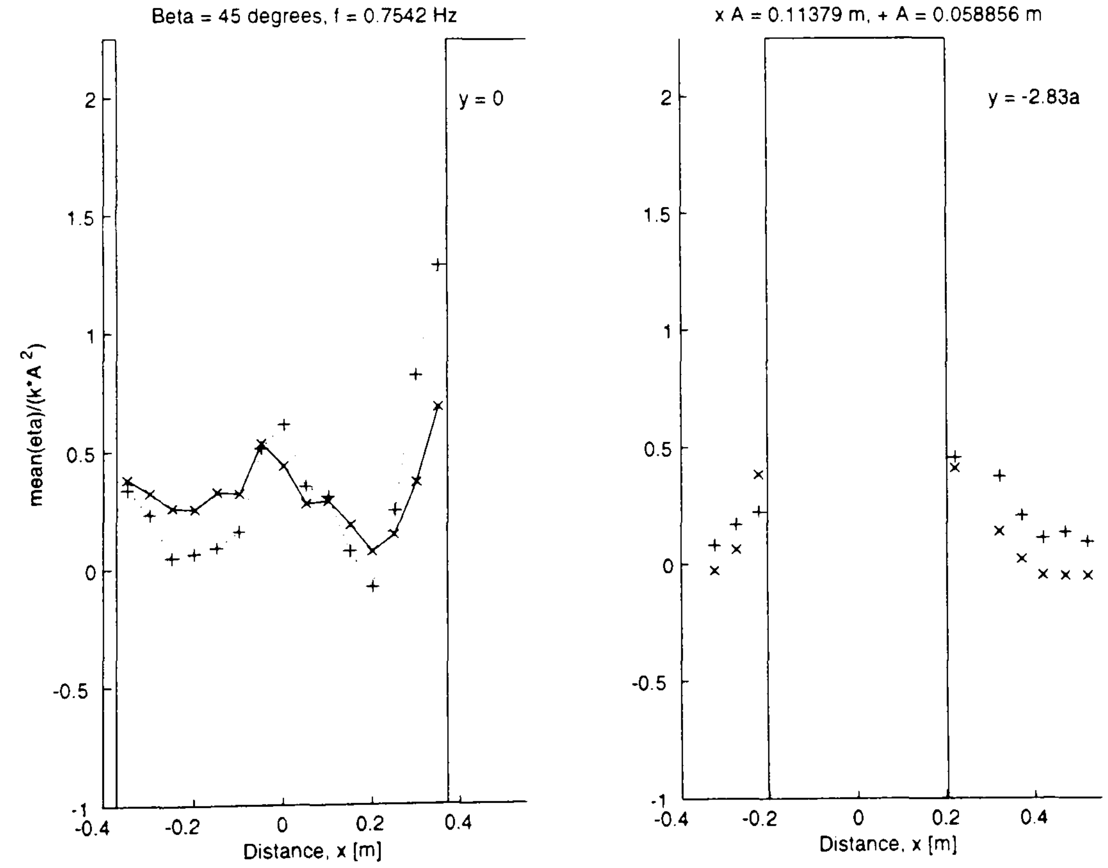

Figure 5.44. Set down versus position; $\beta = 45°$, $f = 0.7542$ Hz

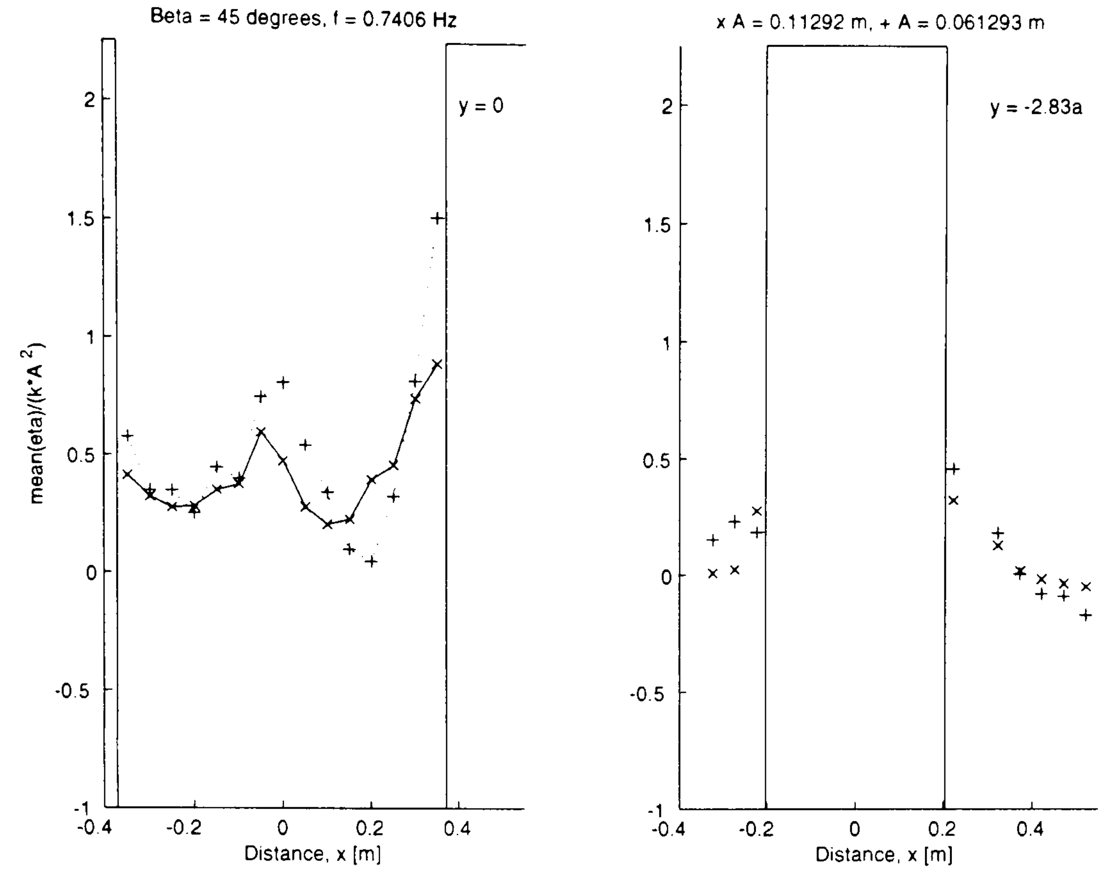

Figure 5.45. Set down versus position; $\beta = 45°$, $f = 0.7406$ Hz

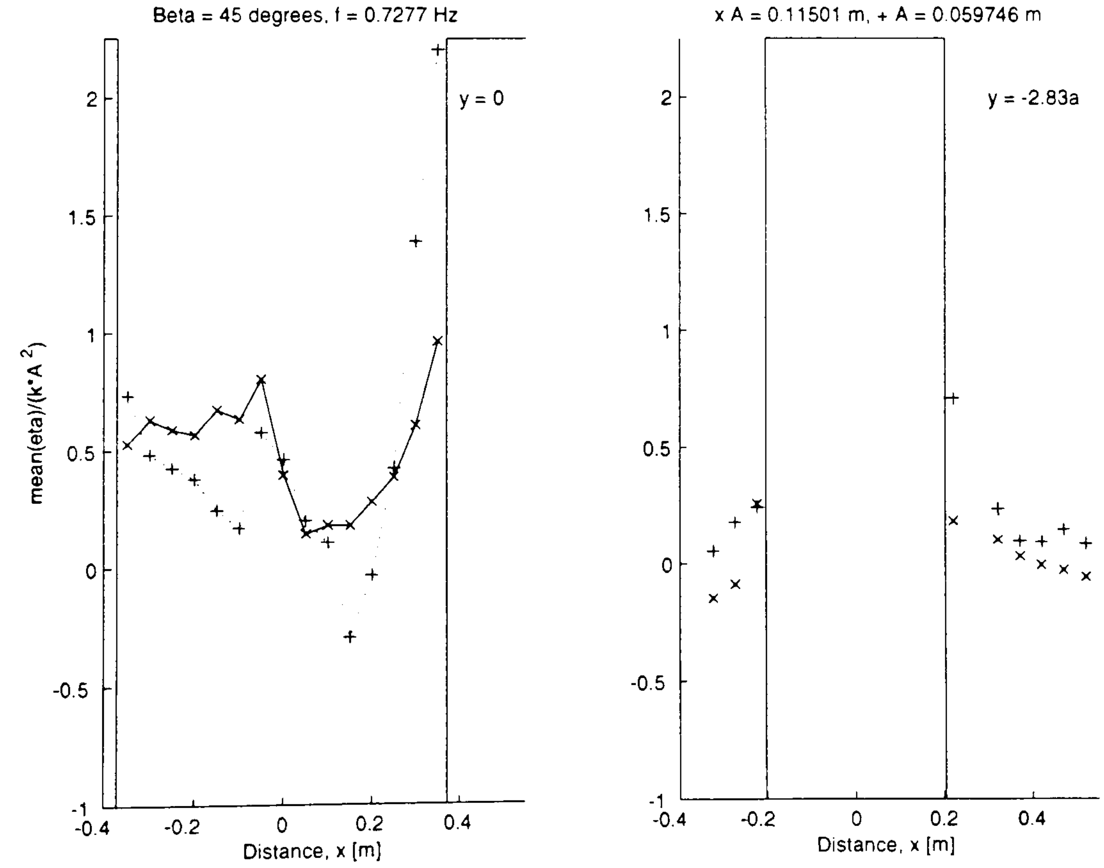

Figure 5.46. Set down versus position; $\beta = 45°$, $f = 0.7277$ Hz

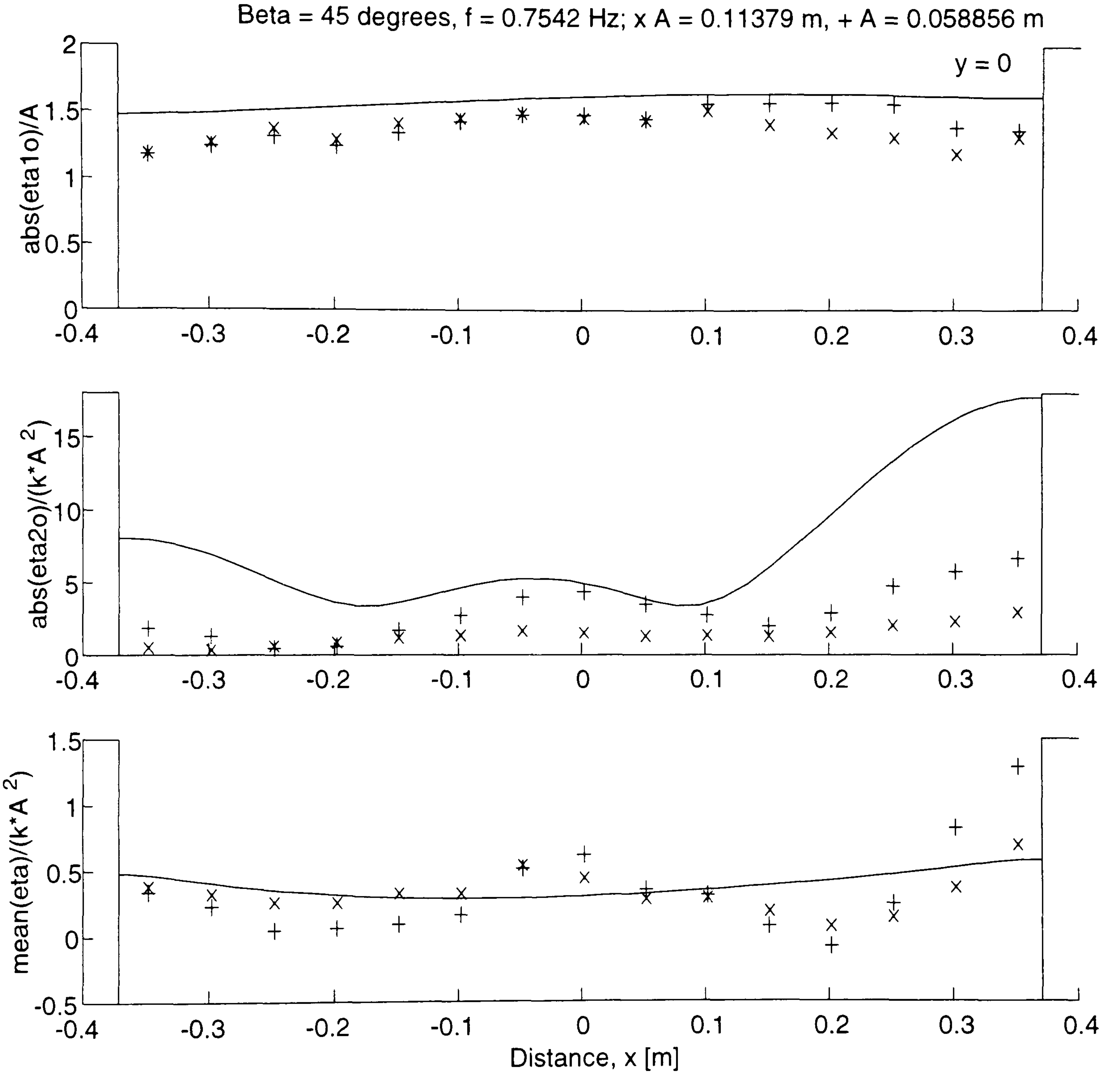

Figure 5.47. Theoretical and experimental results at near trapping; theoretical results reproduced with permission from Malenica, Eatock Taylor, and Huang (1999)

Chapter 6
Irregular Wave Results

6.1 Introduction

Multicylinder diffraction experiments for irregular waves were conducted at HR Wallingford as discussed in Chapter 4. The analysis of free surface elevation data collected is described in detail, as well as the computation of comparisons from the fully analytical linear diffraction theories for random seas and focused wave groups developed in Chapter 2. Results of irregular wave tests in the empty wave basin have been compared to the linear theory for focused wave groups, while tests with the model present are compared with linear wave diffraction theory for random seas and focused wave groups.

As described in Chapter 4, the heading β used in both model configurations is zero in mathematical terms. However, for ease of description, the first model configuration (with two cylinders upstream and two downstream) will be referred to as heading 0°; and the second model configuration (with one cylinder upstream, two abeam the tank centre, and one downstream) will be designated as heading 45°.

As in the preceding chapter, cylinders are distinguished as upwave and downwave in both heading cases and as offset for the centreline cylinders of the 45° heading cases. The upwave and downwave cylinder edges are referred to as the front and rear faces, respectively. The terms inboard and outboard are used to describe direction toward and away from the centre of the model, respectively. In contrast, longitudinal and transverse describe general orientation parallel and perpendicular to the incident wave ray, respectively.

To facilitate comparisons between theory and experiment, a range of subscripts are used throughout this chapter. For the purpose of standardisation, upper case subscripts apply exclusively to focused wave group computations, whereas lower case subscripts apply to all other quantities, such as spectral characteristics, mean square free surface elevation, etc. Thus, incident waves will be distinguished through I and i, while diffracted waves will be designated by D and d respectively. Focused wave group crests and troughs will be distinguished through C and T respectively. For theoretically computed quantities, the subscript t will be used for mean square free surface elevation, while the superscript T will be used for focused wave group computations (this avoids any confusion with the trough subscript T). Again, a summary of the nomenclature used throughout the thesis appears in Appendix B.

6.2 Data Manipulation

As for the previous regular wave tests, measurements of the time variation of free surface elevation $\eta(t)$ were made at prescribed locations in the vicinity of the multicylinder model. Chapter 4 contains detailed description of the exact model configuration, wave tank description, and testing procedures. In the case of the irregular wave tests, data were analysed for comparison to the linear diffraction theory for both random seas and focused wave groups, as presented in Chapter 2.

6.2.1 Repeatability verification

Incident waves for the irregular wave tests were produced by the wave basin paddles through a computer controlled process as discussed in Chapter 4. This provided control over spectral shape, peak frequency, and significant wave height. However, to generate a random sea simulation, pseudo-random white noise was used to determine the phasing of the individual frequency components. As identical noise was used for each test, the irregular wave tests should be fully repeatable.

This repeatability is demonstrated in Figure 6.1, which plots measurements of free surface elevation η as a function of time t at the reference wave probes for one of the irregular wave tests. The upper subplot plots four reference wave probe time histories from the tests with the wave basin empty, while the lower two subplots plot readings from the model tests at headings $0°$ and $45°$. Only a small portion of the test from the middle section of the data is displayed so that the signals may be readily compared. While slight discrepancies may be noted, the various lines are near to overlapping, and the individual tests may be taken as identical.

6.2.2 Data record truncation

As discussed in Chapter 4, the initial data records from the irregular wave tests encompassed measurements of free surface elevation $\eta(t)$ at 2^{14} (16384) data points covering a time of approximately 2^9 (512) peak wave periods. The sampling interval for the data record is then approximately $\triangle t = 2^{-5} T_p$. The highest frequency information that can be resolved through FFTs is then the Nyquist critical frequency given by

$$f_c \equiv \frac{1}{2\triangle t} = \frac{1}{2^{-4}T_p} = 16f_p. \tag{71}$$

This Nyquist frequency is clearly beyond the scope of the work presented here. Thus, to facilitate frequency analysis through fast Fourier transforms (FFTs), the original data record was truncated by removing every other data point. This effectively doubled the sampling interval to $\triangle t = 2^{-4}T_p$, lowering the Nyquist critical frequency to $8f_p$ and reducing the number of data points to a more manageable 2^{13} (8192) points.

Having established a suitable maximum frequency, the level of frequency discretisation is then set through the overall number of data points in the analysed record. To develop a sensibly sized bin for the frequency analysis, the truncated record produced above was then further divided into four equal sections of length 2^{11} (2048) points, representing four distinct time segments from the beginning to the end of each test. Each of these sections was then further divided into four equal subsections of length 2^9 (512) points. This provided very manageable data segments, producing one-sided spectra of 2^8 (256) components with frequency discretisation of

$$\triangle f = \frac{1}{2^9\triangle t} = \frac{1}{32}f_p. \tag{72}$$

This data record truncation is illustrated in Figure 6.2, which plots the entire free surface time history $\eta(t)$ recorded at the reference wave probe during an empty tank test. The vertical dashed lines indicate the divisions between the four sections (these have been labelled A through D for future reference in the discussion of frequency analysis), while the dotted lines indicate the subsection divisions.

6.2.3 Frequency analysis

For the empty tank tests, FFTs of the truncated data sets were used to produce a frequency domain analysis for each subsection of 2^9 (512) points and each wave probe location. These subsection spectra were then averaged to provide mean spectra for each section division of 2^{11} (2048) points. This provided 52 total wave spectra for each of the four sections (13 wave probe locations for each of 4 wave probe configurations). Representing measurements from points in close proximity with one another and showing close agreement, the 52 spectra were deemed to be sufficiently correlated for further averaging to produce one mean spectrum for each section.

The resulting four section spectra were then compared to establish the consistency of the incident wave spectrum throughout each test. For the same empty tank test as Figure 6.2, this comparison of wave spectra is illustrated in the left subplot of Figure 6.3, in which the solid, dashed, dotted, and dash-dotted lines plot the incident wave spectra for sections A, B, C, and D, respectively. As is apparent from the Figure, the spectral shapes and areas beneath the spectra are all reasonably similar, with some discrepancies in the energy of various components which may be attributed to the frequency discretisation and the short length of each time series. Again, these section spectra were deemed to be reasonably well correlated, and so a mean wave spectrum was computed for each incident wave test. The right subplot of Figure 6.3 presents the equivalent mean spectrum for the section spectra in the left subplot. Smooth relative to the section spectra, this mean spectrum appears to be a reasonable representation of the general shape of the spectra. The three mean spectra produced in this manner (for tests f_i1H_s1, f_i2H_s2, and f_i3H_s3) were used in subsequent calculations as the incident wave spectra at all positions for these three irregular wave conditions.

It should be noted that the x-axis scales of both subplots in Figure 6.3 have been restricted to frequency components between $f = 0.4$ and 2.0 Hz in order to provide an adequate representation of the spectral peak. Components outside of this range are sufficiently close to zero energy that they would not appear on the scale. In addition, no smoothing or running averaging has been used at any stage of the analysis.

From these mean incident wave spectra, peak frequency f_p has been identified as the frequency containing maximum energy, while significant wave height has been computed from the spectra as

$$H_s = 4\sigma = \sqrt{\sum_n S_i(\omega_n)\,\Delta\omega}. \tag{73}$$

Table 6.1 details the irregular waves tested with the peak frequency and significant wave height originally requested (as listed in Chapter 4) as well as those computed here. In addition, further significant wave heights have been calculated for the irregular wave spectra following filtering above $1.5f_p$ (i.e. setting all energy above this cutoff frequency to zero and recomputing significant wave height). The aim of this filtering is to eliminate the effects of energy in higher harmonics, beginning with 2nd harmonic energy principally near to $2f_p$.

Using the same procedure above, mean wave spectra for the irregular wave tests with the model present were produced. However, the free surface elevation time histories recorded at different positions in the vicinity of the model clearly represent distinctly different diffraction effects (see for example Figure 2.24 in Chapter 2), and individual wave spectra at each wave probe position were not averaged. This resulted in 52 mean diffracted wave spectra for each incident spectrum (13 wave probe positions for 2 model headings with 2 wave probe configurations each).

6.2.4 Random seas

For comparison with first order diffraction theory for random seas, the experimental mean square free surface elevation $\overline{\eta^2}$ was calculated for the incident and diffracted wave spectra. Experimental mean square free surface elevations at a point (x, y) in the diffracted and incident fields were calculated through

$$\overline{\eta_d^2}(x,y) = \sum_n S_d(x,y,\omega_n)\,\triangle\omega \tag{74}$$

and

$$\overline{\eta_i^2} = \sum_n S_i(\omega_n)\,\triangle\omega, \tag{75}$$

where $S_d(x,y,\omega_n)$ and $S_i(\omega_n)$ are the mean energy density spectra for the diffracted and incident waves, respectively, and $\triangle\omega = 2\pi\triangle f$.

The corresponding theoretical equivalent mean square free surface elevation was produced using the first order diffraction theory developed in Chapter 2 as

$$\overline{\eta_{td}^2}(x,y) = \sum_n |\phi_n(x,y)|^2\, S_i(\omega_n)\,\triangle\omega, \tag{76}$$

where $\phi_n(x,y)$ is the complex diffraction coefficient (the first order modification to free surface elevation) for the n^{th} spectral component. The incident spectrum $S_i(\omega_n)$ is assumed to conform to the mean spectrum for each test as calculated through the method described above.

In addition, to assess the effects of nonlinearity on the experimental results and hopefully obtain a closer match between linear theory and nonlinear experiment, further mean square free surface elevations were calculated for the wave spectra following filtering above $1.5f_p$. This was accomplished by setting all energy above this cutoff frequency to zero and recomputing both experimental and theoretical mean square free surface elevation using the filtered incident and diffracted spectra.

6.2.5 Focused wave groups

Extensive sorting of the crests and troughs was then necessary to provide comparisons to focused wave group theory. As removal of every other data point from the original data could be thought to cause slight deviations in the maxima and minima of troughs and crests, the original data (and not the truncated data described above) were analysed.

The average shape of the largest 5 crests was computed for both the empty tank tests and the tests with the model present. In order to properly assess the effects of diffraction, six separate mean focused wave group time histories $\eta(t)$ were identified, namely:

$\eta_{IC}(t)$	largest incident wave crest from the empty wave basin tests
$\eta_{IT}(t)$	deepest incident wave trough from the empty wave basin tests
$\eta_{D}(t)$	diffracted free surface occurring at the same time as $\eta_{IC}(t)$ above
$\eta_{DC}(t)$	largest diffracted free surface (not necessarily identical to $\eta_{D}(t)$ above)
$\eta_{DT}(t)$	deepest diffracted free surface
$\eta_{I}(t)$	incident free surface occurring at the same time as $\eta_{DC}(t)$ above

As the above measured focused wave groups were to be compared with a first order diffraction theory, they were linearised by both filtering the measured spectra and implementing crest-trough comparisons. The spectral filtering was accomplished by computing the FFT of the measured data, setting all frequency components above $1.5f_p$ to zero, and computing the inverse FFT for a new filtered data set. Crest-trough comparison was then implemented for time histories $\eta_{IC}(t)$ and $\eta_{DC}(t)$ using the same procedure as that of Jonathan & Taylor (1995). Even order nonlinearity may be removed and a somewhat linearised crest time history computed through

$$\begin{aligned} \eta^{1}_{IC}(t) &= \frac{\eta_{IC}(t)-\eta_{IT}(t)}{2} \\ \eta^{1}_{DC}(t) &= \frac{\eta_{DC}(t)-\eta_{DT}(t)}{2}. \end{aligned} \tag{77}$$

The incident focused wave group theory presented in Chapter 2 was used to compute a theoretical comparison to the linearised largest incident wave $\eta^{1}_{IC}(t)$ above through

$$\eta^{T}_{IC}(\tau) = \frac{\alpha}{\sigma^2}\sum_{n} C_{in}\,\mathrm{Re}\left\{\mathrm{e}^{-\mathrm{i}\omega_n\tau}\right\}, \tag{78}$$

where $C_{in} = (S_i(\omega_n)\triangle\omega_n)$, σ is the standard deviation of the incident spectrum, α is the maximum elevation of the incident focused wave group, and τ is the time interval from the time of occurrence at $\tau = 0$.

For comparison to the diffracted largest incident wave $\eta_D(t)$ and the linearised largest diffracted wave $\eta^{1}_{DC}(t)$, theoretical diffracted focused wave groups were produced using the first order diffraction theory developed in Chapter 2 and based on the measured diffracted spectrum. For the diffraction of the largest measured incident wave, the amplitude components of this event were treated as deterministic, and the diffracted time history was computed through

$$\eta_D^T(x,y,\tau) = \frac{\alpha}{\sigma^2}\sum_n C_{in}\,\mathrm{Re}\left\{\phi_n(x,y)\,\mathrm{e}^{-\mathrm{i}(k_n x_0+\omega_n\tau)}\right\}, \tag{79}$$

where the position of occurrence of the large crest is x_0. In contrast, to compute the average shape of the largest waves in the diffracted field, it is necessary to compute the effects of diffraction on the amplitude components of the spectrum. This may be accomplished through

$$\eta_{DC1}^T(x,y,\tau) = \frac{\alpha}{\sigma^2}\sum_n C_{in}\,\mathrm{Re}\left\{|\phi_n(x,y)|^2\,\mathrm{e}^{-\mathrm{i}(k_n x_0+\omega_n\tau)}\right\}. \tag{80}$$

In addition, a subsequent theoretical comparison has been computed from the measured diffracted spectrum at each wave probe location as

$$\eta_{DC2}^T(x,y,\tau) = \frac{\alpha}{\sigma^2}\sum_n C_{dn}(x,y)\,\mathrm{Re}\left\{\mathrm{e}^{-\mathrm{i}(k_n x_0+\omega_n\tau)}\right\}, \tag{81}$$

where $C_{dn}(x,y) = (S_d(x,y,\omega_n)\triangle\omega_n)$ and $S_d(x,y,\omega_n)$ is the measured diffracted spectrum as computed from the time history $\eta_d(t)$ at the point (x,y).

6.3 Data Presentation and Observations

In the descriptions of observed phenomena, distinction is made between centreline plots (along the tank and model longitudinal centreline at $y = 0$), offset plots (to the side of the model at $y = -2a$ or $y \approx -2.83a$), and the location of the transverse centreline (along the tank and model transverse centreline at $x = 0$).

6.3.1 Definition of incident wave spectra

Produced through the method described above, the mean incident wave spectra were defined to be the incident wave spectrum to be used for theoretical calculations and data non-dimensionalisation. For the three incident irregular wave conditions, the incident wave spectra are presented in Figures 6.4, 6.5, and 6.6 corresponding to irregular wave tests f_i1H_s1, f_i2H_s2, and f_i3H_s3, respectively. Presented in plots of energy density S (in units of m^{2}s) versus frequency f (in units of Hz), the x-axis scales have been plotted from 0 to 3 Hz. The range plotted demonstrates that the majority of the incident wave energy present during the tests was within the frequency band 0.5 Hz $< f <$ 1.5 Hz, and that no significant set up or set down was present in the incident condition. The solid line plots the mean incident wave spectra, while the dotted lines plot one standard deviation above and below the mean, as computed from the four separate sections of data identified. Finally, the vertical dashed line indicates the cutoff frequency for filtering at $1.5f_p$ as discussed previously.

Figure 6.7 provides a comparison of the three incident spectra, with solid, dashed, and dotted lines corresponding to the spectra from tests f_i1H_s1, f_i2H_s2, and f_i3H_s3, respectively. It is immediately apparent that the spectral shapes, including the breadth of the peak and the decay in the tail, are very similar. However, the frequencies defining the peaks vary significantly, shifting to lower frequency from f_i1H_s1 to f_i2H_s2 and finally f_i3H_s3. In addition, f_i1H_s1 appears to be somewhat broader with a more jagged peak than the other two spectra.

6.3.2 Definition of incident focused wave groups

As described above, linearised incident focused wave group crests were computed from the mean free surface elevation time history $\eta(t)$ of the largest 5 crests and deepest 5 troughs from a filtered incident spectrum. The distribution of these crests and troughs and their linearised output is demonstrated in Figures 6.8, 6.10, and 6.12 for f_i1H_s1, f_i2H_s2, and f_i3H_s3, respectively. Not limited to only the largest 5 crests and deepest 5 troughs, the number of large events plotted has been extended to 200 to obtain some idea of the relationship between the most extreme events and those of more common occurrence with elevation on the order of the significant wave height H_s. The upper subplot in each figure demonstrates the maximum elevations from the tests in the empty wave basin, while the lower subplot contains the mean maximum diffracted free surface elevation as computed from an average maximum at all the probe positions with the model in the basin. The solid line plots the maximum elevation of the largest crest η_{IC} and η_{DC}, while the dashed line plots the maximum depth of the corresponding trough η_{IT} and η_{DT}, and the dotted line plots the corresponding linearised result $\eta_{IC}^1 = \frac{\eta_{IC}-\eta_{IT}}{2}$ and $\eta_{DC}^1 = \frac{\eta_{DC}-\eta_{DT}}{2}$.

From all three figures, it is apparent that the elevation of the n^{th} extreme event decreases exponentially as expected with increasing n. The maximum elevation of the crests is also clearly larger than the depth of the troughs, with linearised crest elevation falling reasonably between the two values. While the averaging of all probe positions renders the diffracted results difficult to interpret, these plots display considerably larger extreme values relative to the incident measurements for both crest and trough, which is indicative of the amplification of large events due to scattering. In addition, while the largest 5 events vary in maximum elevation by some 15%, they clearly represent extreme elevations relative to the significant wave from each spectrum, with the incident linearised extreme elevation η_{IC}^1 for $n = 1$ of the order of H_s for all three spectra.

Results of the linearised time series representing incident focused wave groups (in the absence of the model) are plotted and compared to the theoretical focused wave group in Figures 6.9, 6.11, and 6.13 for the three incident spectra. The dotted line indicates the linearised crest η^1_{IC} while the solid line plots the theoretical comparison η^T_{IC} as computed from the incident spectra. The theoretical result has been scaled such that its maximum elevation coincides with that of the experimentally measured incident wave. The dashed lines trace an envelope two standard deviations above and below the mean experimental value η^1_{IC}.

For all three spectra, the theoretical focused wave group remains within this error envelope near to the time of focus ($t = 0$) up to the first crest before or after the focus event ($t \approx \pm 1.3$ s $\approx T_p$). This result demonstrates the validity of focused wave group theory when applied to the largest events recorded in a random sea. However, it also details the applicability of this theory to short time intervals near to the focus event, as the dependence of the free surface on the extreme event decreases with increasing time before or after the event as discussed in Chapter 3.

In addition, it should be noted that the agreement between theory and experiment is significantly better after the focus event than before, again for all three spectra. This may be seen most clearly in Figure 6.9 for f_i1H_s1, in which the depth, shape, and time of occurrence of the trough at $t \approx 1.8$ s are matched very well by the theory. In contrast, the corresponding trough before the focus event at $t \approx -1.8$ s is very poorly reproduced, with the theoretical depth outside the estimated error range of two standard deviations and a phase shift of some 0.2 s evident in the time of occurrence. The consistently better agreement after the focus time for all spectra may be indicative of the nonlinear formation of extreme events. This phenomenon is related to the resonant interactions between frequency components of a very steep focused wave group and has been discussed in more detail in Chapter 3.

6.3.3 Contour plots

To obtain some understanding of the general nature of the scattering present during these tests, contour plots of scattering for the three incident wave conditions were produced through the analytical method developed in Chapter 2. These contour plots are presented here in Figures 6.14, 6.16, and 6.18 for heading 0° and Figures 6.15, 6.17, and 6.19 for heading 45°. As in Chapter 5, solid circles denote the cylinder positions while key contours are labelled with magnitude in terms of the amplification modifying the incident spectrum at that point (in this case the modification of root mean square elevation$\sqrt{\frac{\eta_d^2(x,y)}{\eta_i^2}}$). For example, a contour labelled 1 would indicate effectively no modification to the incident elevation statistics along that line, while a value of 1.5 corresponds to a 50% increase in root mean square free surface elevation, significant wave height, etc. at that point. Discussion of these plots is separated according to heading, with some comparison to the equivalent regular wave plots from Chapter 5 (Figures 5.5 to 5.16).

6.3.3.1 Heading 0°

The principal features of the contour plots are significant runup on the front faces of all cylinders as well as broad regions of upwelling in the model centre and upwave of the model. However, a region of somewhat diminished energy ($\sqrt{\frac{\eta_d^2(x,y)}{\eta_i^2}} = 0.9$) does exist just downwave of the downwave cylinders. As before in the regular wave tests, any modification to the incident wave spectrum decreases significantly with increased distance away from the model. This is particularly true for transverse distances, in which very little scattering appears to occur more than two cylinder diameters outboard of the model centre.

While the overall patterns observed for the three incident spectra exhibit much similarity, some key differences may be noted. The most significant first order runup and upwelling effects are noted in Figure 6.14 for f_i1H_s1, for which the incident spectrum is amplified by as much as 50 and 60% on the front face of the downwave and upwave cylinders, respectively. This is in contrast with Figure 6.18 for f_i3H_s3, where runup at the upwave cylinders is amplified by only 40%. However, runup at the downwave cylinders remains at roughly 50% amplification, which is also observed in Figure 6.16 for f_i2H_s2. Upwelling at the model centre appears to be relatively constant at between 20 and 30% for the three incident spectra.

In comparison with the contour plots for regular wave diffraction at this heading from Chapter 5 (Figures 5.5 through 5.10), these plots are very similar. Both sets indicate runup at the front face of all four cylinders and regions of upwelling at the model centre and upwave of the model. However, the regular wave contour plots show regions of significant destructive interference and diminished wave amplitude between the upwave cylinders. The diffracted field clearly has stronger effects at larger distances from the model centre in the regular wave cases; this is most noticeable in the transverse direction, for which modifications of the incident amplitude of the order of 20% occurs beyond 2.5 cylinder diameters from the model centre in Figure 5.5. The upwelling upwave of the model is also significantly greater than the runup at the front face of the upwave cylinders, the reverse of which is shown here. It is reasonable to suggest that these differences are present due to the range of frequencies contributing to the irregular wave contours, which has the effect of smoothing any regions of significant response.

6.3.3.2 Heading 45°

As for the 0° heading, the 45° heading contour plots feature significant runup on the front faces of all cylinders. A broad region of upwelling exists throughout the model centre, and regions of diminished energy are non existent, apart from small regions on the outboard edges of the offset and downwave cylinders in Figure 6.15 and on the downwave cylinder only in Figure 6.17. Also, almost no modification to the incident spectrum is observed more than two cylinder diameters outboard in the transverse direction, three diameters upwave, or two diameters downwave from the model centre.

Again, the overall patterns observed for the three incident spectra are strikingly similar, perhaps even more so than for the 0° heading. Runup on the offset and downwave cylinder front faces appears to be relatively constant at 40 and 50% respectively for all three incident waves, and all three plots exhibit centre upwelling at roughly 30%. However, runup at the front face of the upwave cylinder does vary somewhat. In Figures 6.15 and 6.17 for f_i1H_s1 and f_i2H_s2 this runup reaches 40% enhancement, whereas Figure 6.19 for f_i3H_s3 attains only 30% magnification to the incident energy.

Comparing these irregular wave contour plots to the regular wave plots of Chapter 5 (Figures 5.11 to 5.16), very similar conclusions may be drawn as for the 0° heading above. While the overall features are very similar, with runup at the front faces of all cylinders and upwelling at the model centre, the more complex features of the regular wave plots appear to be considerably smoothed for the irregular wave cases. This is again true for larger distances from the model centre, for which amplification of 20% may be found at the transverse borders in Figure 5.11.

6.3.4 Mean square free surface elevation $\overline{\eta^2}$ and linear theory comparison

As discussed in Chapter 4, wave probes were placed along the centreline of the model ($y = 0$) for both headings. However, for the 0° heading tests additional probes were placed along a line between the centres of the upwave and downwave cylinders (at $y = -2a$), while, for the 45° heading tests, probes were placed upwave and downwave of the cylinder abeam the tank centre (at $y \approx -2.83a$). Plots of mean square free surface elevation versus position were made for the three incident irregular waves and the two headings tested.

As discussed above, mean square free surface elevation was calculated for both the complete incident and diffracted spectra as well as for linearised spectra, with all frequency components above $1.5f_p$ removed. Separated into two plots (unfiltered and filtered) with two subplots for each frequency and heading combination, the complete results are presented here in Figures 6.20 to 6.25 for heading 0° and Figures 6.26 to 6.31 for heading 45°. To facilitate comparison of the unfiltered and filtered results, these are placed adjacent to one another. The upper subplot presents mean square free surface elevation along the centreline of the model, while the lower subplot presents the offset elevation.

Mean square free surface elevation was non-dimensionalised through division by the incident value $\overline{\eta_i^2}$ of each incident spectrum. Thus, the experimental mean square free surface elevation $\frac{\overline{\eta_d^2}}{\overline{\eta_i^2}}$ has been plotted at the measured points with a circle indicating the mean value and errorbars drawn one standard deviation above and below the mean. Computed through the linear diffraction theory developed in Chapter 2 and described explicitly above, the theoretical values $\frac{\overline{\eta_t^2}}{\overline{\eta_i^2}}$ have been plotted as a continuous solid line. It should be noted that in none of the cases does the experimental mean square free surface elevation fall out of the range $1 < \frac{\overline{\eta_d^2}}{\overline{\eta_i^2}} < 3.25$, and as such these values are used as the y-axis limits in all of the plots.

Direct observations which can be made from Figures 6.20 through 6.31 are grouped herein according to heading, beginning with the 0° heading and proceeding to the 45° heading. As in Chapter 5, regions or point locations of vigorous wave activity due to spectral amplification are referred to as peaks, while regions of diminished wave activity are referred to as troughs. Again, use of these words bears no resemblance to the peaks and troughs of individual waves as measured in the time or spatial domains.

6.3.4.1 Heading 0°

The comparison of experimental results with linear theory is very good, particularly for the filtered spectra and along the centreline of the model. The majority of the global trends present in the theoretical lines are followed by the circles of the experimental results. However, there is a consistent discrepancy in the elevation, with experimental mean square free surface elevation up to 25% higher than the theoretical prediction at some points. This discrepancy is somewhat improved in the filtered spectra.

For the centreline plots, the overall trends in both theory and experiment indicate two large peaks, one approximately three cylinder radii ($3a$) upwave of the model centre and the other approximately one cylinder radius downwave of the model centre, separated by a trough approximately one cylinder radius upwave ($x \approx -a$). These trends are almost identical for the three incident spectra, with marginally lower peaks noticeable in Figure 6.24 for f_i3H_s3 relative to Figures 6.20 and 6.22 for f_i1H_s1 and f_i2H_s2 respectively. The same is true for the filtered analogs of these plots.

The only major departure from the theoretical trend is present in the transition from the upwave peak to the trough at $x \approx -0.45$ m, located between the centres of the upwave cylinders. For the unfiltered spectra, experimental mean square free surface elevation at this point indicates a further peak followed by a more drastic transition to the trough value. However, this discrepancy is almost completely removed by filtering the spectra, and this further peak is clearly the result of some nonlinear response near this point, generating energy above the filtering cutoff at $1.5f_p$. In addition, it is worth noting the decrease in standard deviation at the upwave centreline peak from the plots at f_i1H_s1 (both filtered and unfiltered) relative to those at f_i2H_s2, and the further decrease for f_i3H_s3.

The offset plots demonstrate some consistent differences between the theoretical trends and the experimental results. First order theory clearly predicts runup at the front faces of both cylinders (as demonstrated in the contour plots of Figures 6.14, 6.16, and 6.18) with amplification steadily increasing towards the front face of both cylinders. While this is supported for the most part by the two experimental values upwave of the upwave cylinder (showing increased amplification towards the front face), the results between the two cylinders are less in agreement with the theory. For all three spectra, the experimental results indicate a peak in runup at the rear face of the downwave cylinder (exceeding the first order theory again by as much as 25%), followed by a trough near the transverse centreline at $x = 0$, and a further peak just upwave of the downwave cylinder. This complex behaviour is in many ways similar to that observed in the 0° heading offset plots of first order amplitude presented in Chapter 5. While filtering the spectra marginally improves the agreement between theory and experiment, this discrepancy in the global trend is not affected.

6.3.4.2 Heading 45°

Again, as for the 0° heading, the similarity between experimental and theoretical results is quite good, particularly with reference to the global trends. A consistent discrepancy in mean square amplification of the order of 5 to 25% is also present for these plots, and this discrepancy is improved somewhat for the filtered spectra. This is most noticeable in the runup at the front face of the downwave cylinder, which greatly exceeds the theory for the unfiltered plots but shows reasonable agreement after filtering.

For the centreline plots between the upwave and downwave cylinders, the overall trend in the theoretical results is a region of reasonably constant amplification running from the rear face of the upwave cylinder to just downwave of the model centre ($x \approx 0.15$ m). Amplification then increases to the runup location at the front face of the downwave cylinder. However, filtering of the spectra has the effect of somewhat diminishing this increase. This is particularly noticeable in Figure 6.31 for f_i3H_s3, where the theoretical line shows little increase approaching the downwave cylinder.

While the experimental results lie near to their theoretical counterparts, there are some notable discrepancies in the complexity of the amplification region. Beginning from the upwave cylinder, the experimental results indicate at least three peaks in amplification at positions varying between $x \approx -0.25$, -0.1, 0.1, and 0.25 m, dependent on the incident spectrum (e.g. Figure 6.30 for f_i3H_s3 appears to contain peaks at all four locations). Following filtering, the agreement between theoretical and experimental values is somewhat improved, but the global trends persist.

Finally, the offset plots show a large discrepancy between the theoretical and experimental values upwave of the cylinder, while agreement is much closer downwave. First order theory predicts somewhat increased amplification approaching the front cylinder face, with somewhat decreasing amplification away from the rear face. While this trend is supported by the experimental results, runup at the front cylinder face is far in excess of the theoretical prediction (by as much as 50% in Figure 6.26 for f_i1H_s1). This agreement is somewhat improved following filtering. In contrast, the first instance of experimental values falling below the theoretical prediction prior to filtering is evident downwave of the offset cylinder. Following filtering the experimental results are lowered yet further on average. However, this discrepancy is not large and the agreement is still reasonable.

6.3.5 Diffracted spectra and focused wave group diffraction

As discussed above, various incident and diffracted free surface elevation time histories were computed as representative of the experimentally measured behaviour of focused wave groups. In addition, theoretical comparisons to these experimental results were computed from both the measured diffracted spectra and the incident wave spectra, taking into account linear diffraction.

These computations were unique to each wave probe measurement location, as the effect of diffraction varies according to both incident frequency and position in the scattered field. However, this leads to an excessive number of possible comparisons and plots which could be presented (with effectively 24 probe positions for 2 model headings and 3 incident spectra; 144 possible cases). Thus, while all of these cases were analysed, for the purpose of presentation it was decided to focus on one incident wave spectrum and to select some significant cases demonstrating behaviour characteristic of that observed in all 144 cases studied. Based on the contour plot analysis and mean square free surface elevation results presented above, the incident spectrum $f_i 1 H_s 1$ (presented in Figure 6.4 and as the solid line in Figure 6.7) was selected as showing the most potential for large modification to the incident spectrum and therefore a strict test of the first order focused wave group diffraction theory developed in Chapter 2. For this incident spectrum, the following four wave probe positions (listed in terms of cylinder radius and distance in meters) were selected from each heading:

$\beta = 0^\circ$

x [m]		y [m]	
-1.150	$-5.66a$	0	0
-0.350	$-1.72a$	0	0
0.450	$2.21a$	0	0
0.150	$0.74a$	-0.106	$-2a$

$\beta = 45^\circ$

x [m]		y [m]	
0	0	0	0
0.300	$1.48a$	0	0
-0.225	$-1.11a$	0.757	$-2.83a$
0.220	$1.08a$	0.757	$-2.83a$

Plots at these eight positions were then produced to compare both spectral and focused wave group computations.

The results of these analyses are presented here in Figures 6.32 to 6.39 for heading 0° and Figures 6.40 to 6.47 for heading 45°. The spectral comparisons are placed in the upper half of each page, while the focused wave groups are in the lower half of the page. The spectra are plotted in a subplot above the squared diffraction coefficient $|\phi|^2$, which directly modifies the incident wave spectrum S_i, plotted as the dotted line in the upper subplot. The theoretical diffracted spectrum derived from this computation is plotted as the solid line and may be directly compared with the dashed and dotted line of the measured diffracted spectrum S_d.

The focused wave group comparisons in the lower half of the page are somewhat more complex. To begin with, the upper subplots display results for the diffraction of an incident focused wave group (i.e. the diffracted history occurring at the same time as an extreme incident event at $t = 0$). The lower subplots detail the largest diffracted event at $t = 0$ and the incident event measured at that time. In general, solid and dashed lines indicate theoretical diffracted results, while dashed and dotted lines represent the measured diffracted results and dotted lines indicate the measured incident wave.

In the upper focused wave group subplot, the solid line is the diffracted free surface elevation time history η_D^T, as computed through (79), associated with an extreme incident event η_{IC}^1 (the dotted line) occurring at $t = 0$ and linearised through crest-trough subtraction. No dashed line is present in this upper subplot, and the dashed and dotted line represents η_D, the diffracted time history measured at the time corresponding to the incident extreme event.

In the lower subplot, the dashed and dotted line is the largest measured diffracted free surface elevation time history η_{DC}^1 at $t = 0$ produced by an arbitrary incident wave condition η_I (the dotted line) and linearised through crest-trough subtraction. As a theoretical comparison, the solid line is the largest expected diffracted free surface elevation time history η_{DC1}^T, as computed through (80). In contrast, the dashed line in the lower subplot is the equivalent diffracted time history η_{DC2}^T as computed from the measured diffracted spectrum through (81). Due to the similarity of the measured diffracted spectra and the theoretically computed spectra, these solid and dashed lines overlap significantly and obscure one another in the majority of the plots. It should also be noted that these last two lines are symmetrical about $t = 0$, while the experimental results (represented by the dashed and dotted line) are clearly not. In addition, all of these theoretical diffracted free surface time history calculations have been scaled such that their maximum values coincide with the corresponding maximum measured values.

Again, direct observations which can be made from Figures 6.32 through 6.47 are grouped herein according to heading, beginning with the 0° heading and proceeding to the 45° heading. However, discussion of spectral comparisons precedes comparisons of focused wave groups. Note that, in all of these figures comparing spectra and focused wave groups, the y-axis scales have been drawn to accommodate the maxima and minima of the specific case presented and are therefore not consistent between points. However, in the case of the focused wave groups, the consistency of scales is maintained between the two subplots, such that comparison of incident and diffracted extreme events is facilitated.

6.3.5.1 Heading 0°: diffracted spectra

The spectral comparison plots demonstrate that the linear diffraction theory for random seas developed in Chapter 2 is somewhat effective at reproducing the diffraction effects measured in the experiments.

Comparison of the plots of squared diffraction coefficient $|\phi|^2$ versus frequency f demonstrate the variability of diffraction effects at different points in the vicinity of the model. For example, Figure 6.32 at $(-1.15\,\mathrm{m}, 0)$ exhibits rapidly varying values, with multiple large peaks on the order of $|\phi|^2 = 4$ separated by zeros at frequencies for which the incident and scattered waves clearly cancel one another at this point. In contrast, Figure 6.38 at $(0.15\,\mathrm{m}, -2a)$ exhibits far less variation, particularly for frequencies above $f = 2.5$ Hz, where the diffraction coefficient is again zero. In addition, the maxima and minima for these two cases vary considerably, with the largest value in Figure 6.38 clearly at $f \approx 1.5$ Hz, which represents a relative trough in Figure 6.32. However, given that this comparison is drawn between a wave probe location along the centreline of the model and from an offset wave probe location, this disparity may be expected. Indeed, while still displaying unique responses, the plots of $|\varphi|^2$ for the three centreline wave probes in Figures 6.32, 6.34, and 6.36 yield more similarities.

These differences in response are equally apparent in the spectral comparison plots, which also demonstrate the effectiveness with which first order diffraction theory approximates the fully nonlinear spectral diffraction. For the majority of the plots, the solid lines of the theoretical predictions very nearly approximate the dashed and dotted lines of the measured spectra. The appearance of zeros in the plots of squared diffraction coefficient $|\phi|^2$ is also verified in these plots, such that the $|\phi|^2 = 0$ value at $f \approx 0.95$ Hz in Figure 6.32 corresponds to an exceptionally low value for the measured diffracted spectrum.

However, some notable differences are apparent, particularly where significant influence of nonlinearity may be expected. This is most extreme in Figure 6.34 at $(-0.35\,\mathrm{m}, 0)$, which represents a wave probe location along the centreline in between the upwave cylinders. In this case, a relatively large band of energy, with peak value approximately 40% of the incident spectrum peak, is present in the measured diffracted spectrum within the frequency band 1.5 Hz $< f <$ 2 Hz, which may be taken to lie near to a second order response ($2f_p$) for the incident spectrum. It may also be suggested that the presence of this second order nonlinearity contributes to the discrepancies found between the theoretical and measured diffracted spectra in the trough region at $f \approx 1$ Hz and the second peak at $f \approx 1.2$ Hz. Again, some nonlinearity is also found in Figure 6.36, located at $(0.15\ \mathrm{m}, 0)$ between the downwave cylinders. It is worth noting that, for both of these nonlinear measured peaks, the corresponding plots of squared diffraction coefficient $|\phi|^2$ show near zero values. This indicates that these nonlinear peaks are clearly not the result of linear diffraction and that the discrepancy between measured and theoretical diffracted spectra at these frequencies may not be attributed to improperly computed incident spectra.

Overall, these discrepancies between measured and theoretical diffracted spectra are the source of the consistent differences noted in the plots of mean square free surface elevation $\overline{\eta^2}$, computed from the area under these spectra. Comparing the positions chosen here with the corresponding $\overline{\eta^2}$ calculations in Figures 6.20, it may be seen that those points exhibiting considerable higher order behaviour also yield significant discrepancies in mean square free surface elevation. However, following filtering of the spectra above $1.5 f_p$ and removal of the majority of these nonlinear effects, the agreement is much better, as demonstrated in Figure 6.21.

6.3.5.2 Heading 0°: diffracted focused wave groups

While some discrepancies are present for the diffracted incident extreme waves (the upper focused wave group subplots), the largest diffracted free surface elevation time histories in the lower subplots are very well approximated by the theoretical results.

It is clear from the upper subplots that, due to the phase shifting of scattered waves, an incident focused wave group crest η_{IC}^1 occurring at time $t = 0$ does not necessarily generate an equivalent diffracted large crest at $t = 0$. This is most apparent along the model centreline, such that in Figure 6.33 at $(-1.15\ \mathrm{m}, 0)$ the diffracted time history η_D (the dashed and dotted line) in the vicinity of the incident extreme event (the dotted line) yields no crests even as tall as the initial incident event itself. However, this may be compared with Figure 6.39 at $(0.15\ \mathrm{m}, -2a)$, for which the incident extreme event yields a somewhat taller extreme diffracted event shortly thereafter at $t \approx 0.2$ s.

These measured diffracted free surface time histories η_D are matched by the theoretical equivalents η_D^T (the solid lines) with a varying degree of accuracy. The error in this comparison is heavily dependent on the point chosen, with a reasonable match obtained in Figure 6.33 in terms of both the crest and trough elevations and phase relationships. This is in stark contrast with Figure 6.35, for which the phase relationships are so badly predicted that the mirror image of the theoretical result appears to give a closer fit to the measured data. Again, this may be attributed to the effect of the nonlinearity producing the discrepancy between the measured and theoretical diffracted spectra at $f \approx 0.85$ Hz (the previously mentioned higher order nonlinearities in the band 1.5 Hz $< f <$ 2 Hz for Figure 6.34 would not be expected to influence the focused wave group result due to filtering above $1.5 f_p$). However, both Figures 6.37 and 6.39 show more satisfactory agreement in terms of crest and trough elevations, although there are some distinct differences in phasing. Furthermore, the approximate 0.25 s discrepancy in phasing noticeable in Figure 6.37 could again be explained by the presence of nonlinearity above $f \approx 1.45$ Hz in Figure 6.36.

As previously mentioned, in the lower subplots the two theoretically computed extreme diffracted events (the solid line of η^T_{DC1} and the dashed line of η^T_{DC2}) plot virtually over one another, as would be expected due to the close agreement between the spectra. In addition, the agreement with the measured linearised extreme diffracted events η^1_{DC} is extremely good for most of the plots, particularly within the limits of $-T_p < t < T_p$ (i.e. to the first crest before and after the extreme event). This agreement carries yet further for some of the cases, such as Figure 6.35 at $(-0.35\ \mathrm{m}, 0)$, in which the complex trend in the time history is very well reproduced to $t \approx \pm 2$ s (although the agreement is somewhat better for η^T_{DC2} as computed from the measured diffracted spectrum). However, in Figure 6.39 the agreement between the measured and theoretically computed extreme diffracted events is not so impressive. Although the large trough after the event is reasonably well reproduced, the trough prior to the event at $t \approx -0.6$ s is poorly predicted as are the crests occurring both before and after the event.

The dotted lines of the incident free surface time history η_I verify that, due to the phasing of scattered waves from the model, these extreme diffracted events do not necessarily correspond to extreme incident events. This is particularly clear in Figure 6.33 at $(-1.15\ \mathrm{m}, 0)$, in which the incident time history bears no indication of an extreme event in the vicinity of the extreme diffracted event.

6.3.5.3 Heading 45°: diffracted spectra

Again, the comparisons of diffracted spectra demonstrate that the linear diffraction theory for random seas is somewhat effective at matching the measured diffracted spectra.

The squared diffraction coefficient $|\phi|^2$ plots also demonstrate extreme differences at each of the four points selected. The most extreme variation is observed in Figure 6.44 at $(-0.225\text{ m}, -2.83a)$, which represents a point very near to the runup at the front face of the offset cylinder. This plot exhibits multiple peaks on the order of $|\phi|^2 = 8$ and rapid variation with frequency. In contrast, Figure 6.42 at $(0.3\text{ m}, 0)$ along the model centreline exhibits little variation over the majority of the frequency range, but with one massive peak of amplification exceeding $|\phi|^2 = 15$ at $f \approx 1.45$ Hz. More similarities do not appear in comparisons between plots along the centreline versus those in the vicinity of the offset cylinder. This is immediately apparent in the maximum observed along the centreline in Figure 6.40 at $(0, 0)$, exceeding $|\phi|^2 = 6$ at $f \approx 2.55$ Hz. This is roughly half the maximum value in Figure 6.42 at nearly twice the frequency.

As above, the spectral comparison plots further demonstrate the effectiveness of first order diffraction theory for random seas. For this 45° heading, the solid lines of the theoretical diffracted spectra are even more successful at matching the dashed and dotted lines of the measured spectra. The extreme features present in the plots of squared diffraction coefficient $|\phi|^2$ are also well substantiated. This is most clearly seen in the aforementioned maximum in Figure 6.42 at $f \approx 1.45$ Hz, for which the theoretically computed diffracted spectrum exhibits a peak which very nearly matches that of the measured spectrum. In addition, the very complex, often jagged appearance of the measured spectrum in Figure 6.44 is extremely well reproduced by the theoretical prediction.

Some notable discrepancies are again present between the measured and theoretically computed spectra, although in this case they are not so easily attributable to higher order phenomena. A distinct difference may be noted in all four figures, for which a low, broad peak may be observed in the measured spectra within a frequency band of approximately $1.5\text{ Hz} < f < 2\text{ Hz}$. Again for all four positions, this measured peak corresponds to a relative peak in the squared diffraction coefficient $|\phi|^2$. This may then indicate that some of this energy is due to first order diffraction and is somehow not well reproduced here due to possible errors in the computed incident spectrum. However, it should also be noted that this frequency band corresponds to that of the higher order energy observed in Figure 6.34, and could be explained in similar terms as the presence of some second order response at twice the peak frequency. If this peak is accepted as nonlinear in nature, it may further help to explain the discrepancies near the spectral peak in Figure 6.42, for which the theoretical prediction exceeds the measured value by some 30%.

These differences in theoretical and measured diffracted spectra may again be seen in the mean square free surface elevation $\overline{\eta^2}$ plots presented previously. From the positions selected here, the corresponding positions in Figure 6.26 and in the filtered plot of Figure 6.27 indicate that the nonlinearity consistently increases the computed mean square elevation. However, this increase does not necessarily yield $\overline{\eta^2}$ in excess of the theoretical computation. For example, due to the overprediction of energy in frequency components near the peak of the spectrum at $(0.3\,\mathrm{m}, 0)$, the $\frac{\overline{\eta_d^2}}{\eta_i^2}$ lies very near to $\frac{\overline{\eta_t^2}}{\eta_i^2}$ in Figure 6.26; but, following filtering above $1.5f_p$ and removal of the nonlinear peak, the measured result drops below the theoretical prediction.

6.3.5.4 Heading 45°: diffracted focused wave groups

As before for the 0° heading, some discrepancies may be noted in the upper subplots of diffracted incident extreme waves, while the lower subplots indicate very good agreement between theory and experiment for the largest diffracted free surface elevations.

At the 45° heading phase shifts for the scattered incident extreme events are less clear. This is most evident in Figures 6.41 and 6.43 along the centreline and in 6.45 at $(-0.225\,\mathrm{m}, -2.83a)$. In these figures, the time of occurrence of the maximum elevation in the measured diffracted time history η_D (the dashed and dotted lines) is very nearly $t = 0$, the focus time of the incident extreme event η_{IC}^1 (the dotted lines). However, there is a noticeable phase shift in Figure 6.47 at $(0.22\,\mathrm{m}, -2.83a)$ of approximately 0.2 s.

The theoretical diffracted free surface time histories η_D^T match the measured values η_D with varying success. For Figures 6.41 and 6.47 the comparison is rather good, with the phase shift of the latter case predicted to within approximately 0.05 s. However, Figures 6.43 and 6.45 exhibit less than perfect agreement, such that the phase shifts predicted by the theory are virtually absent in the measured diffracted time histories and the trough depth occurring before and after the maximum elevation are also poorly predicted. This may possibly be attributed to the predominance of higher frequency energy in these two cases, which, from Figures 6.42 and 6.44, contain significantly more energy above $1.5f_p$ in comparison to the other two positions. This is in addition to the broad band of nonlinear energy identified between $1.5\ \mathrm{Hz} < f < 2\ \mathrm{Hz}$. While the components above this frequency have been removed for the focused wave groups presented, it is possible that they have had some influence on the phasing and amplitude of other components at the spectral peak.

In the lower subplots, the two theoretically computed extreme diffracted events (the solid line of η^T_{DC1} and the dashed line of η^T_{DC2}) again produce very similar results due to the close agreement between the spectra. The agreement of these theoretical predictions with the experimentally measured η^1_{DC} is also very similar to that of the 0° heading, with exceptionally good accuracy limited to within the range $-T_p < t < T_p$. As for the incident extreme events presented earlier in Figures 6.9, 6.11, and 6.13, the agreement is somewhat better after the focus time as opposed to before. This is most apparent in Figure 6.45 at $(-0.225\text{ m}, -2.83a)$, in which a more complex feature of the measured time history η^1_{DC} at $t \approx -1.8$ s is not reproduced by the theoretical result, while the match after the extreme event ($t > 0$) is extremely close.

In contrast to the 0° heading, the incident free surface time history η_I (represented by the dotted lines) producing the extreme diffracted event is more similar in appearance to an extreme incident crest focusing at $t = 0$. A minor exception to this is Figure 6.47 at $(0.22\text{ m}, -2.83a)$, for which the incident extreme wave crest occurs at $t \approx -0.2$ s. However, it may be imagined that shifting the lower subplot of this figure to the right by 0.2 s would yield a result greatly resembling the upper subplot. Thus, minor phase shifts are present at this point, but they do not have an overwhelming effect.

6.4 Conclusions

The primary results of the analysis presented throughout the chapter are as follows:

(1) Linear diffraction theory for random seas (developed in Chapter 2) has been shown to be a fair method of predicting the shape of diffracted spectra as well as the global trends in diffracted statistics for nonlinear irregular wave conditions.

(2) Subsequently, linear diffraction theory for focused wave groups (also developed in Chapter 2) has also been demonstrated as an effective model.

(3) For both the incident focused wave groups and the most extreme diffracted events, the agreement between theory and experiment was closer after the focus time (at $t = 0$) than before.

(4) The presence of high frequency energy in diffracted wave spectra has been noted, particularly at positions

between the upwave cylinders for the 0° heading tests.

6.4.1 Linear diffraction theory for random seas

For both heading cases, the overall agreement between the theoretically computed diffracted spectra and the measured spectra was found to be decent. Where discrepancies did exist, these could in most cases be attributed to the presence of some energy at higher frequencies, which is discussed further below. Due to this reasonable agreement between the wave spectra, statistics for the random seas also show similarity, with experimental results typically following the global trends of the theory. This agreement is improved somewhat if the spectra are filtered at some reasonable point above the peak frequency, in this case above $1.5f_p$, such that the primary results of nonlinear interactions are effectively removed.

6.4.2 Linear diffraction theory for focused wave groups

Again, first order theory for focused wave groups has been shown to be effective at reproducing the time histories of extreme events in the vicinity of a model. However, it must be noted that the comparisons made here are for filtered spectra, with all components above $1.5f_p$ removed, and linearised extreme events (applying the crest-trough subtraction method of Jonathan & Taylor 1995). While some errors in the theoretically predicted timing of diffracted incident extreme events were found to exist, the overall shape of the most extreme diffracted events was well predicted.

6.4.3 Focused wave group time history agreement for $t > 0$

The theoretical and experimentally measured time histories computed for both incident and diffracted extreme events showed better agreement after the focus time at $t = 0$. Due to the nature of the mathematics, the theoretically computed first order focused wave groups were symmetrical about the focus time $t = 0$ for both the diffracted and incident waves. However, the majority of the extreme events measured during the experiment were not symmetrical, with some notable differences in the time history before and after the focus time by approximately $t = \pm 1.5T_p$, depending on the case presented. These differences tended towards better agreement with the theoretical computations for times after the focus (i.e. $t > 0$).

As previously mentioned, this consistently better agreement after the focus time may be related to nonlinear interactions present during the formation of extreme events. Thus, due to resonant interactions between frequency components of the focused wave group, the group may come into focus and reach an extreme value prior to the prediction of linear theory, particularly for a reasonably steep extreme event. Linear diffraction theory may then be expected to produce more accurate temporal results after the event, when the point of extreme elevation has passed the point of observation. However, this resonant interaction between frequency components of focused wave groups is discussed in more detail in Chapter 3.

6.4.4 Nonlinearity in diffracted wave spectra

While nonlinearity in the diffracted spectra has been observed at several wave probe locations for both the 0° and 45° headings, a high frequency peak in the range 1.5 Hz $< f <$ 2 Hz (i.e. of the order $2f_p$) was observed during the 0° heading tests at $(-0.35\text{ m}, 0)$ and was not predicted by linear theory. In terms of the cylinder radius a and cylinder spacing $2a$, this measurement position corresponds to $(-1.72a, 0)$, which represents a point along the longitudinal model centreline and between the upwave cylinders (just downwave of a line joining the centres of the upwave cylinders at $x = -2a$).

In comparison with Figure 5.20 from Chapter 5, which plots second order amplitude versus position (the left centre subplot) for the regular wave frequency nearest to the peak frequency (f = 0.8000 Hz), measurements at this point indicate significant second order response. In addition, the afforementioned work of Ferrant (1999), using a fully nonlinear BEM for time domain simulations, produced similar results for the diffraction of regular waves from an array of four columns. Again for a square array of cylinders, heading 0°, with twice the spacing considered here ($4a$) and incident waves of $ka = \frac{\pi}{5} \approx 0.63$ (which is close to the range considered here), Ferrant identified higher order scattered waves located predominantly between the upwave cylinders.

Test	f_p selected [Hz]	H_s selected [m]	f_p computed [Hz]	H_s computed [m]	$H_{s\,\text{filtered}}$ $S\,(f > 1.5f_p) = 0$ [m]
f_i1H_s1	0.8000	0.1300	0.8250	0.1141	0.1090
f_i2H_s2	0.7686	0.1400	0.7206	0.1208	0.1124
f_i3H_s3	0.7406	0.1400	0.7406	0.1239	0.1174

Table 6.1. Irregular wave test peak frequencies and significant wave heights

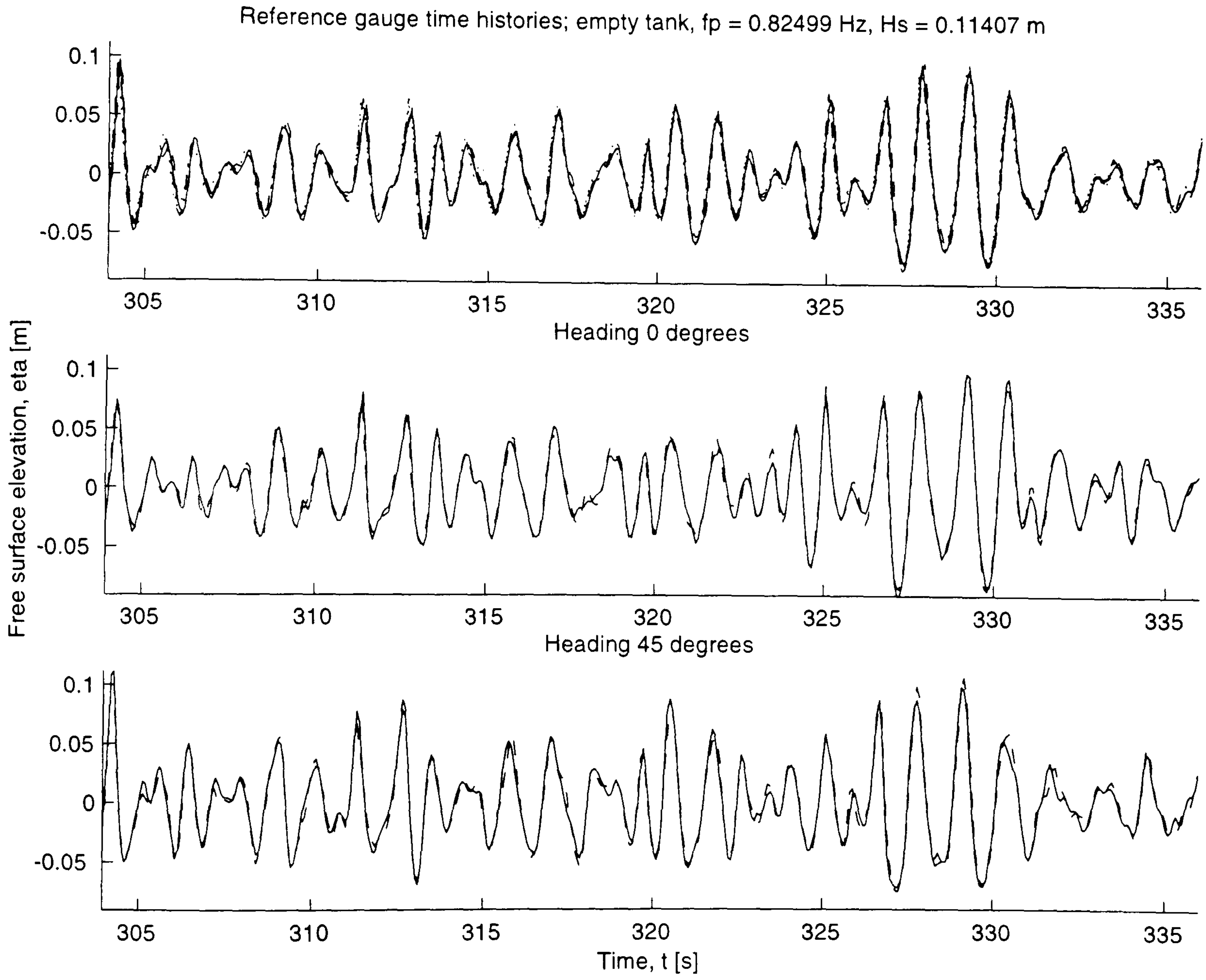

Figure 6.1. Test repeatability demonstrated through free surface elevation vs. time at reference wave probes

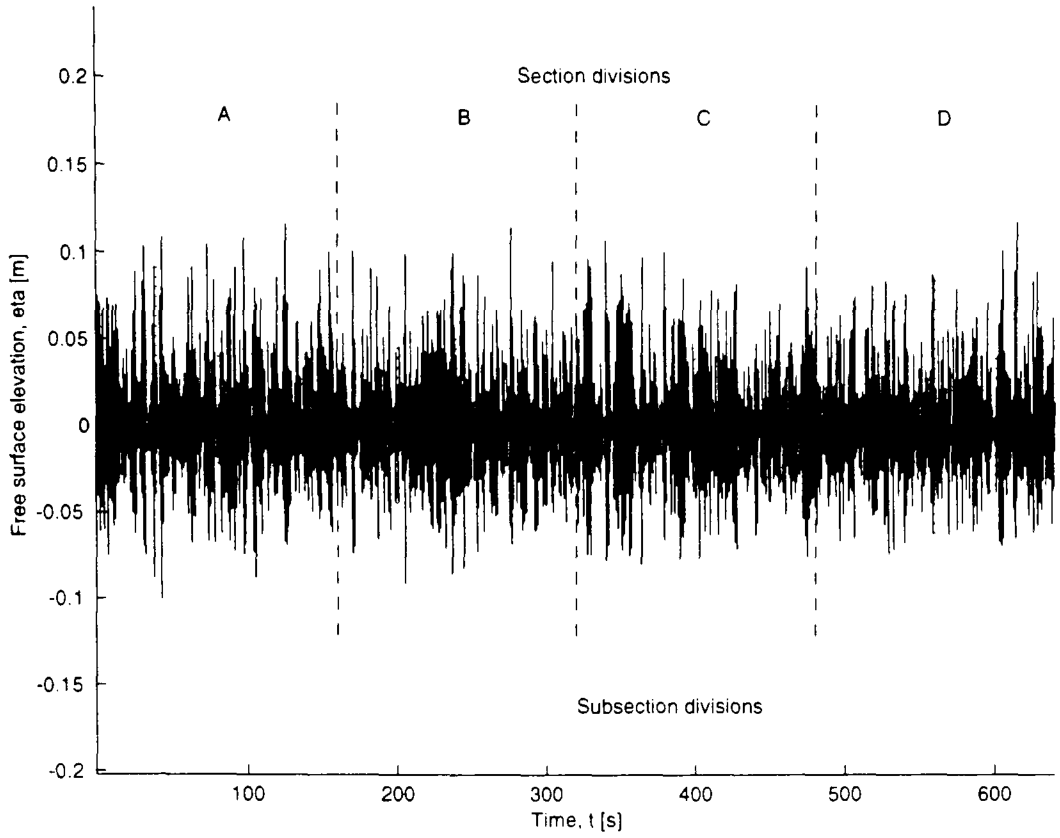

Figure 6.2. Free surface elevation vs. time for the entire data record; measurements at the reference wave probe during the empty tank test

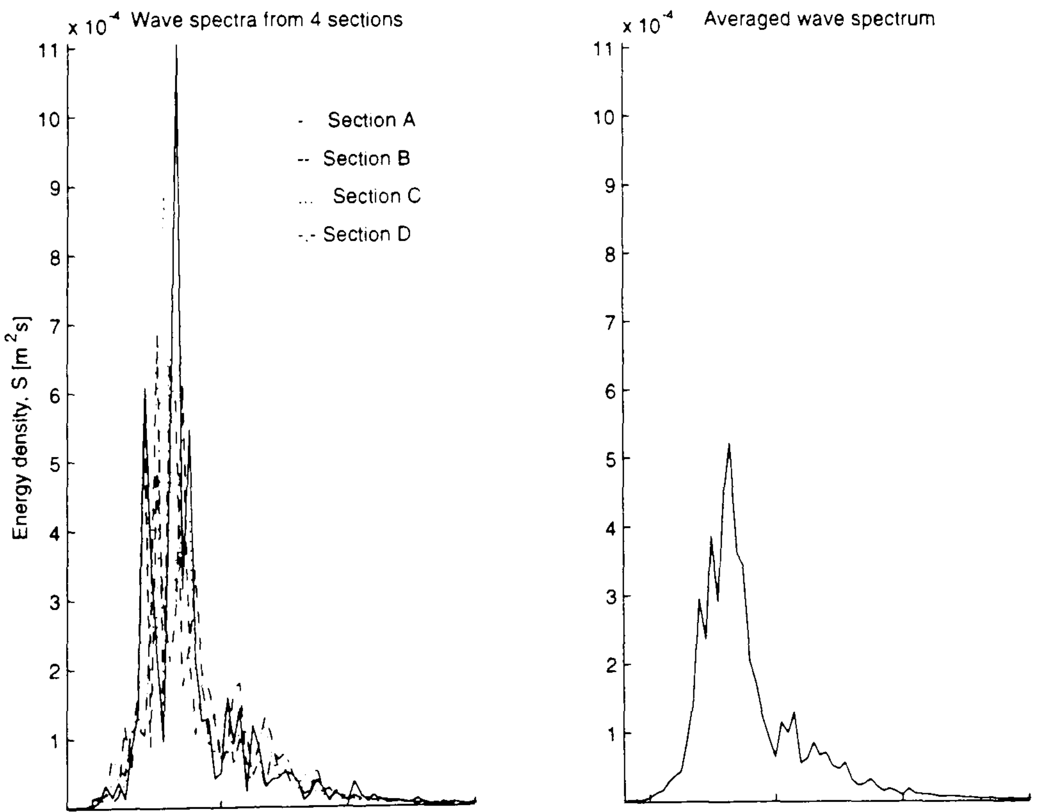

Figure 6.3. Demonstration of average incident wave spectrum computation; wave spectrum from 4 sections are plotted in the left subplot and the mean incident spectrum in the right subplot

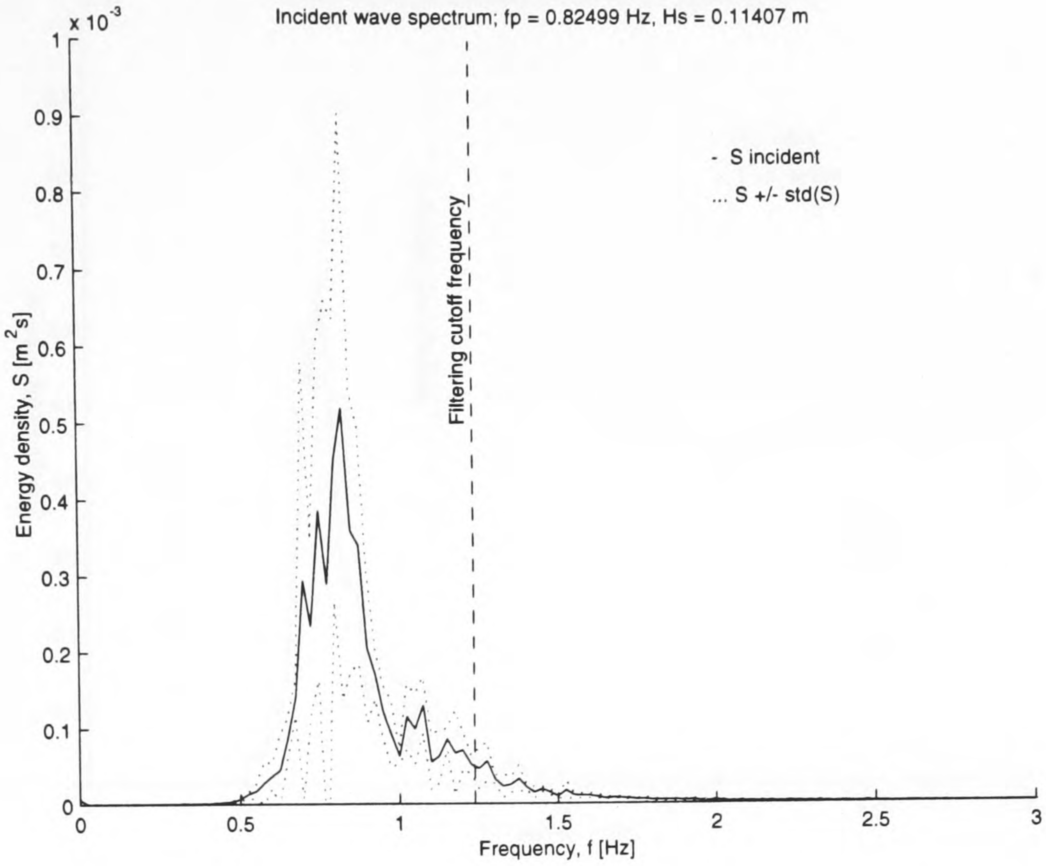

Figure 6.4. Incident wave spectrum $f_i 1 H_s 1$

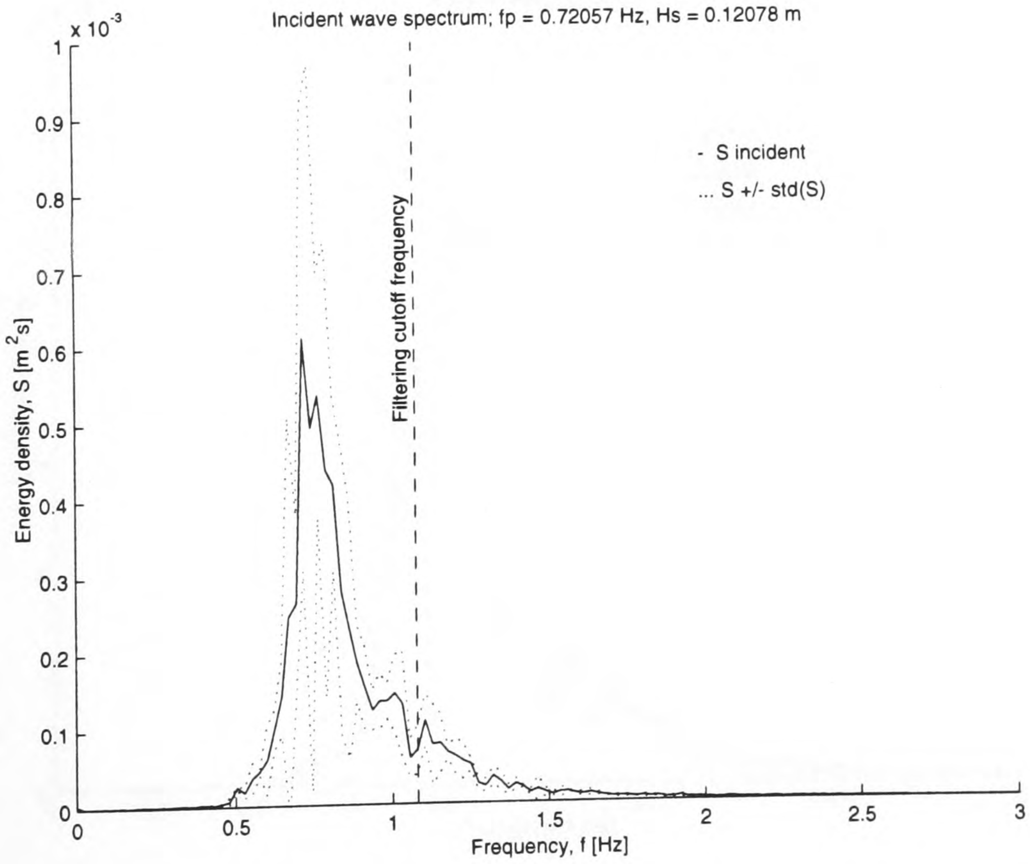

Figure 6.5. Incident wave spectrum $f_i 2 H_s 2$

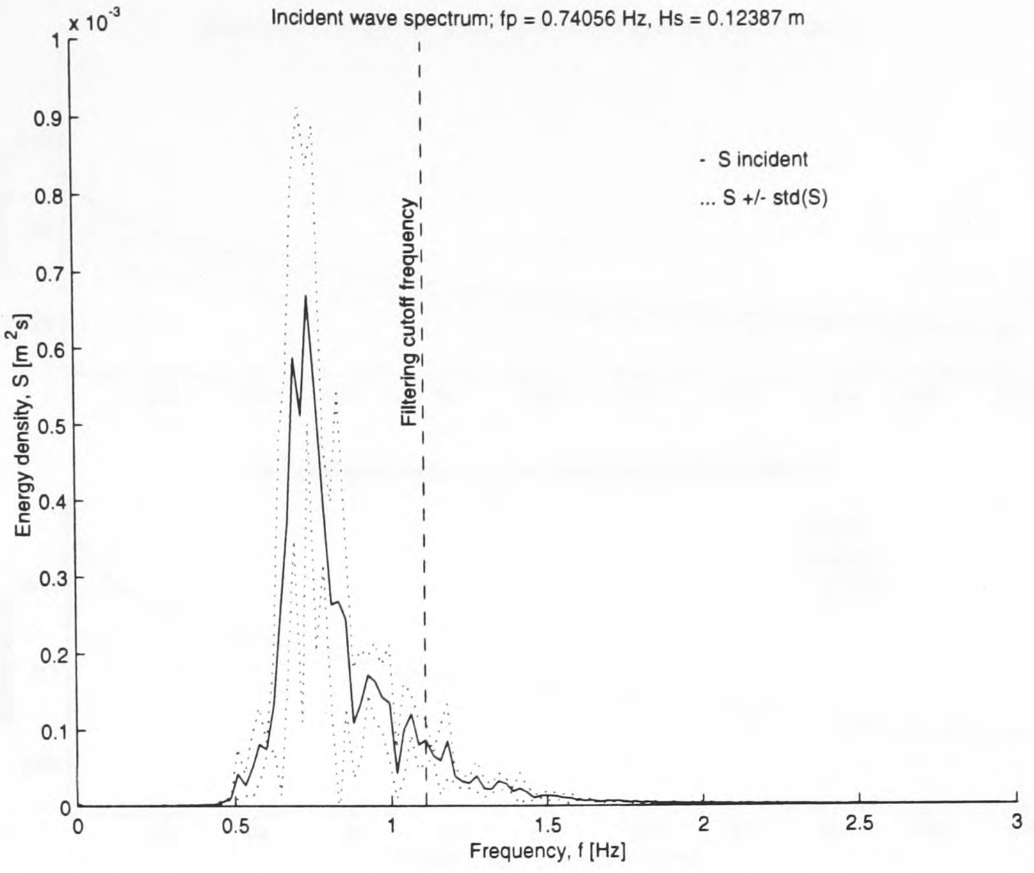

Figure 6.6. Incident wave spectrum f_i3H_s3

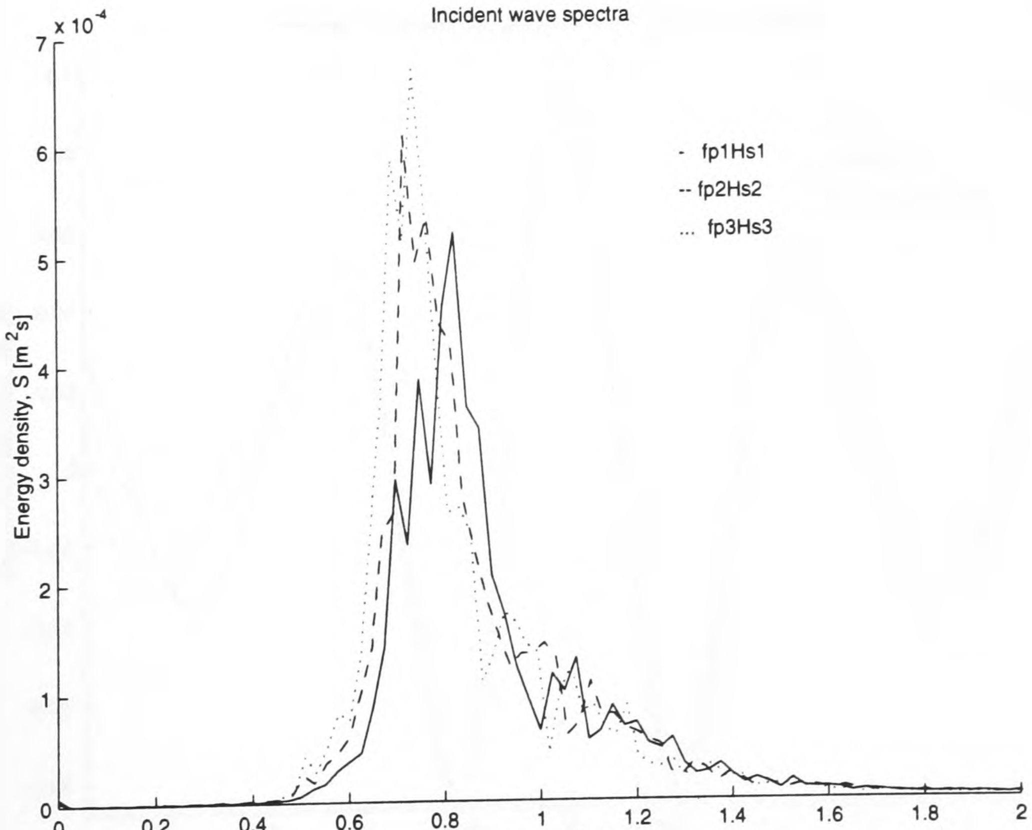

Figure 6.7. Incident wave spectra f_i1H_s1, f_i2H_s2, and f_i3H_s3

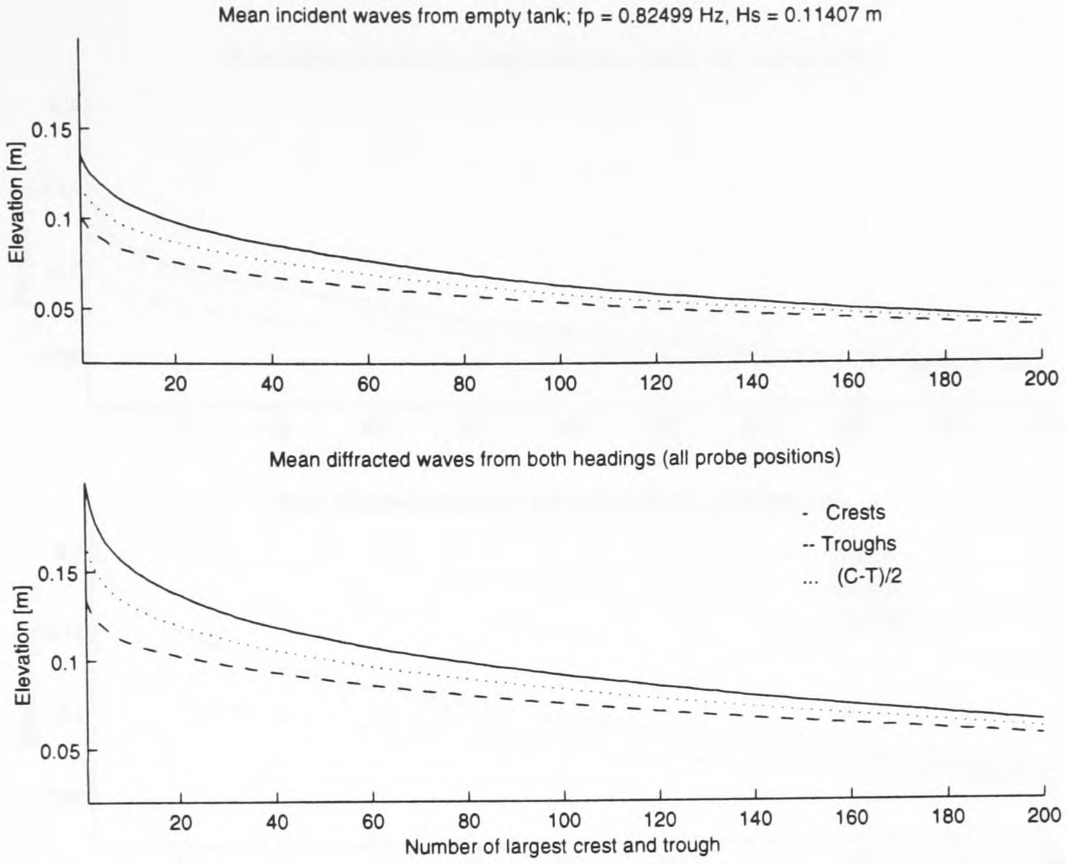

Figure 6.8. Average incident and diffracted large crests and troughs f_i1H_s1

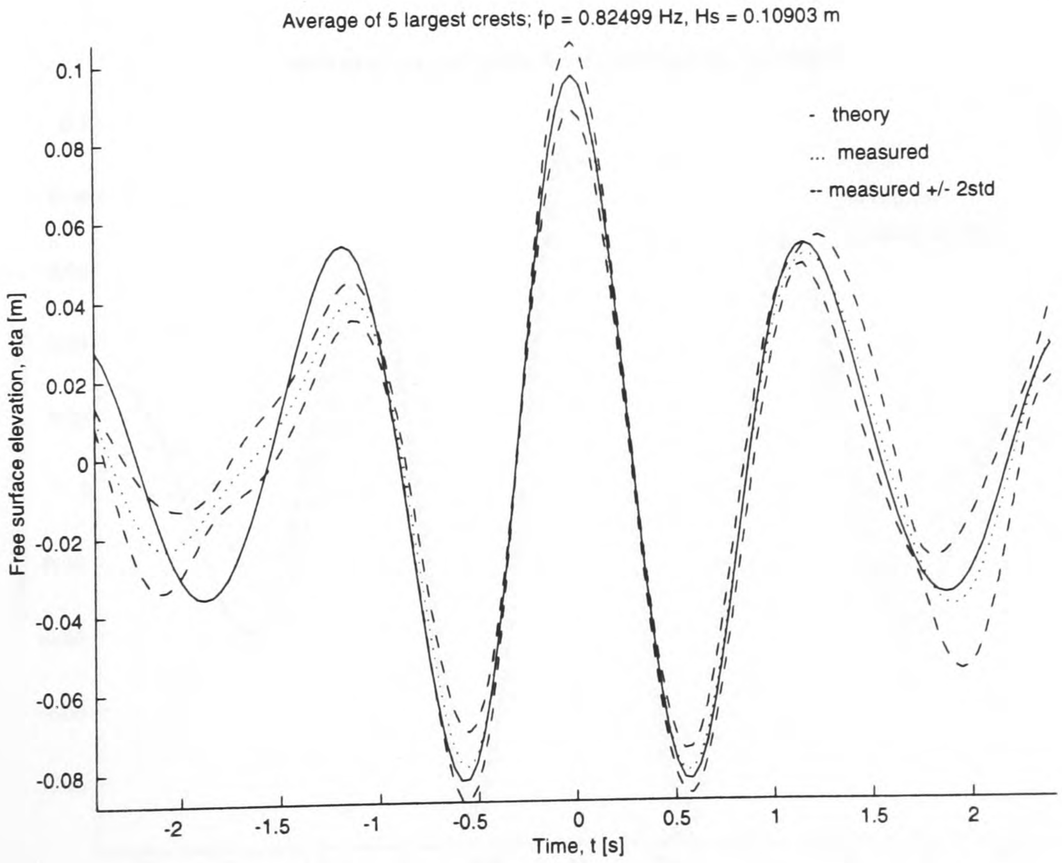

Figure 6.9. Average of 5 largest incident linearised crests f_i1H_s1

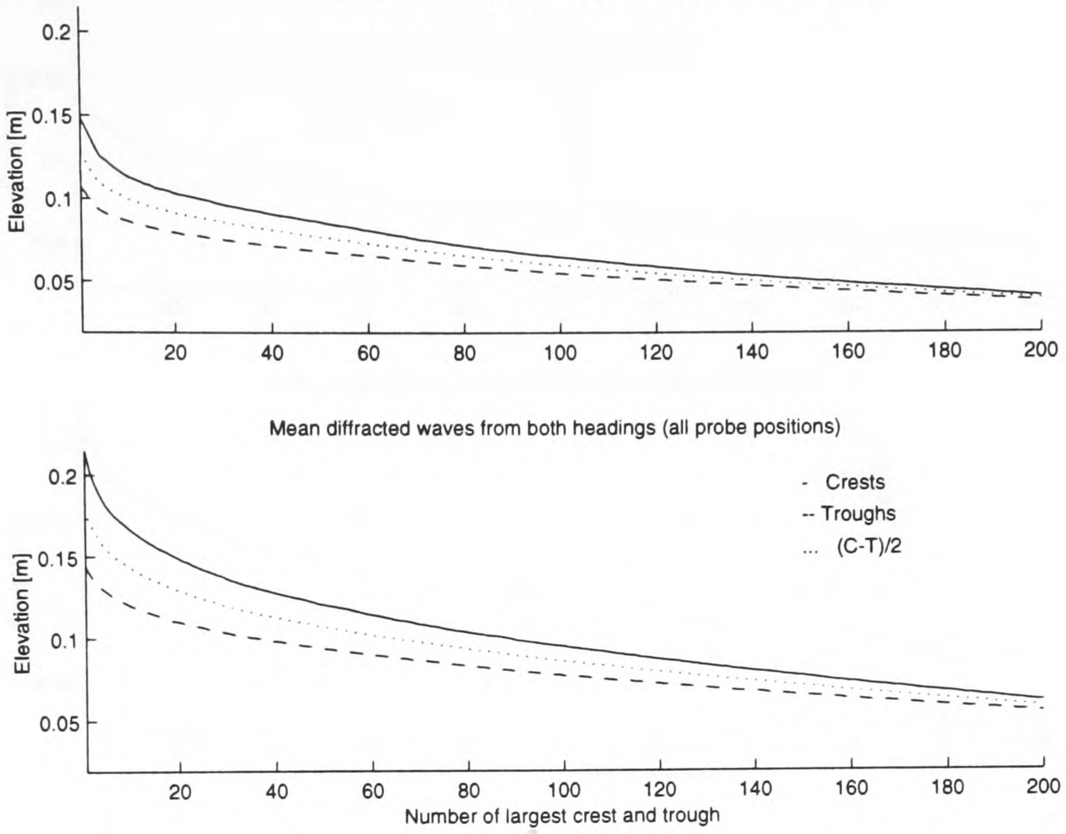
Mean incident waves from empty tank; fp = 0.72057 Hz, Hs = 0.12078 m

Mean diffracted waves from both headings (all probe positions)

Figure 6.10. Average incident and diffracted large crests and troughs f_i2H_s2

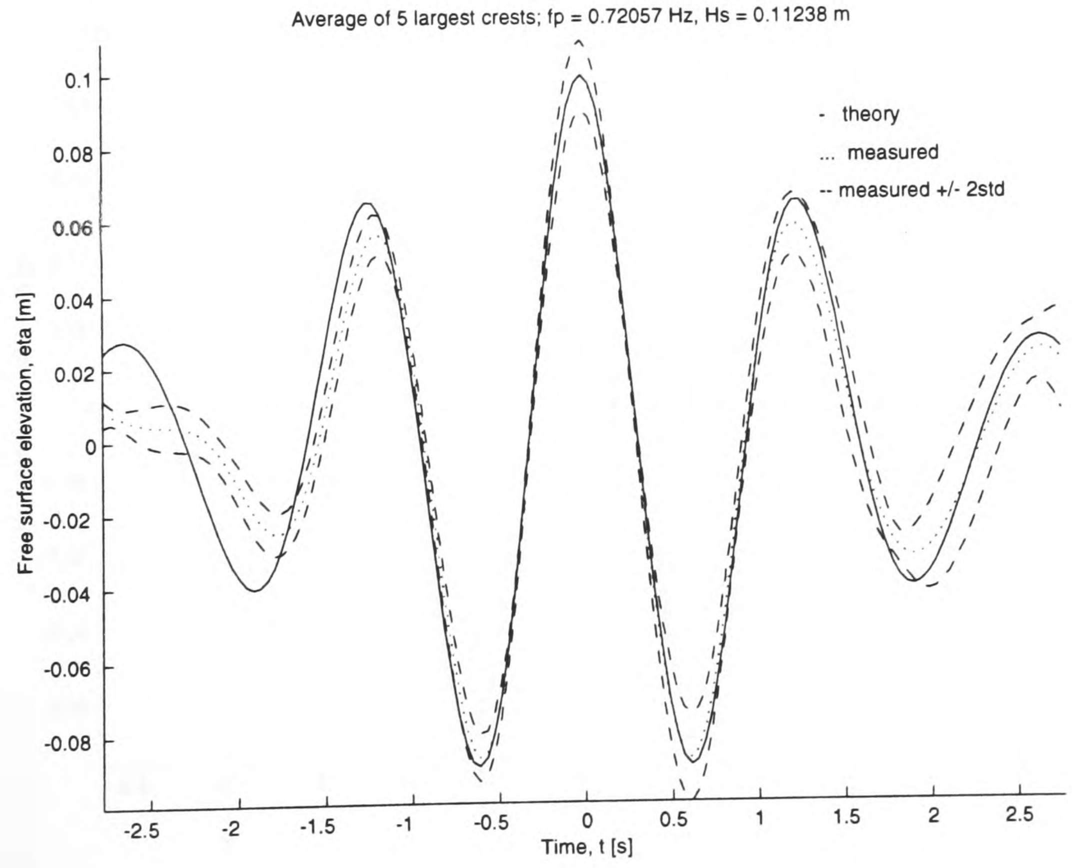
Average of 5 largest crests; fp = 0.72057 Hz, Hs = 0.11238 m

Figure 6.11. Average of 5 largest incident linearised crests f_i2H_s2

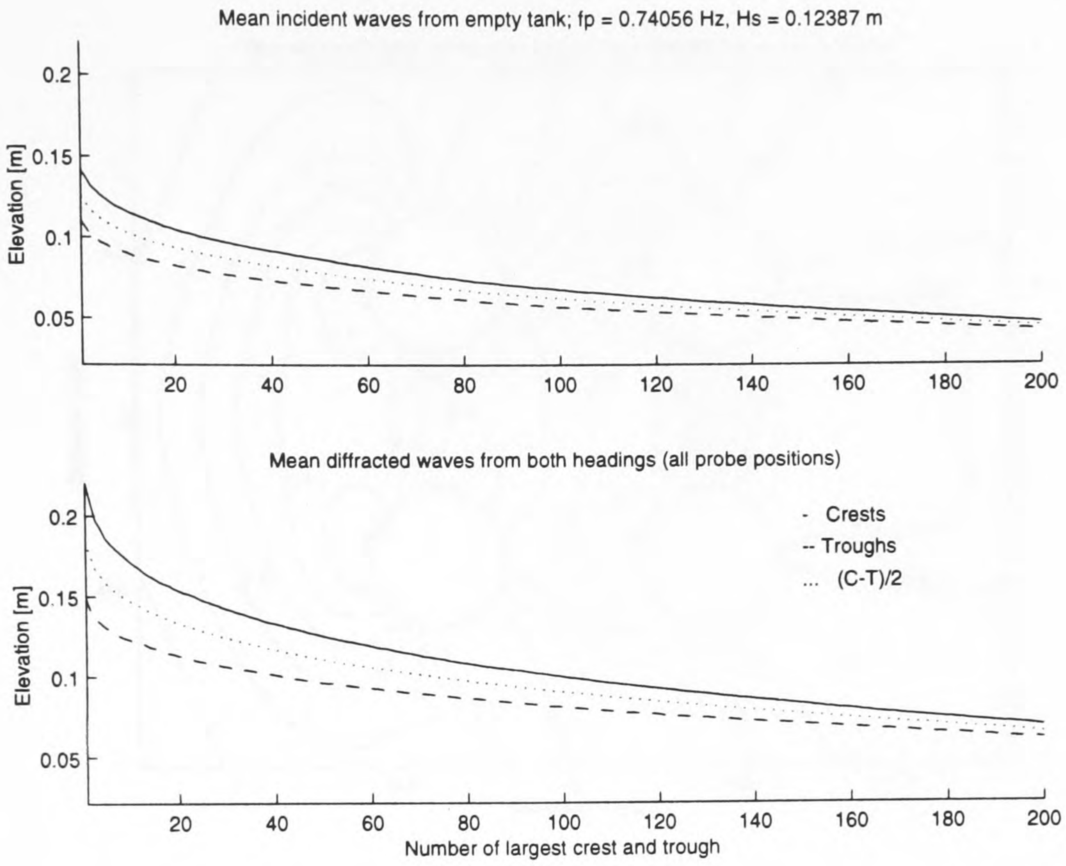

Figure 6.12. Average incident and diffracted large crests and troughs $f_i 3 H_s 3$

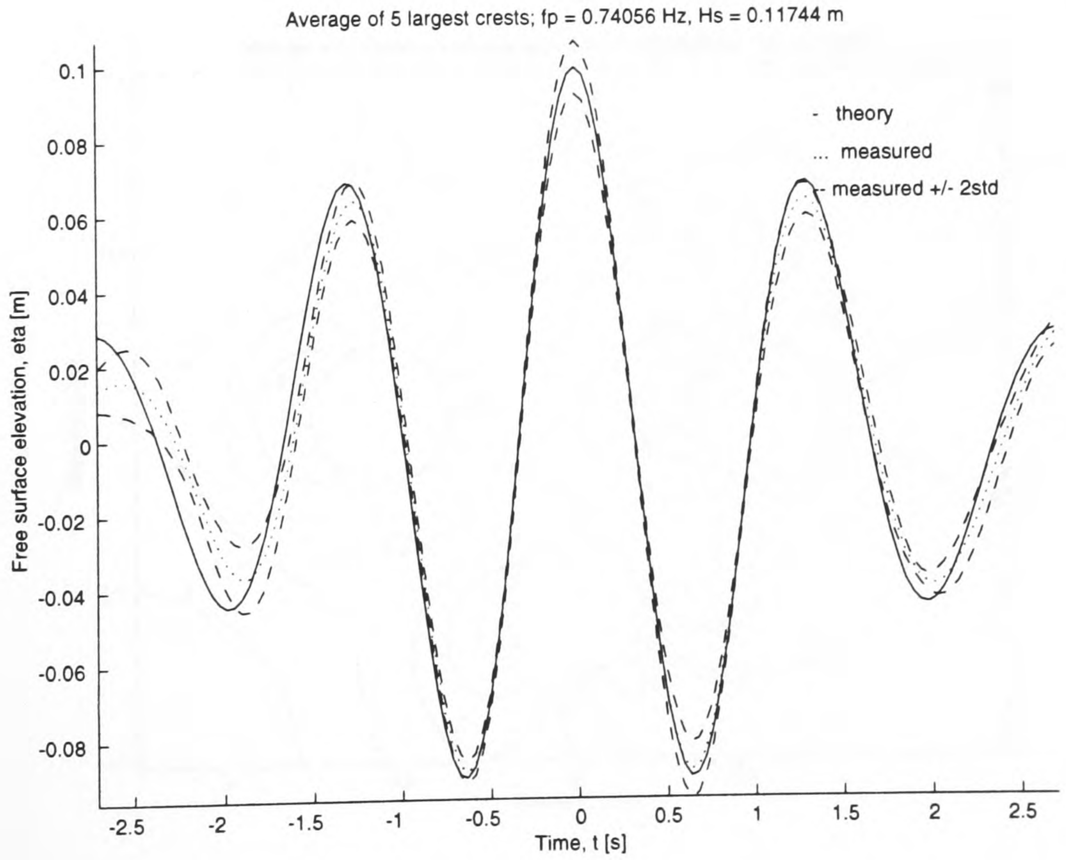

Figure 6.13. Average of 5 largest incident linearised crests $f_i 3 H_s 3$

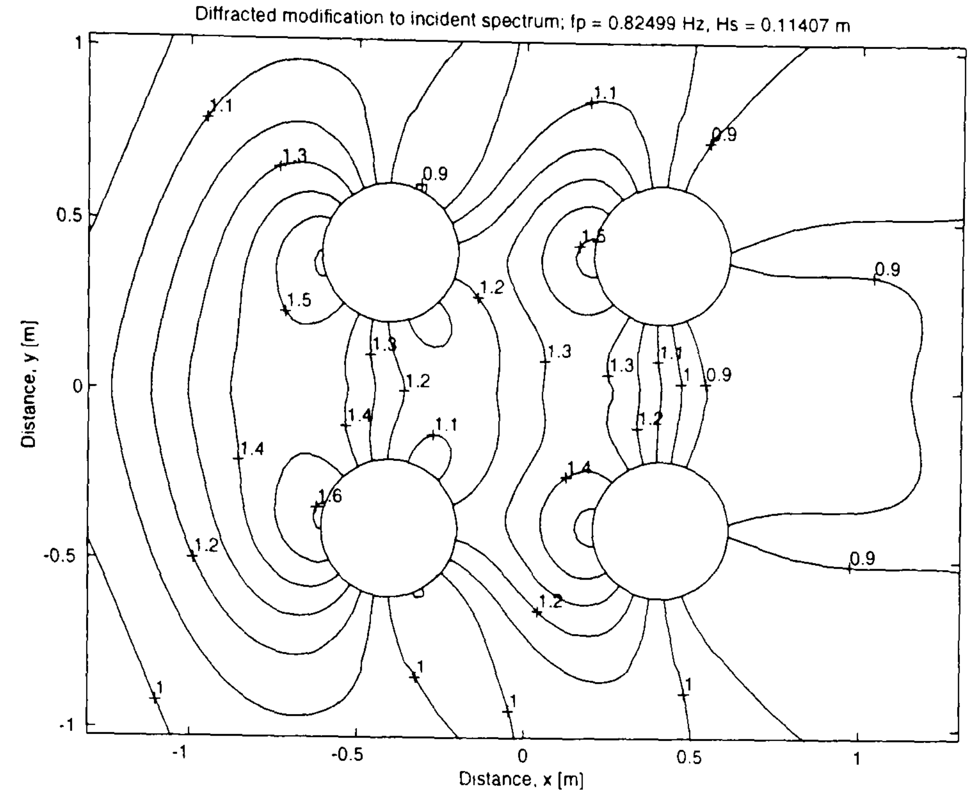

Figure 6.14. Diffracted modification to incident wave spectrum; $f_i 1 H_s 1$ heading 0°

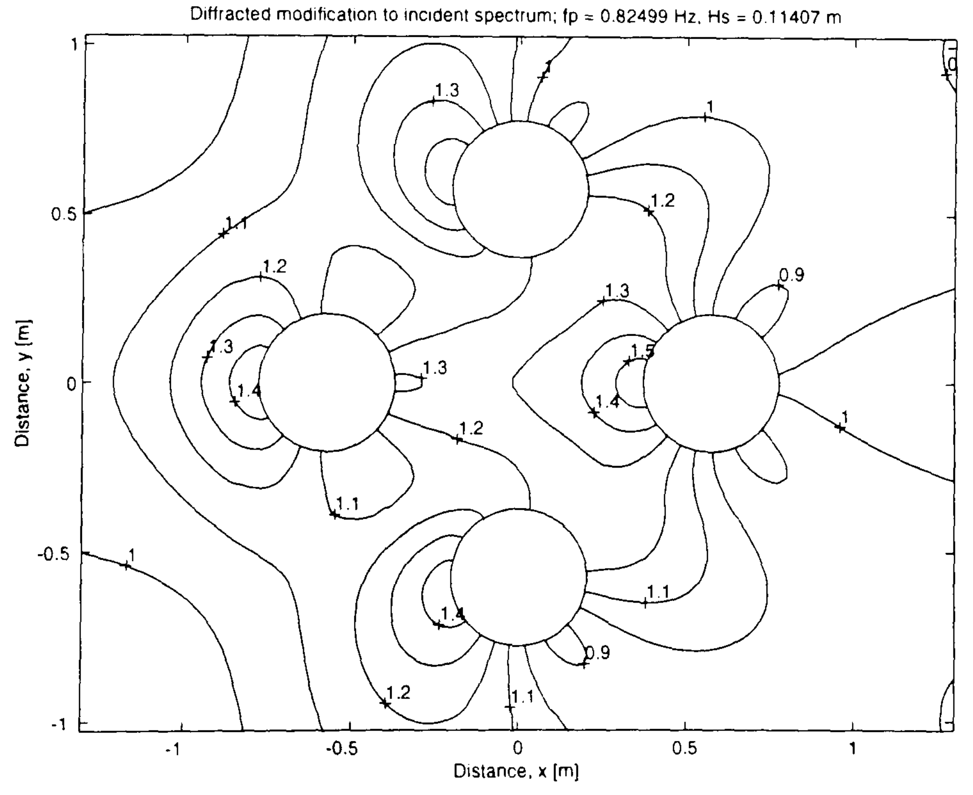

Figure 6.15. Diffracted modification to incident wave spectrum; $f_i 1 H_s 1$ heading 45°

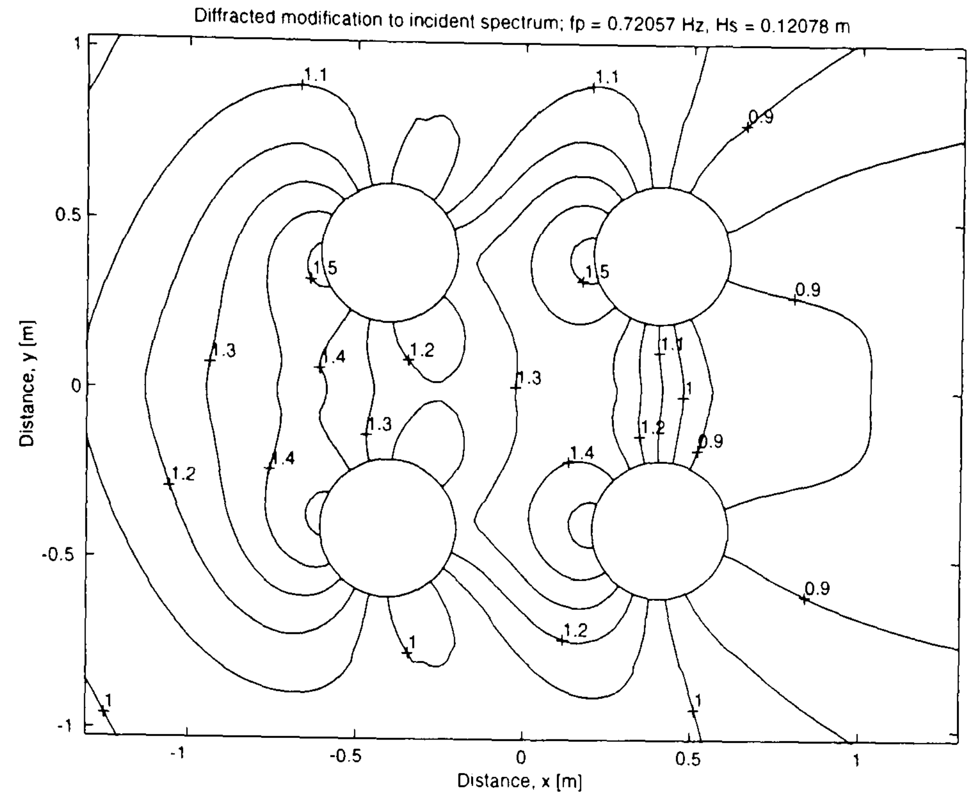

Figure 6.16. Diffracted modification to incident wave spectrum; f_i2H_s2 heading 0°

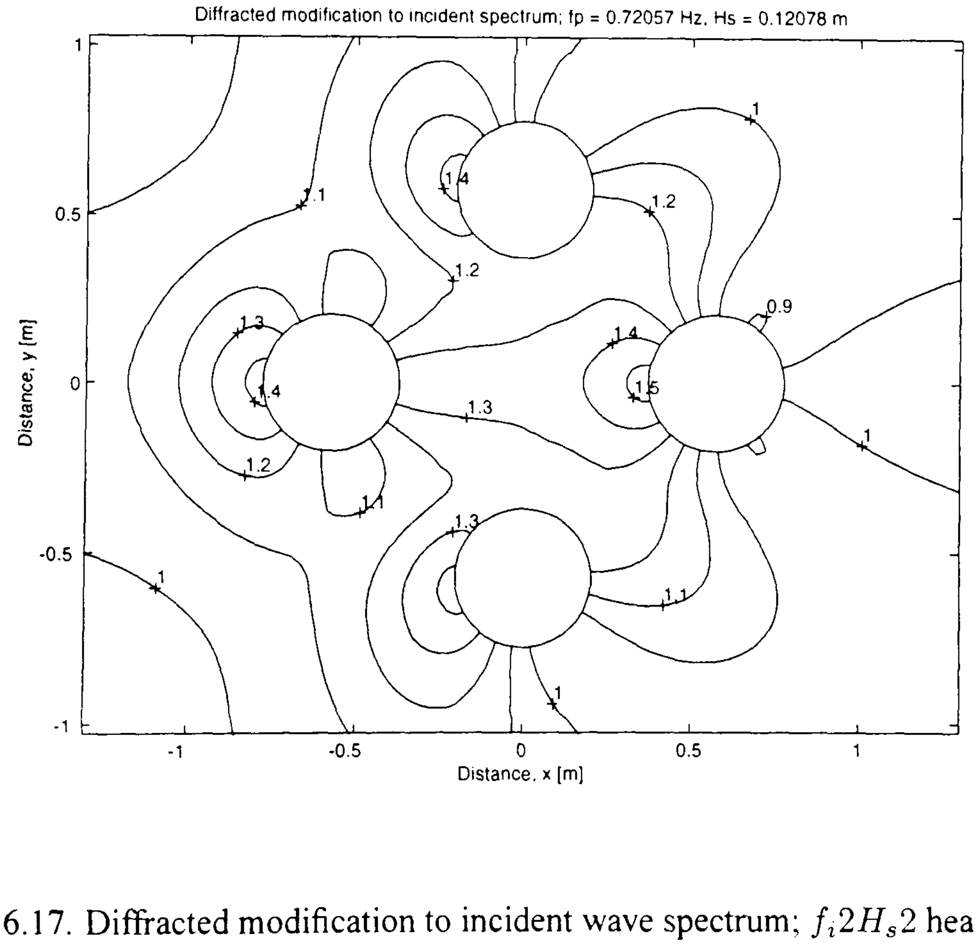

Figure 6.17. Diffracted modification to incident wave spectrum; f_i2H_s2 heading 45°

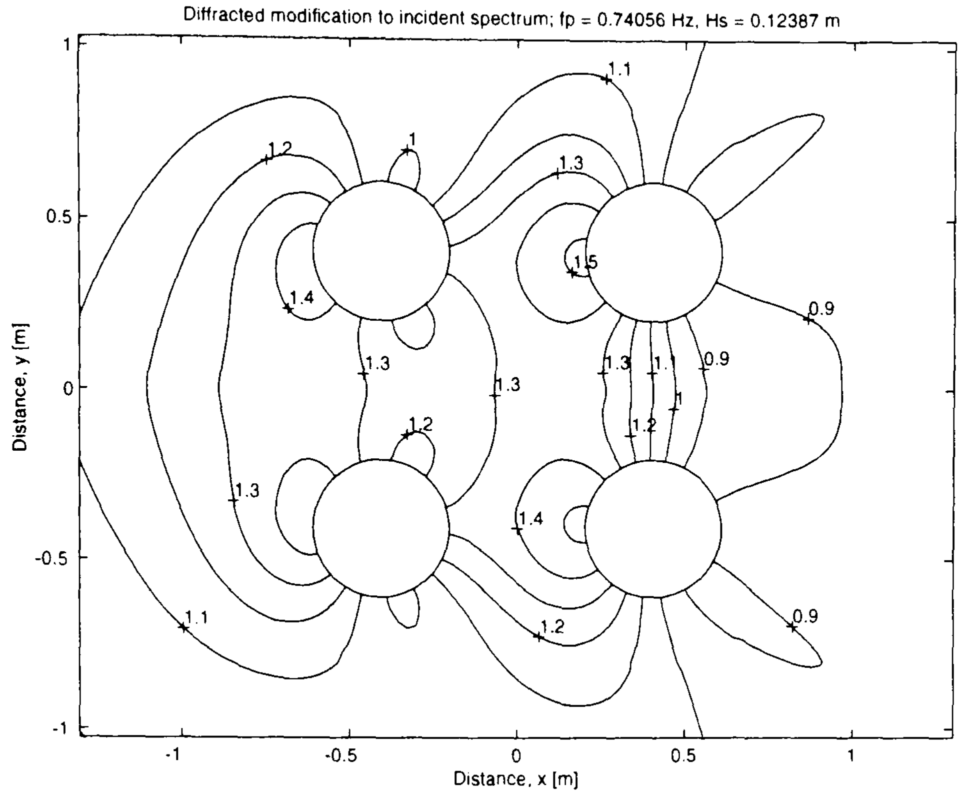

Figure 6.18. Diffracted modification to incident wave spectrum; $f_i 3 H_s 3$ heading 0°

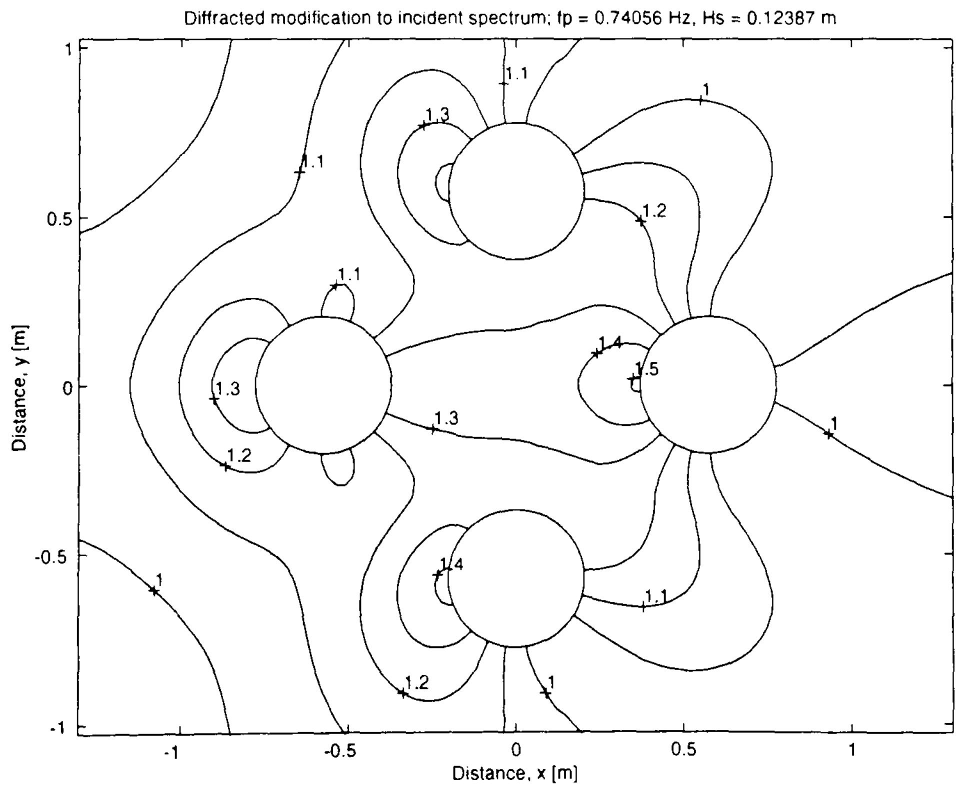

Figure 6.19. Diffracted modification to incident wave spectrum; $f_i 3 H_s 3$ heading 45°

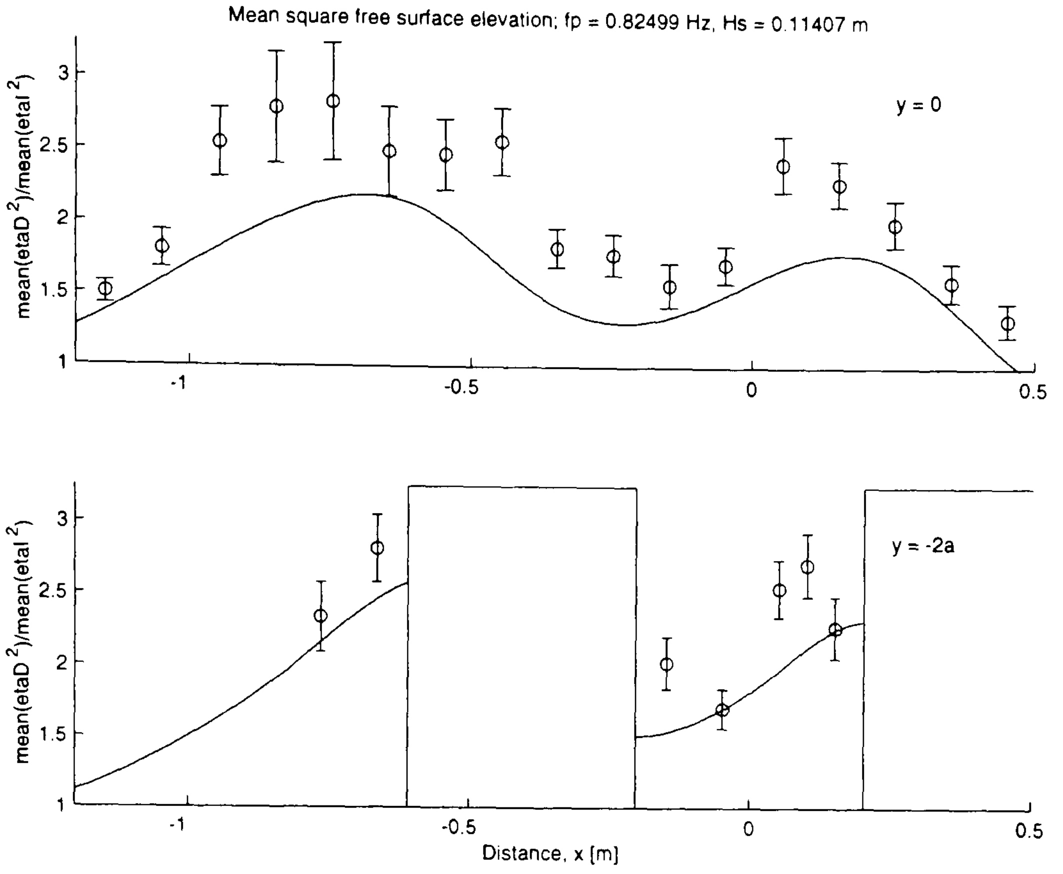

Figure 6.20. Mean square free surface elevation $\overline{\eta^2}$ vs. position; $f_i 1 H_s 1$ heading 0°

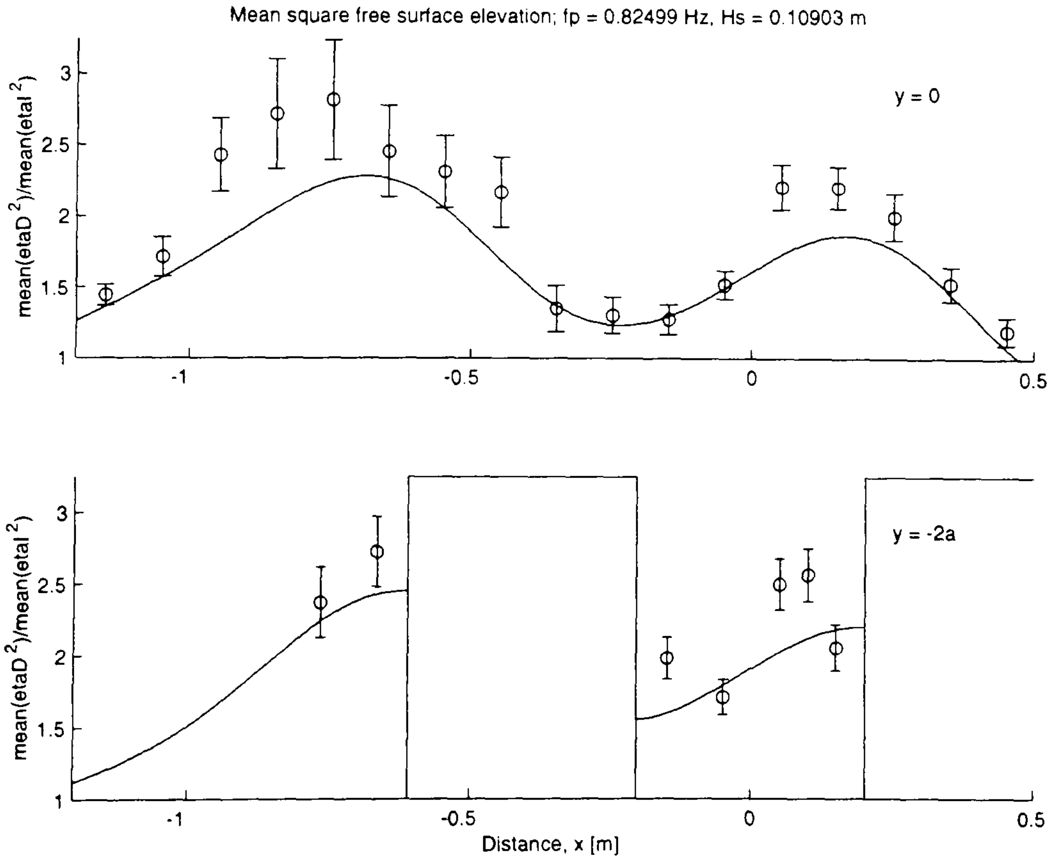

Figure 6.21. Mean square free surface elevation $\overline{\eta^2}$ vs. position; $f_i 1 H_s 1$ heading 0°; spectra filtered above $1.25 f_p$

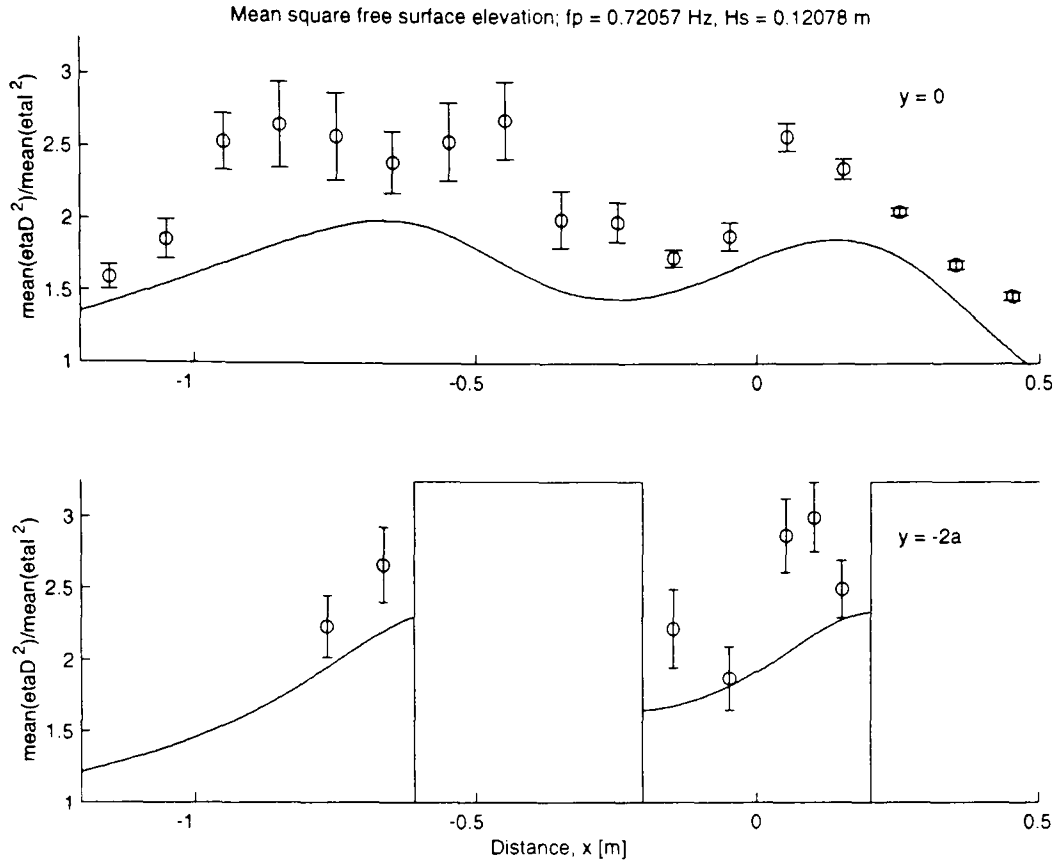

Figure 6.22. Mean square free surface elevation $\overline{\eta^2}$ vs. position; $f_i 2 H_s 2$ heading 0°

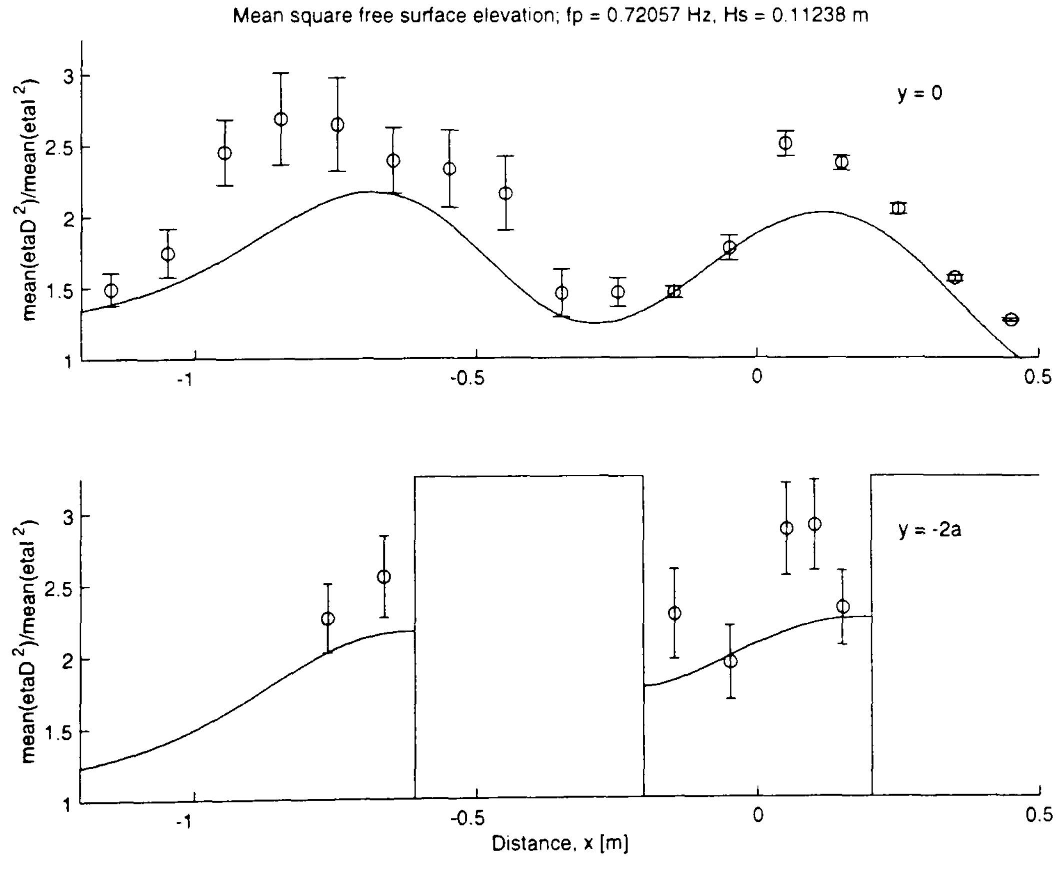

Figure 6.23. Mean square free surface elevation $\overline{\eta^2}$ vs. position; $f_i 2 H_s 2$ heading 0°; spectra filtered above $1.25 f_p$

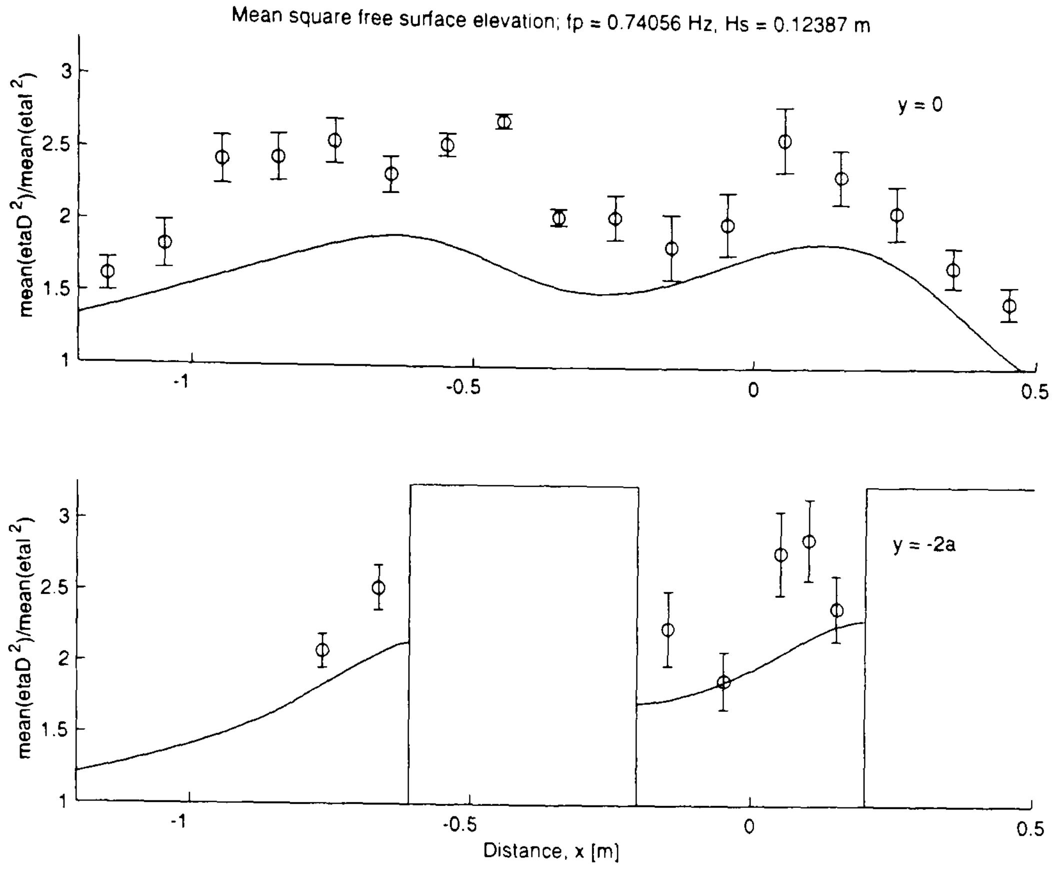

Figure 6.24. Mean square free surface elevation $\overline{\eta^2}$ vs. position; f_i3H_s3 heading 0°

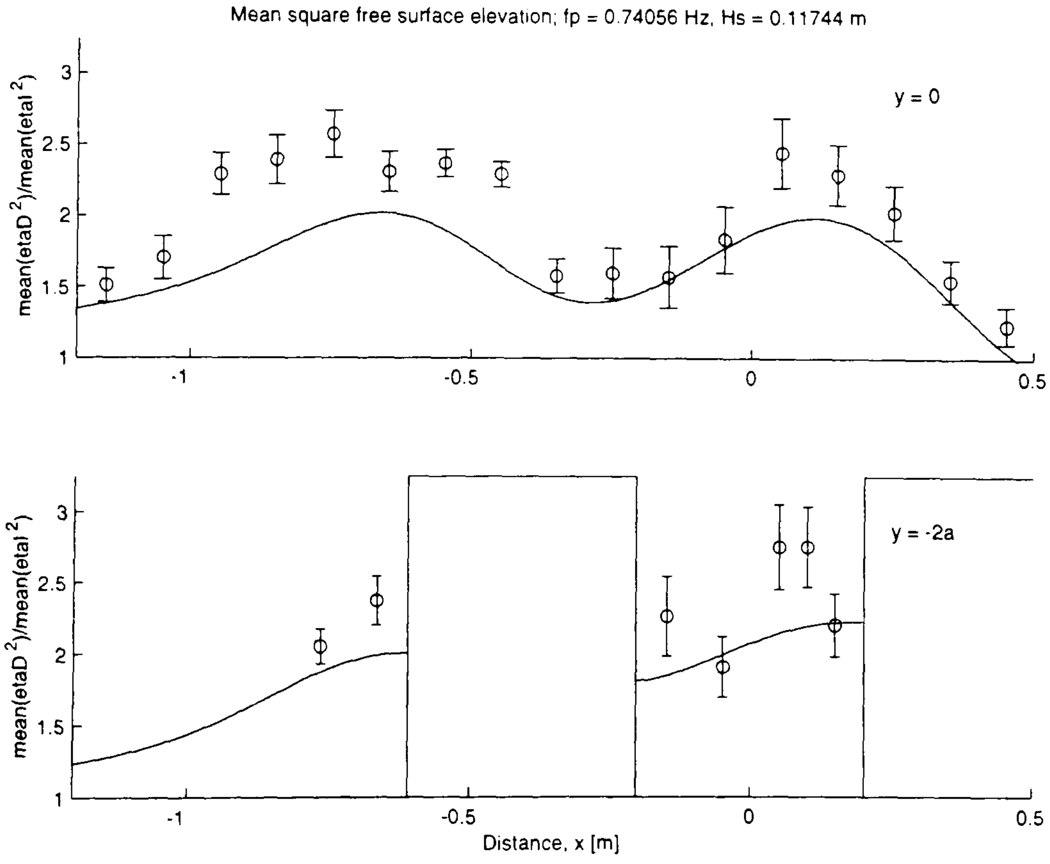

Figure 6.25. Mean square free surface elevation $\overline{\eta^2}$ vs. position; f_i3H_s3 heading 0°; spectra filtered above $1.25f_p$

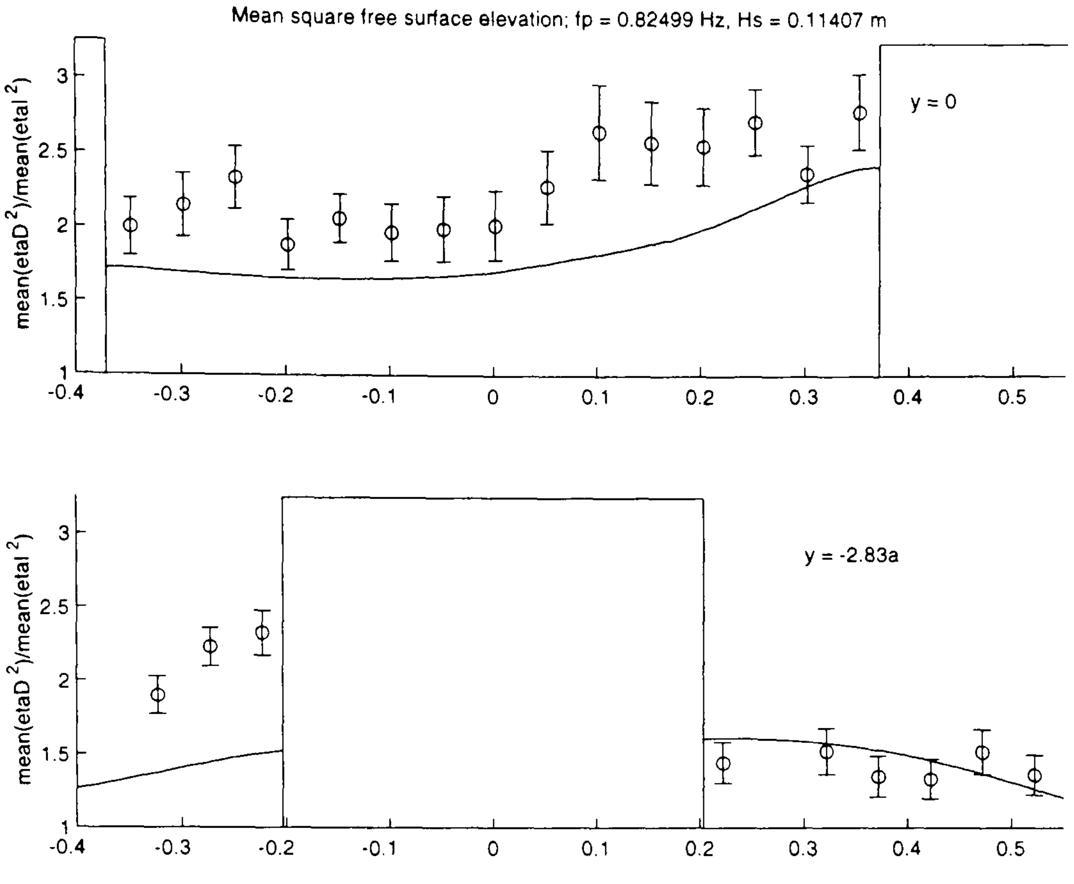

Figure 6.26. Mean square free surface elevation $\overline{\eta^2}$ vs. position; $f_i 1 H_s 1$ heading 45°

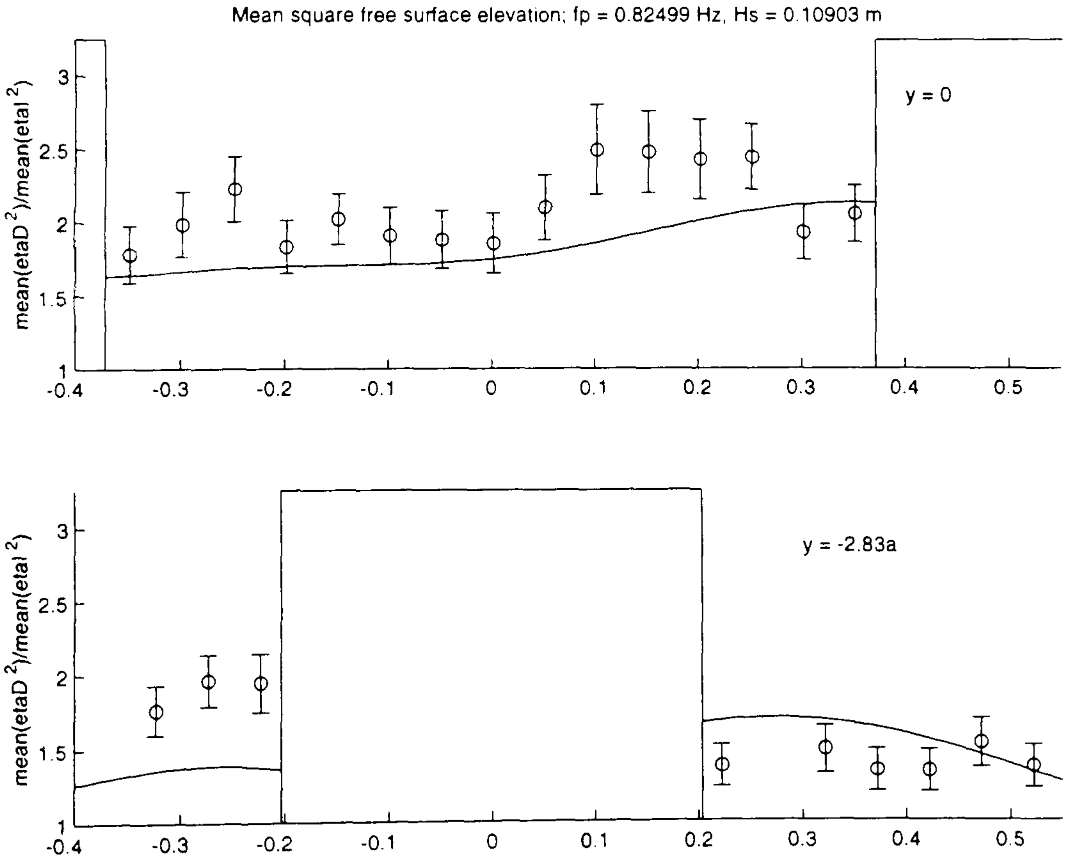

Figure 6.27. Mean square free surface elevation $\overline{\eta^2}$ vs. position; $f_i 1 H_s 1$ heading 45°; spectra filtered above $1.25 f_p$

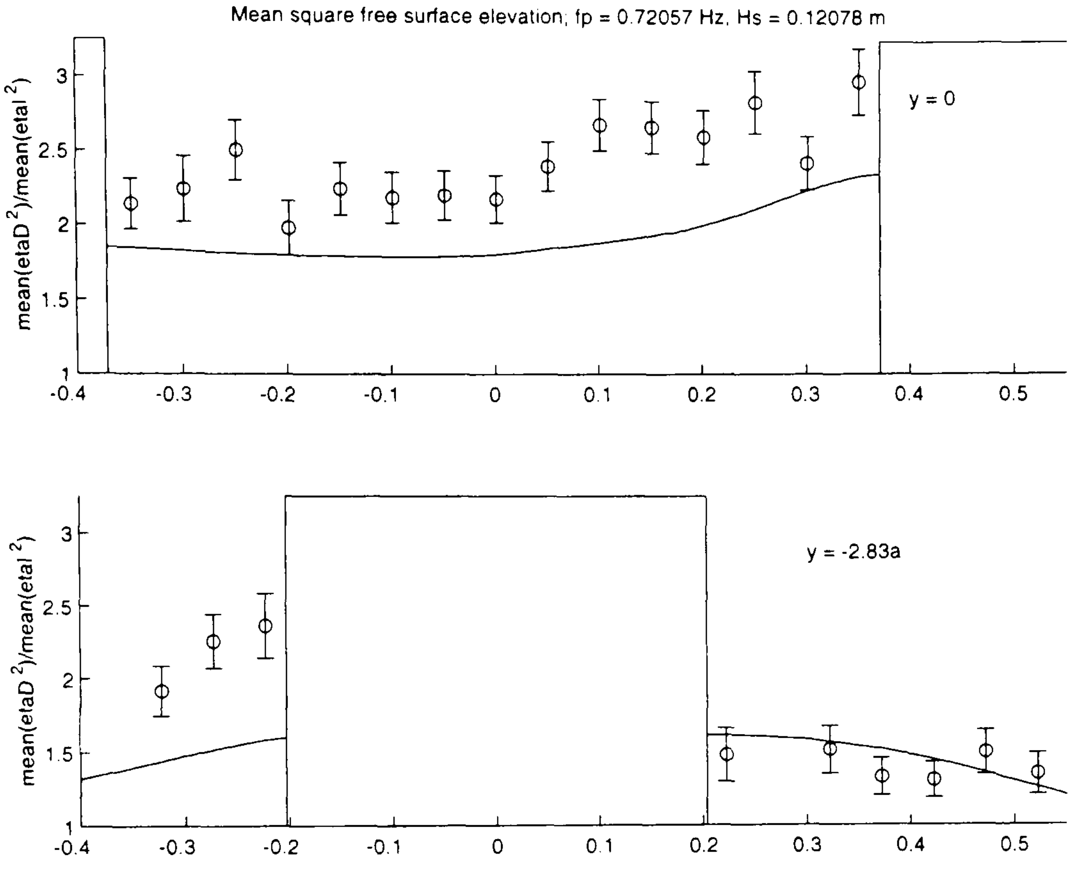

Figure 6.28. Mean square free surface elevation $\overline{\eta^2}$ vs. position; $f_i 2H_s 2$ heading 45°

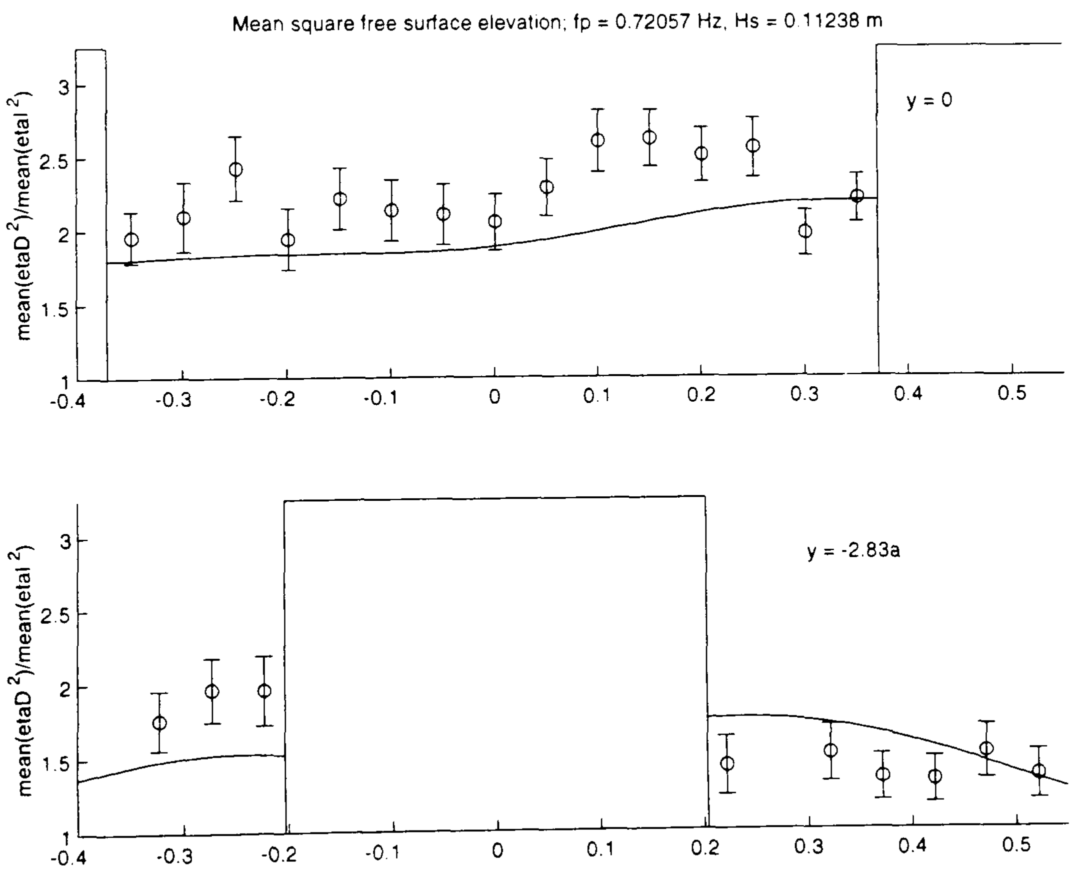

Figure 6.29. Mean square free surface elevation $\overline{\eta^2}$ vs. position; $f_i 2H_s 2$ heading 45°; spectra filtered above $1.25 f_p$

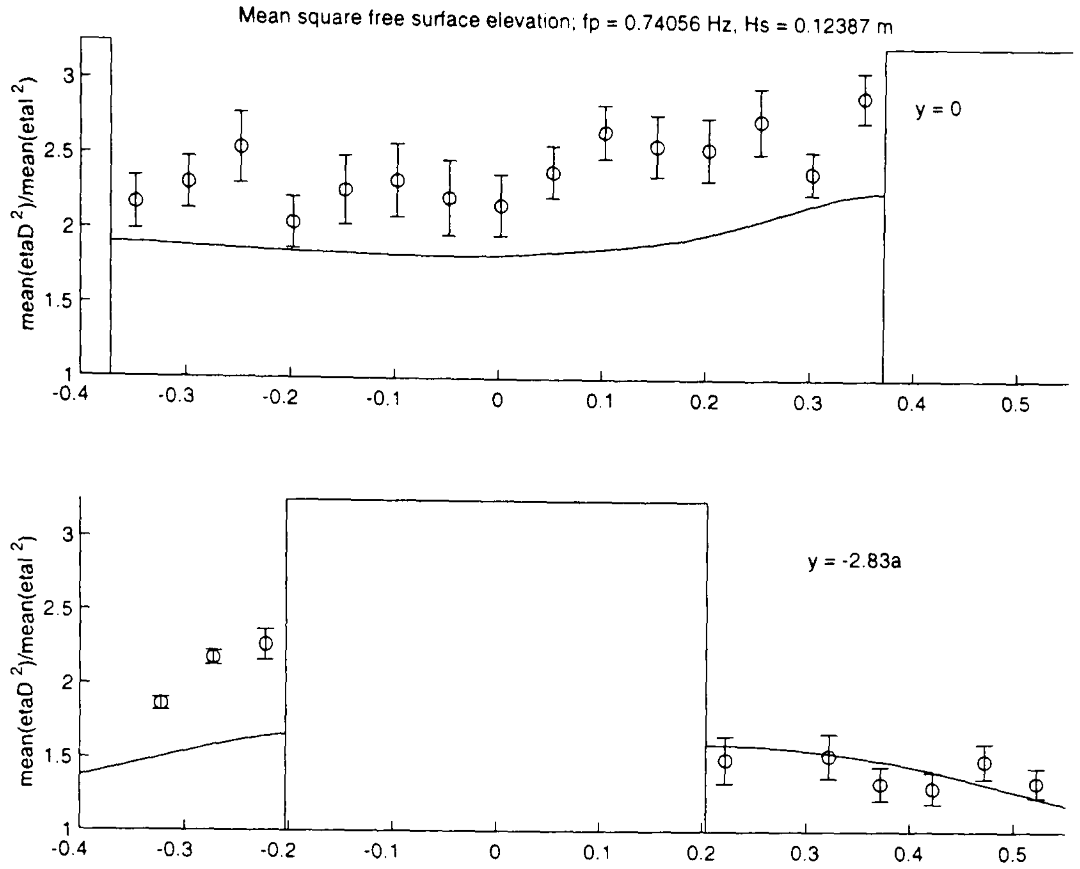
Mean square free surface elevation; fp = 0.74056 Hz, Hs = 0.12387 m

Figure 6.30. Mean square free surface elevation $\overline{\eta^2}$ vs. position; f_i3H_s3 heading 45°

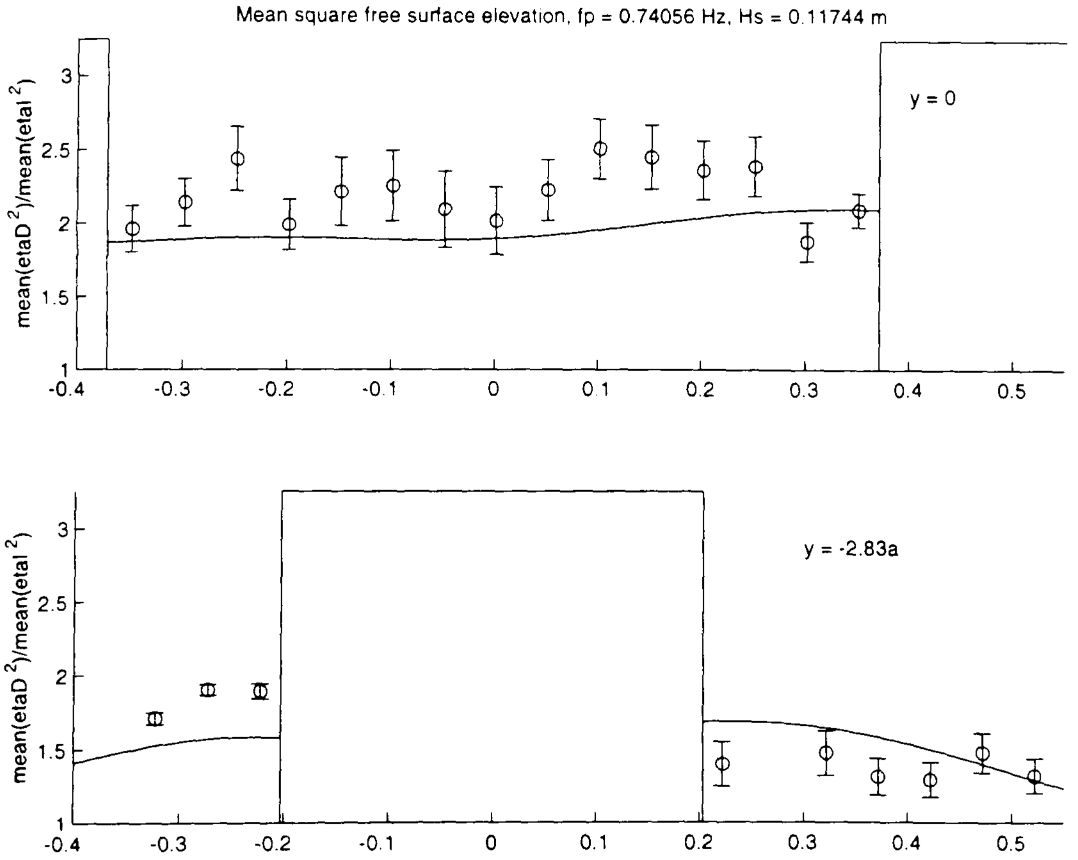
Mean square free surface elevation, fp = 0.74056 Hz, Hs = 0.11744 m

Figure 6.31. Mean square free surface elevation $\overline{\eta^2}$ vs. position; f_i3H_s3 heading 45°; spectra filtered above $1.25f_p$

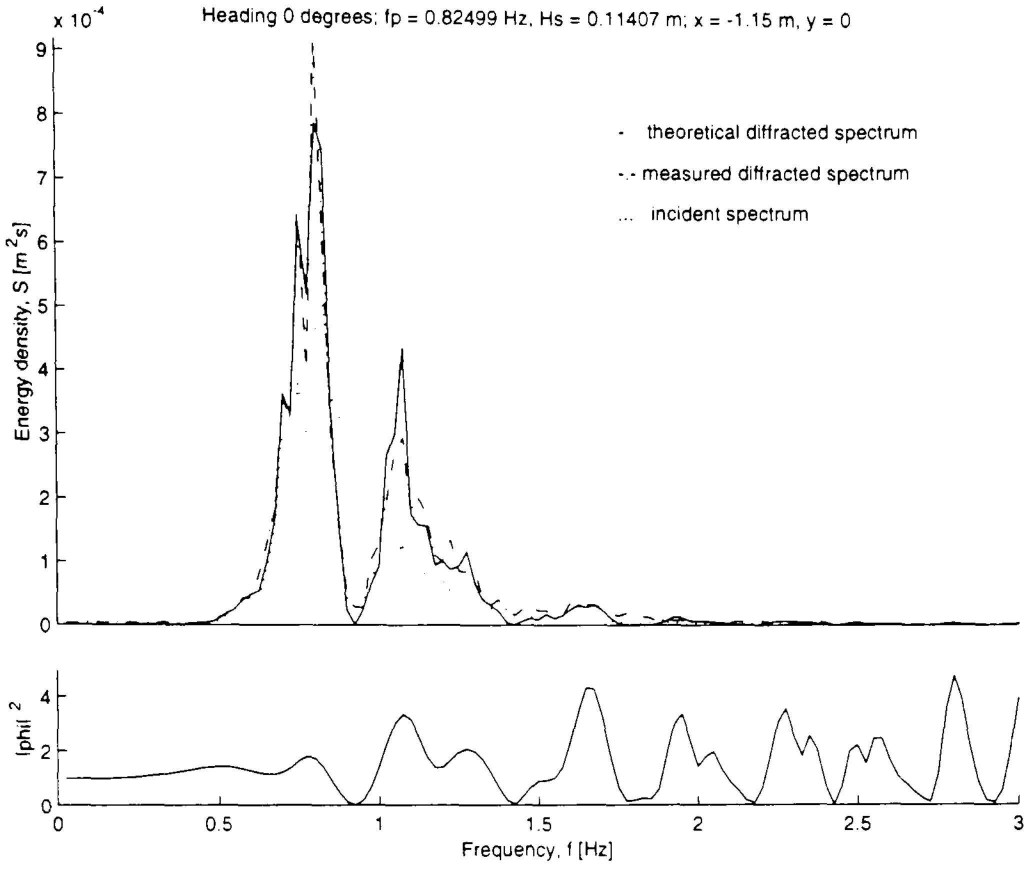

Figure 6.32. Spectral comparison and diffracted modification to incident spectrum at point $(-1.15\,\mathrm{m}, 0)$; $f_i 1 H_s 1$ heading 0°

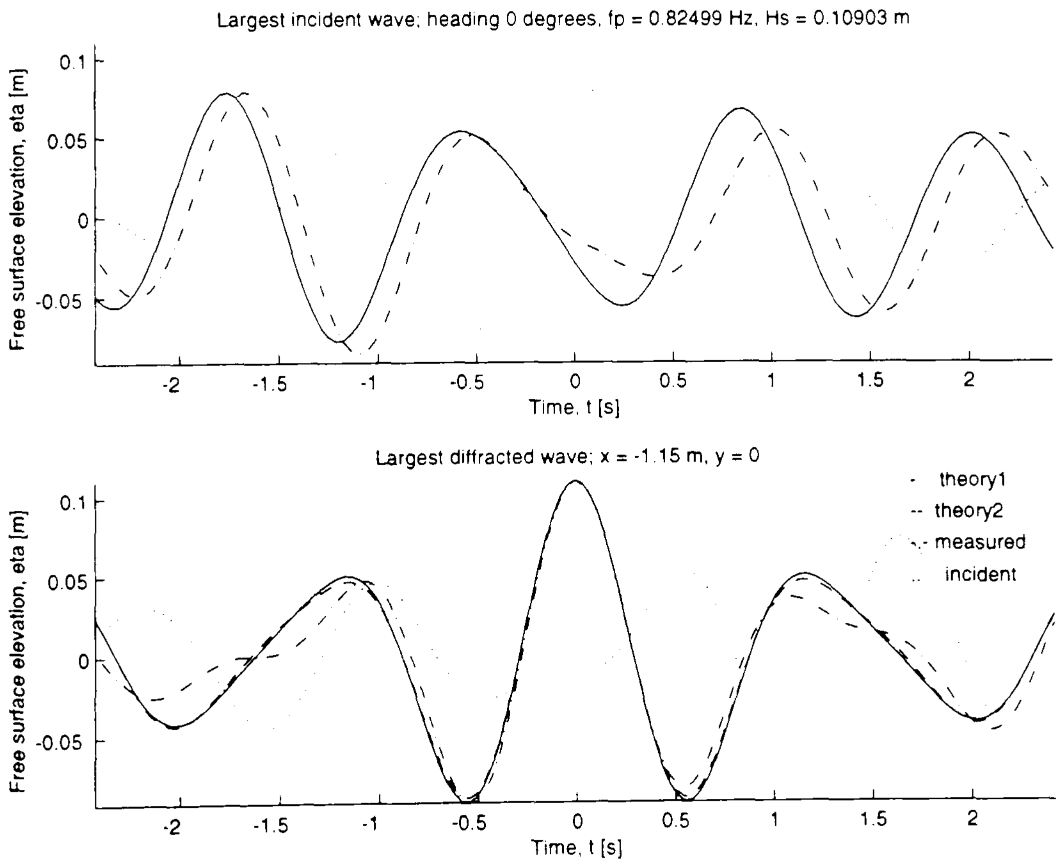

Figure 6.33. Incident and diffracted focused wave group comparison at point $(-1.15\,\mathrm{m}, 0)$; $f_i 1 H_s 1$ heading 0°

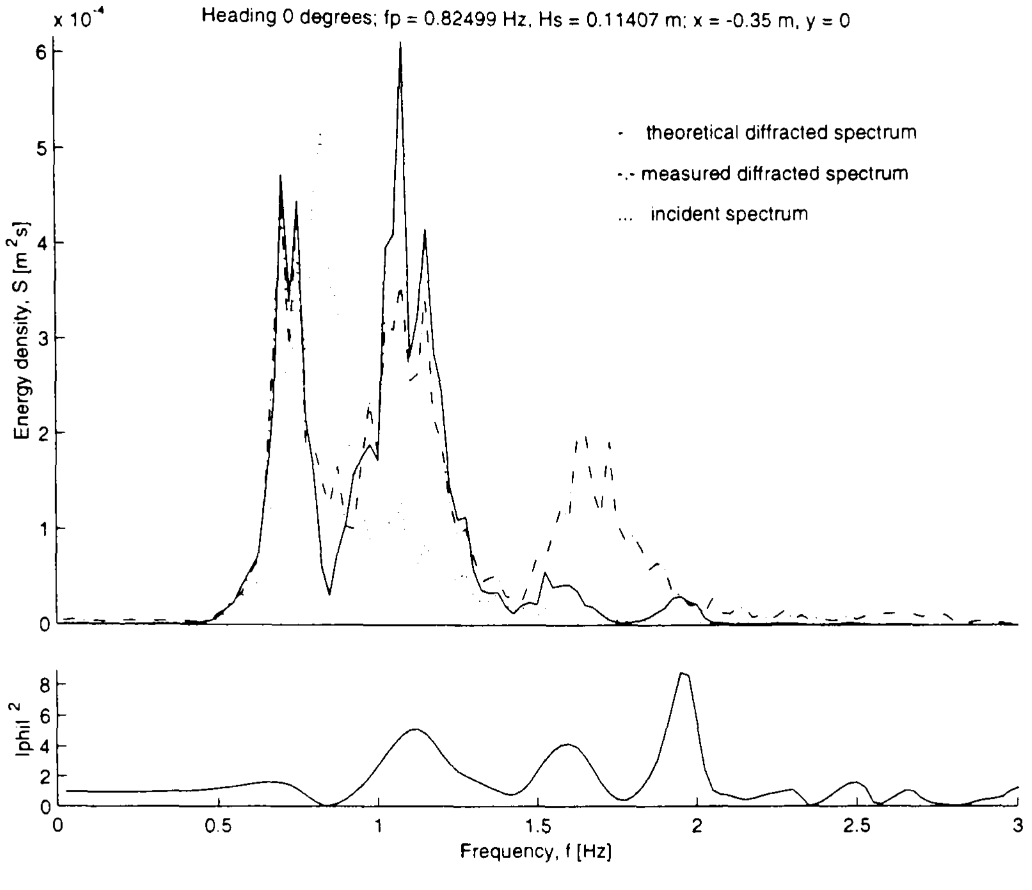

Figure 6.34. Spectral comparison and diffracted modification to incident spectrum at point $(-0.35\,\text{m}, 0)$; $f_i 1 H_s 1$ heading 0°

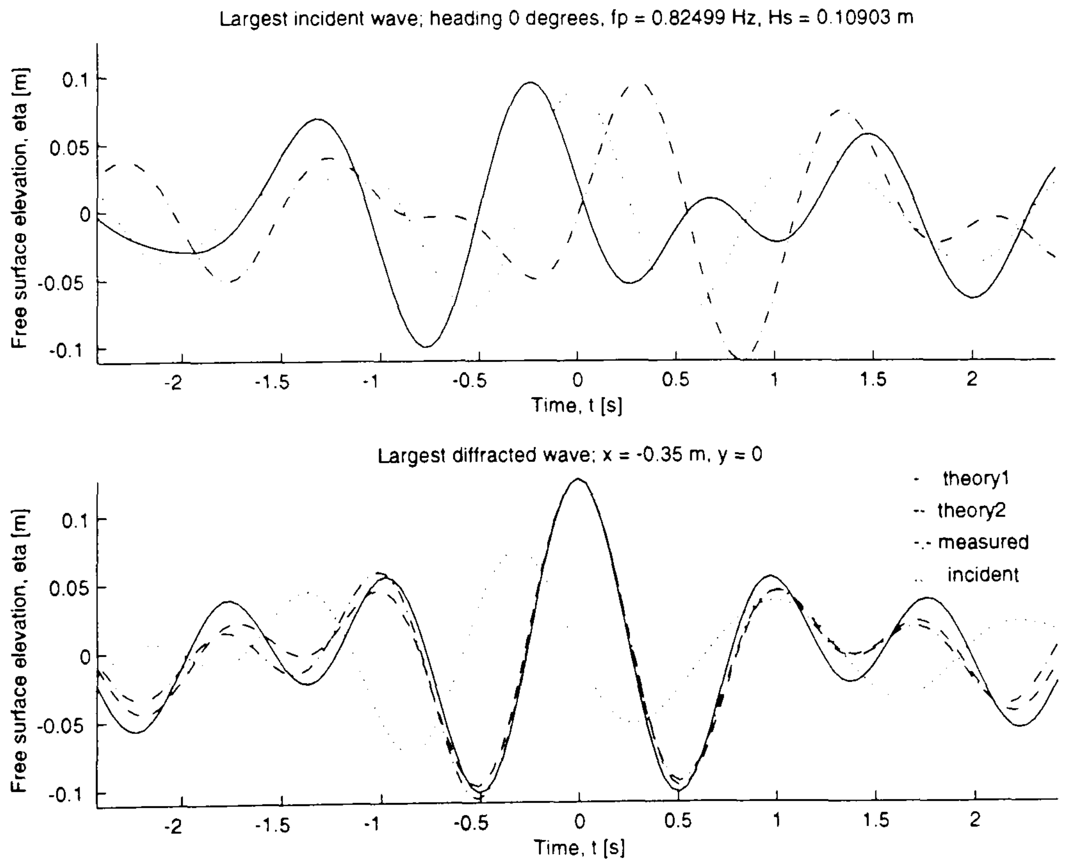

Figure 6.35. Incident and diffracted focused wave group comparison at point $(-0.35\text{ m}, 0)$; $f_i 1 H_s 1$ heading 0°

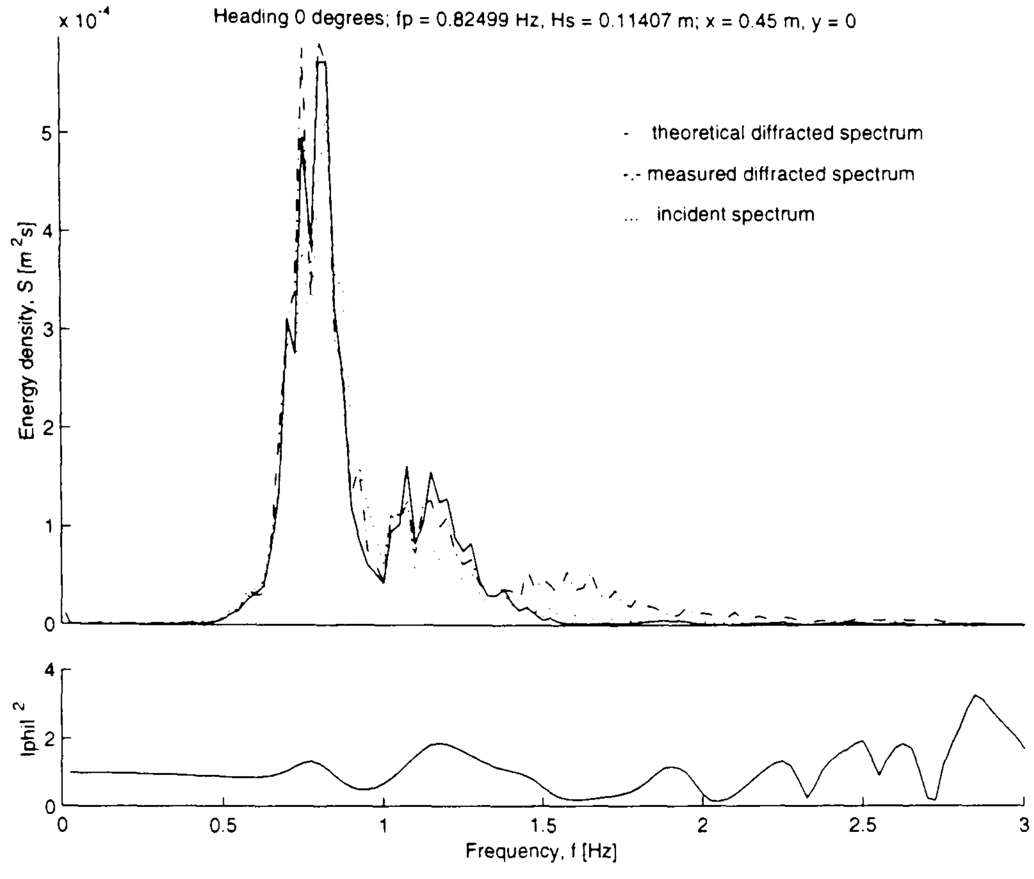

Figure 6.36. Spectral comparison and diffracted modification to incident spectrum at point $(0.45\ \text{m}, 0)$; $f_i 1 H_s 1$ heading 0°

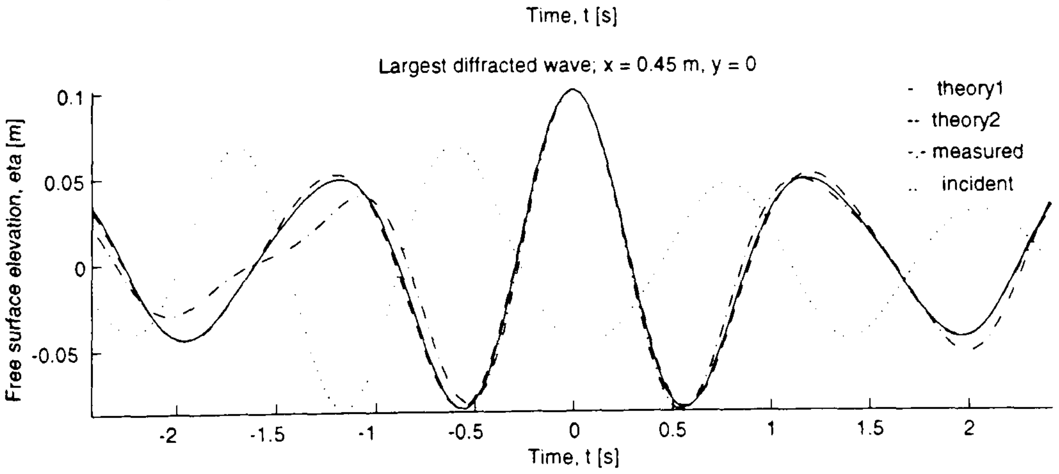

Figure 6.37. Incident and diffracted focused wave group comparison at point $(0.45\ \text{m}, 0)$; $f_i 1 H_s 1$ heading 0°

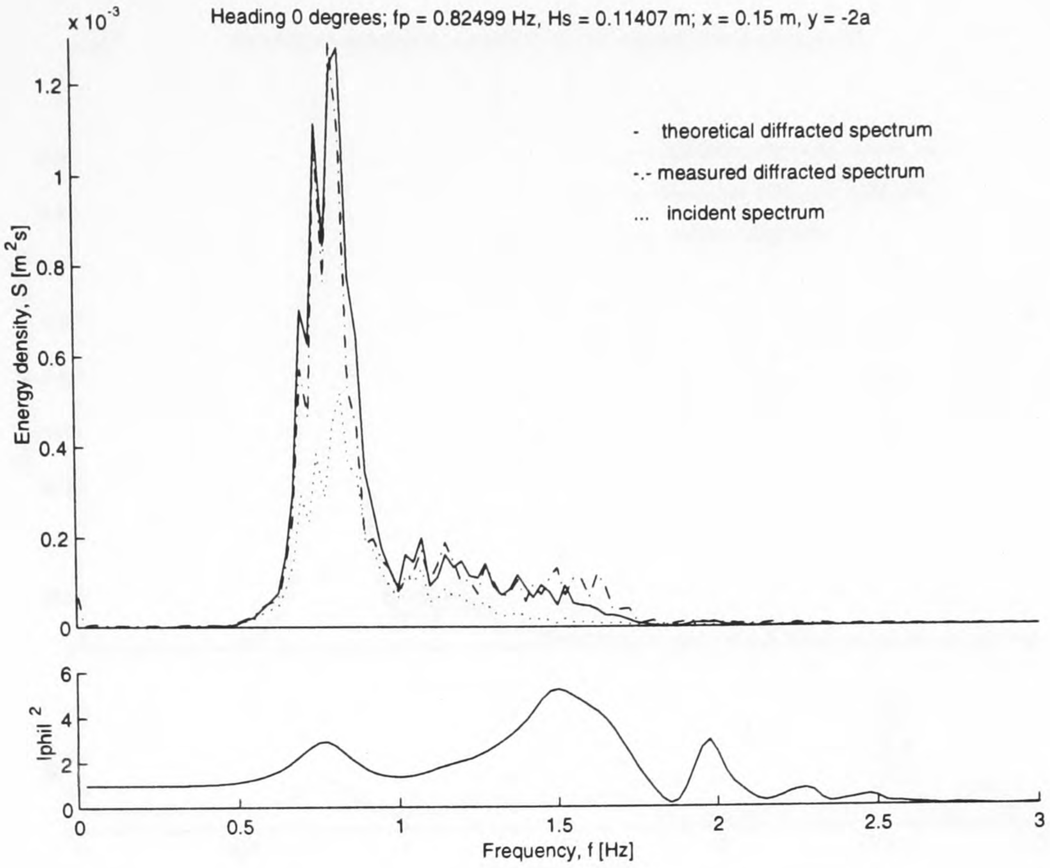

Figure 6.38. Spectral comparison and diffracted modification to incident spectrum at point $(0.15\,\mathrm{m}, -2a)$; $f_i 1 H_s 1$ heading 0°

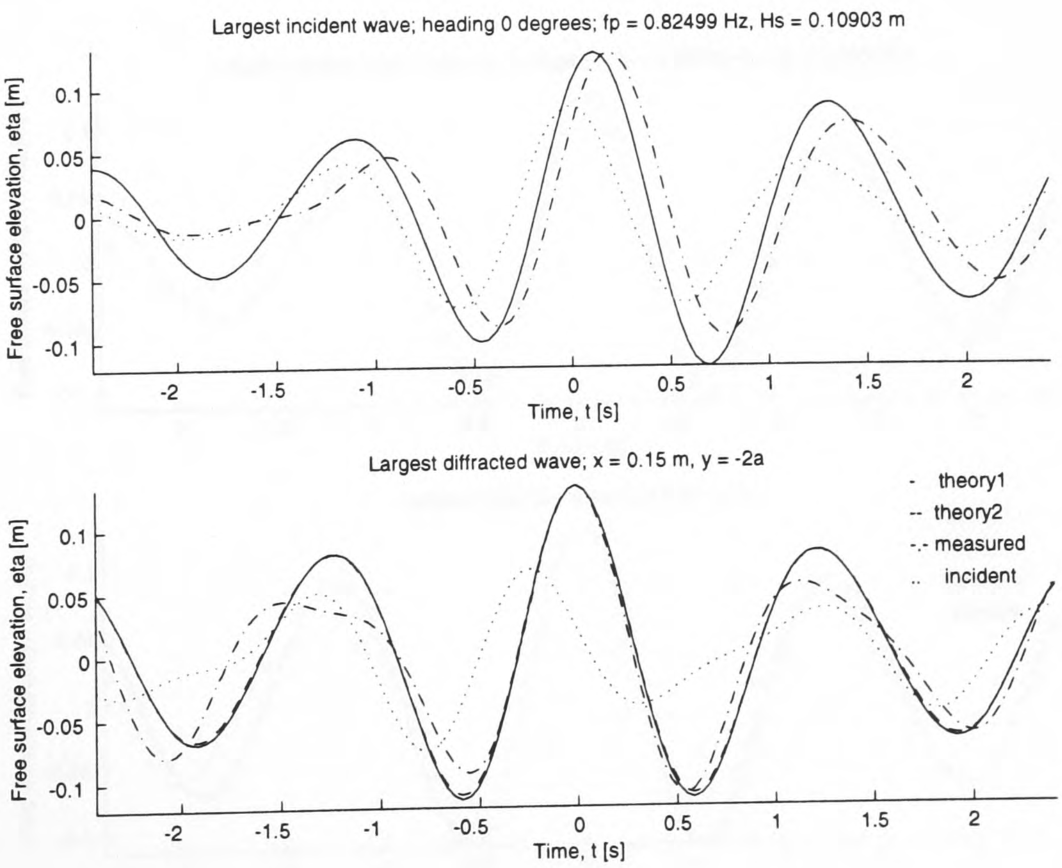

Figure 6.39. Incident and diffracted focused wave group comparison at point $(0.15\,\mathrm{m}, -2a)$; $f_i 1 H_s 1$ heading 0°

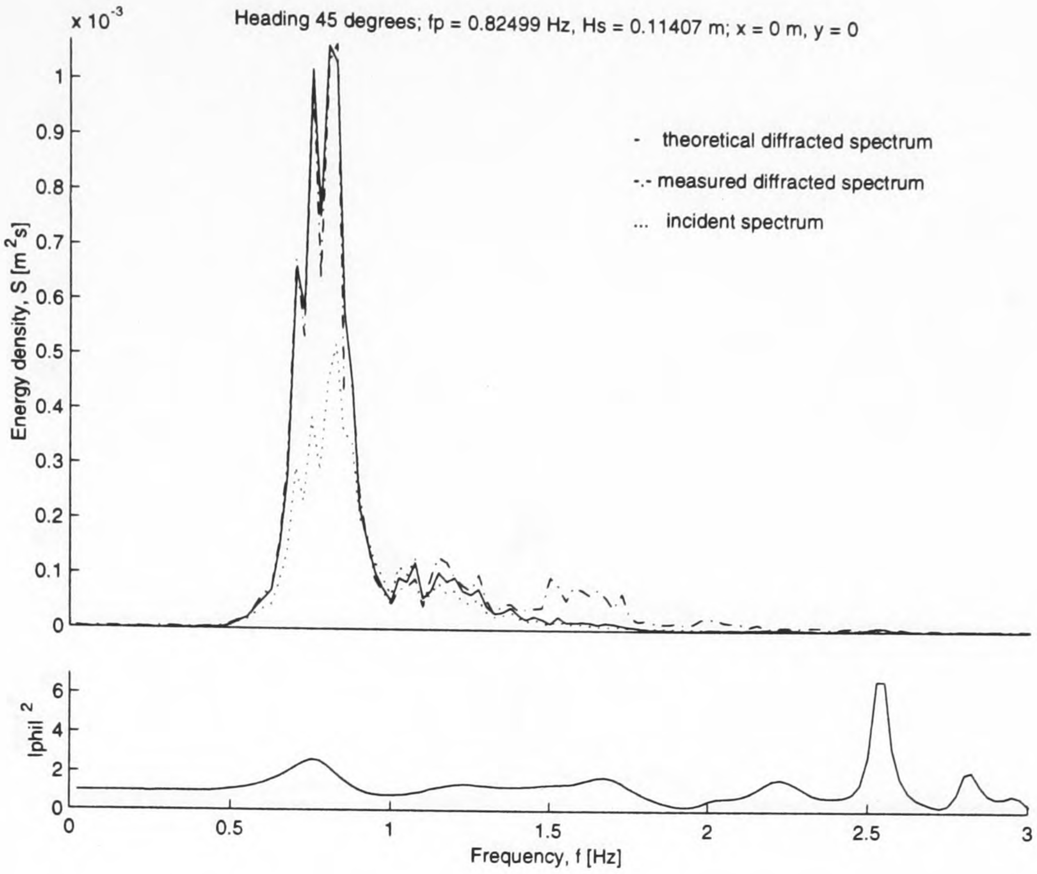

Figure 6.40. Spectral comparison and diffracted modification to incident spectrum at point (0 m, 0); $f_i 1 H_s 1$ heading 45°

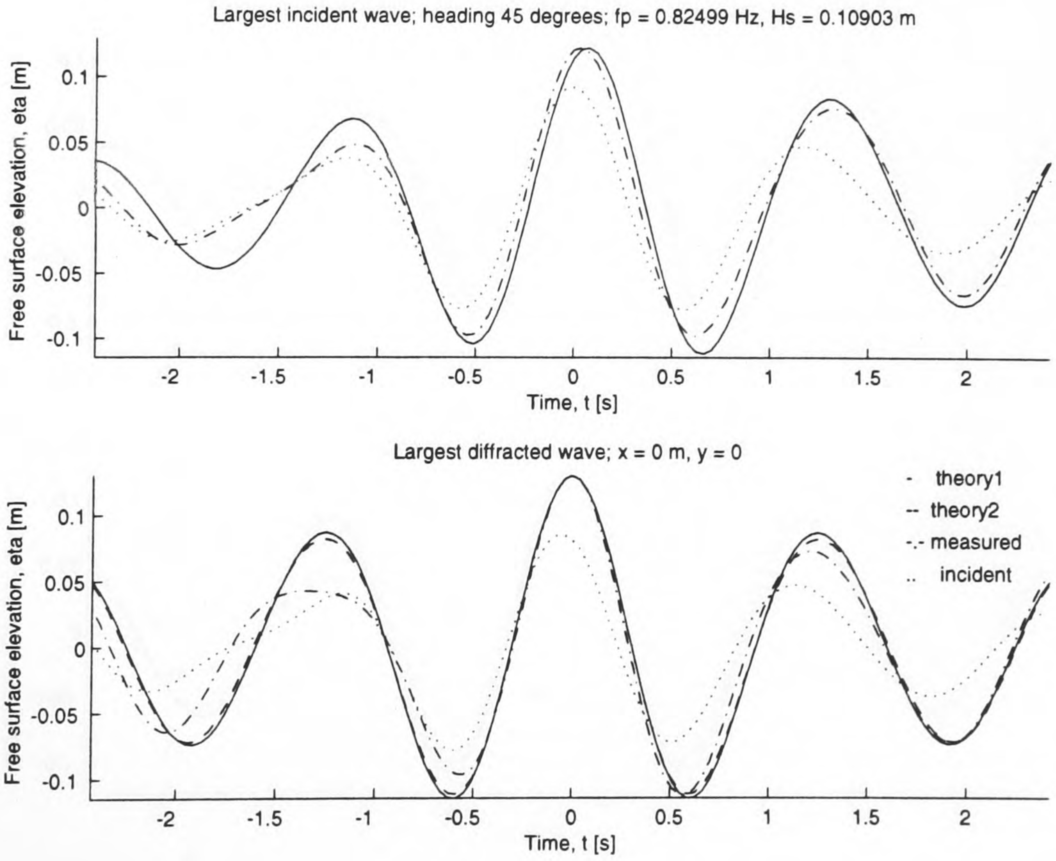

Figure 6.41. Incident and diffracted focused wave group comparison at point (0 m, 0); $f_i 1 H_s 1$ heading 45°

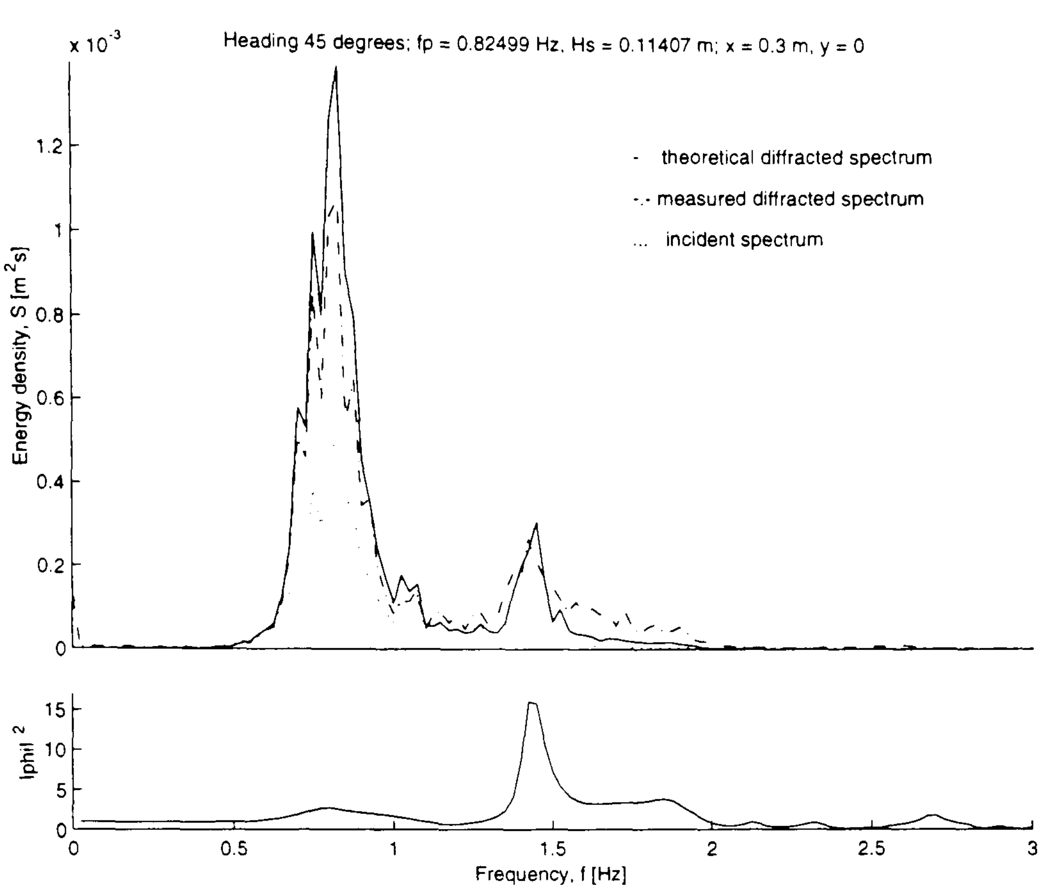

Figure 6.42. Spectral comparison and diffracted modification to incident spectrum at point $(0.3\,\mathrm{m}, 0)$; f_i1H_s1 heading 45°

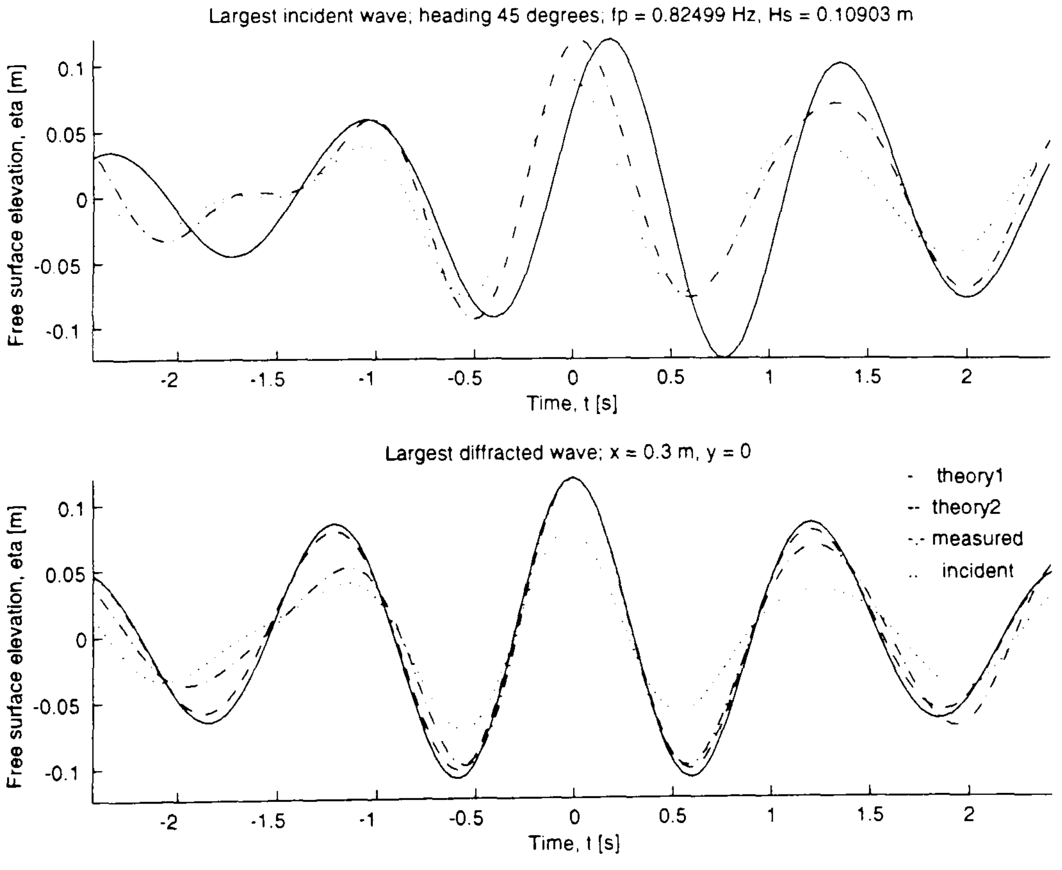

Figure 6.43. Incident and diffracted focused wave group comparison at point $(0.3\,\mathrm{m}, 0)$; f_i1H_s1 heading 45°

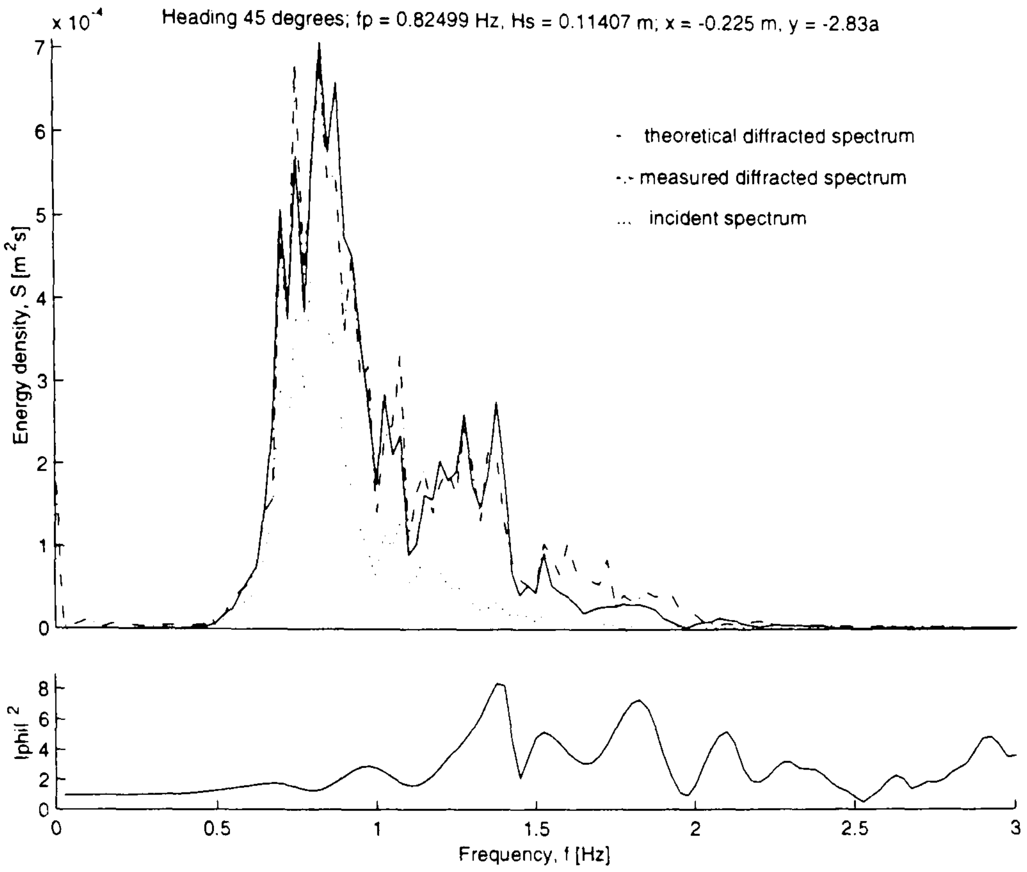

Figure 6.44. Spectral comparison and diffracted modification to incident spectrum at point $(-0.225\text{ m}, -2.83a)$; $f_i 1 H_s 1$ heading 45°

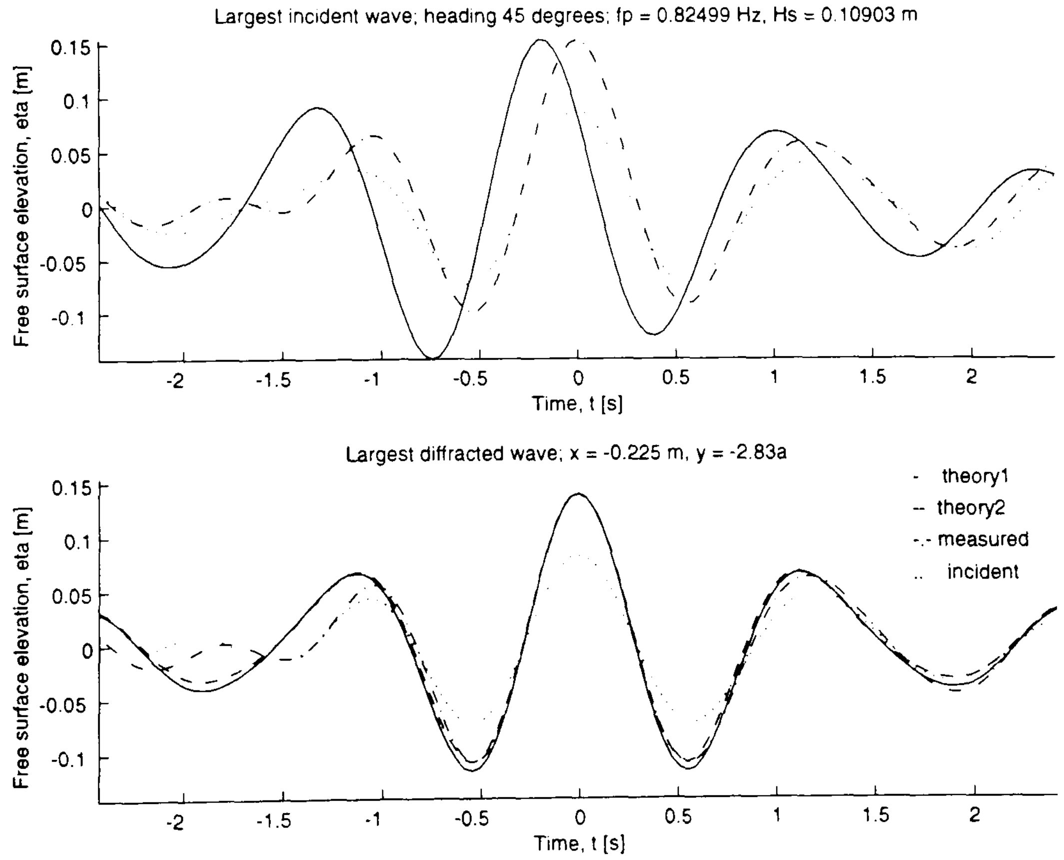

Figure 6.45. Incident and diffracted focused wave group comparison at point $(-0.225\text{ m}, -2.83a)$; $f_i 1 H_s 1$ heading 45°

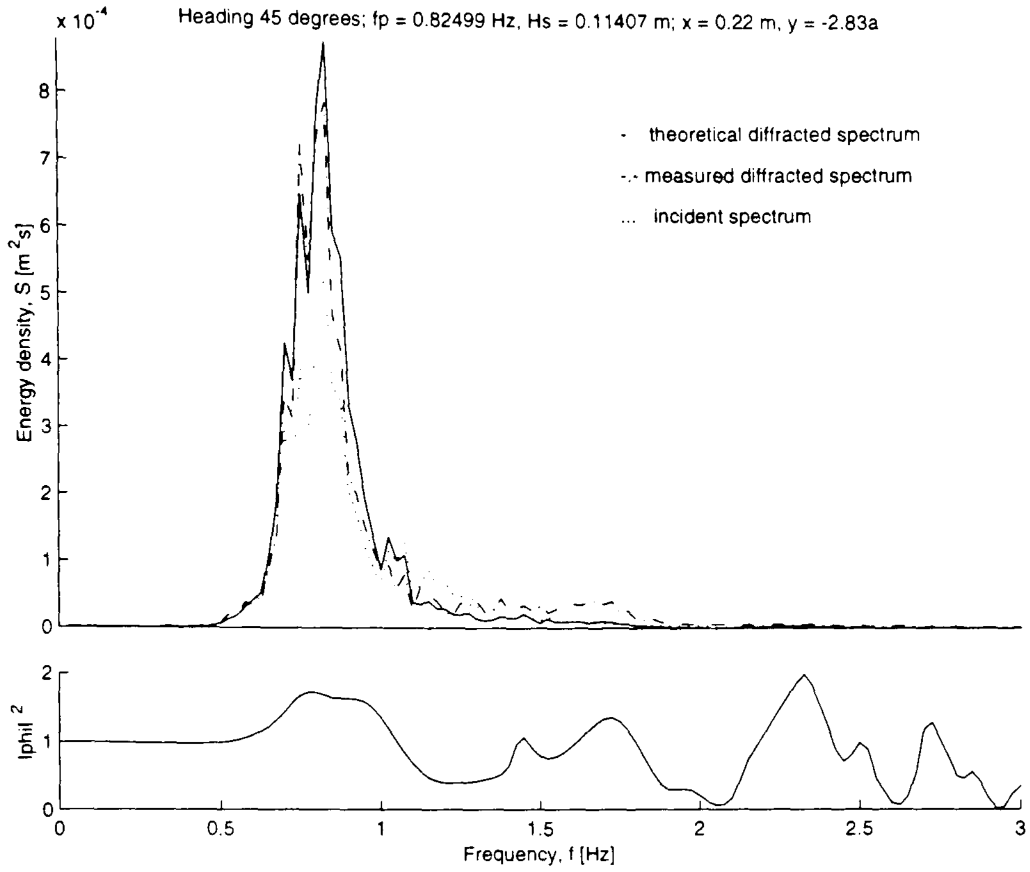

Figure 6.46. Spectral comparison and diffracted modification to incident spectrum at point $(0.22\,\mathrm{m}, -2.83a)$; f_i1H_s1 heading 45°

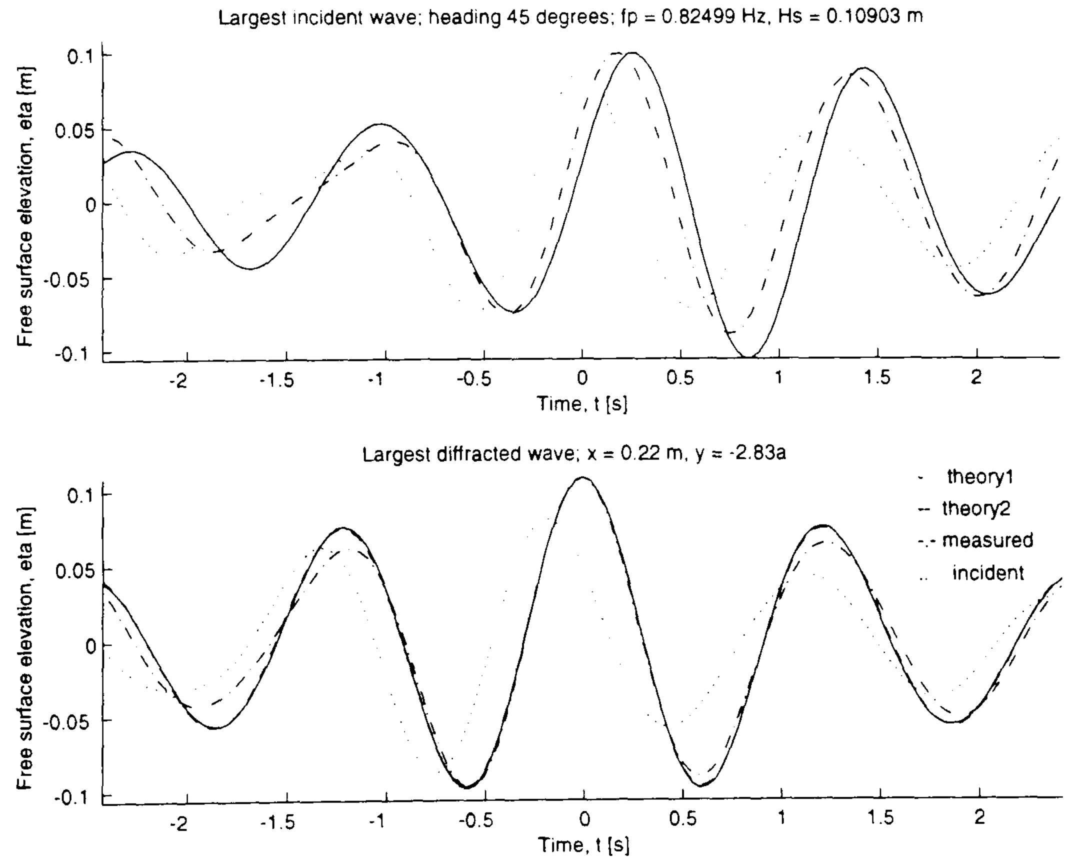

Figure 6.47. Incident and diffracted focused wave group comparison at point $(0.22\,\mathrm{m}, -2.83a)$; f_i1H_s1 heading 45°

Chapter 7
Conclusions and Recommendations

7.1 Linear Diffraction Theory

- Linear diffraction theory for arrays of bottom mounted circular cylinders (Linton & Evans 1990) has been reviewed. An alteration in the derivation yielded a better conditioned matrix for the solution of the complex coefficients A_n^j.
- Linear diffraction theory has been extended to the treatment of incident focused wave groups and random seas for cylinder arrays.
- A simplified expression has been derived for the maximum possible free surface elevation $\eta_m(x, y)$ achieved by a focused wave group of known amplitude components but arbitrary phase angle and arbitrary focus point.
- Mathematical formulations are presented for the effects of linear diffraction on the energy density in an incident spectrum. Hence, modified free surface elevation statistics may be computed in the vicinity of a multicolumn structure.

7.2 Creamer Nonlinear Transform

- By calculating the effects of bound waves as non-resonant interactions, the Creamer nonlinear transform (CNT) has been shown to be an effective tool for simulating the nonlinear free surface elevation from a given linear free surface spatial profile.
- Fully nonlinear kinematics computed through the CNT have shown excellent agreement with the numerical wave tank (NWT) results of Bateman *et al.* (1999a). Thus, for a given nonlinear free surface elevation spatial profile, the associated free surface kinematics may be computed to a high degree of accuracy.
- The primary limitation of the CNT has been identified as its inability to predict the long time scale evolution of steep waves.
- In the analysis of focused wave group NWT data (Bateman *et al.* 1999a), the CNT has been shown as a useful tool in the identification of bound waves for the study of resonant wave-wave interactions.

- For focused wave groups of high steepness, resonant wave-wave interactions have been shown to modify both amplitude and celerity of individual wavenumber components over long time scales.
- The reluctance of steep localised wave groups to defocus following the formation of an extreme event has been observed for uni-directional deep water waves.

7.3 Experimental Procedures

- Free surface elevation $\eta(t)$ has been measured effectively at multiple locations in the vicinity of a large surface piercing structure.
- Use of resistance wave probes to define the free surface precludes the measurement of spray or foam generated during particularly violent events.

7.4 Comparisons between Experimental and Theoretical Results

7.4.1 Regular waves

- Contour plots of the diffracted free surface amplitude have been produced through linear diffraction theory. These have been shown to provide excellent predictions of visually observable regions of enhanced wave activity.
- Linear diffraction theory has been shown to be a good model of the first order free surface elevation response, particularly for incident waves of low steepness. However, from the results presented, it is also clear that higher order diffraction effects are significant, even for waves of relatively low steepness.
- As predicted by linear theory, it has been shown experimentally that global features present in first order amplitude profiles shift consistently upwave with increases in incident wavelength. This has also been observed for experimentally computed profiles of local mean sea level, a second order quantity.
- Through both video observations and data analysis, highly nonlinear wave breaking has been identified as induced by diffraction for high steepness incident waves.
- With local wave elevation enhancement, increased mean sea level (set up) at the model centre, and diminished

far field radiation, near-trapping has been observed experimentally for ka within 0.64% of a second order near trapping event (Malenica *et al.* 1999) for the 45° heading tests.

- However, the experimentally measured second order contributions to free surface elevation were significantly lower than predicted by the semi-analytical diffraction theory of Malenica *et al.* (1999). This discrepancy may be attributed to either the aforementioned diffraction induced breaking of steep incident waves, or the insufficient length of the data record, or the sensitivity of the near-trapping phenomenon to small changes in ka.
- For this near-trapping frequency, corresponding tests at heading 0° have yielded high far field radiation and decreased mean sea level (set down) at the model centre. As observed visually for this less sheltered geometry, this is indicative of increased wave scattering in the far field associated with radial flow from the model centre.

7.4.2 Irregular waves

- Linear diffraction theory for random seas (developed herein) has been shown as a good method for estimating the profiles of the measured spectra. However, inclusion of higher order diffraction theory would clearly improve the correlation between measured and theoretical spectra.
- Statistics computed from these theoretical diffracted wave spectra have been shown to reproduce global trends in the experimental data. Consistent discrepancies between the theoretical and experimental results may be attributed to nonlinear interactions. Again, it is clear that higher order diffraction theories must be investigated in order to better reproduce the observed experimental behaviour.
- Linear diffraction theory for focused wave groups (also developed herein) has been demonstrated to be an effective model for linearised extreme events, produced through crest-trough subtraction.
- For both incident and diffracted focused wave groups, the most extreme events recorded in the experimental data have shown improved agreement with theoretical predictions after the focus time ($t = 0$).
- High frequency energy components related to nonlinear interactions have been observed in the measured diffracted spectra.
- This nonlinearity has been shown to be particularly dominant at locations between the upwave cylinders for

the 0° heading tests. This is in agreement with results from the regular wave tests and as demonstrated in the BEM results of Ferrant (1999).

7.5 Opportunities for Further Research

The preceding investigations have drawn attention to some areas which should be pursued in future investigations. These include:

- Space to time transformations have been investigated through the Creamer nonlinear transform (i.e. starting with a nonlinear free surface spatial profile, an equivalent nonlinear time history is produced). A more significant result would be the reverse of this, beginning with temporal information (perhaps at multiple locations) and reconstructing the free surface at multiple locations at an instant of time. While the CNT alone may be capable of this for short time scales, some method of accounting for resonant interactions between different wavenumber components must be developed in order to simulate the evolution of steep waves over long time intervals.
- More comprehensive comparisons between second order amplitude measured during the regular wave tests should be made with semi-analytical second order diffraction theory, such as the method presented by Malenica *et al.* (1999). In addition, comparison of first, second, and third order responses may also be made with other fully nonlinear numerical approaches, such as the BEM method of Ferrant (1999) and the modified MAC method of Park *et al.* (1999). This should provide some indication of the overall effectiveness of the various nonlinear numerical schemes for predicting the behaviour of steep regular waves.
- Significant additional analysis may be made of the irregular wave data from the experiments presented herein. This could include the effects of diffraction on waves of varying steepness. However, such analysis would be facilitated by additional experimental data representing the inverted initial condition and thus allowing better linearisation through crest-trough subtraction of corresponding events. Video image processing could be conducted to assess runup and splashing for extreme events and for comparison with the results presented here. In addition, whilst development of higher order diffraction theory for random seas is a significant challenge, valuable comparison could be made with the experimental results contained herein.

- Finally, this thesis has focused on free surface elevation as a strict test of diffraction theory. While wave phase and celerity have been discussed and studied at several points, these phenomena have not been fully investigated. The relationship between time of occurrence for incident and diffracted first, second, and third harmonic wave components remains to be examined. These issues need to be addressed for both the regular and irregular wave tests described herein.

References

BALDOCK, T. E., SWAN, C. & TAYLOR, P. H. 1996 A laboratory study of nonlinear surface waves on water. *Phil. Trans. R. Soc. Lond.* A **354**, 649-676.

BATEMAN, W. J. D., SWAN, C. & TAYLOR, P. H. 1999a Efficient numerical simulation of directionally-spread water waves. Paper in preparation for *J. Fluid Mech.*

BATEMAN, W. J. D., SWAN, C. & TAYLOR, P. H. 1999b Steep multi-directional waves on constant water depth *18th Int. Conf. Offshore Mechanics and Arctic Eng.* OMAE99/S&R-6463.

CALLAN, M., LINTON, C. M. & EVANS, D. V. 1991 Trapped modes in two-dimensional wave guides. *J. Fluid Mech.* **229**, 51-64.

CELEBI, M. S., KIM, M. H. & BECK, R. F. 1998 Fully nonlinear 3D numerical wave tank simulation. *J. Ship Res.* **42**, 33-45.

CHAU, F. P. 1989 The second order velocity potential for diffraction of waves by fixed offshore structures. PhD thesis, University College London, London University.

CHAU, F. P. & EATOCK TAYLOR, R. 1992 Second order wave diffraction by a vertical cylinder. *J. Fluid Mech.* **240**, 571-599.

CHEN, X. B., MOLIN, B. & PETITJEAN, F. 1995. Numerical evaluation of the springing loads on tension leg platforms. *Marine Structures.* **8**, 501-524.

CREAMER, D. B., HENYEY, F., SCHULT, R. & WRIGHT, J. 1989 Improved linear representation of ocean surface waves. *J. Fluid Mech.* **205**, 135-161.

DEAN, R. G. & DALRYMPLE, R. A. 1991 *Water Wave Mechanics for Engineers and Scientists.* Vol. 2. World Scientific.

EATOCK TAYLOR, R. & HUANG, J. B. 1997a Second order wave diffraction by an axisymmetric body in monochromatic waves. *Proc. R. Soc. Lond.* A **453**, 1515-1541.

EATOCK TAYLOR, R. & HUANG, J. B. 1997b Semi-analytical solution for second order diffraction by a vertical cylinder in bichromatic waves. *J. Fluids and Structures* **11**, 465-484.

EATOCK TAYLOR, R. & SINCOCK, P. 1989 Wave upwelling effects in TLP and semisubmersible structures. *Ocean Eng.* **16**, (3) 281-306.

EATOCK TAYLOR, R. & WU, G. X. 1997 Interaction of steep waves with offshore structures. *Phil. Trans. R. Soc. Lond.* A **355**, 593-605.

EVANS, D. V., LEVITIN, M. & VASSILIEV, D. 1994 Existence theorems for trapped modes. *J. Fluid Mech.* **261**, 21-31.

EVANS, D. V. & LINTON, C. M. 1991 Trapped modes in open channels. *J. Fluid Mech.* **225**, 153-175.

EVANS, D. V. & PORTER, R. 1997a Trapped modes about multiple cylinders in a channel. *J. Fluid Mech.* **339**, 331-359.

EVANS, D. V. & PORTER, R. 1997b Near-trapping of waves by circular arrays of vertical cylinders. *Applied Ocean Research* **19**, 83-99.

FERRANT, P. 1999 Seakeeping simulations in nonlinear waves. *Paper presented at the 7th Int. Conf. on Numer. Ship Hydro., Nantes, July 1999.*

HAVELOCK, T. H. 1940 The pressure of water waves upon a fixed obstacle. *Proc. R. Soc. Lond.* A **175**, 409-421.

HIRT, C. W. & NICHOLS, B. D. 1981 Volume of fluid (VOF) method for the dynamics of free boundaries. *J. Comp. Phys.* **39**, 201-225.

HUANG, J. B. & EATOCK TAYLOR, R. 1996a Semi-analytical solution for second order wave diffraction by a truncated circular cylinder in monochromatic waves. *J. Fluid Mech.* **319**, 171-196.

HUANG, J. B. & EATOCK TAYLOR, R. 1996b Second order interaction between waves and multiple bottom-mounted vertical circular cylinders. *Proc. 11th Workshop on Water Waves and Floating Bodies, Hamburg.*

HUNG, S. M., SINCOCK, P. & EATOCK TAYLOR, R. 1987 Frequency domain analysis of upwelling effects. *Final Report of the Managed Programme of Research into Dynamics of Compliant Structures.* Project 1.

HUSEBY, M. & GRUE, J. 1998 An experimental investigation of higher harmonic forces on a vertical cylinder in long waves. *Proc. 13th Workshop on Water Waves and Floating Bodies, Aalphen an den Rijn.*

JOHANNESSEN, T. B. & SWAN, C. 1998 Steep transient waves in a directionally spread sea. *Ocean Wave Kinematics, Dynamics and Loads on Structures, ASCE Proc. of the 1998 Int. OTRC Symp. Houston.* 17-24.

JONATHAN, P. & TAYLOR, P. H. 1995 Irregular, nonlinear waves in a spread sea. *ASME Trans. J. of Offshore Mech. and Arctic Eng.* **119**, (1) 37-41.

JONES, D. S. 1953 The eigenvalues of $\nabla^2 u + \lambda u = 0$ when the boundary conditions are given on semi-infinite domains. *Proc. Camb. Phil. Soc.* **49**, 668-684.

JOHNSON, R. A. & WICHERN, D. W. 1998 *Applied Multivariate Statistical Analysis.* Ed. 4. New Jersey: Prentice Hall.

KAGEMOTO, H. & YUE, D. K. P. 1986 Interactions among multiple three-dimensional bodies in water waves: an exact algebraic method. *J. Fluid Mech.* **166**, 189-209.

KINSMAN, B. 1965 *Water Waves: Their Generation and Propagation on the Ocean Surface.* Prentice-Hall, Inc., Englewood Cliffs, NJ.

KIM, M. 1993 Interaction of waves with *N* vertical circular cylinders. *J. Waterway, Port, Coastal, and Ocean Eng.* **199**, (6) 671-689.

KIM, M. & YUE, D. K. P. 1989 The complete second-order diffraction solution for an axisymmetric body. Part 1. Monochromatic incident waves. *J. Fluid Mech.* **205**, 235-264.

KIM, M. & YUE, D. K. P. 1990 The complete second-order diffraction solution for an axisymmetric body. Part 2. Bichromatic incident waves and body motions. *J. Fluid Mech.* **211**, 557-593.

KRIEBEL, D. L. 1990 Nonlinear wave interaction with a vertical circular cylinder. Part 1. Diffraction theory. *Ocean Eng.* **17**, (4) 345-377.

KRIEBEL, D. L. 1990 Nonlinear wave interaction with a vertical circular cylinder. Part 2. Wave Runup. *Ocean Eng.* **19**, (1) 75-99.

LIGHTHILL, J. 1979 Waves and hydrodynamic loading. *Proc. 2nd Int. Conf. Behaviour of Offshore Structures.* **1**, 1-40.

LINDGREN, G. 1980 Extreme values and crossings for the chi-squared and other functions of multi-dimensional Gaussian processes. *Adv. Appl. Prob.* **12**, 746.

LINTON, C. M. & EVANS, D. V. 1990 The interaction of waves with arrays of vertical circular cylinders. *J. Fluid Mech.* **215**, 549-569.

LONGUET-HIGGINS, M. S. 1966 On the trapping of wave energy round islands. *J. Fluid Mech.* **29**, 781-821.

MALENICA, Š. 1997 Second order interaction of water waves with arrays of vertical cylinders. *Proc. 2nd Congress of Croatian Society of Mechanics, Supetar, Croatia,* pp. 599-606.

MALENICA, Š., EATOCK TAYLOR, R. & HUANG, J. B. 1999 Second order water wave diffraction by an array of vertical cylinders. *J. Fluid Mech.* **390**, 349-373.

MALENICA, Š. & MOLIN, B. 1995 Third-harmonic wave diffraction by a vertical cylinder. *J. Fluid Mech.* **302**, 203-229.

MANIAR, H. D. & NEWMAN, J. N. 1997 Wave diffraction by a long array of cylinders. *J. Fluid Mech.* **339**, 309-330.

McAMY, R. C. & FUCHS, R. A. 1954 Wave forces on a pile: a diffraction theory. *Tech. Memo. No. 69, U.S. Army Board, U.S. Army Corps of Engineers.*

McIVER, P. & EVANS, D. V. 1984 Approximation of wave forces on cylinder arrays. *Applied Ocean Research.*

6, (2) 101-107.

McIVER, P. & PEREGRINE, D. H. 1981 Comparison of numerical and analytical results for waves that are starting to break. *Proc. Int. Symp. On Hydrodyn. In Ocean Eng., Trondheim, Norway.* 203-215.

MEI, C. C. 1978 Numerical methods in water-wave diffraction and radiation. *Ann. Rev. Fluid Mech.* **10**, 393–416.

MEI, C. C. 1983 *The Applied Dynamics of Ocean Surface Waves.* Ed. 2. John Wiley & Sons.

MERCIER, R. S. & NIEDZWECKI, J. M. 1994 Experimental measurement of second-order diffraction by a truncated vertical cylinder in monochromatic waves. *Proc. 7th Int. Conf. Behavior of Offshore Structures.* **2**, 265-287.

MOE, G. (Ed.) 1993 Vertical resonant motions of TLPs. Final Report. *NTH Rep.* R-1-93.

MOLIN, B. 1979 Second order diffraction loads upon three-dimensional bodies. *Applied Ocean Research.* **1**, (4) 197-202.

NEWLAND, D. E. 1993 *Random Vibrations, Spectral & Wavelet Analysis.* Ed. 3. Singapore: Longman.

OWEN, D. G. & PADILLA PEREZ, I. A. 1987 Experimental investigation of upwelling and interaction effects within blocked structures. *Vol. 1, Final Report, Programme of Research into Dynamics of Compliant Structures 1985-87.*

PARK, J.-C., KIM, M. H. & MIYATA, H. 1999 Fully non-linear free-surface simulations by a 3D numerical wave tank. *Int. J. Numer. Meth. Fluids* **29**, 685-703.

RENARDY, Y. 1983 Trapping of water waves above a round sill. *J. Fluid Mech.* **132**, 105-118.

SIMON, M. J. 1982 Multiple scattering in arrays of axisymmetric wave-energy devices. Part 1. A matrix method using a plane-wave approximation. *J. Fluid Mech.* **120**, 1-25.

SOMMERFELD, A. 1949 *Partial Differential Equations in Physics.* Academic Press Inc.

SROKOSZ, M. A. & EVANS, D. V. 1979 A theory for wave-power absorption by two independently oscillating bodies. *J. Fluid Mech.* **90**, 337-362.

SWAN, C., TAYLOR, P. H. & VAN LANGEN, H. 1997 Observations of wave-structure interaction for a multi-legged concrete platform. *Applied Ocean Research.* **19**, (5-6) 309-327.

TAYLOR, P. H. 1992 On the kinematics of large ocean waves. *Proc. 6th Int. Conf. Behaviour of Offshore Structures.* **1**, 134-145.

TAYLOR, P. H. & HAAGSMA I. J. 1994 Focusing of steep wave groups on deep water. *Proc. Int. Symp. Waves - Physical and Numerical Modelling, U. British Columbia, Vancouver.* **2**, 862-870.

TAYLOR, P. H. 1998 The Creamer transform - a non-linear model for steep waves on deep water. *Proc. 17th Int. Conf. Offshore Mechanics and Arctic Eng.* OMAE98/S&R-1422.

TAYLOR, P. H., OHL, C. O. G., & SAUVEE, J. 1999 Focussed wave groups I: Local structure, kinematics and the Creamer transform. *Proc. 18th Int. Conf. Offshore Mechanics and Arctic Eng.* OMAE99/S&R-6461.

TAYLOR, P. H. & OHL, C. O. G. 1999a Focussed wave groups II: Global nonlinearity and resonant wave-wave interactions. *18th Int. Conf. Offshore Mechanics and Arctic Eng.* OMAE99/S&R-6462.

TAYLOR, P. H. & OHL, C. O. G. 1999b The Creamer-transform: a realistic model for steep waves. *Proc. Workshop on Refined Flow and Transport Modelling in Shallow Water Environment, Budapest, 18-21 April, 1999.*

TAYLOR, P. H. & VIJFVINKEL, E. M. 1998 Focused wave groups on deep and shallow water. *Ocean Wave Kinematics, Dynamics and Loads on Structures, ASCE Proc. of the 1998 International OTRC Symposium, Houston,* 420-427.

TROMANS, P. S., ANATURK, A. R. & HAGEMEIJER, P. 1991 A new model for the kinematics of large ocean waves: Application as a design wave. *Proc. 1st Int. Offshore and Polar Engineering Conf., Edinburgh.* **3**, 64-71.

TWERSKY, V. 1952 Multiple scattering of radiation by an arbitrary configuration of parallel cylinders. *J. Acoust. Soc. Am.* **24**, (1) 42-45.

URSELL, F. 1951 Trapping modes in the theory of surface waves. *Proc. Camb. Phil. Soc.* **47**, 347-358.

URSELL, F. 1987 Mathematical aspects of trapping modes in the theory of surface waves. *J. Fluid Mech.* **183**, 421-437.

UTSUNOMIYA, T. & EATOCK TAYLOR, R. 1999 Trapped modes around a row of circular cylinders in a channel. *J. Fluid Mech.* **386**, 259-279.

VAN DE GRAAF, J. W. & TROMANS, P. S. 1991 Statistical verification of predicted loading and ultimate strength against observed damage for an offshore structure. *Proc. of the 23rd Offshore Technology Conference, Houston.*

YEUNG, R. W. 1982 Numerical Methods in Free Surface Flows. *Ann. Rev. Fluid Mech.* **14**, 395-442.

AppendixA
Glossary

air gap	the vertical distance from the underside of an offshore platform to the highest wave crest elevation from extreme design storm conditions
beach	passive wave absorbers that minimize energy reflection in offshore wave basins
BEM	Boundary Element Method
BIE	Boundary Integral Element
BSE	Boundary Series Element
CNT	Creamer Nonlinear Transform
DBIEM	Desingularized Boundary Integral Equation Method
downwave	in the direction of the incident wave ray
extreme wave	also freak wave or NewWave, the random generation of a large crest from a wave spectrum due to the formation of a focused wave group
first order	elsewhere first-order; used to indicate first harmonic, a response at the incident frequency, in some chapters
focused wave group	a group of large waves formed from the spectral components of a random sea that come into phase and coincide
GBS	Gravity Based Structure
inboard	direction towards the model centre
incident wave ray	a dimensionless vector indicating the direction of propagation (i.e. energy propagation) of a wave
irregular waves	random waves generated from a wave spectrum of many frequency components
JONSWAP	JOint North Sea WAve Program; used to refer to a standardised spectral shape
linear	first-order
longitudinal	direction parallel to the incident wave ray (here parallel to the y-axis)
MAC	Marker And Cell method
NS	Navier-Stokes
near trapping	the near containment of energy at specific frequencies for a given structural geometry with minimal radiation in the far field
nonlinear	elsewhere non-linear; of order higher than linear
NWT	Numerical Wave Tank
offset cylinder(s)	centreline cylinders for the 45 degree heading tests
outboard	direction away from the cylinder centre
pdf	probability density function
regular waves	monochromatic waves (i.e. containing energy principally in one frequency component)
runup	local modification of the incident surface wave immediately adjacent to a hull form
second order	elsewhere second-order; used to indicate second harmonic, a response at twice the incident frequency, in some chapters
spatial	elsewhere spatial; in the distance domain; dependent on or varying with position in space
temporal	in the time domain; dependent on or varying with change in time
third order	elsewhere third-order; used to indicate third harmonic, a response at three times the incident frequency, in some chapters
TLP	Tension Leg Platform
transverse	direction perpendicular to the incident wave ray (here parallel to the x-axis)
trapping	for waves in a channel, the complete containment of energy at specific frequencies with no raditaion
upwave	directionally opposite to the incident wave ray
upwelling	local modification of the incident surface wave in the vicinity of a hull form
VOF	Volume Of Fluid method
wave probe	a stationary device measuring free surface elevation η as a function of time t

AppendixB
Nomenclature

a_j	radius of cylinder j in meters
A	incident wave amplitude in meters
A_n	amplitude of spectral component n
α	the maximum free surface elevation for a focused wave group extreme wave
d	water depth in meters
$E(x)$	the mean or expected value of random variable x
f	wave frequency in Hz ($f = \frac{1}{T} = \frac{\omega}{2\pi}$)
$f_0(z)$	depth attenuation function
$f(\omega_n, \beta_n)\, S(\omega_n)$	directional surface power spectrum
$f(x)$	pdf of the random variable x
$f(x \mid y, z)$	pdf of the random variable x given the occurrence of both y and z
g	acceleration due to gravity ($g \approx 9.80665 \frac{\text{m}}{\text{s}^2}$)
h	cylinder spacing parameter in meters (here $h = 2a$; centre to centre distance $2h$)
H_n	Hankel function of the first kind of order n
H_s	significant wave height in meters (average height of $\frac{1}{3}$ largest waves or $H_s = 4\sigma$)
i	square root of negative one ($\mathrm{i} = \sqrt{-1}$)
J_n	Bessel function of the first kind of order n
k	wavenumber in m^{-1} ($k = \frac{2\pi}{\lambda}$)
k_p	peak wavenumber of a spectrum
k_c	cutoff wavenumber for near trapping
kA	wave steepness
p	pressure in Pascals
N	the number of waves observed in a random sea
r_j, θ_j, z	cylindrical coordinates with origin at the centre of cylinder j in meters and radians
R_{jk}, α_{jk}	distance and angle between cylinders j and k in meters and radians
t	time in seconds
τ	time interval from the formation of an extreme event
T	wave period in seconds ($T = \frac{1}{f} = \frac{2\pi}{\omega}$)
T_p	peak wave period of a spectrum ($T_p = \frac{1}{f_p}$)
x, y, z	Cartesian coordinates with origin at the array centre
β	heading (angle between the x-axis and the incident wave ray in radians)
β_n	heading of spectral component n
η	free surface elevation in meters
$\dot{\eta}, \eta'$	time and spatial derivatives of the free surface elevation ($\dot{\eta} = \frac{\partial \eta}{\partial t}$; $\eta' = \frac{\partial \eta}{\partial x}$)
$\eta_d^\star$	expected and most probable free surface elevation in the vicinity of an extreme crest
η_m	maximum possible diffracted free surface elevation for a focused wave group
$\overline{\eta^2}$	mean square free surface elevation in m^2
$\overline{\eta_d^2}, \overline{\eta_i^2}, \overline{\eta_{td}^2}$	diffracted, incident, and theoretical diffracted mean square free surface elevation
$\eta_{IC}(t), \eta_{IT}(t)$	largest incident wave crest, deepest incident wave trough time histories
$\eta_{IC}^T(t)$	theoretical largest incident wave crest (comparison to $\eta_{IC}(t)$ above)
$\eta_D(t)$	diffracted free surface time history occurring at the same time as $\eta_{IC}(t)$ above
$\eta_D^T(t)$	theoretical diffracted free surface time history (comparison to $\eta_D(t)$ above)
$\eta_{DC}(t), \eta_{DT}(t)$	largest diffracted wave crest, deepest diffracted wave trough time histories
$\eta_{DC1}^T(t)$	theoretical comparison to $\eta_{DC}(t)$ above based on computed diffracted spectrum
$\eta_{DC2}^T(t)$	theoretical comparison to $\eta_{DC}(t)$ above based on measured diffracted spectrum
$\eta_I(t)$	incident free surface time history occurring at the same time as $\eta_{DC}(t)$
$\eta_{IC}^1(t)$	linearised largest incident wave crest time history ($\eta_{IC}^1(t) = \frac{\eta_{IC}(t) - \eta_{IT}(t)}{2}$)
$\eta_{DC}^1(t)$	linearised largest diffracted wave crest time history ($\eta_{DC}^1(t) = \frac{\eta_{DC}(t) - \eta_{DT}(t)}{2}$)

$\dot{\rho}, \ddot{\rho}$	correlation coefficients
$\rho(\tau)$	autocorrelation function
ρ_w	density of water in $\frac{\text{kg}}{\text{m}^3}$
ω	wave frequency in $\frac{\text{rad}}{\text{s}}$ ($\omega = 2\pi f = \frac{2\pi}{T}$)
ω_n	wave frequency of spectral component n
ω_c	cutoff wave frequency for near trapping
λ	wavelength in meters ($\lambda = \frac{2\pi}{k}$)
ϕ	diffraction coefficient (velocity potential with time dependence removed; dimensionless)
Φ	velocity potential in $\frac{\text{m}^2}{\text{s}}$
Re	real part of a complex quantity
$\mathbf{\nabla}$	gradient vector, $\mathbf{\nabla} = \langle \partial x, \partial y, \partial z \rangle$
ς_n	a random phase angle of spectral component n in radians
σ_i^2	the variance of random variable x_i
σ_{ij}	the covariance between random variables x_i and x_j
Σ	the covariance matrix